



**HAL**  
open science

# Wireless Inductive Charging for Electrical Vehicules : Electromagnetic Modelling and Interoperability Analysis

Mohammad Ibrahim

► **To cite this version:**

Mohammad Ibrahim. Wireless Inductive Charging for Electrical Vehicules : Electromagnetic Modelling and Interoperability Analysis. Electric power. Université Paris Sud - Paris XI, 2014. English. NNT : 2014PA112369 . tel-01127163

**HAL Id: tel-01127163**

**<https://theses.hal.science/tel-01127163>**

Submitted on 7 Mar 2015

**HAL** is a multi-disciplinary open access archive for the deposit and dissemination of scientific research documents, whether they are published or not. The documents may come from teaching and research institutions in France or abroad, or from public or private research centers.

L'archive ouverte pluridisciplinaire **HAL**, est destinée au dépôt et à la diffusion de documents scientifiques de niveau recherche, publiés ou non, émanant des établissements d'enseignement et de recherche français ou étrangers, des laboratoires publics ou privés.

UNIVERSITE PARIS-SUD

ÉCOLE DOCTORALE

Sciences et Technologie de l'Information, des Télécommunications  
et des Systèmes

Laboratoire de *Génie Electrique de Paris (LGEP)*

*DISCIPLINE : Génie Electrique*

THÈSE DE DOCTORAT

Soutenue le 09/12/2014

par

Mohammad IBRAHIM

Wireless Inductive Charging for Electrical  
Vehicles: Electromagnetic Modelling and  
Interoperability Analysis

Composition du jury :

*Examineur (Président):* François COSTA  
*Rapporteurs:* Jean-Paul FERRIEUX  
Christian VOLLAIRE  
*Directeur de thèse:* Lionel PICHON  
*Co-Encadrants :* Adel RAZEK  
Laurent BERNARD  
*Membres invites:* Olivier CAYOL  
Dimitrios LADAS

Professeur des Universités à l'IUFM Créteil  
Professeur des Universités à l'UJF Grenoble  
Professeur des Universités à l'ECL Lyon  
Directeur de Recherche CNRS  
Directeur de Recherche CNRS Emérite  
Ingénieur de Recherche CNRS  
Chef de Projet VE Technologie Avancée (Renault)  
Responsable Technique Système de Charge pour VE (Schneider  
Electric)



## ***Acknowledgment***

*The researches presented in this thesis memory have been developed in the LGEP laboratory (Laboratoire de Génie Electrique de Paris) under the project CINELI (Chargeur par Induction Electrique et Inteopérabilité) with industrial partners: Renault, Schneider Electric and Newtech Concept.*

*First of all, I want to especially thank my thesis director M. Lionel PICHON for his support during the three years of my PhD work. The most kind and quiet person I have met in France. I also thank my thesis co-supervisors M. Adel RAZEK (Big Boss) and M. Laurent BERNARD (my friend in football team) for their help and discussion in the field of electromagnetic modelling and radiation. My three supervisors made this memory to be valuable as best as could be with their scientific and humane qualities.*

*I don't forget, surely, to thank M. Eric LABOURE (who couldn't assist as an invited member in the jury as he was a reviewer for another PhD thesis at Toulouse) for his help and time for all explication and discussion in the domain of power electronics, especially for resonant converters and control of the EV battery charger.*

*I want to thank all persons of our industrial partners in CINELI project for all important discussions during the meetings and the practical tests. So my special thanks go to: M. Olivier CAYOL (Chief of the project, Renault) for the interoperability discussion and M. Jean-Luc BUTOT (Renault) who helped me in measurements and gave me the geometries of EV developed in CATIA. I want to thank also Mme. Jeanne HOIUVET for her help in the practical test at Renault laboratory. My thanks addressed also for M. Dimitrios LADAS (Schneider Electric) for all discussion in the package of EV charger. My thanks also for all persons in Newtech Concept company.*

*I thank, with honor, M. François COSTA for his acceptance to be the president of my thesis jury and his best remarks. I also thank, with honor, the two specialist reviewers of my thesis M. Jean-Paul FERRIEUX and M. Christian VOLLAIRE for their time for examining my thesis memory and their scientific contributions in this work that have enriched their valuable comments. Also I thank M. Olivier CAYOL and M. Dimitrios LADAS for their contribution as*

*invited members of the jury. So with all remarks of the jury members and their discussion at the day of the PhD defense, this thesis memory has been finished with its valuable scientific and practical form with its important contribution for an interoperable inductive EV charger. I had the honor to stand next these eight specialist persons of my thesis jury at the end of the PhD defense.*

*I want to thank also, all researchers and friends in LGEP for the discussion and for unforgettable three years during my work in this thesis memory. Many thanks for the administration office persons and the computer network responsible M. Olivier HUBERT and calculation server responsible M. Laurent SANTANDRIA. Thank you all LGEP members for the political discussion in the Palestinian case and your support for Palestine. Thanks for my friends for enjoying the time of playing football with full of vitality and activity during all matches. Our LGEP team won the champions league thanks to skilled players including the best goalkeeper.*

*I want to thank also, the members of the association Bezons-West BaniZeid that supports the Palestinian case, for their help in my family residence in France with the help of the mayor and the agreeable people of Bezons. Many thanks also for the department of electrical engineering members at Birzeit University/Palestine who gave me the opportunity to have a visiting professor position for two days before 6 months of the end of this PhD work.*

*For the amazing and nice moments that I never forget, here in France and in Palestine, I thank all my friends with all nationality. You are many, my friends, and I need a book to write down all of your names, thank you all for your wishes and support. Thank you for everything you had made to me and always what you do.*

*Finally, all thanks, with effusive feeling to my family in Palestine, my mother, sisters and my brother and all my nephews. Specially, thanks for who always stands beside me and encourages me, my lovely wife. Surely, for our gift, my beloved son who was born during the writing of this memory. And TO THE SOUL OF MY FATHER.*

*JE VOUS REMERCIE CHALEUREUSEMENT, YOU ARE ALL IN MY HEART*

*Mohammad IBRAHIM*

## ***Table of Contents***

Table of Contents .....	iii
List of Figures .....	vii
List of Tables.....	xv
Abstract .....	xvii
Résumé.....	xviii
General Introduction .....	1
Chapter I : Global View .....	7
I.1. Introduction .....	8
I.2. Inductive Coupling (IC) .....	9
I.2.a. Inductive Coupling Transformer (ICT) .....	10
I.2.b. ICT Electrical Model .....	12
I.2.c. ICT Modelling for Parameter and Performance Characterization.....	14
I.3. Capacitive Coupling (CC).....	17
I.4. Compensation of Inductive Behavior and Resonant Converter .....	18
I.4.a. Inductance Compensation and Resonance Frequency.....	18
a) SS Leakage Compensation .....	20
b) SS Self Compensation .....	21
c) SP Compensation.....	21
I.4.b. Resonant Converters.....	22
I.5. Battery .....	23

## Table of Contents

---

I.5.a. Battery Characteristics.....	23
I.5.b. Modelling.....	24
I.5.c. Charging Profile.....	25
I.6. Losses.....	27
I.7. Radiation of Inductive Power Transfer (IPT) System.....	29
I.8. CINELI Project Goals and Thesis Novelty.....	33
Chapter II : Finite Element Modeling and Interoperability Study of ICT.....	35
II.1. Introduction.....	36
II.2. Modelling of ICT.....	36
II.3. Circular Pads of Type RNO-RNO.....	39
II.3.a. Modelling without EV Chassis.....	39
II.3.b. Modelling with EV Chassis.....	43
II.4. Validation Test.....	50
II.5. Square Pads of Type NTC-NTC.....	52
II.6. Study of the Interoperability.....	54
II.6.a. Prototypes Description.....	55
II.6.b. Comparison.....	56
II.7. Conclusion.....	60
Chapter III : Resonant IPT System and Control.....	63
III.1. Introduction.....	64
III.2. Comparison between Different Compensation Topologies.....	65

## Table of Contents

---

III.2.a. General Electrical Model Presentation.....	65
III.2.b. Compensation Topologies .....	68
A) SS Self Inductances ( <b>SSL</b> ) Compensation.....	71
B) SS Leakage Inductances ( <b>SSL</b> ) Compensation .....	75
C) SP Inductances Compensation.....	75
III.2.c. Comparison of The Compensations .....	78
III.2.d. <b>SSL</b> Compensated Interoperable Systems Study .....	84
III.3. <b>SSL</b> Compensated ICT Model in COMSOL with Electrical Coupling.....	89
III.4. <b>SSL</b> Resonant IPT Full System and Control .....	92
III.4.a. Open Loop System.....	92
III.4.b. Closed Loop System .....	96
III.5. Conclusion .....	104
Chapter IV : Interoperability Experimental Tests and Models Validations.....	107
IV.1. Introduction .....	108
IV.2. RNO-RNO Prototype (Test Bench V1).....	108
IV.3. SE-RNO, NTC-RNO, NTC-NTC and SE- NTC Prototypes (Test Bench V1)...	114
IV.4. Comparison between Different Prototypes for Test Bench V1.....	115
IV.4.a. RNO-RNO Prototype.....	115
IV.4.b. SE-RNO, NTC-RNO, NTC-NTC and SE- NTC Prototypes.....	116
IV.5. Test Bench V2 .....	117
IV.5.a. NTC-NTC Prototype (Test Bench V2 (EV)).....	118



## Table of Contents

---

IV.5.b. NTC-RNO Prototype (Test Bench V2 (EV)) .....	120
IV.5.c. SE-NTC Prototype (Test Bench V2 (EV)) .....	121
IV.6. Comparison between Different Prototypes for Test Bench V2.....	123
IV.7. Conclusion.....	126
General Conclusion & Perspectives.....	129
References .....	133
Appendices .....	143
Appendix A: Equivalent Resistive Load <b>Re</b> .....	144
A.I: SS Resonant DC-DC Converter .....	144
A.II: SP Resonant DC-DC Converter.....	145
Appendix B: Frequency Behavior for a Resistive Load .....	147
B.I: SS Self Inductances Compensations <b>SSL</b> .....	147
B.II: SS Leakage Inductances Compensations <b>SS<math>\ell</math></b> .....	150
B.III: SP Inductances Compensations .....	152
Appendix C: Simulation Results for Test Bench V1 for Different Prototypes.....	154
C.1 SE-RNO Prototype (Test Bench V1).....	154
C.2 NTC-RNO Prototype (Test Bench V1).....	155
C.3 NTC-NTC Prototype (Test Bench V1).....	156
C.5 SE-NTC Prototype (Test Bench V1) .....	157

***List of Figures***

Fig. 0.1: EV battery charging for KANGOO-RENAULT: with and without cables [1] .....2

Fig. 0.2: PRAXITELE Wireless EV battery charging using electric billing payment [1]...3

Fig. 0.3: Contactless EV battery charging for KANGOO-RENAULT [2].....4

Fig. 0.4: Implementation of contactless EV battery charging for KANGOO-RENAULT by induction pads [1].....4

Fig. I.1: General block diagram for a contactless charger for EV .....8

Fig. I.2: Nicolas Tesla Giant Coil (Left) [8], and Wardencllyffe Tower (Right) [7] .....10

Fig. I.3: IC coils shapes: a) circular, b) square and c) elliptical.....11

Fig. I.4: ICT planar coils with shielding; a) 1 layer [16] b) 2 layers [18].....11

Fig. I.5: Schematic of ICT.....12

Fig. I.6: Electrical circuit of physical coupling model of ICT, a) simplified b) frequency extended model .....13

Fig. I.7 : Two winding transformer; a) T-model b) Cantilever model .....14

Fig. I.8: Power Pad [15] .....16

Fig. I.9: Ferrite arrangement comparison for the power pads in [15] .....16

Fig. I.10: EV battery wireless charging using CC with two capacitors systems: transfer and return [37].....18

Fig. I.11: Resonant Topologies, a) SS b) SP c) PS and d) PP.....19

Fig. I.12: SS leakage compensation .....20

Fig. I.13: SS self-compensation .....21

Fig. I.14: SP compensation .....22

Fig. I.15: EV battery IPT charger system: a) full schematic stages and b) DC-DC resonant converter main stages .....23

Fig. I.16: Cell discharge curves for different types [47] .....24

## List of Figures

---

Fig. I.17: Simplified electrical model of a battery [48].....	25
Fig. I.18: Li-ion cell charging profile [45].....	26
Fig. I.19: ICT thermal study in [34] a) FE simulation b) thermal model.....	29
Fig. I.20: Frequency band for ionizing and non-ionizing radiation [53].....	30
Fig. I.21: EMC Plot for near field radiation intensity of IPT system caused by L1 used in [54].....	31
Fig. I.22: Scanned magnetic field intensity for a small spiral coil shown in [55].....	31
Fig. I.23: ICNIRP reference levels for exposure to time varying $B$ published in 1998 and 2010.....	32
Fig. I.24: Magnetic field measurement results for 5kW system operating under worst conditions in [32]: a) charging pads and b) four point measurements test on a 1500 mm female body.....	33
Fig. II.1: ICT circular prototype without EV chassis: Air Gap ( $d$ ) and axes shift ( $sh$ ).....	40
Fig. II.2: $L_1$ , $L_2$ and $M$ as a function of air gap $d(m)$ : a) $sh=0$ and b) $sh=0.1m$ .....	41
Fig. II.3: Variation of $k$ with respect to air gap $d(m)$ when $sh=0$ and $0.1m$ .....	41
Fig. II.4: Magnetic flux lines for 2D cut plane ( $xy$ ) for the system in Fig. II.1 with primary excitation for: a) $sh = 0, d = 0.1 m$ , b) $sh = 0, d = 0.25 m$ and c) $sh = 0.1, d = 0.25 m$ . The figures show the flux cancelation phenomenon.....	42
Fig. II.5: Magnetic flux density and norm $B$ (mT) for a distance $d= 0.15m$ ; a) $sh=0$ b) $sh=0.1 m$ .....	43
Fig. II.6: RNO-RNO prototype with EV chassis: a) model in COMSOL and b) top view of the EV to show the considered chassis and the position of secondary pad.....	44
Fig. II.7: Simulation results considering; a) modelling the real chassis b) chassis as a perfect conductor. Meshing results (left) and EM calculation results (Right).....	45
Fig. II.8: $L_1$ , $L_2$ and $M$ as functions of the air gap $d(m)$ : a) $sh=0$ and b) $sh=0.1m$ .....	46
Fig. II.9: Variation of $k$ with respect to air gap $d(m)$ when $sh=0$ and $0.1m$ .....	46
Fig. II.10: Magnetic flux density (arrows) and norm $B$ (mT) for a distance $d= 0.15m$ ; a) $sh=0$ b) $sh=0.1 m$ .....	47

## List of Figures

---

Fig. II.11: Comparisons between different configurations of ICT described in TABLE IV as a function of $d$ (m); .....	48
Fig. II.12: Coupling factor $k$ for different configurations of ICT described in TABLE IV as a function of $d$ (m) .....	49
Fig. II.13: EV Renault-Kangoo chassis: a) practical b) CAD and c) CAD with the simplified presentation .....	51
Fig. II.14: Values of $(L1, L2, M)$ for different air gap $d$ (m): Simulated (solid lines) and Measured (dashed lines), a) $sh = 0$ and b) $sh = 0.1$ m .....	51
Fig. II.15: NTC-NTC prototype: a) square power pads b) with EV chassis .....	52
Fig. II.16: $(L1, L2, M)$ for NTC-NTC prototype with EV chassis.....	53
Fig. II.17: $k$ for NTC-NTC prototype with EV chassis.....	53
Fig. II.18: Interoperability prototypes: a) RNO-NTC b) NTC-RNO c) SE-NTC and d) SE-RNO .....	54
Fig. II.19: Values of $L1$ for different prototypes in function of air gap distance $d(m)$ : a) $sh=0$ and b) $sh=0.1$ m. ....	58
Fig. II.20: Values of $L2$ for different prototypes in function of air gap distance $d(m)$ : a) $sh=0$ and b) $sh=0.1$ m. ....	58
Fig. II.21: Values of $M$ for different prototypes in function of air gap distance $d(m)$ : a) $sh=0$ and b) $sh=0.1$ m. ....	59
Fig. II.22: Values of $k$ for different prototypes in function of air gap distance $d(m)$ : a) $sh=0$ and b) $sh=0.1$ m. ....	59
Fig. II.23: Comparison of relative difference of the coupling factor for two groups of reference prototype: a) $k_{ref}$ : RNO-RNO and b) $k_{ref}$ : NTC-NTC.....	60
Fig. III.1: Overall system of contactless battery charger .....	64
Fig. III.2: Three different compensation topologies shown in Chapter I: a) SS leakage b) SS self and c) SP .....	66
Fig. III.3: Global T-model (left) compared with the physical model (right) for ICT .....	67
Fig. III.4: Different compensation topologies with the general connections .....	69
Fig. III.5: FHA of the SS compensation topology circuit .....	72

## List of Figures

---

Fig. III.6: SP topology connection for the developed T-model. ....	76
Fig. III.7: Plot of $Z_{in}$ and their phases as a function of $\omega N$ for different values of $k$ . Markers added to show the resonance frequency corresponding to each case of $k$ for the three topologies .....	79
Fig. III.8: Different topologies $Pf$ .plot as a function of $\omega N$ for different values of $k$ .....	79
Fig. III.9: Values of the normalized resonance frequency for each topology at different $k$ ( $k_1 < k_{2ref} < k_3$ ) .....	80
Fig. III.10: Impedance and inverse of gain for each topology at the resonance frequency for different $k$ (following Fig. III.9).....	80
Fig. III.11: Normalized voltages for each topology at the resonance frequency for different $k$ (following Fig. III.9) .....	80
Fig. III.12: Normalized currents for each topology at the resonance frequency for different $k$ (following Fig. III.9).....	81
Fig. III.13: Normalized elements power for each topology at the resonant frequency for different $k$ (following Fig. III.9) .....	81
Fig. III.14: $Gv$ plot as a function of $\omega N$ for different values of $Re$ for $k_2$ (ref. case) for the three topologies .....	82
Fig. III.15: $SSL$ compensation topology normalized frequencies for the primary, the secondary and the whole system for different values of $k$ ( $k_1 < k_{2ref} < k_3$ ). .....	84
Fig. III.16: Compensated SS interoperability prototypes discussed in Chapter II.....	85
Fig. III.17: Interoperability study for SS self parameters plot as a function of $\omega N$ for $k_1$ : $Z_{inSSL}$ , its phase and $Pf$ .....	86
Fig. III.18: Interoperability study for SS self parameters plot as a function of $\omega N$ for $k_3$ : $Z_{inSSL}$ , its phase and $Pf$ .....	86
Fig. III.19: Interoperability study of $1/Gv$ for SS self compensation as a function of $k$ ..	87
Fig. III.20: Normalized primary resonant frequency ( $\omega_{01N}$ ) for all topologies for $k_1$ and $k_3$ .....	87
Fig. III.21: Normalized voltages for each $SSL$ resonant interoperable prototype at the resonant frequency for different $k$ .....	89

## List of Figures

---

Fig. III.22: Electrical interface of <i>SSL</i> compensated ICT in COMSOL: a) FHA equivalent circuit b) FE calculation results.....	90
Fig. III.23: Electrical behavior results of the calculation in Fig. III.22: a) primary and secondary currents, b) primary and secondary voltages and c) voltage stress over the primary and secondary coils.....	91
Fig. III.24: IPT full system main blocks with <i>SSL</i> compensation.....	92
Fig. III.25: Electrical circuit of <i>SSL</i> compensated IPT system with: a) resistive load and b) model of battery .....	93
Fig. III.26: Simulation results of the circuit shown in Fig. III.25 a) for voltages (left axe) and currents (right axe): a) primary and secondary and b) output .....	94
Fig. III.27: Simulation results of the circuit shown in Fig. III.25 a) primary and secondary for voltages (left axe) and currents (right axe), b) output voltage (left axes) and voltage ripple (right axes) and c) output current (left axes) and current ripple (right axes) .....	94
Fig. III.28: Waveforms of the command signals, inverter output voltages and inverter input and output currents [23]. .....	96
Fig. III.29: Closed loop full IPT system with frequency and power loops controllers.....	98
Fig. III.30: Closed loop IPT system with frequency controller using MPPT algorithms ..	98
Fig. III.31: MPPT algorithm flow charts used in our IPT system to control the frequency; where: $k$ is the iteration number, $P_k = U_{ik}I_{ik}$ , $\Delta P = P_k - P_{k-1}$ , $\varepsilon = 1$ , $\Delta f = 100\text{Hz}$ (if not set to zero). Same algorithm used in [70] to control the duty cycle $D$ with fixed frequency.....	99
Fig. III.32: MPPT controller for battery model plots for initial frequency $26\text{ kHz}$ : plot of: the output power with frequency and time response, and the controller frequency in time response .....	101
Fig. III.33: MPPT controller for battery model plots for initial frequency $26\text{ kHz}$ : input current with frequency, and the output voltage in frequency and time domaine.....	101
Fig. III.34: MPPT controller for battery model plots for initial frequency $34\text{ kHz}$ : plot of: the output power with frequency and time response, and the controller frequency in time response .....	102
Fig. III.35: MPPT controller for battery model plots for initial frequency $34\text{ kHz}$ : input current with frequency, and the output voltage in frequency and time domaine.....	102
Fig. III.36: MPPT controller for <i>RL</i> model plots for initial frequency $26\text{ kHz}$ : plot of: the output power with frequency and time response, and the controller frequency in time response ..	103

## List of Figures

---

Fig. III.37: MPPT controller for $RL$ model plots for initial frequency $26\text{ kHz}$ : input current with frequency, and the output voltage in frequency and time domain.....	103
Fig. III.38: Primary voltage and current at the resonant frequency value found by the MPPT controller for a battery model load and starting frequency $26\text{ kHz}$ . Following the simulations in Fig. III.32 and Fig. III.33.....	105
Fig. IV.1: Electrical circuit of $SSL$ compensated IPT system.....	109
Fig. IV.2: a) 3D structure of an ICT with shielding, simple EV chassis and measurement positions (stars) for the magnetic field density, b) top view of the EV to show the considered chassis and the position of secondary pad.....	109
Fig. IV.3: Picture of the experimental test equipment installation for RNO-RNO IPT prototype.....	110
Fig. IV.4: Values of $(L1, L2, M)$ for different air gap $d$ (m): Simulated (solid lines) and Measured (dashed lines), a) $sh = 0$ and b) $sh = 0.1\text{ m}$ .....	112
Fig. IV.5: 3D Cartography for $B$ in $\mu\text{T}$ , maximum data range is $2.2481 * 10^4\ \mu\text{T}$ and maximum color range is $6.25\ \mu\text{T}$ .....	112
Fig. IV.6: Schematic configuration of the line where the calculation of $B$ is performed (outside the EV).....	114
Fig. IV.7: Plot of $B$ ( $\mu\text{T}$ ) calculated in a $1\text{ m}$ line outside the EV that shown in Fig. IV.6 for two excitation currents. The values compared with ICNIRP 1998 public and occupational and standard norms: a) $d = 0.1\text{ m}$ and b) $d = 0.15\text{ m}$ .....	114
Fig. IV.8: Comparison between simulation and test values for RNO-RNO bench test V1: a) electrical parameters and b) $B$ levels values for the points in Fig. IV.2.....	116
Fig. IV.9: Comparison of values of $B$ levels of interoperability prototypes for bench test V1: a) simulation results normalized to test ones and b) tests results normalized to $6.25\ \mu\text{T}$ .....	116
Fig. IV.10: ICT installation in the full EV: a) and b) real system, c) full EV chassis developed in CAD 3D and c) 3D ICT structure with simplified chassis and the desired points to test the $B$ levels.....	118
Fig. IV.11: Plots of $u1$ , $i1$ and $i2$ for NTC-NTC Bench V2: a) experimental test measurements and b) simulation results.....	119
Fig. IV.12: Comparison between simulation and test values for NTC-NTC prototype of bench test V2: a) electrical parameters and b) $B$ levels values.....	119

## List of Figures

---

Fig. IV.13: Plots of $u_1$ and $i_1$ for NTC-RNO Bench V2: a) experimental test measurements and b) simulation results.....	121
Fig. IV.14: Comparison between simulation and test values for NTC-RNO prototype of bench test V2: a) electrical parameters and b) $B$ levels values .....	121
Fig. IV.15: Plots of $u_1$ and $i_1$ for SE-NTC Bench V2: a) experimental test measurements and b) simulation results. ....	122
Fig. IV.16: Comparison between simulation and test values for SE-NTC prototype of bench test V2: a) electrical parameters and b) $B$ levels values .....	122
Fig. IV.17: Comparison between tests of normalized $B$ values for different prototypes of bench test V2.....	124
Fig. IV.18: Normalized electrical parameters of the different prototypes tests bench V2 results to NTC-NTC prototype (practical results).....	124
Fig. IV.19: Overall resonant frequency and efficiency for the practical results of test bench V2 .....	125
Fig. IV.20: Spectrum of electrical field intensity using NARDA EHP 200 for two points : a) 1 m and b) 0.5 m far from ICT power pads of SE-NTC test bench V2. The ICNIRP 1998 $E$ norm is 87 V/m .....	126
Fig. IV.21: Effect of ICT interoperable prototypes position installation to EV on the coupling factor with respect to a reference prototype .....	127
Fig. A.1: Schematics of secondary side Series compensation: full circuit (left) and equivalent circuit of FHA (right) .....	145
Fig. A. 2: Schematics of secondary side Parallel compensation: full circuit (left) and equivalent circuit of FHA (right) .....	146
Fig. B.1: SS self parameters plot as a function of $\omega N$ for different values of $k$ : a) $Z_{inSS}$ b) phase of $Z_{inSS}$ and c) $Pf$ .....	147
Fig. B.2: Plot of: a) $Gv$ and b) $1Gv$ as a function of $\omega N$ .....	148
Fig. B.3: SS self $Gv$ plot as a function of $\omega N$ for different values of $Re$ for $k_2$ (ref. case) .....	148



## List of Figures

---

Fig. B.4: SS leakage compensation topology normalized L's and C's Currents of the resonant circuit as a function of the normalized frequency $\omega N$ for different $k$ .....	149
Fig. B.5: SS leakage compensation topology normalized L's and C's Currents of the resonant circuit as a function of the normalized frequency $\omega N$ for different $k$ .....	149
Fig. B.6: SS leakage parameters plot as a function of $\omega N$ for different values of $k$ : a) $Z_{inSS}$ b) phase and c) $Pf$ .....	150
Fig. B.7: Plot of: a) $Gv$ and b) $1Gv$ as a function of $\omega N$ for $SS\ell$ .....	150
Fig. B.8: SS leakage $Gv$ plot as a function of $\omega N$ for different values of $Re$ for $k2$ (ref. case).....	151
Fig. B.9: $SS\ell$ topology normalized L's and C's Voltages as a function of $\omega N$ for different $k$ .....	151
Fig. B.10: $SS\ell$ topology normalized L's and C's Currents as a function of $\omega N$ for different $k$ .....	151
Fig. B.11: SP parameters plot as a function of $\omega N$ for different values of $k$ :a) $Z_{inSP}$ b) its phase and c) $Pf$ .....	152
Fig. B.12: SP topology, Plot of: a) $Gv$ and b) $1Gv$ as a function of $\omega N$ .....	152
Fig. B.13: SP $Gv$ plot as a function of $\omega N$ for different values of $Re$ for $k2$ (ref. case)..	153
Fig. B.14: SP topology normalized L's and C's Voltages as a function of $\omega N$ for different $k$ .....	153
Fig. B.15: SP topology normalized L's and C's Currents as a function of $\omega N$ for different $k$ .....	153
Fig. C.1: Plots of $u1$ and $i1$ SE-RNO Bench V1 simulation results.....	155
Fig. C.2: Plots of $u1$ and $i1$ NTC-RNO Bench V1 simulation results .....	156
Fig. C.3: Plots of $u1$ and $i1$ NTC-NTC Bench V1 simulation results.....	157
Fig. C.4: Plots of $u1$ and $i1$ SE-NTC Bench V1 simulation results .....	158

***List of Tables***

TABLE I: PARAMETERS OF THE T-MODEL AND THE CANTILEVER MODEL .....	14
TABLE II: POWER PADS DEFINITIONS .....	36
TABLE III: ICT AND EV CHASSIS PARAMETERS (RNO-RNO PROTOTYPE) .....	40
TABLE IV: ICT CONFIGURATION .....	47
TABLE V: POWER PADS SPECIFICATIONS .....	55
TABLE VI: DIFFERENT COUPLING CASES PARAMETERS (RNO-RNO PROTOTYPE) .....	68
TABLE VII: FREQUENCY SYMBOLS AND THEIR DEFINITIONS .....	71
TABLE VIII: COMPUTATIONS OF $C_1$ AND $C_2$ FOR THE THREE COMPENSATION TOPOLOGIES .....	78
TABLE IX: COMPARISON BETWEEN THEORETICAL AND EXPERIMENTAL ELECTRICAL PARAMETERS AND QUANTITIES FOR RNO-RNO IPT PROTOTYPE BENCH V1 .....	113
TABLE X: $B$ LEVELS VALUES FOR RNO-RNO TEST BENCH V1 .....	113
TABLE XI: $B$ LEVELS VALUES FOR DIFFERENT PROTOTYPES TEST BENCH V1 .....	115
TABLE XII: VALIDATION TEST PARAMETERS FOR NTC-NTC IPT PROTOTYPE BENCH V2 .....	118
TABLE XIII: $B$ LEVELS VALUES FOR NTC-NTC TEST BENCH V2 .....	119
TABLE XIV: VALIDATION TEST PARAMETERS FOR NTC-RNO IPT PROTOTYPE BENCH V2 .....	120
TABLE XV: $B$ LEVELS VALUES FOR NTC-RNO TEST BENCH V2 .....	120
TABLE XVI: VALIDATION TEST PARAMETERS FOR SE-NTC IPT PROTOTYPE BENCH V2 .....	121
TABLE XVII: $B$ LEVELS VALUES FOR SE-NTC TEST BENCH V2 .....	122
TABLE XVIII: SIMULATION PARAMETERS FOR SE-RNO IPT PROTOTYPE BENCH V1 ...	154
TABLE XIX: $B$ LEVELS VALUES SE-RNO TEST BENCH V1 .....	155

List of Tables

---

TABLE XX: SIMULATION PARAMETERS FOR NTC-RNO IPT PROTOTYPE BENCH V1 ....	155
TABLE XXI: <i>B</i> LEVELS VALUES NTC-RNO TEST BENCH V1 .....	156
TABLE XXII: SIMULATION PARAMETERS FOR NTC-NTC IPT PROTOTYPE BENCH V1 ..	156
TABLE XXIII: <i>B</i> LEVELS VALUES NTC-NTC TEST BENCH V1 .....	157
TABLE XXIV: SIMULATION PARAMETERS FOR SE-NTC IPT PROTOTYPE BENCH V1 ....	157
TABLE XXV: <i>B</i> LEVELS VALUES SE-NTC TEST BENCH V1 .....	158

## ***Abstract***

*Development of contactless battery charging is an opportunity for electric vehicles. Compared to regular plugin cables, this solution is easy to use, robust and weather resistant. The power is transferred thanks to the magnetic coupling of inductive coils and a reduced magnetic circuit. The aim of this thesis is to contribute to propose a standard that would make possible to couple emitters with receivers from different suppliers, that is, to insure interoperability.*

*As the system should also be tolerant to positioning and should respect human exposure recommendations, many configurations must be tested. In this thesis, an advanced and reliable modeling of the whole system is proposed. Using the finite element methods, the electrical characteristics (self, mutual inductances and coupling factor) of the inductive coupler are computed for different geometric and interoperability configurations. These values allow the dimensioning of the resonant converter. At this stage, different compensation topologies are considered. It is shown that the global resonant frequency can be derived and the topologies compared from a classical first harmonic approximation and analytical model. Then, a circuit model of the full system is developed in order to evaluate precisely the currents and voltages. Finally, the performance of a MPPT (Maximum Power Point Tracking) as frequency regulation algorithm is evaluated. From the currents computed at resonant frequency for the nominal operating point and the finite element model of the coupler, including the chassis of the vehicle, the radiated magnetic field is evaluated in order to check safety compliance. At each step of the modeling, the sensitivity of the system to the configuration parameters (positioning, interoperability) is analyzed. Measurements at the coupler level and for the full system are also used in this analysis and allow validating the model.*

***Keywords: EM modelling, resonant topologies, power electronics, interoperability, inductive charging.***

## **Résumé**

*Le développement de la recharge sans contact de batteries comporte divers avantages pour les véhicules électriques. Cette solution est facile à utiliser, robuste et résistante aux intempéries par rapport aux câbles généralement utilisés. Le principe est basé sur le couplage magnétique entre un émetteur et un récepteur. L'objectif de cette thèse est de contribuer à proposer une norme pour permettre l'interopérabilité, c'est-à-dire, permettre à plusieurs émetteurs de fonctionner avec des récepteurs de différents fournisseurs.*

*Comme le système doit aussi être tolérant au positionnement et doit respecter les recommandations concernant l'exposition humaine, de nombreuses configurations doivent être envisagées. Dans cette thèse, une modélisation avancée et fiable du système complet est proposée. La méthode des éléments finis est exploitée pour déterminer les caractéristiques électriques du coupleur inductif (inductances propres et mutuelles, facteur de couplage) dans différentes configurations de positionnement et d'interopérabilité. Ces valeurs permettent le dimensionnement du convertisseur à résonance. A ce stade différentes topologies de compensation sont considérées. Un modèle analytique au premier harmonique est mis en œuvre pour comparer les topologies et déterminer la fréquence de résonance globale du système. Un modèle circuit du système complet est ensuite développé pour évaluer précisément les courants et tensions. Enfin, un algorithme de régulation basé sur une méthode MPPT (Maximum Power Point Tracking) est évalué pour le réglage automatique de fréquence. A partir des courants calculés à la fréquence de résonance pour un point de fonctionnement nominal et grâce au modèle éléments finis incluant le châssis du véhicule le champ magnétique rayonné est calculé et comparé aux valeurs limites recommandées. A chaque étape de la modélisation, la sensibilité du système aux paramètres de configuration (positionnement, interopérabilité) est analysée. Des mesures effectuées au niveau du coupleur inductif et sur le système complet sont aussi utilisées dans l'analyse et permettent de valider le modèle.*

**Mots Clés:** *modélisation EM, topologies de résonances, électronique de puissance, interopérabilité, charge inductive.*

## ***General Introduction***

The automotive industry is currently undergoing a major technological transformation in a context where environmental concerns are at the forefront. Restrictions in terms of CO<sub>2</sub> emissions lead manufacturers to work on "cleaner" concept cars as the Electrical Vehicle (EV) and Hybrid Electrical Vehicle (HEV). Such vehicles currently use a regular cable connection for the recharge (on board battery) in charging stations Fig. 0.1 [1].

Although this kind of charging, developed in recent years, is known to be very fast ( $\sim 15 - 30 \text{ min}$ ) for full EV battery charge with proper energy, it may include elements tedious and/or inconvenient for the user who deals with the charger cables that needed to be plugged in the station. In addition, the charging cable needs to be checked for maintenance, is not easy to handle, it may be dirty because of ground contact and it implies daily tedious movements. In this context, to avoid cables disadvantages, contactless charging (wireless charging) Fig. 0.1, is an attractive alternative solution with more flexibility.

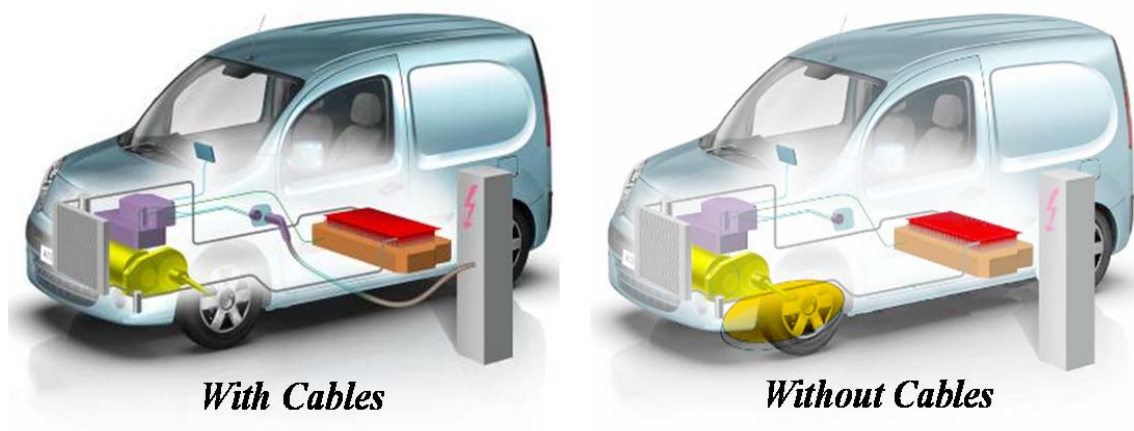


Fig. 0.1: EV battery charging for KANGOO-RENAULT: with and without cables [1]

Following the first contactless charging for PRAXITELE project developed in St. Quentin En Yvelines, France (1997-1999) using the electric billing payment as shown in Fig. 0.2 [1], the project CINELI (Chargeur Inductif Électrique Interopérable) has been announced and launched in May 2011.



Fig. 0.2: PRAXITELE Wireless EV battery charging using electric billing payment [1]

The goal of this project with respect to PRAXITELE concerns the tolerance about positioning at parking and the requirement to avoid mechanical system to raise the ground antenna. CINELI, aims to develop a standard for interoperability between contactless charging systems for EV batteries by Inductive Coupling (IC). A vehicle from any manufacturer complying with the standard should be able to be charged over an integrated inductive ground loop. This project focuses on the development of two different wireless technology systems that ultimately must be compatible. The result will be offered to other manufacturers as part of a consortium to allow an increase in the diffusion of electric vehicles and thus a reduction of CO<sub>2</sub> emissions.

The project includes four partners; three industrial companies: RENAULT (RNO), SCHNEIDER Electric (SE), and Newtech Concept (NTC). They are in charge of the practical elements setups and tests. The LGEP (Laboratoire de Génie Électrique de Paris) is the fourth partner who is responsible for all theoretical issues in the project. This PhD thesis describes the aims and synthesis of work. The project is labeled by Movéo, and the funding organizations are: Oséo (Fond Unique Interministériel) and Ile-de-France region.

The Inductive Power Transfer (IPT) to charge an EV battery is used in this project. The EV tested is KANGOO fabricated by Renault. The system where this vehicle is charged wirelessly is shown in Fig. 0.3 [2]. The battery is on board of the EV, and the coils could have different forms (circular and square). The term ‘interoperability’ should be understood as the ability for a primary (ground) system and a secondary (board) system that were “independently”



dimensioned (i.e designed by different manufacturers) to work together and insure battery charging.

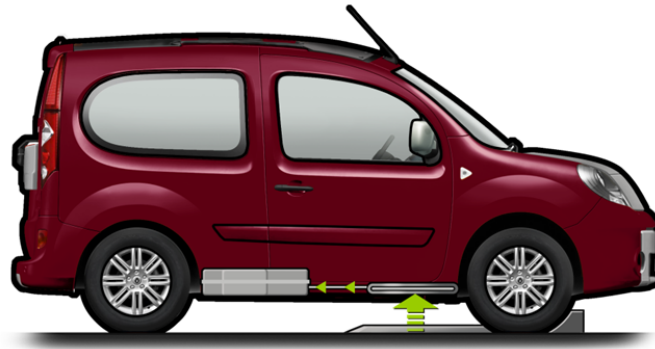


Fig. 0.3: Contactless EV battery charging for KANGOO-RENAULT [2]

The general functional architecture for the global design in CINELI project is shown in Fig. 0.4 [1]. It is divided into two main parts: primary installed in the ground and secondary integrated on board of the EV. They include: two inductive loops, power electronics stages, battery, control and communication technologies (CAN/WiFi) between the interoperable systems. This communication aspect and EV detection are out of scope in this thesis memory.

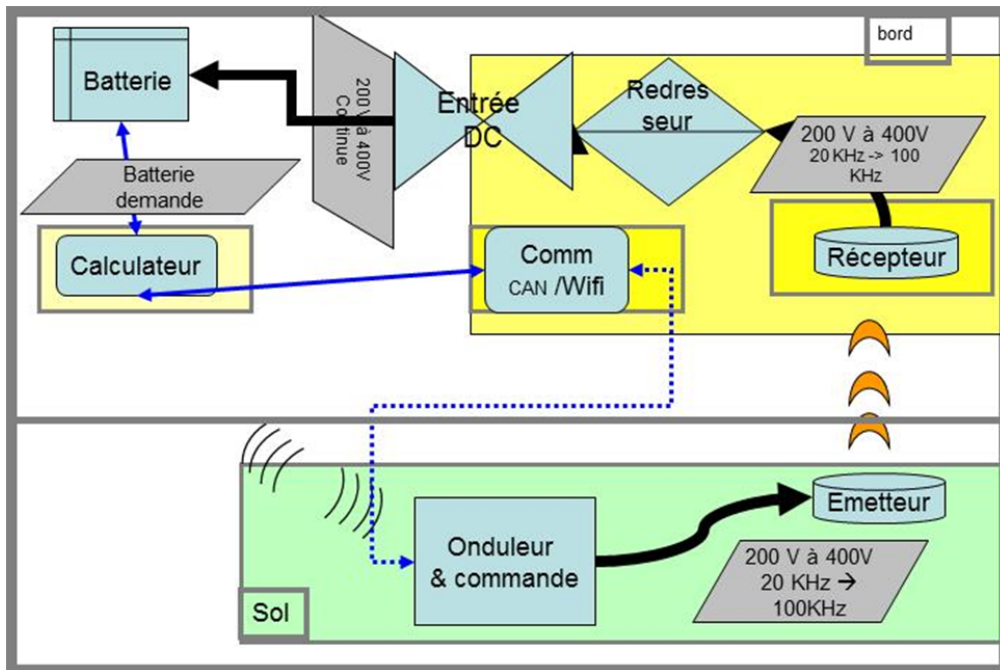


Fig. 0.4: Implementation of contactless EV battery charging for KANGOO-RENAULT by induction pads [1]

This thesis memory synthesizes the principles of electromagnetic modelling and the analysis of the interoperability for the inductive charging of EV. The studies are based on the system dimensions given by the industrial partners. So the first three chapters highlight in details the theoretical aspects for the work in CINELI project, and the last chapter includes the practical tests and validations for the theoretical calculations.

The first chapter scopes the global view for the wireless charging application especially in the domain of EV. It illustrates the overall system design stages from the source to the battery. Also constraints to respect the standard norm for human expositions for electromagnetic fields are shown due to inductive charging.

The second chapter presents the models of the different prototypes for the inductive planar coupler defined by the industry. The modelling by finite element method is done using COMSOL. The results help to calculate the self and mutual inductances of the inductive coupling transformer. The interoperability study is detailed based on these electrical values and also for the physical behavior drawn from modelling by COMSOL.

The third chapter concerns the power electronics stages linked to the inductive coupling transformer modeled in second chapter. In a first step, a comparison between three types of compensation topologies is done using the first harmonic approach. Then the chosen resonant topology is used to show the behavior of the resonant interoperable transformers. The second step, simulation for the full system using a battery model is illustrated using MATLAB/Simulink. A system frequency regulation in order to operate at global resonance is shown using the MPPT algorithm for the static charging.

Finally, the fourth chapter includes the practical tests done at Renault laboratory for the interoperable full systems. Comparison between the results of simulations and tests are shown at first time. Then comparison between the test results for the interoperability aspects are highlighted. Conclusions are drawn thanks to these comparisons.



## *Chapter I : Global View*

## I.1. Introduction

Wireless charging consists in transferring energy from the source to the load without physical contact. This technology can be applied to EV battery charging for which daily recharge is mandatory. The tedious and inconvenient aspects of connecting the power cable hinder some users and may hinder the development of the EVs. A user-friendly solution consists in using a system of power transmission without contact. This solution provides ease of use and a good robustness to vandalism [3]. A general block diagram for the contactless charger for EV battery is shown in Fig. I.1.

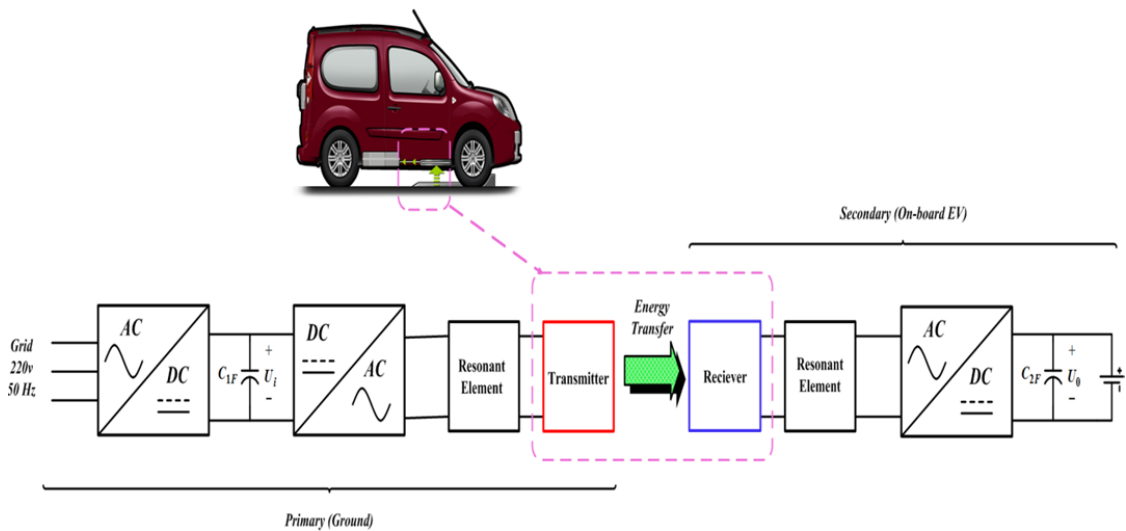


Fig. I.1: General block diagram for a contactless charger for EV

The overall system is made of two main parts: the contactless coupler and the power electronics system connected to it. Before of the wireless stage, there are two conversion steps: The low frequency AC from the grid is converted to DC, and then the DC to AC high frequency. These conversion stages allow adjusting the power level by controlling the input voltage and the frequency. After the wireless stage, a final conversion from high frequency AC to DC is done to provide energy to the battery. Power levels typically range from 0.5 W to 50 kW for a gap of 1 to 150 mm [4], [5].

Because of the large distance between the primary and secondary sides, the coupling is weak. In consequence, in order to reach the desired transferred power, high reactive power must

be managed and the use of resonant elements in both sides is necessary as compensation to ensure good efficiency. Also the output parameters at the load side should be regulated in order to keep the charger operating at a certain voltage with the desired current demanded by the battery. Furthermore, controlling the output parameters insures load protection.

There are two types of coupling for the contactless transformer: Inductive Coupling (IC) and Capacitive Coupling (CC). The IC Transformer (ICT) which depends on the magnetic field induction ensures galvanic isolation between the source and the load [6]. The CC type transformer depends on the electric field for transferring the energy.

This chapter highlights the general presentation of the system and its main blocks. It also contains, as a state of art, the context of the recent works related to the same topic of this project. The end of this chapter will carry a summary of the objectives and original points of this thesis as well as the CINELI project.

## ***1.2. Inductive Coupling (IC)***

As James C. Maxwell predicted the existence of radio waves in 1864, the researches went through to data and energy transfer wirelessly, and the idea of energy transmission was firstly tried experimentally by Nicolas Tesla in 1899 [7]. He tried to transfer electromagnetic energy using the principle of electrodynamics without contact between America and Europe building the Wardencllyffe Tower (Fig. I.2) [7], [8].

In the history of wireless charging, scientists faced many difficulties because of the limited power that can be transferred from the transmitter to the receiver antenna as the distance gets larger between them. Nowadays, and especially from 1978, wireless energy transfer is applied in different applications: EV [3]-[5], [9], [10], biomedical applications [11], portable phones battery charging [12], semiconductors commands [13] and induction heating [14].

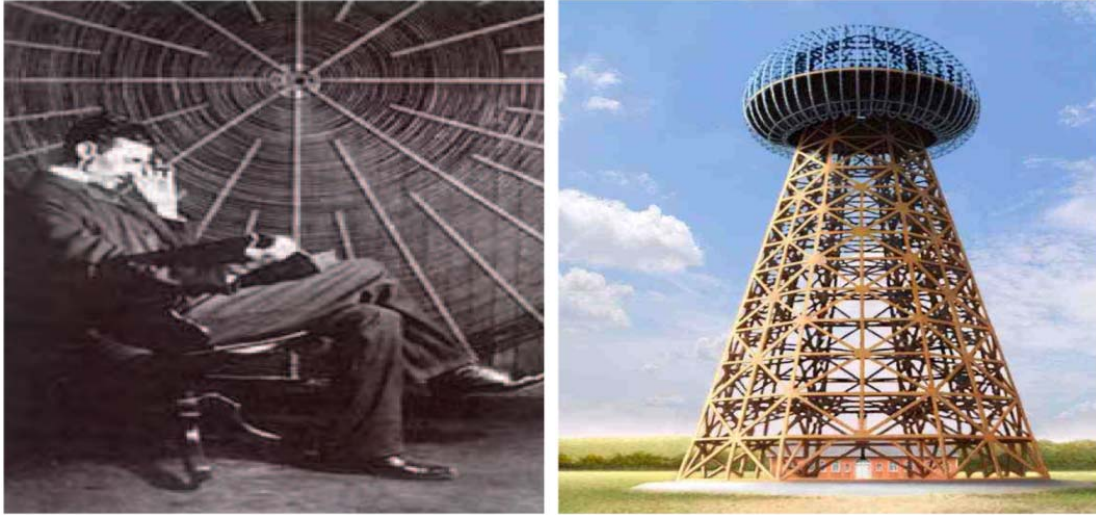


Fig. I.2: Nicolas Tesla Giant Coil (Left) [8], and Wardencliff Tower (Right) [7]

### **I.2.a. Inductive Coupling Transformer (ICT)**

Many shapes of coils can be chosen for both the primary and secondary parts: circular, squared or elliptical coils as shown in Fig. I.3. The fabricated coils usually used in this application are made of isolated Litz wire, for which skin and proximity effects are very small in the considered frequency range [15]. In general, primary and secondary coils are designed at the same time in order to reach given performances of the whole system.

To improve the coupling between the coils some shielding is used to increase the mutual inductance  $M$  by increasing the magnetic flux between the coils. A non-conducting magnetic material is sometimes added as shielding, and the two coils are sandwiched between two shielding layers as shown in Fig. I.4 a) [16].

Ferrites are generally used because they are almost loss-free at frequencies up to several hundreds of kHz, even for the lowest cost materials. Thanks to this magnetic circuit, induction is mainly concentrated between the two coils which helps in improving the coupling and also prevents from heating up the conducting parts near the inductive coupler [17], [18].

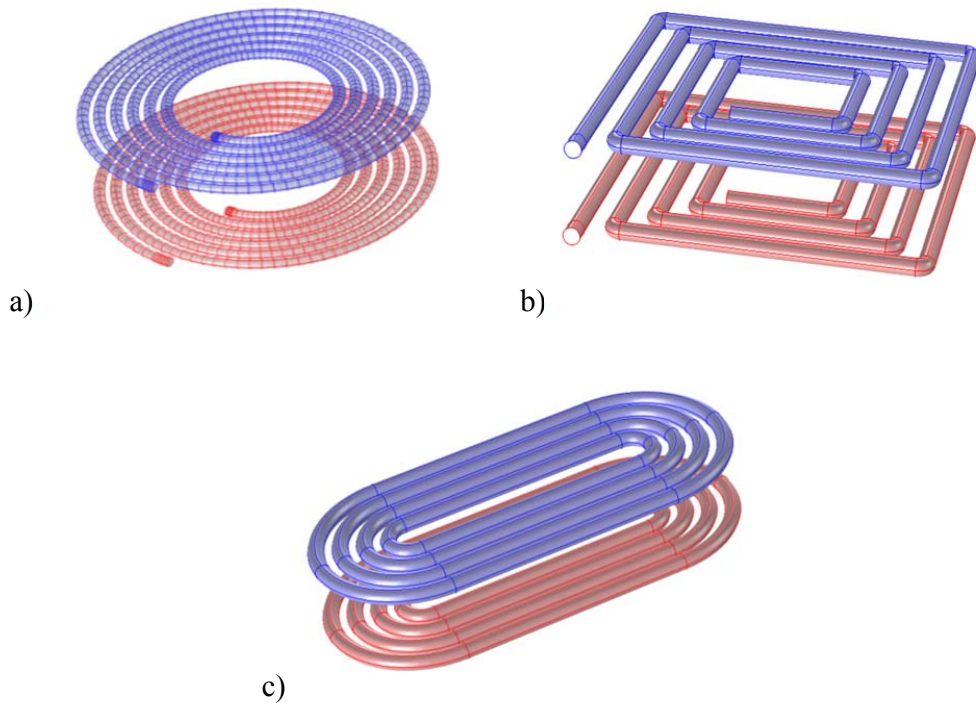


Fig. I.3: IC coils shapes: a) circular, b) square and c) elliptical

Some designers add other materials (like Aluminum) as in Fig. I.4 b) that cover the ferrites, which in particular cases can also decrease the leakage flux, and act as additional shielding [19]. This solution is expensive, increases the weight embedded in the EV and may generate additional losses at high frequencies because of the aluminum resistivity [18], [19]. However, in a real configuration, the presence of the EV chassis above the inductive coupler can also be considered as an additional shielding with respect to people or devices being inside the car.

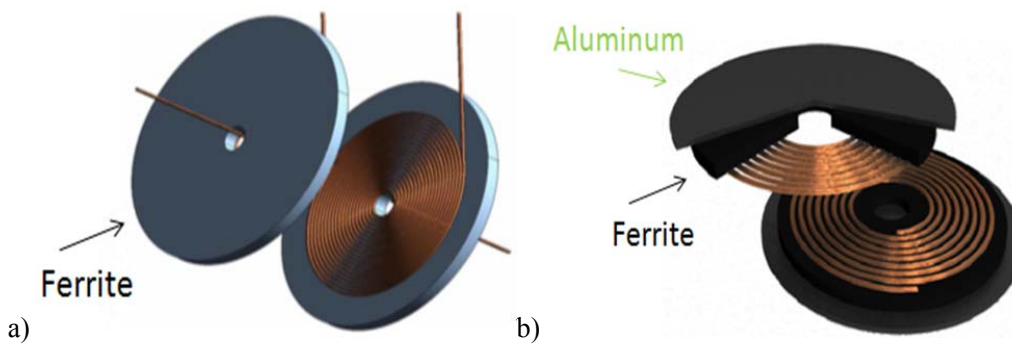


Fig. I.4: ICT planar coils with shielding; a) 1 layer [16] b) 2 layers [18]



**I.2.b. ICT Electrical Model**

The alternative supplying current in the transmitter coil  $L_1$  creates a varying magnetic field and then a magnetic flux ( $\Phi_{21}$ ) through the circular area ( $S_2$ ) inside the  $L_2$  (Fig. I.5).

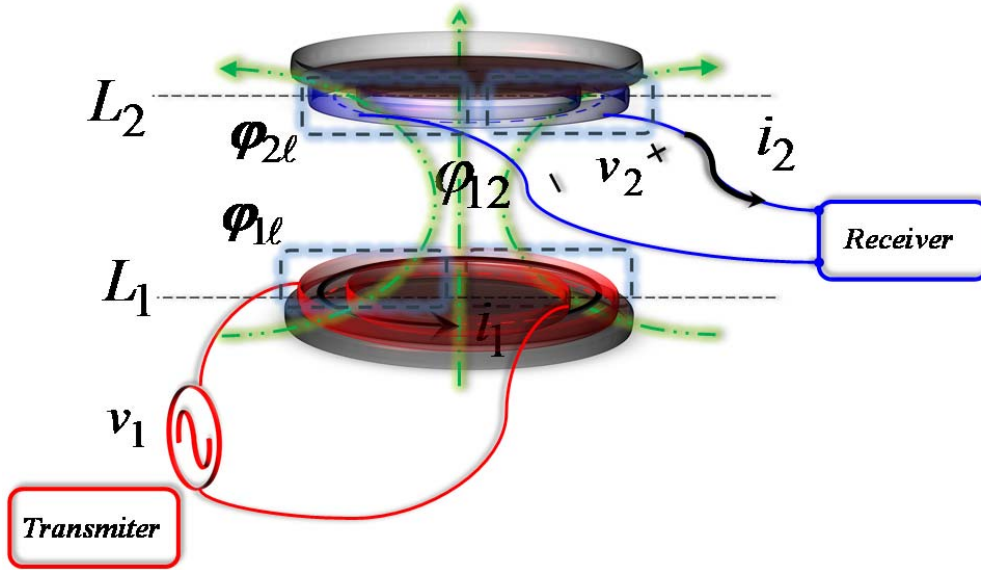


Fig. I.5: Schematic of ICT

The mutual inductance between the  $L_1$  coil and the  $L_2$  coil is;

$$M_{12} = M_{21} = M \quad (1)$$

The quality of the linkage between the coils is evaluated through the magnetic linkage coefficient:

$$k = \frac{M}{\sqrt{L_1 L_2}} \quad (2)$$

Taking into account the DC resistances of the coils ( $R_{1\omega}, R_{2\omega}$ ), the radiation resistances ( $R_{1\beta}, R_{2\beta}$ ) that represent the far field radiation power loss (they are very small), and the resistances caused by the skin effects ( $R_{1\delta}, R_{2\delta}$ ), the equivalent electrical model of ICT can be described as in Fig. I.6 [20], [21].

where:

$$\begin{cases} R_1 = R_{1\alpha} + R_{1\beta} + R_{1\delta} & , & R_2 = R_{2\alpha} + R_{2\beta} + R_{2\delta} \\ v_1 = i_1 \cdot R_1 + e_1 & , & v_2 = -i_2 \cdot R_2 + e_2 \end{cases} \quad (3)$$

Or

$$\begin{pmatrix} v_1 \\ v_2 \end{pmatrix} = \begin{pmatrix} R_1 + j\omega L_1 & -j\omega M \\ j\omega M & -(R_2 + j\omega L_2) \end{pmatrix} \cdot \begin{pmatrix} i_1 \\ i_2 \end{pmatrix} \quad (4)$$

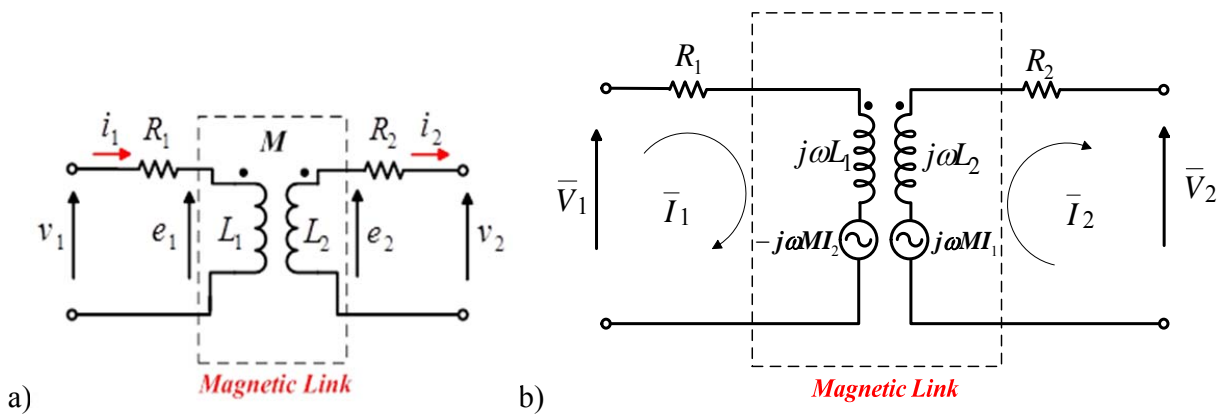


Fig. I.6: Electrical circuit of physical coupling model of ICT, a) simplified b) frequency extended model

Actually, the authors use different equivalent circuit model to describe ICT, but there are two main models: the T-model and the Cantilever model [22]. The basic T model of the two winding transformer contains four parameters: two leakage inductances, a magnetizing inductance, and a turn's ratio as shown in Fig. I.7 a).

However, only three parameters are needed to describe the two winding transformer. When one of the leakage inductances is chosen to be zero, (ex. the second one), then the Cantilever model of Fig. I.7 b) is obtained. This simple model contains three parameters: magnetizing inductance, leakage inductance, and the effective turn's ratio [22].

The parameters for the models are described in TABLE I, the secondary inductance of the Cantilever Model can be found as:  $L_2 = k^2 L_1 m_2^2$ . As it can be noticed, the cantilever model is simpler than the T one; since it contains less parameters and it is suited for simplify the design and calculations [22], [23], [24].

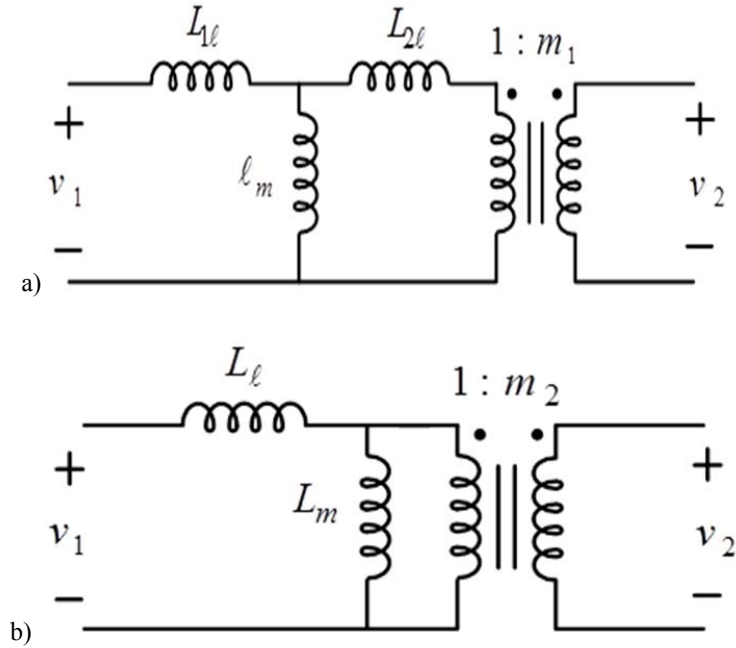


Fig. I.7 : Two winding transformer; a) T-model b) Cantilever model

TABLE I: PARAMETERS OF THE T-MODEL AND THE CANTILEVER MODEL

Model	Turns ratio	Leakage Inductance	Magnetizing Inductance
T-model	$m_1 = \frac{n_2}{n_1}$	$L_{1l} = L_1 - \ell_m = (1 - k)L_1$ $L_{2l} = L_2 - \ell_m = (1 - k)L_2$	$\ell_m = M = kL_1$
Cantilever-model	$m_2 = \frac{n_2}{n_1} \frac{1}{k} \sqrt{\frac{L_2}{L_1}}$ (effective turns ratio)	$L_\ell = (1 - k^2)L_1$	$L_m = k^2L_1$

### I.2.c. ICT Modelling for Parameter and Performance Characterization

The frequency of the IPT systems depends of the rated power of the application. Low power applications (tens of Watts) can reach up to several MHz [25], [26], [27], whereas in applications with rated powers ranging from few kW to hundreds of kW the frequencies are

restricted to a few kHz or tens of kHz [28], [27]. In this frequency range, the magnetic field generated by the ICT can be studied considering the quasi-static magnetodynamic approximation.

Generally the analytical calculations of the magnetic fields and the ICT parameters are complex, especially when considering the ferrite layers (shielding). For example, in [17] and [18], Bessel functions are used to determine the EMF distribution. However, to handle more complex geometries and configurations, these calculations can be done by using FEM tools. As examples, in France, the team of G2ELab studied a 2D axisymmetric modeling of circular coils of IPT system for EV battery charging in 1998 [29]. Recently, this team also investigated an IPT for a tramway with ALSTOM company. A 3D modeling of an ICT with the shape shown in Fig. 1.3 c) was performed. The study highlighted the impact of total losses in the ICT and the interest of an optimization of the geometry.

In the study of performance of the ICT during the process of charging and/or the predesign procedures, the effects of variations of the ICT parameters (coils dimensions, air gap distance, shielding geometry, materials) are crucial [17], [18], [9], [24], [30], [31]. In fact, many works were dedicated before to IPT system design (where ICT is the heart of the design) and its applications. In [18] the authors from the University of Zaragoza (Spain) performed theoretical and analytical calculations for the self and mutual inductances of a planar inductive for general application of wireless energy transfer using a 2D axisymmetric FE modelling. The authors investigated with a practical test several parameters included in the ICT design: frequency, coil sizes, misalignments and the properties of the media that could be placed above and below the ferrite to form a multilayer system (as aluminum for example). It has been shown and concluded that if nonconductive magnetic slabs with an appropriate thickness are placed beneath the coils, the mutual inductance can be increased in a factor 4 when compared to the mutual of the coils in the air. However, if metallic (like aluminum) slabs are located in the proximity of coils the mutual inductance is reduced.

The University of Auckland (Newzeland) is considered as the leader in this domain of application. Many papers were conducted from this center of research for the structure design of ICT and for optimization of the total efficiency of the system and control methods. As an example, an optimized arrangement of ferrites sectors is proposed in [15] for a power pad. The

pad is the unit that describes all materials included in primary side or secondary one as seen in Fig. I.8 . In the scope of 3D FE modelling as shown in Fig. I.9, they tested for circular pads many ferrites shapes (total cover, bars) and arrangements of the ferrite bars that give the most cost effective, weight and best coupling factor  $k$ . They concluded that the narrow and evenly spaced ferrite bars give the most effective performance to weight result. A test of 2 kW for 700 mm diameter pad is implemented to verify the work. Also the simulations in [15], [32] for the same research center, included the influences of variation of the distance and position of secondary coil on the electrical parameters.

In [3], the authors from Sojo University (Japan) studied an ICT with no ferrite shielding over the secondary coil, which makes it cheaper but may cause unwanted heating by induced current losses and increases radiated fields that may exceed the human exposure recommendations limits.

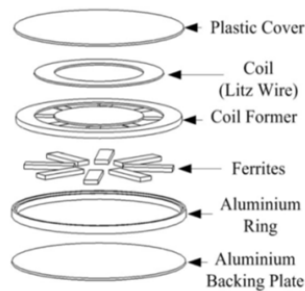


Fig. I.8: Power Pad [15]

Pad Topology	(a)	(b)	(c)	(d)	(e)
$P_{in}$ at given Separation (VA)	100mm 3841 150mm 1236 200mm 435	100mm 3832 150mm 1212 200mm 420	100mm 3479 150mm 1102 200mm 383	100mm 2825 150mm 868 200mm 293	100mm 2480 150mm 775 200mm 264
No. of bars	32.5	31.5	33	21	18
Use (VA/cm <sup>3</sup> )	3.34	3.44	2.98	3.80	3.89

Fig. I.9: Ferrite arrangement comparison for the power pads in [15]

The Power Electronic Systems Laboratory, Swiss Federal Institute of Technology (ETH) Zurich (Switzerland) studied the IPT system for EV inductive charging in collaboration with

ABB company in Switzerland [27], [33], [34]. They worked on the inductor optimization of an IPT system to improve the efficiency  $\eta$  and area related power density  $\alpha$ . The  $\eta - \alpha$  Pareto front is found using parametric sweep study for the inductor coil parameters (area, total diameter, diameter of each turn, number of turns and separation between them) by 2D axisymmetric FE modelling method. Three configurations were taken into account: coils in air, coils with ferrites, and coils with aluminum without ferrites. They found from the  $\eta - \alpha$  Pareto front that with a large enough inductor a very high transmission can be achieved, but the increase of one of the objectives ( $\eta$  or  $\alpha$ ) leads to decrease the other. Also for the configuration with shielding, the leakage flux is reduced but the efficiency decreases due to additional core loss. The different types of losses are also studied in the design taking in account the effects of the operating frequency on the system efficiency.

### ***I.3. Capacitive Coupling (CC)***

The capacitive coupling consists in the transfer of energy via electric field as in capacitors. The application of this kind of coupling is relatively recent in the literature. CAMARUTI and BONDAR published a proposal for technical views in order to transfer the energy by dielectric medium, their patent was announced in 2007 [35]. Toyota being interested in this field of charging, in 2011, a power transfer through a capacitor composed of a steel belt in a tire and a metal plate attached to the road has been proposed [36] and Renault launched researches in this area in 2012 [37]. In 2011, Murata Manufacturing Co. has developed a CC for small mobile wireless energy transfer [38].

To illustrate the basic principle of CC process; a system in Fig. I.10 is considered [37]. It consists of a transmitter electrode and a receiver electrode. Both electrodes form a system of electrically coupled capacitor in air. An alternating voltage in the transmitter electrode generates an electric field ( $E$ ) where the electric charge ( $Q$ ) transfers to the receiver electrode and a charging current to the load. So the CC can be also used for EV battery contactless charging, but in this case two systems of planar electrodes are needed, one for transfer and the other for the return to complete the circuit and energy transfer from the ground to the board of the EV as shown in Fig. I.10 [37]. The two electrodes for each capacitor should be well isolated with the

ground and the chassis of the EV [39]. This kind of charging needs a very high oscillating source voltage to create high  $E$  in order to be capable to transfer high energy.

Resonant elements are also used for this type of contactless charging to compensate the reactive part, which is capacitive in this case, for maximum power transfer [35]-[39]. Two inductors are inserted in both primary and secondary sides and they work at resonance to tune out the capacitors where the energy is transferred via the action of electrical field. An advantage of the capacitive coupling is that it is less sensible to the misalignment than the inductive coupling [37].

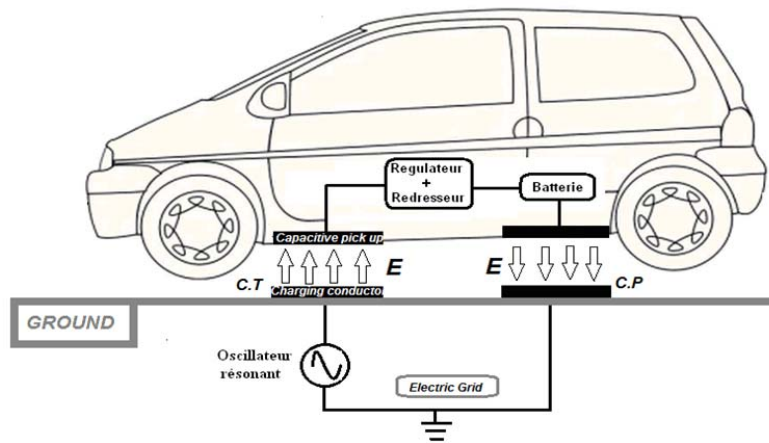


Fig. I.10: EV battery wireless charging using CC with two capacitors systems: transfer and return [37]

## I.4. Compensation of Inductive Behavior and Resonant Converter

### I.4.a. Inductance Compensation and Resonance Frequency

The next step after ICT construction and modelling is the compensation part. As mentioned before, the ICT has a large air gap that causes a weak coupling between its sides. In addition, a reactive part of the power transfer should be compensated in order to transmit the maximum real power to the load. In consequence, resonant capacitors are needed to cancel the reactive parts at given frequency. The compensation is here associated to a given inductance of the electrical model. The compensation of an inductance consists in connecting a capacitor (in series or in parallel depending on the topology) and choosing its value in order to cancel the equivalent impedance at a given frequency. The resonance frequency of the global system (which

may be different of the frequency considered in the compensation) is defined as the frequency for which the imaginary part of the power in (5) is canceled.

$$S = P + jQ \quad (5)$$

where  $S$  is the complex power (VA),  $P$  is the real power (W) and  $Q$  is the reactive power (VAR).

There are four major topologies of resonant circuit that could be used in IPT system. They are named after the way of inserting the resonant capacitors at each winding side; Parallel (P) and/or Series (S) connections. Therefore, the topologies can be described as: SS, SP, PS and PP, each of them is illustrated on Fig. I.11 [10], [40]. The transfer of appreciable electric power requires the compensation of the inductive parts, the capacitors ( $C_1, C_2$ ) are used to compensate and tune them out. A resonant receiver can improve the power transfer, and the resonant transmitter minimizes the VA ratings of the input source and insures an active power transmission to the receiver [40], [41]. The counterparts consist in the high voltage or current that can appear on the resonant elements.

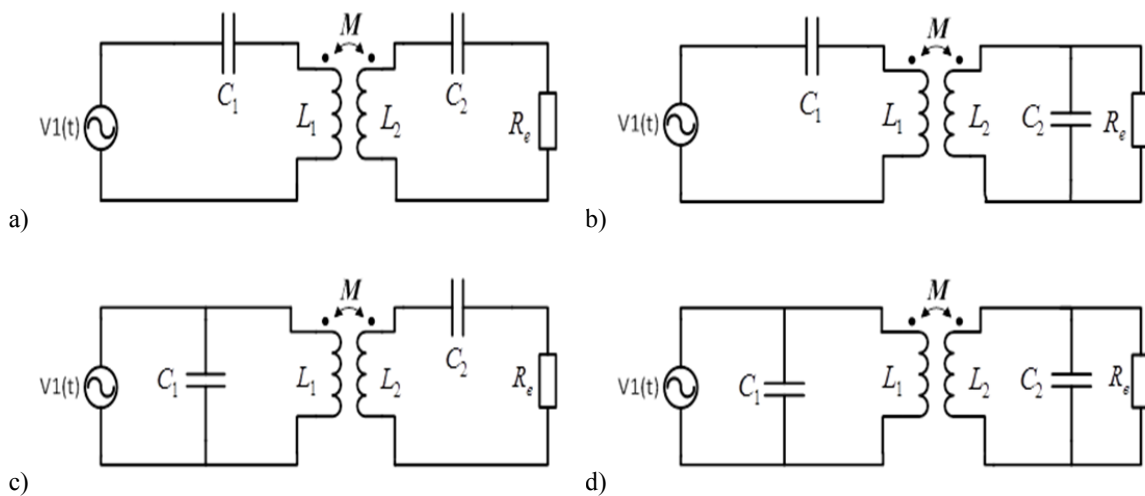


Fig. I.11: Resonant Topologies, a) SS b) SP c) PS and d) PP

The question is: which topology of compensation should be used? In fact, several works highlighted the compensation using Series (S) or Parallel (P) connections and made comparisons between them [9], [40], [41]. The design of the resonant IPT system will depend on the chosen topology. In some applications, the type of resonant topology is imposed by the designer. However comparisons between the topologies can be made, and decision for a suitable type will



be drawn depending on the result obtained from numerical calculations, simulations and experimental tests.

This thesis memory puts the light on three types of compensations as they are explained in next subsections. The primary compensation topology for them is chosen to be Series (S). It is because the inverter in the application is a voltage source one. Another reason is that the Parallel (P) primary resonant capacitor  $C_1$  value depends on the load; that means that it should be retuned every time the load changes [10]. This is not the preferred solution in our application. Here in next subsections, the transformer models that are used depend on the type of compensation in order to illustrate clearly the corresponding resonant elements.

**a) SS Leakage Compensation**

To understand the purpose of this topology, the T-model of two winding transformer shown before in Fig. I.7 b) is considered. Here, this topology is named after the compensations of  $L_{1\ell}, L_{2\ell}$  which are the *leakage* inductors of this model.

Then the values of the compensation capacitors  $C_1, C_2$  at a frequency  $f_0$  in Fig. I.12 are given:

$$f_0 = 1/2\pi\sqrt{L_{1\ell}C_1} \tag{6}$$

$$f_0 = 1/2\pi\sqrt{m_1^2L_{2\ell}C_2} \tag{7}$$

where  $m_1 = \frac{n_2}{n_1}$  is the transformation ratio.

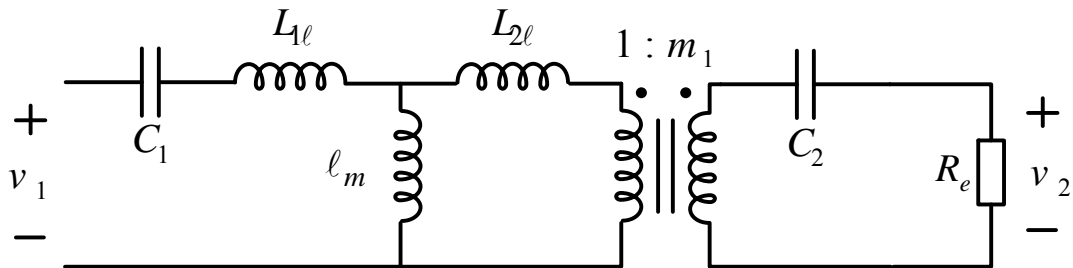


Fig. I.12: SS leakage compensation

### b) SS Self Compensation

For this type of compensation, the model of the transformer shown before in Fig. I.6 is considered. This topology is named after the compensations of  $L_1$ ,  $L_2$  which are the *self* inductors of the transformer model.

Then the values of the compensation capacitors  $C_1$ ,  $C_2$  at a frequency  $f_0$  in Fig. I.13 are given by:

$$f_0 = 1/2\pi\sqrt{L_1 C_1} \quad (8)$$

$$f_0 = 1/2\pi\sqrt{L_2 C_2} \quad (9)$$

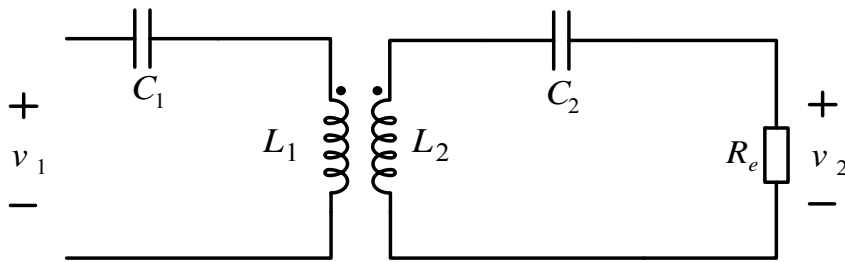


Fig. I.13: SS self-compensation

### c) SP Compensation

The cantilever model shown before in Fig. I.7 a) is considered to illustrate this topology. The primary capacitor  $C_1$  is inserted in series while  $C_2$  is in parallel at the secondary side. Here,  $C_1$  compensates the *total leakage* of the equivalent transformer seen from primary, and  $C_2$  tunes out the *self inductance* of the secondary of the equivalent transformer.

Then the values of the compensation capacitors  $C_1$ ,  $C_2$  at a frequency  $f_0$  in Fig. I.14 are given:

$$f_0 = 1/2\pi\sqrt{L_\ell C_1} = 1/2\pi\sqrt{((1 - k^2)L_1)C_1} \quad (10)$$

$$f_0 = 1/2\pi\sqrt{L_m C_2} = 1/2\pi\sqrt{m_2^2(k^2 L_1)C_2} = 1/2\pi\sqrt{L_2 C_2} \quad (11)$$

where  $m_2 = \frac{n_2}{n_1} \frac{1}{k} \sqrt{\frac{L_2}{L_1}}$ .

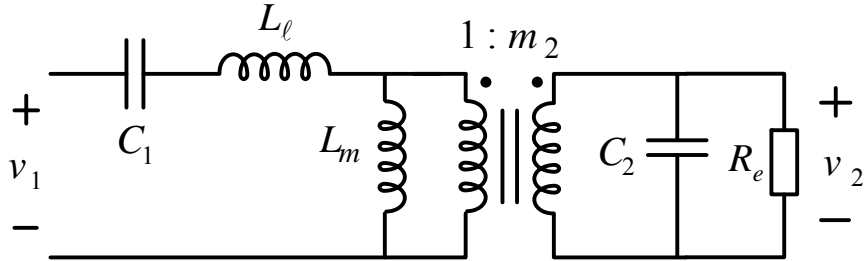


Fig. I.14: SP compensation

#### I.4.b. Resonant Converters

The power supply technology development requires high efficiency and high power density in the conversion of power. Using the resonant converter is known as a feasible topology to meet this trend and has become popular in various switching-mode power supply applications [42], [43], [23]. The wireless battery charger is one of these applications where the DC-DC conversion is its main process as in Fig. I.15.

Recently proposed architectures are made from resonant converters. Overall, the main advantages of these chargers are that they are safe and comfortable to use with galvanic isolation, and very suitable for the principle of charging without power cable [44]. Resonant converters with their control help in operating at the point of the compensation of the inductive parts of the system and improve the efficiency of power transfer of the IPT system.

A resonant DC-DC converter can be constructed by two main parts that are connected to the compensated ICT sides as shown in Fig. I.15:

- DC/AC Conversion: The DC input is obtained from rectifying the alternative source into DC and filtering by an input capacitor  $C_{1F}$ . Then this DC input stage is followed by an inverter that works at a switching frequency  $f_s$ . So this step converts the input DC to high AC line where the output current of the inverter is an input current to the primary resonant side  $i_1(t)$  at a frequency  $f_s$ .

- AC/DC Conversion: the AC output of a resonant inverter (via the transformer) is then rectified and filtered. The approximately sinusoidal current  $i_2(t)$  is rectified by a diode bridge rectifier and filtered by a large capacitor to supply a DC load having constant current  $I_o$  and voltage  $V_o$ .

The overall system works at a switching frequency  $f_s$  that imposed by the AC inverter.

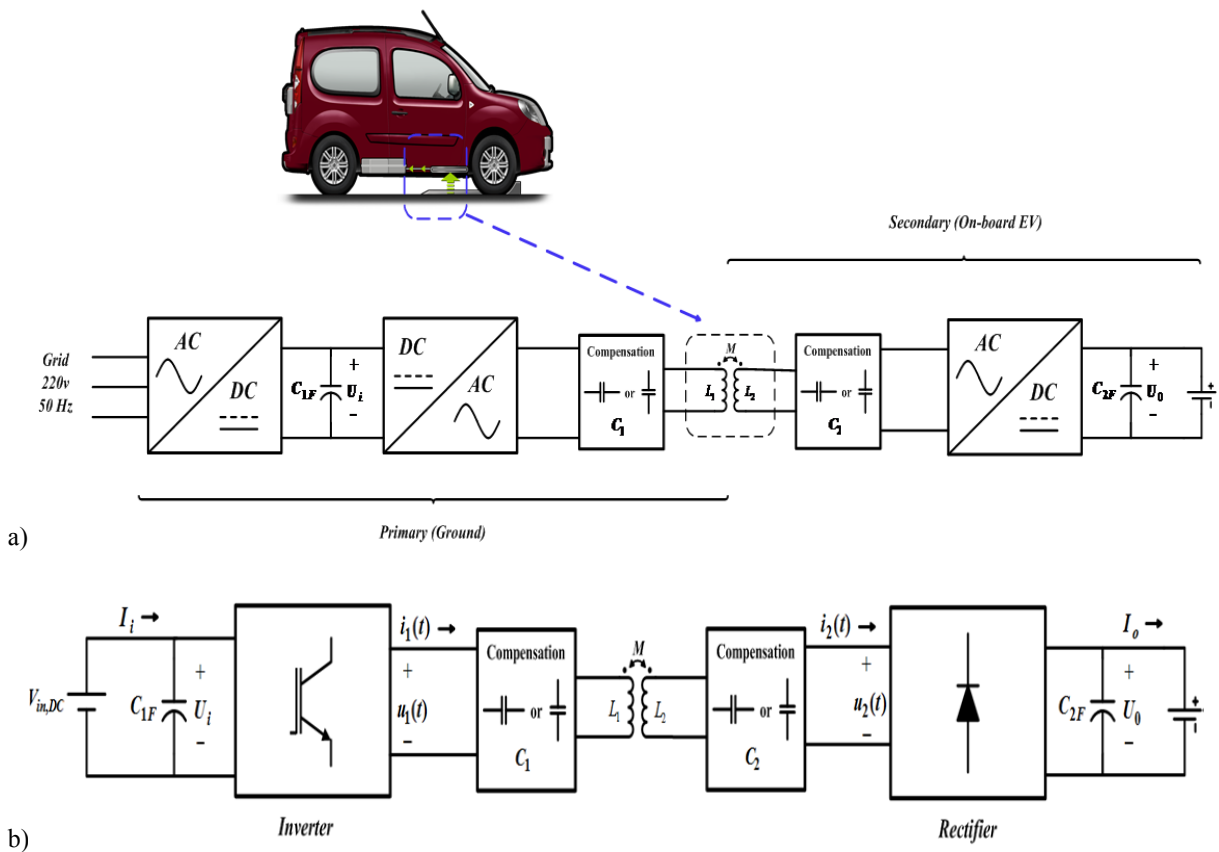


Fig. I.15: EV battery IPT charger system: a) full schematic stages and b) DC-DC resonant converter main stages

## I.5. Battery

### I.5.a. Battery Characteristics

The technology of on-board batteries is an important solution to EV and HEV in transportation domains [45]. Many factors define the characteristics and specifications of the battery and its operating conditions: fabrication type of battery (cell, modules, pack...etc), chemistry of the battery, temperature, discharge current rate, capacity of the battery (AH),

conditions of the battery (State of Charge SOC%, Depth of Discharge DOD%, terminal voltage, open circuit voltage, internal resistance, cycle time of life...) [46].

Many battery technologies are used by commercial EV&HEV companies in the world, for examples: NiMH (Toyota JAPAN, Honda JAPAN, Nissan JAPAN), Lithium polymer (Hyundai SOUTH KOREA), NiMH (BMW GERMANY, Daimler Benz GERMANY), Li-ion (Ford USA, GM USA, Mitsubishi JAPAN, Daimler Benz GERMANY) and Li-ion, sodium/Metal Chloride (Think Norway) [45]. So the most two used technology are: NiMH and Li-ion. Many recent researches and developments consider these types of batteries and their managements for the on-boards EV&HEV. The discharge curves for these two batteries cells are plotted in Fig. I.16. [47].

The nominal voltage of Li-ion (3.6V) cell is bigger than that of NiMH (1.25V), it means that 3 cells of NiMH connected in series are needed to supply same voltage as Li-ion. In other hand, the curve of NiMH is more flat than that of Li-ion, this means that NiMH curve is closer to an ideal battery behavior. So NiMH batteries are suitable for linear regulators but Li-ion batteries need switching converters to have good conversion efficiency in the power supply [47].

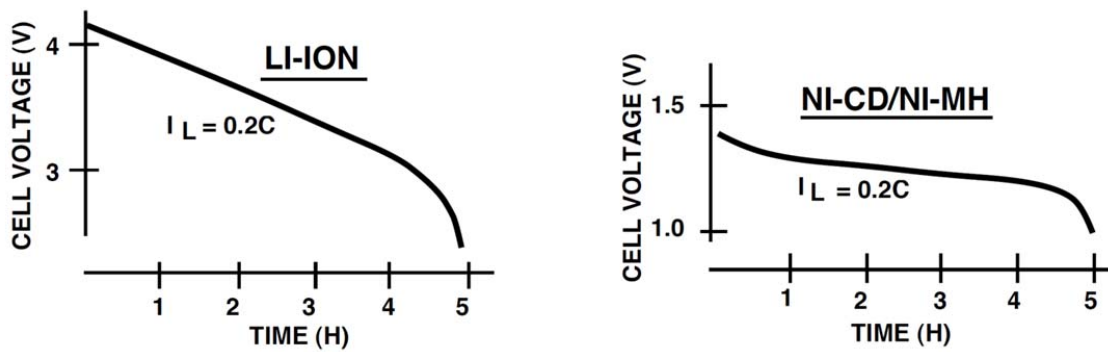


Fig. I.16: Cell discharge curves for different types [47]

### I.5.b. Modelling

One of the complicated issues for battery application is its electrical model. Since the battery has many variables that affect its performance and operation, it's difficult to find a precise model to represent the battery. However many researchers suggested and developed models for the battery to test the charger with the realist battery behavior [48].

The simplest model of battery contains a voltage source connected to a small internal resistance as in Fig. I.17 [48]. The voltage source here depends on the charging current that changes the SOC of the battery during the operation of charging. Also chemical and electrical equations can be embedded in the battery model as well as the ambient temperature. Other complex models can be found in [45], [48].

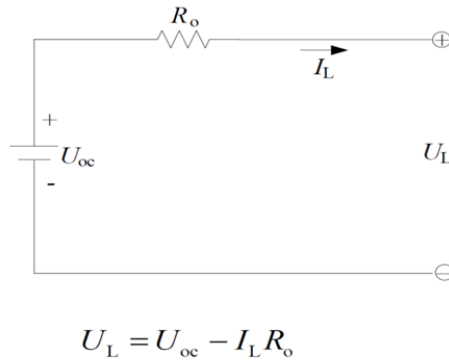


Fig. I.17: Simplified electrical model of a battery [48]

### I.5.c. Charging Profile

Several conversion structures lead to different types of charger, depending on the available power that is transmitted to the battery; the charging time is changing. As more power is delivered to the load; the charging time is short. The concepts of slow and fast charging therefore depend on the power supplied [44].

Many common methods are used to charge a battery of EV, they can be summarized as following [29], [45]:

- Constant Voltage: This method charges the battery at a constant voltage. It can be used for all types of batteries. The current absorbed by the battery varies along the charging process. The problem of this method is that it needs a high power in the starting cycle of charging process.
- Constant Current: for this method, the charging voltage applied to the battery is controlled to maintain a constant current to the battery. The SOC will increase linearly versus time for a constant current method. The challenge of this method is to

determine the completeness of a charge with SOC = 100%. The cut-off can be determined by the combination of temperature raise, temperature gradient raise, voltage increase, and charging time.

- Constant voltage and Constant Current: This method combines the last two methods during the charging process of a battery.

As an example, Fig. I.18 shows a charging profile of a Li-ion cell. At the initial stage, the battery can be pre-charged at a low, constant current if the cell is not pre-charged before. Then, it is switched to charge the battery with constant current at a higher value. When the battery voltage (or SOC) reaches a certain threshold point, the charging is changed to constant voltage charge. Constant voltage charge can be used to maintain the battery voltage afterward if the DC charging supply is still available [45].

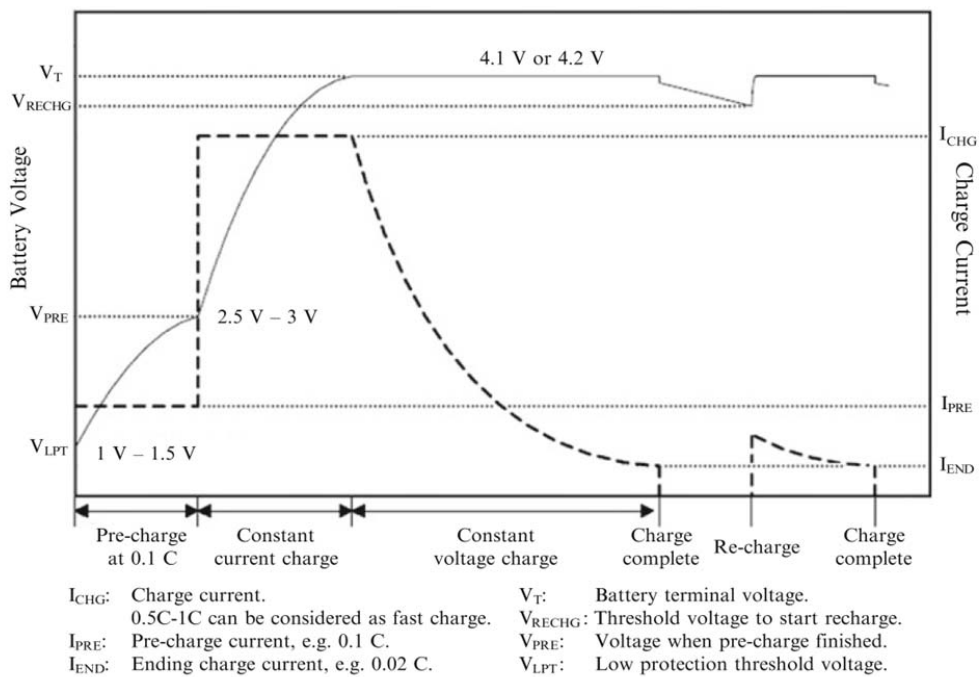


Fig. I.18: Li-ion cell charging profile [45]

## **I.6. Losses**

One of the important limiting factors of the process of energy transfer is the losses of overall system. There are many losses types in the IPT systems during the process of charging, the goal is to minimize these losses in order to maximize the overall efficiency. In the study of system optimization, the behavior of the system is analyzed taking into account the losses associated with their sources. In general, the losses in IPT systems can be qualified as:

### **- Joule Losses**

Practically, the total resistances of the turns of each side of the transformer are taken into account as seen before in Fig. I.6, then the losses by Joule effect or Copper losses can be calculated as [23], [34]:

$$P_{copper} = I_{i,rms}^2 R_i$$

where  $i = 1$  denotes for primary and  $i = 2$  for the secondary [34].

This type of losses is unavoidable and depends on the currents and the type of wires that form the inductances.

### **- Magnetic losses**

The magnetic losses in an ICT may come from magnetic material (ferrite) losses which include: hysteresis losses and eddy current losses that are caused by magnetic induction. Also eddy currents losses can be found in other parts of the ICT like the chassis and cables. They can be expressed per unit volume as [23], [34], [49]:

$$P_{ferrite,i} = P_{hysteresis,i} + P_{eddy\_ferrite,i} = \kappa_f f^\alpha B^\beta$$

$$P_{eddy,i} = \kappa_e f^2 B^2$$



where  $\kappa_f, \alpha, \beta$  and  $\kappa_e$  are constants that depend on the material,  $f$  is the operating frequency and  $B$  is the magnetic induction. These losses can be minimized by well choosing the materials for the application.

- **Switching losses**

The semiconductors components of the power electronics stages in IPT systems also add an important factor to the overall losses. The losses in the switch are found as: conduction losses due to the semiconductor internal resistance at the ON state mode, and switching losses (transient losses) that are caused by the transient period of switching from OFF to ON state mode or vice versa. They can be expressed for one component as [50]:

$$P_{switching} = \frac{V I_{avg}}{2} (t_{on} + t_{off}) f$$

$$P_{conduction} = R_{on} I_{rms}^2$$

$$P_{drive} = f V_{gs} Q_{gs} \text{ (MOSFET)}, \quad P_{drive} = f V_{ge} Q_{ge} \text{ (IGBT)}$$

The switching losses can be minimized by soft switching control. There are two types of switching: Zero Voltage Switching (ZVS) and Zero Current Switching (ZCS). The conduction losses can be minimized by choosing a semiconductor with small ON resistance. And the commande losses can be also decreased by minimizing the internal gate charge  $Q_{int}$ .

- **Other losses:**

Some radiation losses may appear because of the EMF radiation:  $P_{radiation} \left( \frac{W}{m^2} \right) = \frac{1}{2} \oint_s (\vec{E} \times \vec{H}) \cdot \vec{ds}$ . Also parastic or stray losses of the parasitic internal capacitances of the semiconductors and of the coils appear at high frequencies.

- **Consequences:**

The losses will lead to a thermal heating in the system, the heat transfer can be classified as: conduction, convection and radiation. A thermal model for an ICT is established in [34]. A 2D axisymmetric model of an ICT system with the thermal modelling is shown in Fig. I.19.

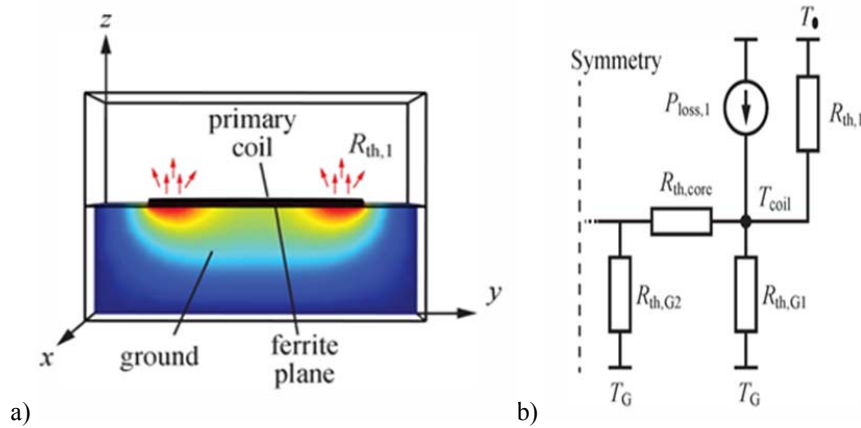


Fig. I.19: ICT thermal study in [34] a) FE simulation b) thermal model

### I.7. Radiation of Inductive Power Transfer (IPT) System

There are many sources of perturbation in IPT systems that produce conducted interference caused by high switching frequency and EMF emission as they are classed in the area of Electromagnetic Interference (EMI). All of them should respect an international standard to reduce their dangerous effect on the victims. These victims here are the electronics devices and they should be kept from failure and harmful effects. However, the most important requirement of international standard that is highly recommended to be fulfilled in IPT systems and especially for its biomedical applications is the Electromagnetic Compatibility (EMC) [51]. As high power is wanted to be transferred, the radiation will be more important and standards should be verified in order to validate the design.

The standards that define the acceptable exposure of human to EMF cover a wide frequency range (0 - 300 GHz) from static electric and magnetic fields (power frequencies, i.e. 50/60Hz) through radiofrequency, infrared, and visible light to X-rays as shown in Fig. I.20 [52], [53]. As an example from the literature [54], a 3D plot of the near-field radiation intensity of a

primary coil  $L_1$  integrated in a PCB system that centralized at the origin is shown in Fig. I.21. It shows that the radiation intensity is proportional to the inverse of the distance from the origin ( $B \propto 1/r ; 1/r^2 ; 1/r^3$ ) where the maximum is in a region close to the origin. This example is for a small amount of energy transfer, and for others applications like the case of EV battery charging, the radiation will be huge for sure as the primary current  $i_1$  is larger as well as the transferred power to the EV battery. So careful design and tests are necessary to limit the radiation levels and insure safety of human exposure of time varying EMFs.

Another example for measuring the EMC of a planar spiral coil integrated in a platform for portable wireless charging is investigated in [55]. A Noise Ken EPS-3000 EMC scanner is used to scan the magnetic field with a sensor Probe-A100 k (100kHz-100MHz). A 4-turn prototype with maximum radius of 66 mm is injected with a current of 10 mA at a 400kHz frequency. The scanned magnetic field intensity is shown in Fig. I.22.

These EMFs cause an induced current in a human body that circulates in the conductive tissues. In the case of implementable biomedical devices [56], [57] health risks as well may be increased.

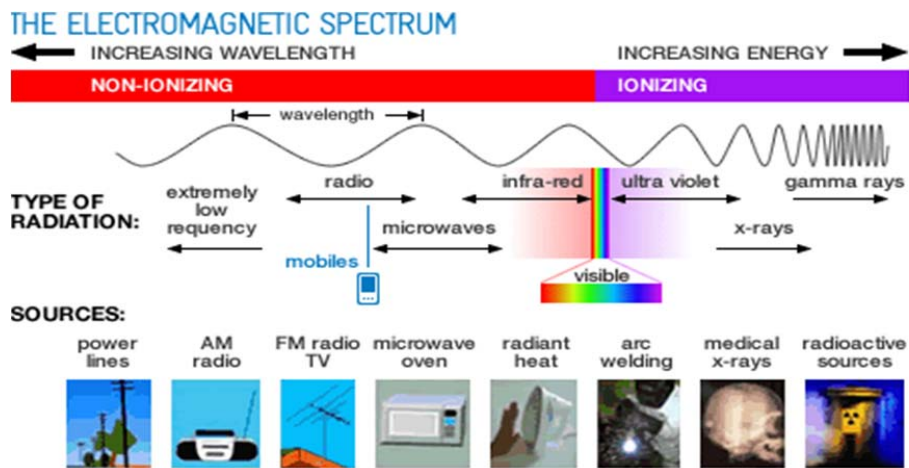


Fig. I.20: Frequency band for ionizing and non-ionizing radiation [53]

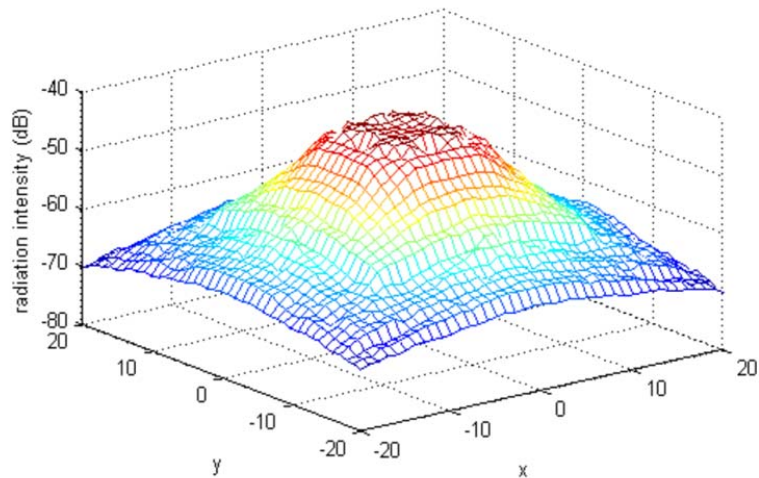


Fig. I.21: EMC Plot for near field radiation intensity of IPT system caused by L1 used in [54]

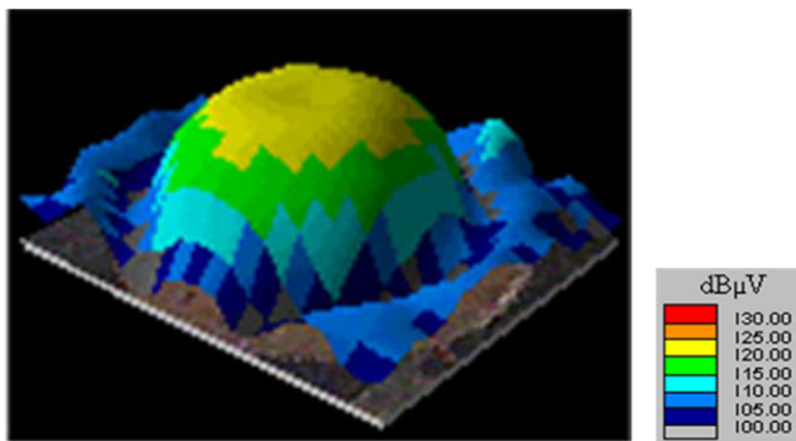


Fig. I.22: Scanned magnetic field intensity for a small spiral coil shown in [55]

International committees have defined the levels of human exposure corresponding to the operating frequency of IPT applications. Several guidelines announced by these international committees that should be respected to insure the design will avoid biological harmful effects on the human body. The famous commissions groups are: the International Commission on Non-Ionizing Radiation Protection ICNIRP (recommendations were published in 1998 and 2010), Australian Radiation Protection and Nuclear Safety Agency ARPANSA, the World Health Organization WHO, International Agency for Research in Cancer IARC and other groups. The limits for the occupational and general publics' exposure with operating frequency that were published by ICNIRP 1998 and 2010 [58], [59] are illustrated in Fig. I.23. It can be shown for our

applications with an operating frequency range (3 – 150 kHz) that the maximum magnetic field density  $|B|$  should not exceed  $6.25 \mu T$  for general public (1998). The limit is modified to  $27 \mu T$  for general public in 2010. What is taken into account here in the framework of CINELI project and this thesis memory for design validation are the guidelines published by ICNIRP 1998,  $|B|_{max} < 6.25 \mu T(rms)$ .

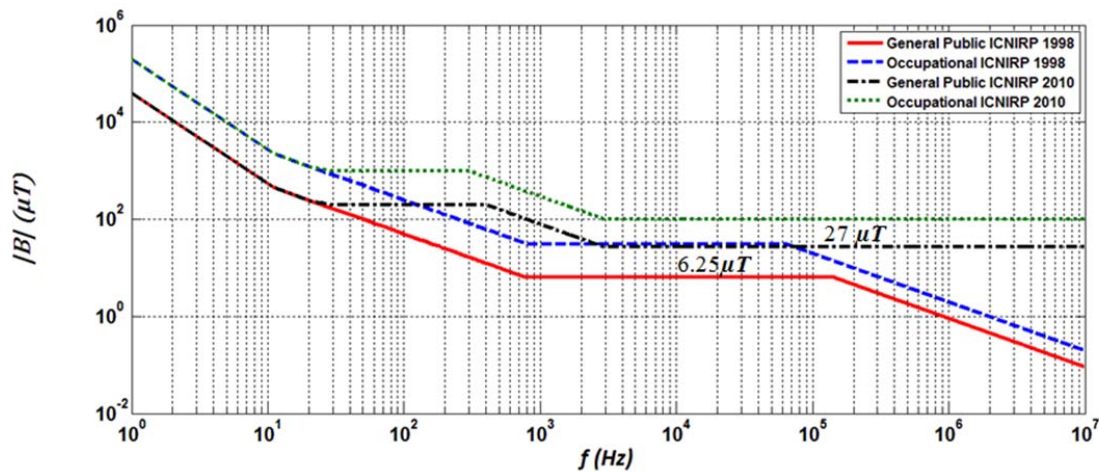


Fig. I.23: ICNIRP reference levels for exposure to time varying  $B$  published in 1998 and 2010

Up to date, there is a shortage in the literature and researches publications that concern the validation of human safety to EMFs exposure of the IPT design especially for the case of EV battery charging. However what is in hand up to now is the test of human exposure due to battery charging of EV by IPT system that has been done recently by [15], [32].

The test verified that, for a transmission of 5kW, the measurement of magnetic field at each situation of varying the system parameters (vertical and horizontal misalignment) for an ICT system shown in Fig. I.24 a) meets the stringent ICNIRP standards by using the measurement technique proposed by ARPANSA [15]. According to [32], there are two limits to meet: 1) Absolute maximum magnetic field exposed to the body must not exceed  $27.3 \mu T$  and 2) The average field strength by taking measurements at the head, chest, groin and knees must be below  $6.25 \mu T$ . Fig. I.24 a) shows that the absolute maximum magnetic field strength can be met at 0.82m, which is less than half of the width of a typical passenger vehicle. Body average measurements for 4 points on a 1500mm tall female human body were investigated. The body average of  $4.36 \mu T$  is measured for the worst case in as in Fig. I.24 b) [15], [32].

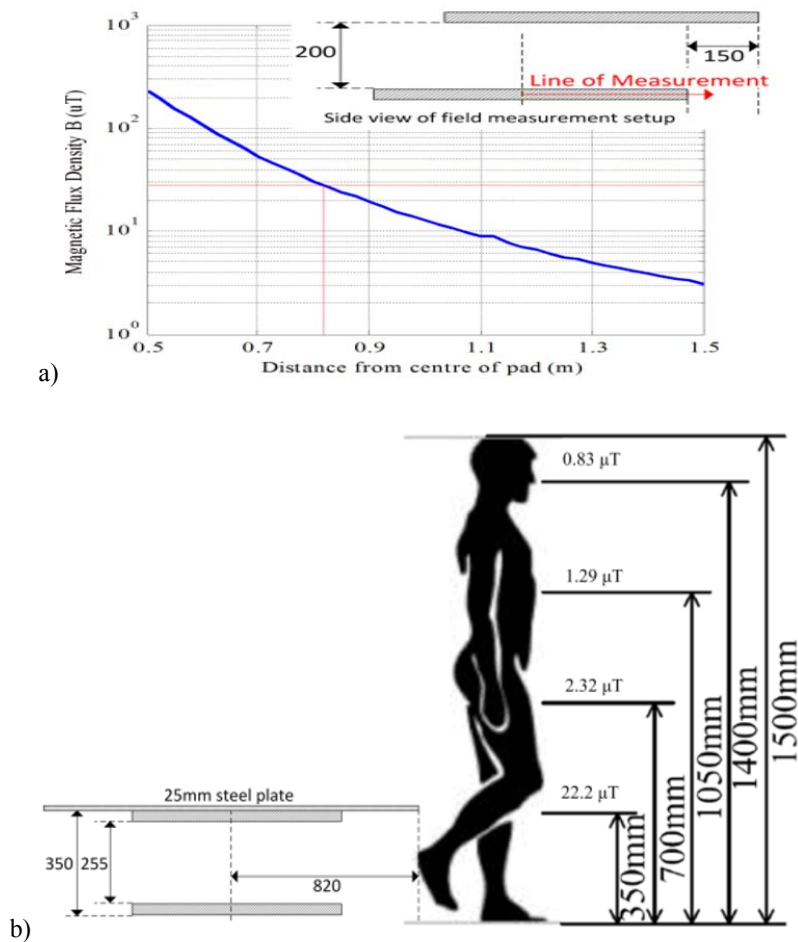


Fig. I.24: Magnetic field measurement results for 5kW system operating under worst conditions in [32]: a) charging pads and b) four point measurements test on a 1500 mm female body

### I.8. CINELI Project Goals and Thesis Novelty

The aim of CINELI project is to propose a standard in order to couple emitters with receivers from different suppliers. It's also an opportunity to have industrial companies (Renault, Schneider Electric and NewTech Concept) working in a partnership with our research center (LGEP). This would lead to improve the development times for electrical cars and to make a step forward in research and practical design against competitors who are trying to develop and impose their standards.

CINELI project aims at developing knowledge and methods to make it possible for carmakers to control:

- I. The magnetic radiation generated by the transfer of electrical power through induction, by addressing the problem in a scientific and practical way in relation to positional tolerance and emitter and receiver system interoperability.
- II. The performance of the system in mass-produced vehicles, in terms of energy efficiency and positional tolerance (efficient coupling with variable impedance).

This thesis which is the academic part of CINELI project, here the objectives and thesis novelty are summarized:

- I. Electromagnetic modelling by finite elements methods (FEM) of the ICT with the presence of the EV chassis of a real electrical car (KANGOO-Renault (Fig. I.1 & Fig. I.3)). Equations are derived with the help of the FEM that allows to calculate the self and mutual inductances. Tolerance in EV position and different air gaps of the ICT are considered. It will be shown that the EV chassis has a strong influence.
- II. Interoperability study for IPT system design and testing is a new idea and main goal in this memory. The interoperability is studied by testing and simulating different primary or secondary prototypes developed by each industrial partner and then integrated together in the IPT system.
- III. Objective criteria allowing the comparison between the different compensations topologies are presented. Thanks to these criteria, a proper topology is chosen for our application and more general conclusions are drawn.
- IV. The use of a Maximum Power Point Tracking (MPPT) frequency control to find the resonance of the whole system that corresponds to the maximum power that can be delivered from the primary (ground) to the secondary (EV on board) is studied.
- V. Finally, the radiated magnetic field is studied to check compliance with the standards proposed by the ICNIRP (1998). Simulation and measurements are shown for each system in different configurations (positioning) and interoperability is also considered.

***Chapter II : Finite Element Modeling and Interoperability Study of ICT***



## II.1. Introduction

The first step in the design study is the ICT stage, which is the heart of the system. This chapter carries the modelling of the ICT by a Finite Element Method (FEM) so as to study the physical behavior of the system. COMSOL [60] is considered in this thesis work as a calculation tool. In the first part of this chapter, identical coil forms of ICTs will be modeled in order to calculate the electrical parameters of self and mutual inductances ( $L_1$ ,  $L_2$ ,  $M$ ). In the scope of the study, each ICT prototype has its own parameters that differ from others; however some parameters are the same. There are three power pads considered in this thesis, they are named after the industrial partner who fabricated them, they are shown in TABLE II. These power pads are determined in the predesign of CINELI project considering: power transmission, operating frequency, mass (< 23Kg), volume and the mechanical integration in board of a KANGOO EV that limits the available space to insert the secondary (receiver) pad.

TABLE II: POWER PADS DEFINITIONS

<b>Company</b>	<b>Symbol</b>	<b>Pad Type</b>
<b>RENAULT</b>	<b>RNO</b>	<b>Circular</b>
<b>SCHNEIDER</b>	<b>SE</b>	<b>Circular</b>
<b>New-Tech Concept</b>	<b>NTC</b>	<b>Square</b>

The EMF distribution can be obtained using a finite element model of the ICT. A validation test will be shown to verify the agreement between the calculations and test data and allows us to use the same modeling method for the other prototypes.

The second part highlights the interoperability study of ICTs. It means that different pad structures at each side (primary, secondary) of the ICT will be modelled and studied. Finally, a comparison between all prototypes will be performed.

## II.2. Modelling of ICT

To study the operation of the system, an ICT schematic is drawn for circular pads model (for an example) as in Chapter I, Fig. I.5. We assume that the coils have the following characteristics:

- numbers of turns for the coils are  $(n_1, n_2)$
- outer radii are  $(r_1, r_2)$ .
- their vertical axis are parallel (for simplification)
- the ferrites are considered linear and not saturated.

The alternative supplying current in the transmitter coil  $L_1$  creates a varying magnetic field and then a magnetic flux ( $\Phi_{21}$ ) through the circular area ( $S_2$ ) inside the  $L_2$  coil [20]:

$$\Phi_{21} = \int_{S_2} B_1 \cdot ds_2 \quad (12)$$

$$\varphi_{21} = \int_{S_2} (\nabla \times A_1) \cdot ds_2 = M_{21} i_1 \quad (13)$$

where  $M_{21}$  (H) is the mutual inductance between the  $L_1$  coil and the  $L_2$  coil.

Then the induced electromotive force in the  $L_2$  coil of  $n_2$  turns is:

$$e_{21} = -n_2 \frac{d\varphi_{21}}{dt} = -M_{21} \frac{di_1}{dt} \quad (14)$$

And the electromotive force induced by its own flux is:

$$e_{22} = -n_2 \frac{d\varphi_{22}}{dt} = -L_2 \frac{di_2}{dt} \quad (15)$$

Therefore, the total electromotive force in the  $L_2$  coil of turns  $n_2$  is:

$$e_2 = e_{21} + e_{22} = -M_{21} \frac{di_1}{dt} - L_2 \frac{di_2}{dt} \quad (16)$$

Similarly, the total electromotive force in the  $L_1$  coil is:

$$e_1 = e_{11} + e_{12} = -L_1 \frac{di_1}{dt} - M_{12} \frac{di_2}{dt} \quad (17)$$

$$M_{12} = M_{21} = M \quad (18)$$

The coupling factor can be found from the self and mutual fluxes as [61]:

$$k = \sqrt{k_1 k_2} = \sqrt{\frac{\varphi_{12} \varphi_{21}}{\varphi_{11} \varphi_{22}}} \quad (19)$$

$$\varphi_{11} = \varphi_{12} + \varphi_{1l} \quad (20)$$

$$\varphi_{22} = \varphi_{21} + \varphi_{2l} \quad (21)$$

$$k = \frac{M}{\sqrt{L_1 L_2}} \quad (22)$$

where  $\varphi_{1l}$  and  $\varphi_{2l}$  are the primary and secondary leakage fluxes respectively as was shown in Fig. I.5. In order to compute the values of the inductances (self and mutual), the electromagnetic field problem is solved in the frequency domain using a magnetodynamic A, V formulation:

$$\nabla \times (\mu^{-1} \nabla \times A) = J \quad (23)$$

In conducting regions;

$$J = \sigma(-i\omega A - \nabla V) \quad (24)$$

and  $J = J_e$  in the coils.

where  $A$  is the magnetic vector potential,  $V$  is the electric scalar potential,  $\mu$  is the permeability,  $\omega$  is the pulsation,  $\sigma$  is electric conductivity and  $J_e$  is the imposed current density. Ferrites are considered as linear materials because the induction does not exceed 0.4T.

The self and mutual inductances ( $L_1, L_2, M$ ) are calculated for different values of the parameters  $d$  and  $sh$ . These inductances are computed by volume integrals derived from the expression of the magnetic energy [62], [63]. We denote by  $A_\varphi$  the azimuthal component of the magnetic vector potential in the cylindrical coordinate system associated with the considered coil:

$$L_1 = \Re \left\{ \iiint_{v_1} \frac{n_1 A_\varphi}{I_1 \cdot s_1} \partial v \right\} \text{ when } I_2 = 0 \quad (25)$$

$$L_2 = \Re \left\{ \iiint_{v_2} \frac{n_2 A_\varphi}{I_2 \cdot s_2} \partial v \right\} \text{ when } I_1 = 0 \quad (26)$$

$$M = \Re \left\{ \iiint_{v_2, I_2=0} \frac{n_2 A_\varphi}{I_1 \cdot s_2} \partial v \right\} = \Re \left\{ \iiint_{v_1, I_1=0} \frac{n_1 A_\varphi}{I_2 \cdot s_1} \partial v \right\} \quad (27)$$

where  $s_1, s_2$  are the coil cross sections,  $n_1, n_2$  the number of turns of each coil and  $v_1, v_2$  are the volumes of the coils. The notation  $\Re\{.\}$  presents the real value, and the currents that imposed (or the current densities) in the simulation are real values.

### II.3. Circular Pads of Type RNO-RNO

This section shows two types of ICTs: the first one is the system without the EV chassis, and the second one, which is the realistic one, is the system with the EV chassis. The two systems have the same power pads, and the same geometrical parameters, they are of RNO-RNO prototype. We study the influence on the electric parameters of two geometric parameters: the distance between the coils (or the air gap), and the axis shift between the coils centers;  $d$  and  $sh$  respectively. TABLE III schedules the parameters that define the RNO-RNO ICT prototype. In this model,  $s_1 = s_2$  and  $n_1 = n_2$ ,  $v_1$  and  $v_2$  are the volume of the coils. The coils are made of isolated Litz wire, and the operating frequency is  $30kHz$ .

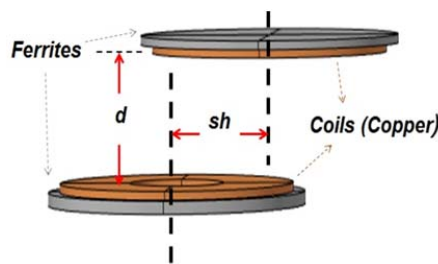
#### II.3.a. Modelling without EV Chassis

The structure of this system is shown in Fig. II.1. As illustrated before, it contains two circular coils and circular ferrites that cover the coils. Since the distance between the  $n$  turns coils is very small the coils are considered as one turn whose section is equal to  $n$  multiplied by the section of a single wire. So the total volume is kept the same. The corresponding solution will not be different for the cases of  $n$  turns structure or a single turn structure as soon as they have the same volume for an operating frequency of  $30kHz$ . Also the current density is uniform for all turns in real test, and it is uniform in the section of the modeled inductor in simulation. As mentioned before, the current in calculation is imposed and the inductor is nonconductive.

TABLE III: ICT AND EV CHASSIS PARAMETERS (RNO-RNO PROTOTYPE)

Side	Type	Parameter	Value
Primary	Ferrite (N27)	Width	10 mm
		Diameter	550 mm
	Coil	Number of Turns	20
		Cross Section	855 mm <sup>2</sup>
		Outer Diameter	500 mm
Secondary	Ferrite (N27)	Width	5 mm
		Diameter	550 mm
	Coil	Number of Turns	20
		Cross Section	855 mm <sup>2</sup>
		Outer Diameter	500 mm
	Chassis	Width	5 mm
Length×Depth		1.6×1.6 m <sup>2</sup>	

Based on the 3D FEM modeling using COMSOL, the values of  $L_1$ ,  $L_2$  and  $M$  are calculated using equations (25) to (27). The calculation also includes the influences of variation of the parameters ( $d$  and  $sh$ ). Fig. II.2 shows the influence of  $d$  (m) variations at axis shift 0 and 0.1 m. The coupling factor is plotted in Fig. II.3 as a function of  $d$  and  $sh$ .

Fig. II.1: ICT circular prototype without EV chassis: Air Gap ( $d$ ) and axes shift ( $sh$ )

It can be noticed from Fig. II.2 that the variations in the self-inductances  $L_1$  and  $L_2$  are large at a small air gap  $d$ , and they are small for large air gaps. This is because the ferrites highly contribute to the magnetic flux  $\Phi$  distribution in the coupler for small air gaps. The mutual

inductance  $M$  always decreases by increasing the air gap due to the increase of the leakage magnetic flux and so the coupling factor  $k$  drops as shown in Fig. II.3. Without chassis the system is symmetrical and the two inductances of  $L_1$  and  $L_2$  have the same value, this value varies with the position changes.

The drop in the values of self-inductances  $L_1$  and  $L_2$  are also due to the flux cancellation phenomenon. To show the distribution of the magnetic flux lines generated by the primary coil excitation for example, the system is simulated as shown in Fig. II.4. This model is considered in order to illustrate the flux cancellation phenomenon. However, the same phenomenon occurs when the chassis is present. This figure shows that the positive flux is added to negative ones, the cancellation will be larger for the case of increasing of air gap and also if there is an axes shift between the centers. The number of positive lines and negatives ones are different for every plot.

The magnetic flux density norm  $B$  (mT) is plotted in Fig. II.5, and also the arrows for  $B$  are shown for a 3kW, with  $i_1 = 40A$  and  $f = 30kHz$  at  $d = 15cm$  and two values of  $sh$  (0, 10cm). This figure shows that the maximum of the  $B$  increases in the secondary ferrite plate with an axes shift, however this value is also under the 0.4T and the ferrites are still linear and don't saturate.

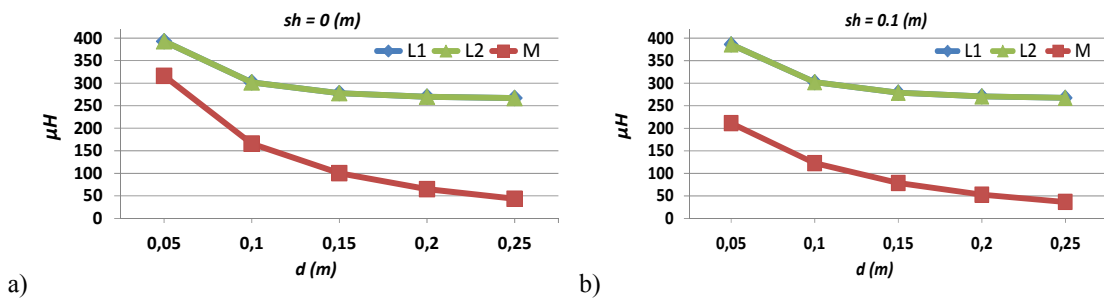


Fig. II.2:  $L_1$ ,  $L_2$  and  $M$  as a function of air gap  $d(m)$ : a)  $sh=0$  and b)  $sh=0.1m$ .

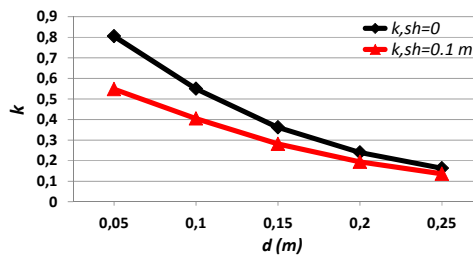


Fig. II.3: Variation of  $k$  with respect to air gap  $d(m)$  when  $sh=0$  and  $0.1m$

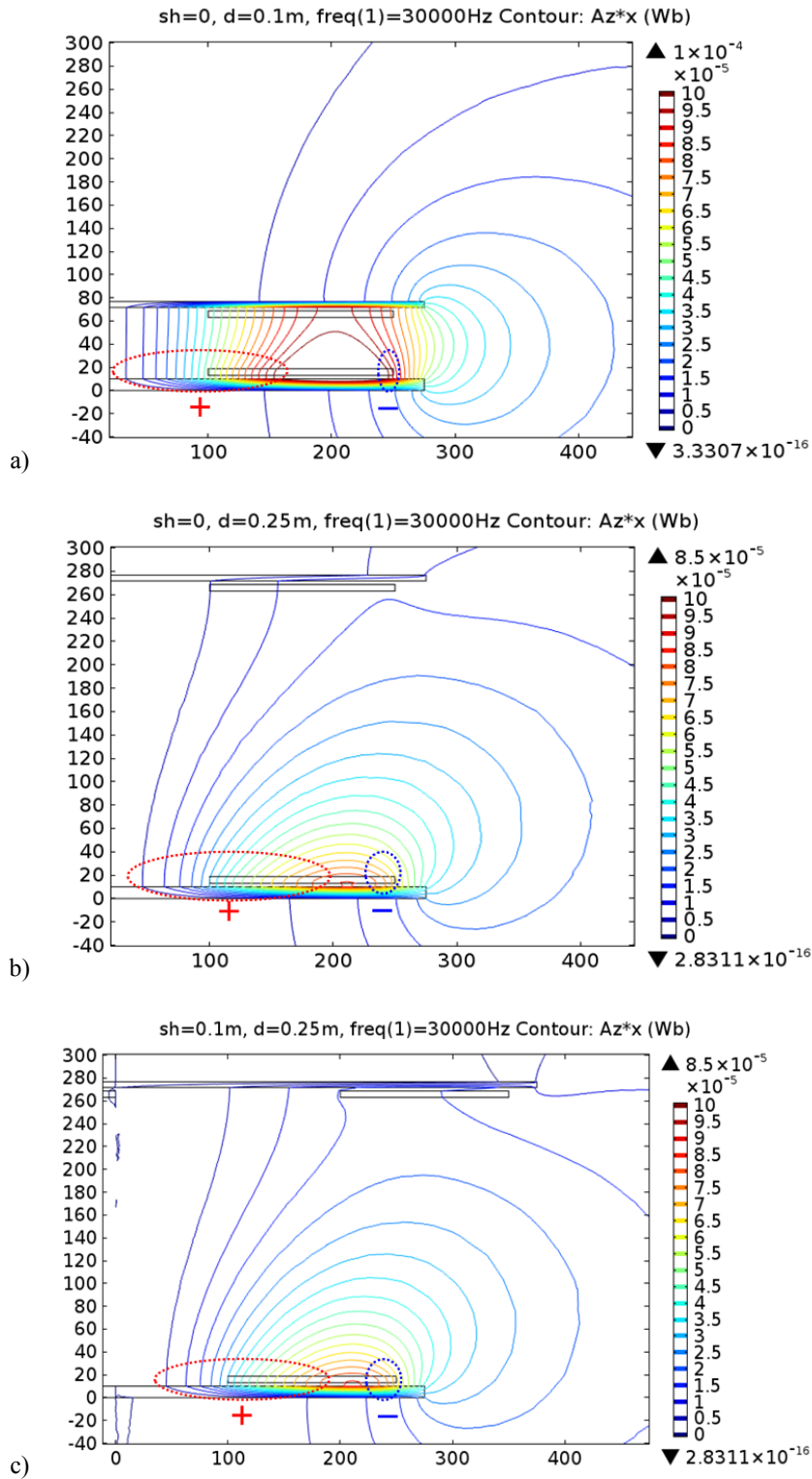


Fig. II.4: Magnetic flux lines for 2D cut plane (xy) for the system in Fig. II.1 with primary excitation for: a)  $sh = 0, d = 0.1\text{ m}$ , b)  $sh = 0, d = 0.25\text{ m}$  and c)  $sh = 0.1, d = 0.25\text{ m}$ . The figures show the flux cancellation phenomenon

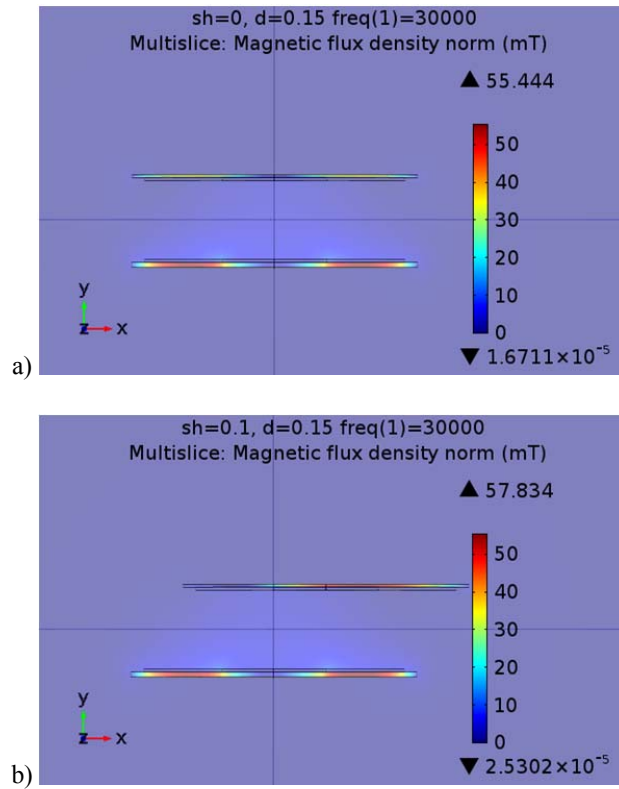


Fig. II.5: Magnetic flux density and norm  $B$  (mT) for a distance  $d = 0.15\text{ m}$ ; a)  $sh = 0$  b)  $sh = 0.1\text{ m}$

### II.3.b. Modelling with EV Chassis

The 3D structure of the ICT with the chassis is illustrated in Fig. II.6. It consists of a transmitter coil, a receiver coil and two ferrites plates that completely cover the coils. A steel plate which describes a simplified model of EV chassis is added in the design. The presence of the chassis has significant effect on the values of  $(L_1, L_2, M)$ . It ensures better protection for the embedded electronic devices and reduces passengers' exposure to magnetic field.

To model the chassis by FEM in COMSOL, two cases are considered and compared:

- The chassis is made of a  $5\text{ mm}$  width stainless steel ( $\mu_r \sim 1000 \frac{H}{m}$ ,  $\sigma \sim 10^6\text{ S/m}$ ) sheet. With the real characteristics the skin depth is very thin ( $\sim 100\mu\text{ m}$ ) at  $f = 30\text{ kHz}$ . For this case the element size in the finite element mesh size should be less than  $\frac{1}{3}$  the skin depth in order to have correct results with the FEM.



- The chassis is considered as a perfect electric conductor. ( $n \cdot J = 0, n \times A = 0$ ). Therefore only the mesh of the outer surface of the chassis is considered.

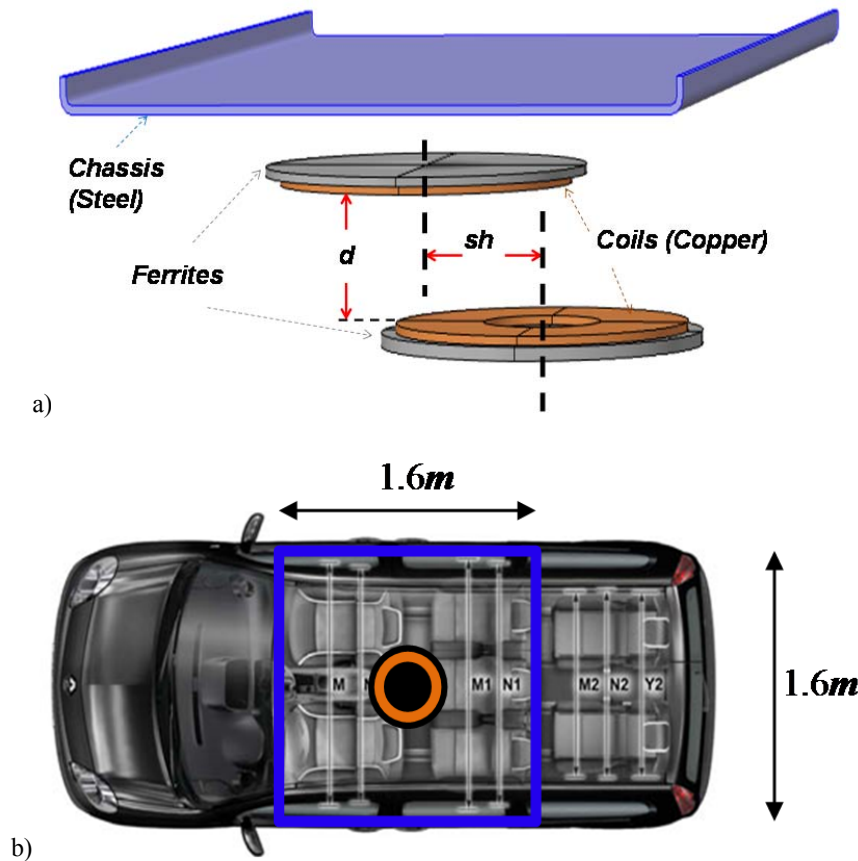


Fig. II.6: RNO-RNO prototype with EV chassis: a) model in COMSOL and b) top view of the EV to show the considered chassis and the position of secondary pad

Also for simplification, 2D axisymmetric studies are drawn for the two cases due to heavy time of calculation caused by a high number of finite elements (especially for the first case) and limited processor capacity. The simulation results are shown in Fig. II.7. For the first case, the number of elements (19.8 million) is extremely high. The calculation capacity was very heavy (96 Giga of RAM) and the computational time also was long (6 hours). On the other hand, for the second case, the number of elements is much lower (17513). The calculation time is faster, and the capacity of the processor is very low and can be done by an ordinary machine.

As the results of FEM calculation are the same for the two cases, and taking into account the advantages of the comparisons as stated before, the EV chassis is modeled as a perfect conductor for

all cases for the next modeling studies. So the chassis is modeled by a perfectly conductive 2D surface. Losses due to induced currents in the chassis are then not taken into account in our model. These losses could be evaluated using the distribution of the surface current density given by the model and the penetration depth determined by the frequency and the real material parameters.

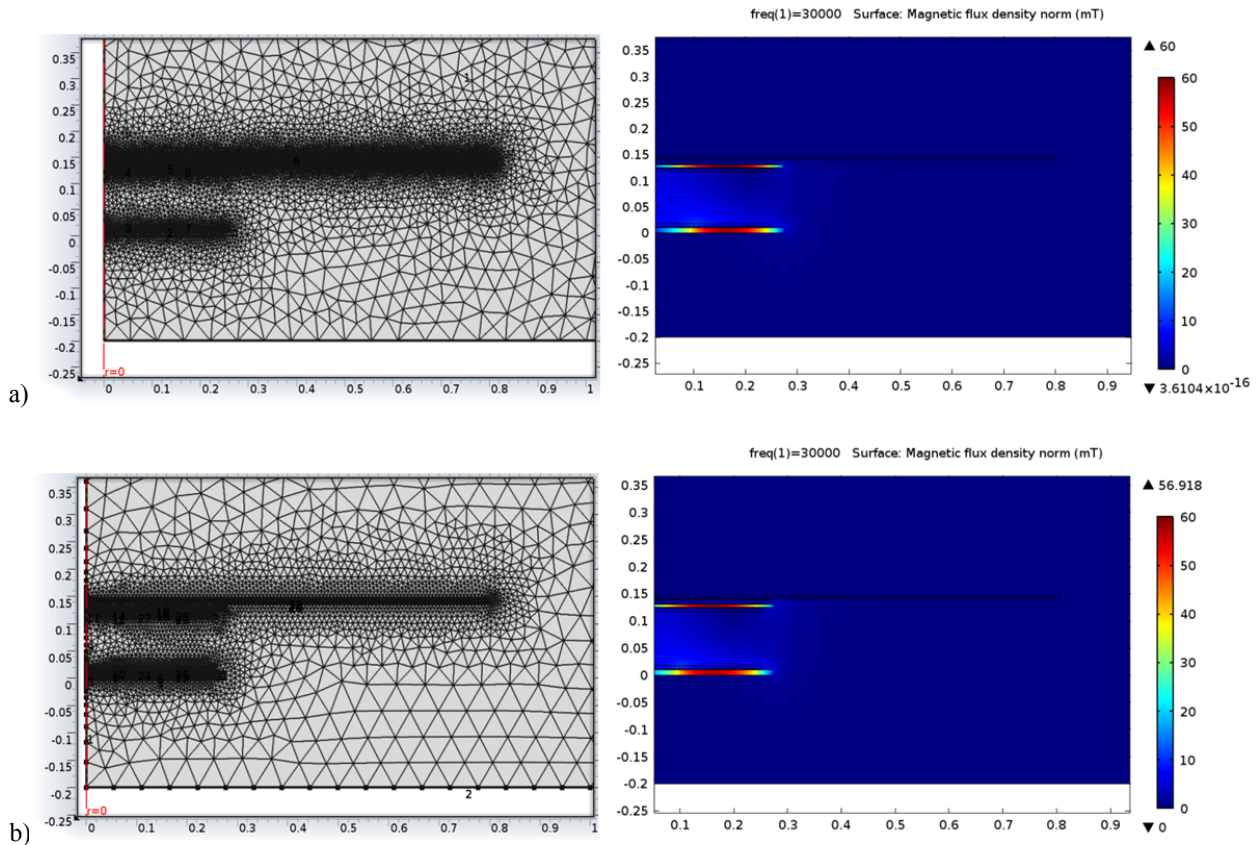


Fig. II.7: Simulation results considering; a) modelling the real chassis b) chassis as a perfect conductor. Meshing results (left) and EM calculation results (Right)

Therefore a 3D FEM modeling is performed considering the chassis as a perfect conductor. The values of  $L_1$ ,  $L_2$  and  $M$  are calculated using equations (25)-(27). The calculation also includes the influences of variation of the parameters ( $d$  and  $sh$ ). Fig. II.8 shows the influence of  $d$  ( $m$ ) variations at axis shift  $0$  and  $0.1$   $m$ . Also the coupling factor is plotted in Fig. II.9.

It can be seen from Fig. II.8 that the variations in the self-inductances  $L_1$  and  $L_2$  are large with a small air gap  $d$ , and they are small for large air gaps. This is because the ferrites and the EV chassis highly contribute to the magnetic flux  $\Phi$  distribution in the coupler for small air gaps. The mutual inductance  $M$  always decreases by increasing the air gap due to the increase of the leakage

magnetic flux and so the coupling factor  $k$  drops as shown in Fig. II.9. Because of the presence of chassis, the ICT is not symmetrical, and so  $L_1 \neq L_2$  in general.

It can also be noticed that  $L_1$  and  $L_2$  do not have exactly the same variations with respect to  $d$  and  $sh$ . So without chassis the two inductances of  $L_1$  and  $L_2$  have the same value, this value varies with the position changes. The presence of the chassis leads to unsymmetrical magnetic field distributions for  $L_1$  and  $L_2$ , and so, their inductances are different. The two values of these inductances vary independently with the position changes.

The magnetic flux density norm  $B$  (mT) is plotted in Fig. II.10, and also the arrows for  $B$  are shown for a 3kW, with  $i_1 = 40A$  and  $f = 30kHz$  at  $d = 15cm$  and two values of  $sh$  (0, 10cm). Resonant capacitors can be tuned with respect to  $L_1$  and  $L_2$  in a reference configuration (i.e.  $d=0.15m$  and  $sh=0$ ) in order to work with a “single resonance frequency  $f_0 = 30kHz$ ”. Then, when the configuration is changed, the resonant frequencies at primary and secondary are different.

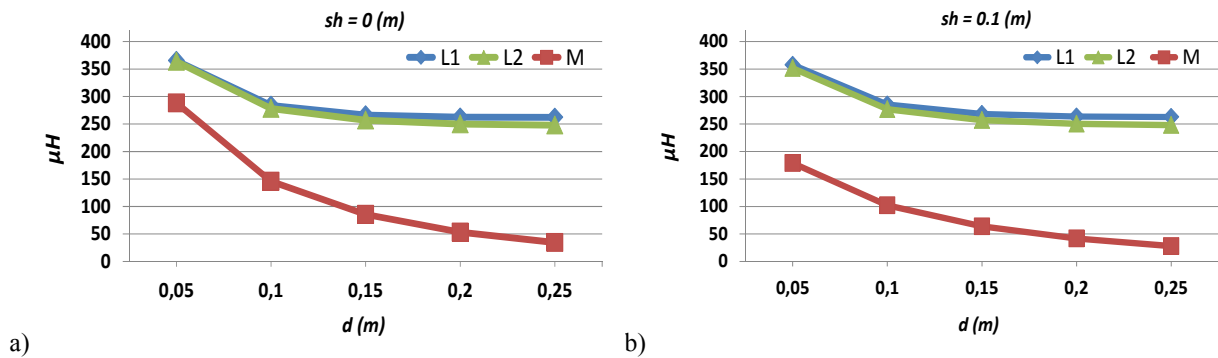


Fig. II.8:  $L_1$ ,  $L_2$  and  $M$  as functions of the air gap  $d(m)$ : a)  $sh=0$  and b)  $sh=0.1m$

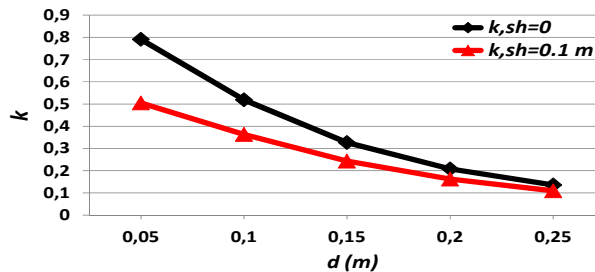


Fig. II.9: Variation of  $k$  with respect to air gap  $d(m)$  when  $sh=0$  and  $0.1m$

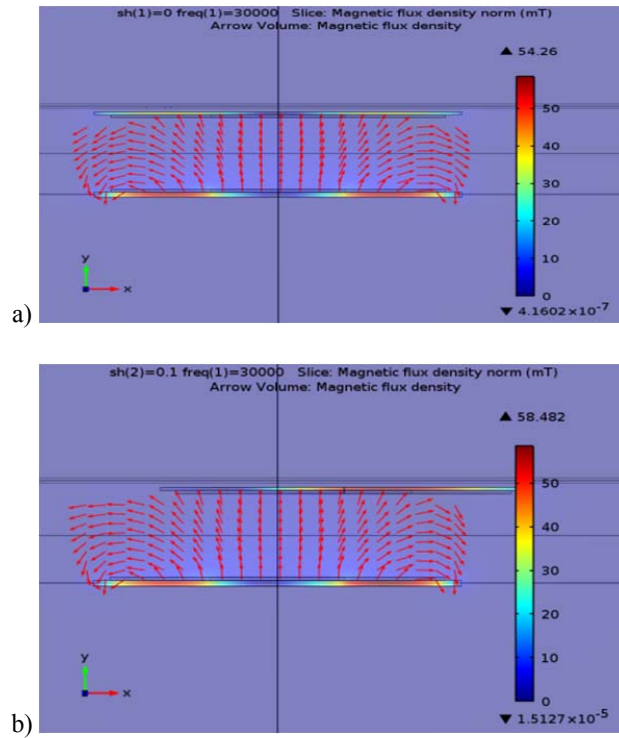


Fig. II.10: Magnetic flux density (arrows) and norm  $B$  (mT) for a distance  $d=0.15\text{m}$ ; a)  $sh=0$  b)  $sh=0.1\text{ m}$

Now a comparison can be established between the ICT without and with chassis. Two other configurations are also added in the study: coils in air (without ferrites and without the chassis) and coils with the chassis without ferrites. The considered configurations are described in TABLE IV. The parameters which are compared are the self and mutual inductances, and the coupling factor  $k$ . The results of the four configuration study are plotted in Fig. II.11 and Fig. II.12.

TABLE IV: ICT CONFIGURATION

<b>Symbol</b>	<b>Configuration</b>
<b>A</b>	The system in Fig. II.6 that includes the coils, ferrites and the chassis
<b>B</b>	The system without the chassis (with coils and ferrites)
<b>C</b>	The system with only the coils (without ferrites and chassis)
<b>D</b>	The system with coils and chassis (without ferrites)

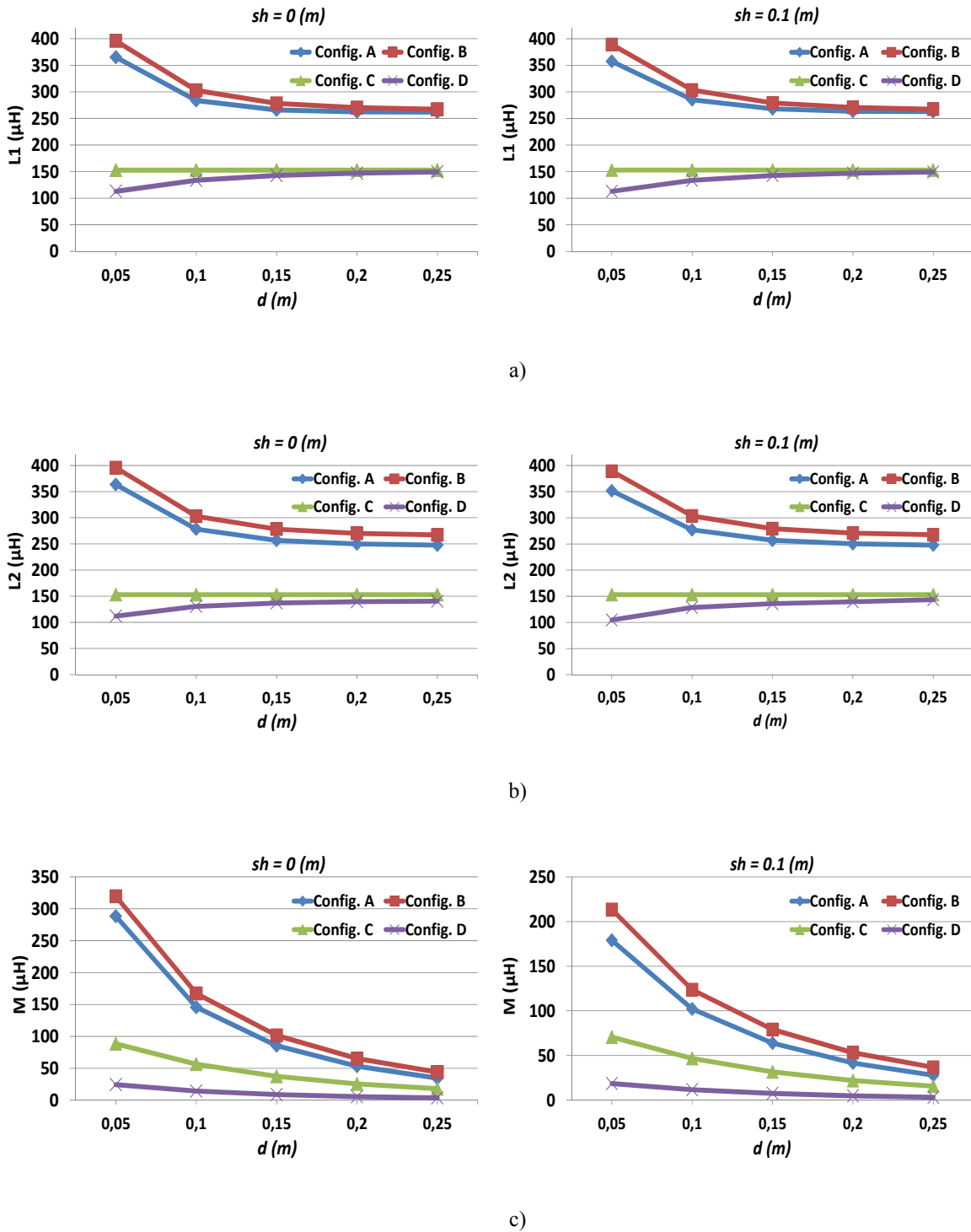


Fig. II.11: Comparisons between different configurations of ICT described in TABLE IV as a function of  $d$  (m);

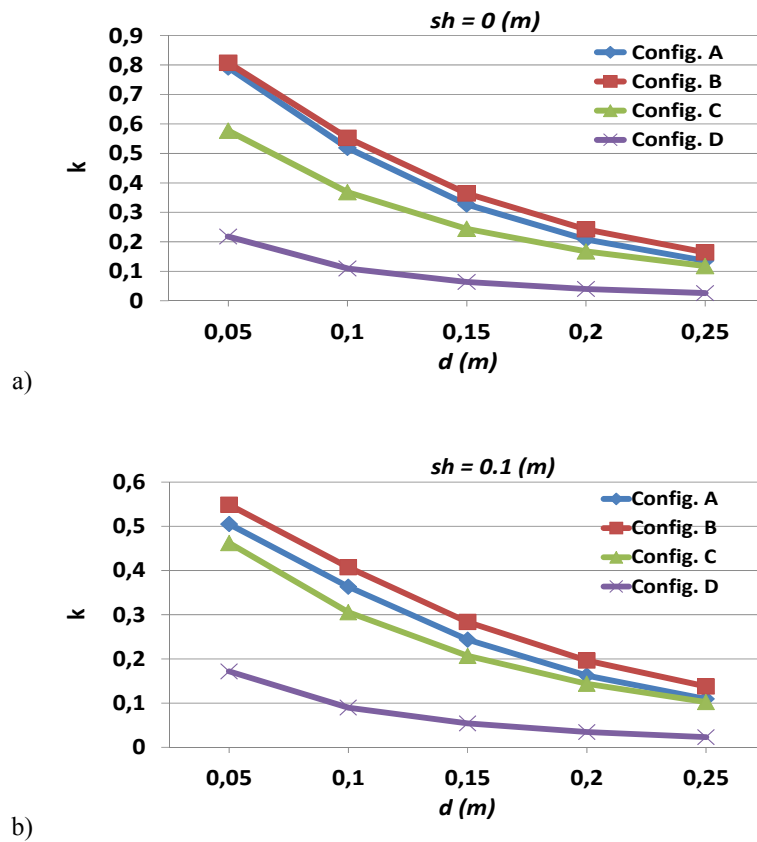


Fig. II.12: Coupling factor  $k$  for different configurations of ICT described in TABLE IV as a function of  $d$  (m)

From the plots we can state the followings:

- For  $L_1$  and  $L_2$ : The largest values are obtained in configurations with ferrites. In all configurations the axis shift has a small effect. Increasing the distance between the coils has opposite effects in configurations with and without ferrites (with chassis). In Config. A and Config. B, inductances decrease with increasing distance. In Config. D, the inductances increase with distance. Also it can be seen that the value of  $L_2$  is still slightly lower than  $L_1$  in the presence of the chassis thus making the non-symmetrical system.
- For  $M$ : The presence of ferrite provides much larger values than in the other configurations. The values of  $M$  in Config. A is smaller than that in Config. B but is less sensitive to the axes shift. The effect of increasing the distance between coils is similar for all configurations.

In conclusion, the use of magnetic shielding, where the ferrite is mostly used, as explained in Chapter I, is essential in ICT. This configuration leads to the best mutual between the two pads. The presence of the chassis (realistic configuration) decreases the values of the self and mutual inductances. It also has the effect of introducing an asymmetry in the system and makes it less sensitive to the axes shift.

Finally, from the plot of coupling factor  $k$  shown in Fig. II.12, and as expected, the best coupling is for Config. B then for Config. A (where there are ferrites). So it is important to consider the chassis in the FEM as a real case for EV as the values of coupling factors in Config. A differ from Config. B.

#### **II.4. Validation Test**

In this section a test to verify the calculations of FEM is investigated. The RNO-RNO prototype with the EV shown before in Fig. II.6 is tested. This will allow to evaluate the accuracy of the FEM by a comparison between the simulation results and the experimental results. Other tests that handle all the design for different prototypes will be shown in Chapter IV.

The test bench for the developed full model including the EV (KANGOO-RENAULT) chassis is shown in Fig. II.13. The test equipment installation that includes the power pads of RNO-RNO prototype with the EV chassis was shown in Fig. II.6. The positioning parameters are:  $d = [0.05, 0.1, \dots, 0.25]$  (m), and  $sh = [0, 0.1]$  (m). The dimensions of the ICT elements with the EV chassis are listed in TABLE III. The values of self and the mutual inductances shown before in Fig. II.8 are presented here with their corresponding measurements in Fig. II.14.

The results of simulations show good agreement with respect to the measured ones. However there are some errors between them that can be noticed, especially for  $L_1$ . The errors between the results of calculations and measurements could be come from: fabrications of the coils, accuracy of measurement devices and the hypothesis here to take a simplified perfect conductor EV chassis rather than the exact complex shape. This last one will have the major impact for relative error between simulations and measurements, especially for  $L_1$ . A full test with the other parts of the IPT system will be shown in Chapter IV.

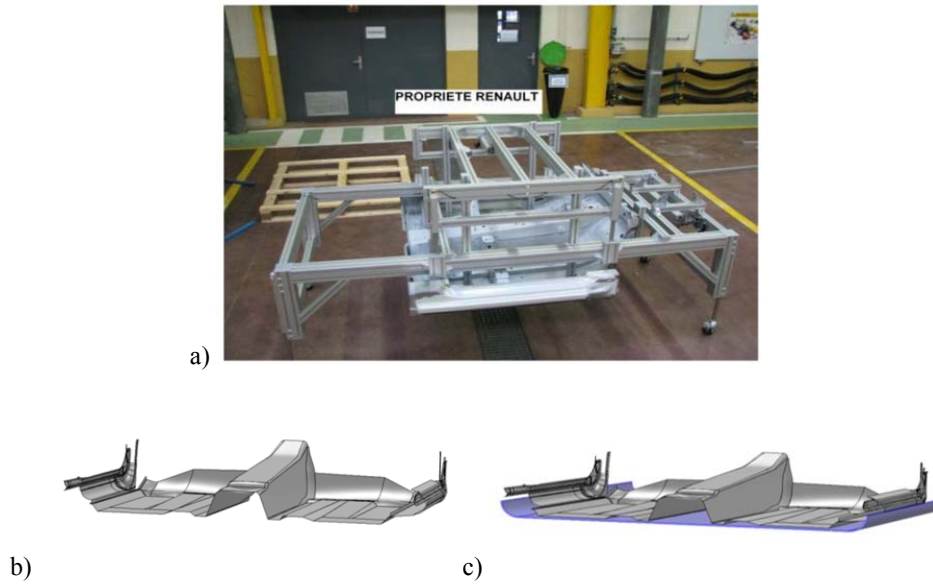


Fig. II.13: EV Renault-Kangoo chassis: a) practical b) CAD and c) CAD with the simplified presentation

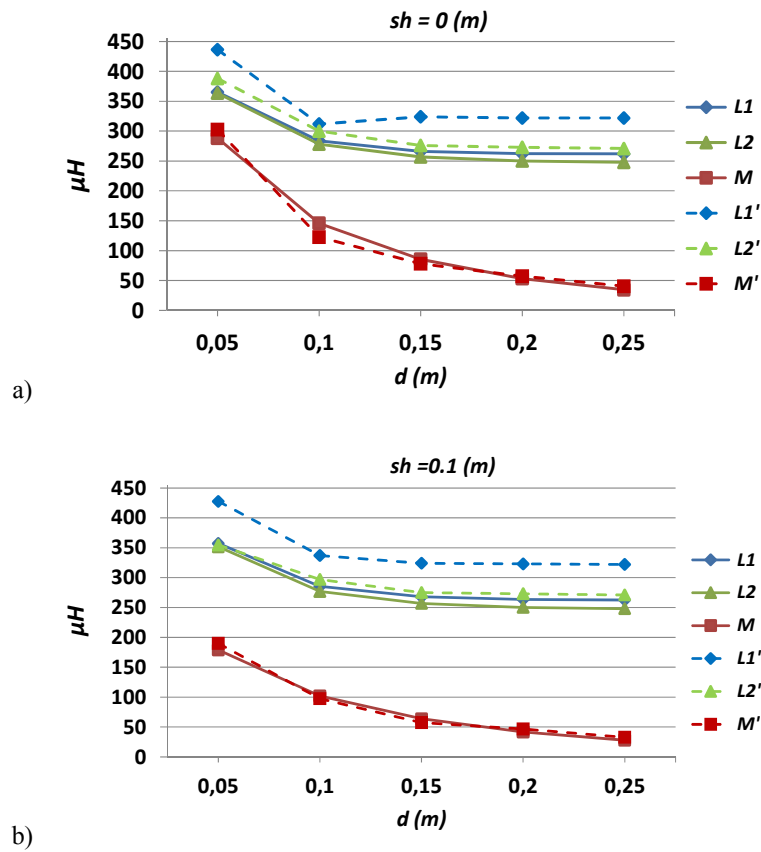


Fig. II.14: Values of  $(L_1, L_2, M)$  for different air gap  $d$  (m): Simulated (solid lines) and Measured (dashed lines), a)  $sh = 0$  and b)  $sh = 0.1$ m



## II.5. Square Pads of Type NTC-NTC

The NTC-NTC prototype of square pads ICT with the EV chassis is shown in Fig. II.15, all the parameters are the same as for RNO-RNO prototype (TABLE III) except for the shape of square coils, the length of the side is  $500mm$  and for the square shape ferrites side length is  $550mm$ . The FE modelling also includes the variation of the air gap  $d$  and lateral axis shift  $sh$ .

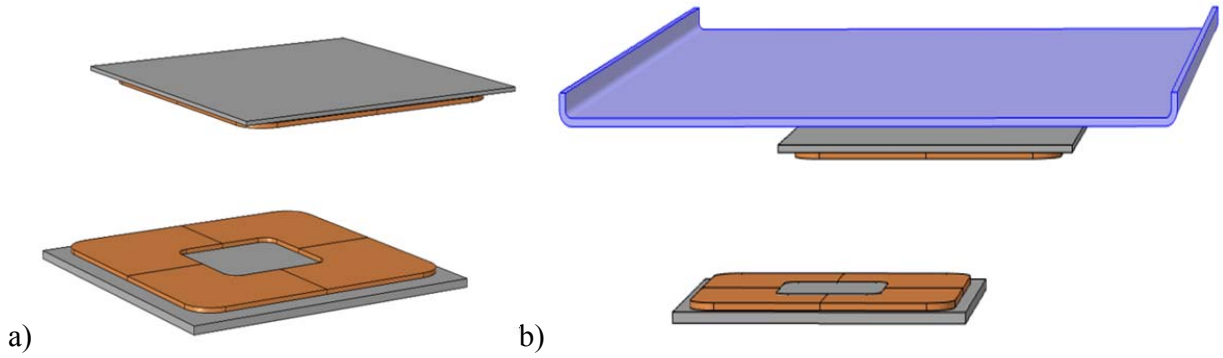


Fig. II.15: NTC-NTC prototype: a) square power pads b) with EV chassis

In order to calculate the self and mutual inductances ( $L_1, L_2, M$ ) for different values of the parameters  $d$  and  $sh$ , the same procedure is implemented as illustrated before in section II.3 a) (eqs. (25)-(27)).

But for the square shape coils, the cross section is not the same for all parts of the coil. The cross sections at the corners are bigger. Therefore, to avoid using the constant cross sections  $s_1$  and  $s_2$  in the equations for the circular coils (eqs. (25)-(27)), the expressions of the self and mutual inductances are derived from the energy calculation using the current density  $\vec{J}$ . Finally, the results for any coil shapes are:

$$L_1 = \Re \left\{ \iiint_{v_1} \frac{\vec{A} \cdot \vec{J}_1}{I_1^2} \partial v \right\} \text{ when } I_2 = 0 \text{ A} \quad (28)$$

$$L_2 = \Re \left\{ \iiint_{v_2} \frac{\vec{A} \cdot \vec{J}_2}{I_2^2} \partial v \right\} \text{ when } I_1 = 0 \text{ A} \quad (29)$$

$$M = \Re \left\{ \iiint_{v_2} \frac{\vec{A} \cdot \vec{J}_2}{I_1 \cdot I_2} \partial v \right\} \text{ when } I_2 \ll I_1$$

$$= \Re \left\{ \iiint_{v_1} \frac{\vec{A} \cdot \vec{J}_1}{I_2 \cdot I_1} \partial v \right\} \text{ when } I_1 \ll I_2$$
(30)

We note that the values in the equations (28)-(30) are complex quantities, but as the currents that imposed are real so their conjugates are same as their real ones.

The calculation results of these equations are shown in Fig. II.16. The coupling factor  $k$  is also plotted in Fig. II.17.

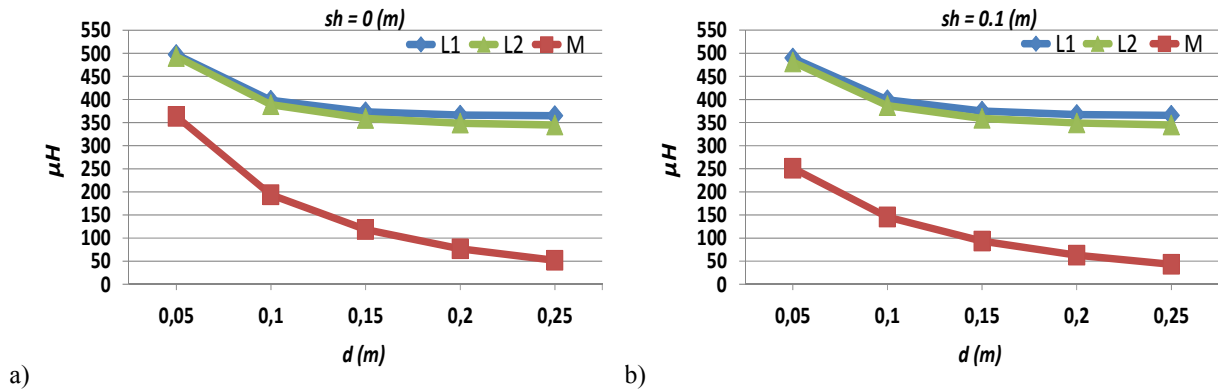


Fig. II.16: ( $L_1, L_2, M$ ) for NTC-NTC prototype with EV chassis

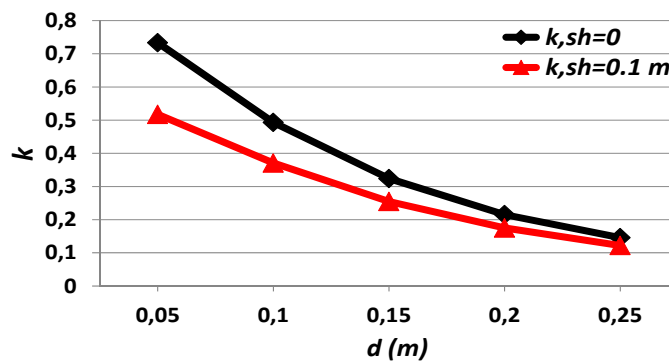


Fig. II.17:  $k$  for NTC-NTC prototype with EV chassis

## II.6. Study of the Interoperability

The interoperability study is a major point in the project CINELI. In this study, different power pads are concerned to build the ICT. The goal is to check the ability for different systems to work together. As there are three power pads (RNO, SE, NTC), a combination between two of them is performed to build the ICT.

In CINELI project, there are four essential interoperable prototypes that are studied: NTC-RNO, SE-RNO, SE-NTC and RNO-NTC. Any other combination can be also implemented like: NTC-SE or RNO-SE, but in the project CINELI, the SE power pad takes only a place in the primary side (ground). The other two pads can be in primary side or mounted in the secondary side (EV). The specifications of each power pad are illustrated in TABLE V, and the considered interoperable combinations are shown in Fig. II.18.

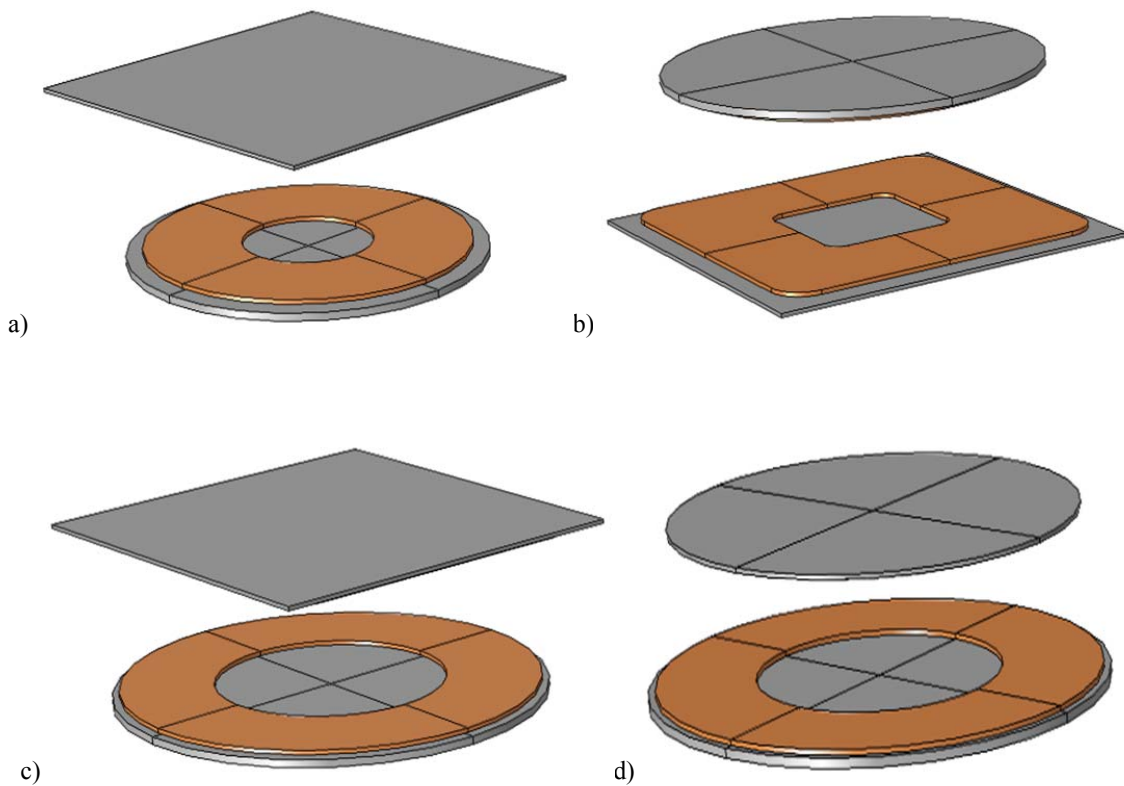
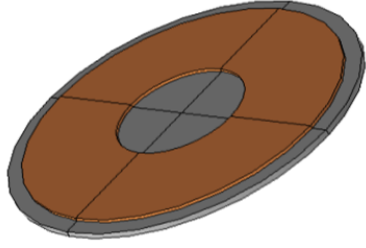
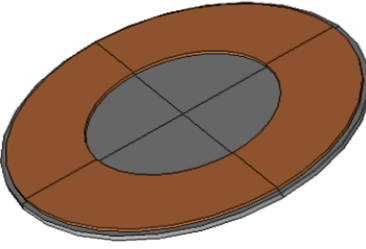
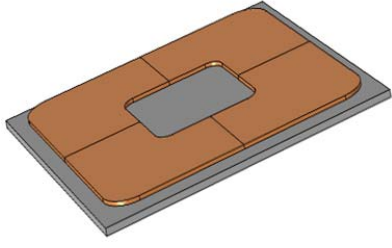


Fig. II.18: Interoperability prototypes: a) RNO-NTC b) NTC-RNO c) SE-NTC and d) SE-RNO

TABLE V: POWER PADS SPECIFICATIONS

Power Pad	Type	Specifications	
RNO		coil	20 Turns
			Copper width 150 mm
External Diameter 500 mm			
		ferrite	External Diameter 550 mm
SE		coil	18 Turns
			Copper width 135 mm
External Diameter 600 mm			
		ferrite	External Diameter 620 mm
NTC		coil	20 Turns
			Copper width 150 mm
External width 500 mm			
		ferrite	External width 550 mm

### II.6.a. Prototypes Description

All prototypes are modeled using the FE method, the self and mutual inductances are calculated for a parametric sweep of  $(d, sh)$  with the presence of the chassis.

The RNO-NTC prototype is made of RNO coil as primary and NTC coil as secondary as shown before in Fig. II.18. The RNO-NTC prototype power pads have the same parameters (TABLE V) except for the shapes. The NTC-RNO prototype is the reversal of the last prototype; it is made of NTC coil as primary and RNO coil as secondary as shown before in Fig. II.18.

The SE-RNO prototype has same power pad shapes but different dimensions as shown in TABLE V. The calculation for the self and mutual inductances for these types can be found using either (25)-(27), or (28)-(30). Finally, The SE-NTC prototype has different power pads in shapes

and parameters (TABLE V). The equations (28)-(30) are used for the self and mutual inductances calculation for the prototypes have at least a NTC coil.

### II.6.b. Comparison

In order to check the capability of each interoperable prototype to exchange the power between their sides, a comparison is made. Here, all prototypes discussed before are taken into account. Also the prototypes for the same power pads (RNO-RNO & NTC-NTC) are considered.

The comparison includes: self-inductances, mutual inductances and the coupling factor. It is done for  $(d, sh)$  parametric sweeps. The comparison between different prototypes is shown in Fig. II.19, Fig. II.20, Fig. II.21 and Fig. II.22 for  $L_1$ ,  $L_2$ ,  $M$  and  $k$  respectively.

From the figures of the interoperability the following conclusions are drawn:

- For  $L_1$ : The biggest values are for NTC-NTC prototype while RNO-RNO prototype has the smallest values for both configurations with and without axis shift. It can be noticed that all configuration that have the same system in primary will reach the same value of  $L_1$  at high air gaps for both cases of axes shift. That is because the ferrites and the chassis highly contribute for small air gaps and in contrary they have no more effects at high air gaps. It is also noticed that for small air gaps, if the dimensions of the ferrites at the secondary is smaller than the dimensions of the primary side (SE-RNO and NTC-RNO), the primary self-inductance is reduced compared to cases where the secondary ferrites are wider (respectively, SE-NTC and NTC-NTC). This behavior is due to the presence of the chassis on the secondary side.
- For  $L_2$ : The biggest value is of SE-NTC prototype while RNO-RNO prototype is the smallest value for both configurations with and without axis shift. This is true for small air gaps. But as the distance between the coils increases the values of  $L_2$  will meet for the configurations where the secondary pads are the same.
- For  $M$ : the best values of the mutual are NTC-NTC and SE-NTC prototypes. The weak values for small air gaps are of SE-RNO prototype. With an axes shift, all prototypes mutual values are lower than the configuration without an axis shift. It can also be noticed, as for the primary self-inductance, that the mutual is strongly reduced when the

secondary side is reduced and gets smaller than the primary pad because of the effect of the chassis. For example,  $M$  (NTC-RNO) is smaller than  $M$  (NTC-NTC) and may even be smaller than  $M$  (RNO-RNO) when there is no axis shift. In fact there are many factors that impact the value of the mutual: the chassis, ferrites, flux cancelation phenomenon and the effective area of the coils. So as the system is complex, it is difficult to draw general conclusion on the behavior of mutual for each interoperability configuration. However, it can be noticed that when there are more ferrites, the mutual will be stronger.

- For  $k$ : The coupling factors for all prototypes are closed to each other's at high air gaps for the two configurations with and without axis shift. However for small air gaps, and if there is no axis shift, the highest coupling factors are for RNO-RNO prototype while the smallest one is for NTC-RNO prototype. In the other hand where there is an axis shift, the high coupling is for SE-NTC and NTC-NTC prototypes, and the smallest coupling factor is for NTC-RNO prototype. Moreover, the coupling factor values are smaller where there is an axes shift between the power pads of the different ICT prototypes.

To illustrate the behavior of the coupling factor, two sets of interoperability configurations are studied separately with respect to the corresponding reference prototype. The first group includes the prototypes that have RNO pad either in the primary or secondary. The reference prototype of this group is RNO-RNO configuration. The second group contains the prototype where NTC pad exists either in primary or secondary. So the reference prototype for them is NTC-NTC configuration.

The relative differences of the coupling factor  $(\frac{k_{ICT}-k_{ref}}{k_{ref}})$  for the two cases of study are shown in Fig. II.23. It can be drawn that starting from a reference system for which the primary and the secondary are the same size, the configuration with a smaller secondary system will tend to decrease the coupling factor, on the contrary, the configuration with greater secondary will tend to increase the coupling factor (effect of the chassis) subsystem.

In all cases, the coupling factor depends on the ratio of the mutual and the square root of the self inductances of the primary and the secondary. So the decision to show which one of the three parameters that have the large impact on the coupling factor is difficult as soon as all parameters are

changing in the same behavior. However, for large air gaps, it can be said that the mutual has the main effects in the coupling factor since  $L_1$  and  $L_2$  will have small variations.

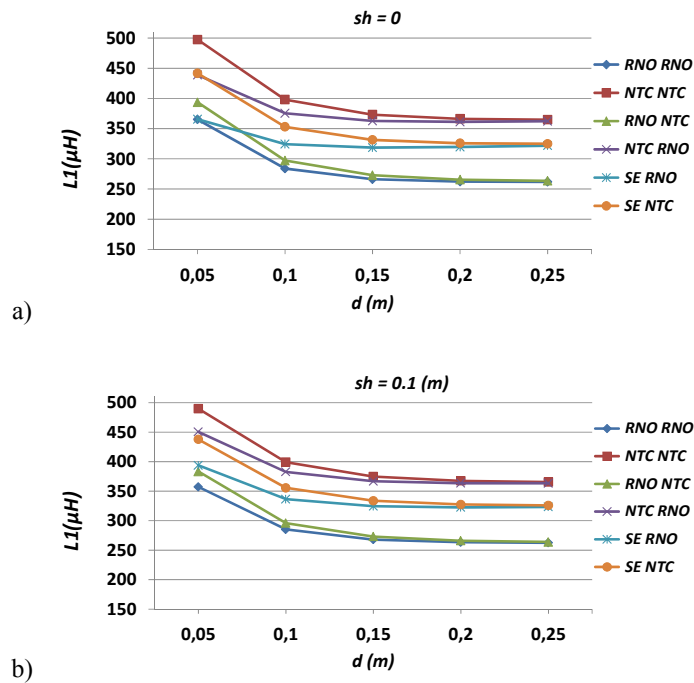


Fig. II.19: Values of  $L_1$  for different prototypes in function of air gap distance  $d(m)$ : a)  $sh=0$  and b)  $sh=0.1 \text{ m}$ .

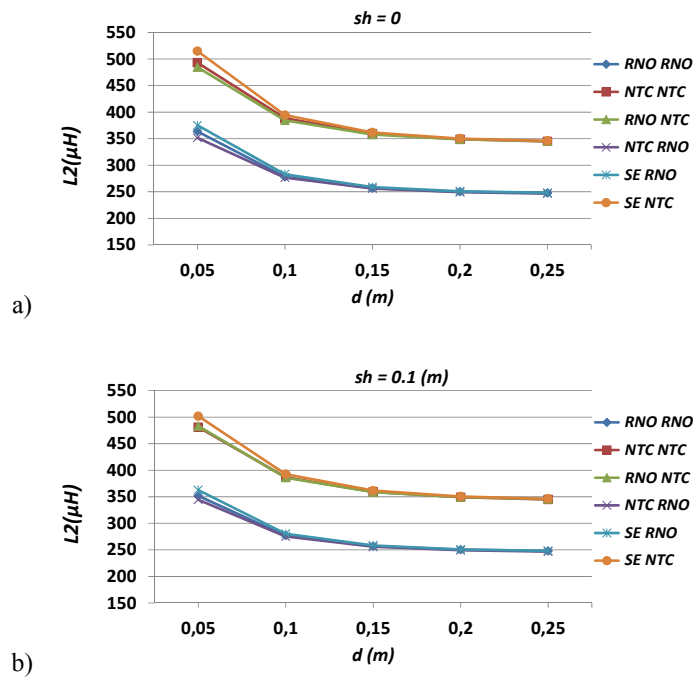


Fig. II.20: Values of  $L_2$  for different prototypes in function of air gap distance  $d(m)$ : a)  $sh=0$  and b)  $sh=0.1 \text{ m}$ .

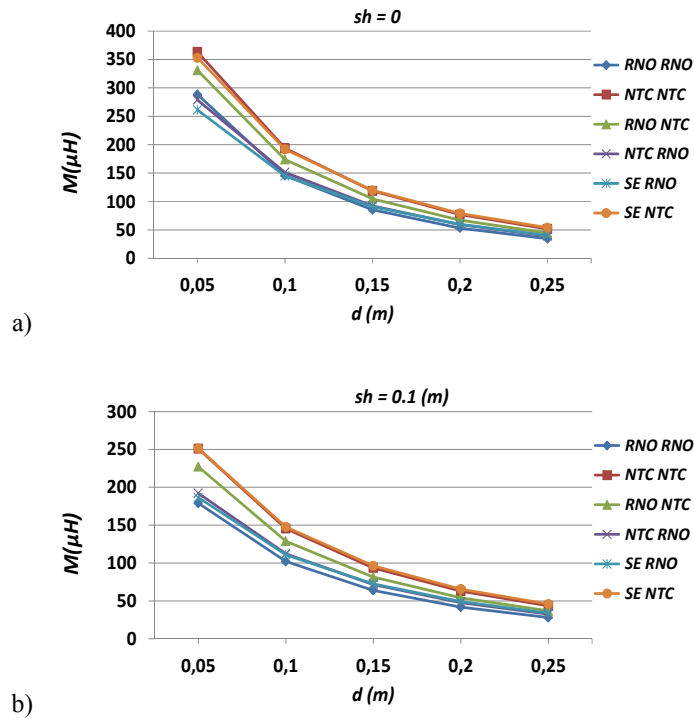


Fig. II.21: Values of  $M$  for different prototypes in function of air gap distance  $d(m)$ : a)  $sh=0$  and b)  $sh=0.1$  m.

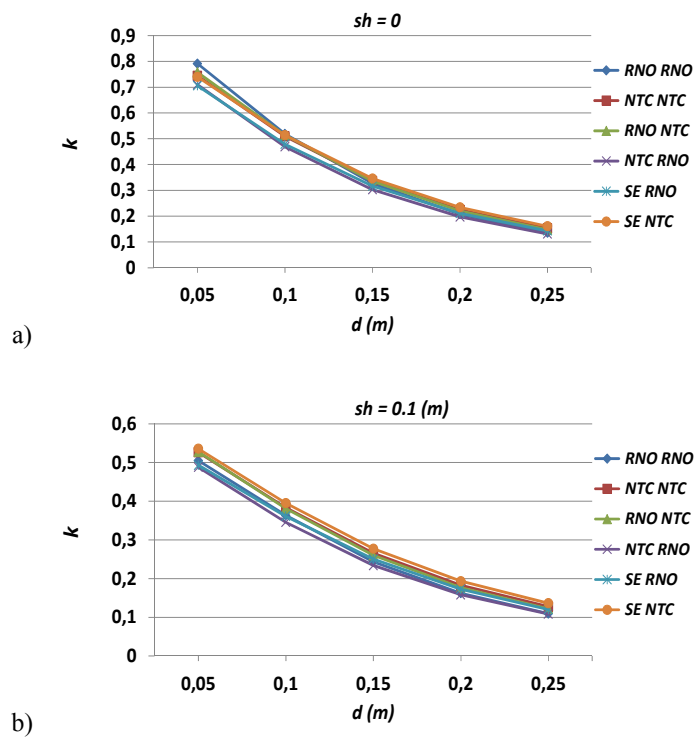


Fig. II.22: Values of  $k$  for different prototypes in function of air gap distance  $d(m)$ : a)  $sh=0$  and b)  $sh=0.1$  m.



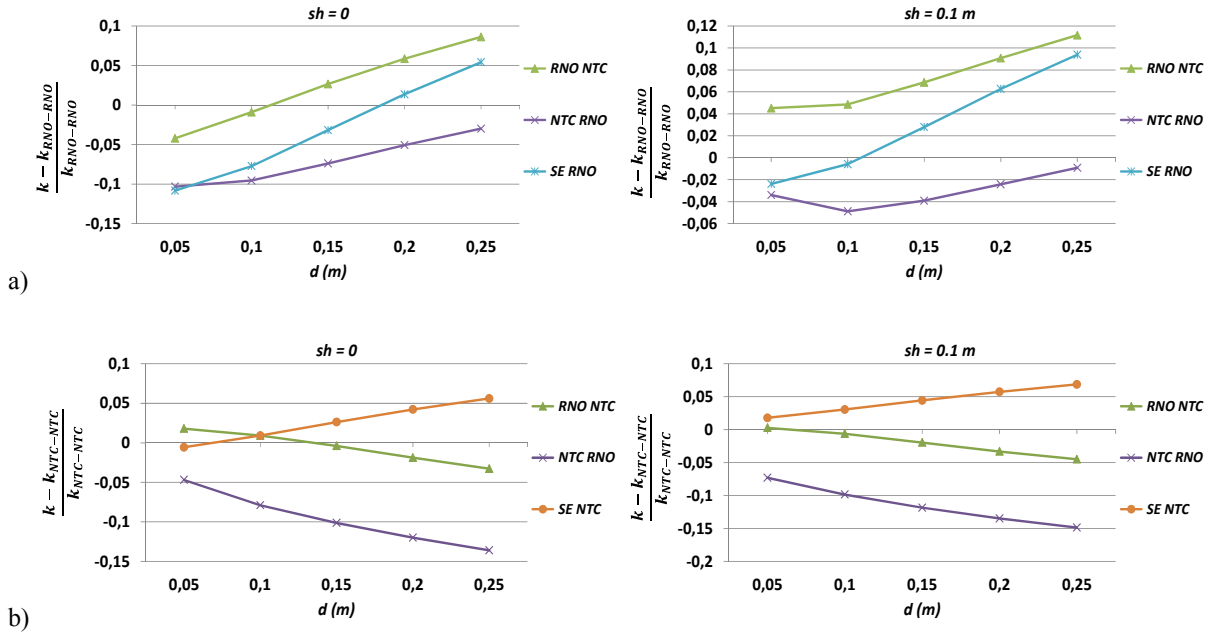


Fig. II.23: Comparison of relative difference of the coupling factor for two groups of reference prototype: a)  $k_{ref}$ : RNO-RNO and b)  $k_{ref}$ : NTC-NTC

## II.7. Conclusion

This chapter focuses in the EM modeling of the ICT by FE. This leads to calculate the electrical parameters of the ICT elements and their behavior with respect to the variations of the ICT geometrical parameters that are considered here: the air gap distance  $d$  and the axes shift between the power pads  $sh$ .

In the scope of this chapter, different configurations of the ICT are studied and compared. The configurations of the ICT are: the system without chassis, system with chassis, system in air and system in air with the chassis. The presence of the chassis affects the values of the self and mutual inductances and makes the values of self-inductances at each side non equal due to the asymmetry of the system. It also affects in the EM radiation in the EV and the surroundings. An experimental test is presented to verify the validation of the considered prototype with the real EV chassis.

The second part of this chapter highlights the interoperability study which concerns different types of power pads in the ICT system. Three different power pads are considered: RNO, SE and NTC, the combinations of them to construct the interoperable prototype are shown. The study takes

into account the variation of each prototype parameters and their sensitivity for geometrical parameters variations.

Finally, a comparison between all prototypes is stated. The results and the concept drawn from this chapter will help in finding the appropriate compensation capacitances and the behavior of the system for different coupling as explained in the next chapter.



### ***Chapter III : Resonant IPT System and Control***

### III.1. Introduction

As the ICT system is studied for different prototypes, the connection of the resonant elements and the power electronics devices are developed. This results in the Inductive Power Transfer (IPT) system. The IPT system, where the resonant conversion is the main process, allows power transfer from the AC grid to the DC load (battery) as mentioned in Chapter I. The overall system of IPT system is shown in Fig. III.1. We note here that for a parallel resonant capacitor  $C_2$ , the output DC filter is a  $LC$  one as explain in Appendix A ( $L_{2f}$ ,  $C_{2f}$ ). However a DC filter with only  $C_{2f}$  can also be used for a parallel secondary resonant compensation [33], [64]. But this requires a complex analysis and the rectifier input current at the secondary part should be in phase with the rectifier input voltage in order to apply the FHA [64].

This chapter studies three types of inductance compensation that can be used in the resonant transformer. The first harmonic analytic model with a resistive load (representing the battery for a given operating point) is used to make comparisons between the different types of compensation. The pertinent electrical characteristics of each system are evaluated at the global resonance frequency. An appropriate compensation topology is finally chosen for our application. For the chosen compensation topology, the interoperability is studied and conclusion is drawn based on the results obtained in the previous chapter.

Finally, the overall system frequency control is considered and some characteristics of the regulation are shown using the method of Maximum Power Point Tracking (MPPT). This type of control schematic can be applied to the IPT systems and insures the transfer of the maximum power from the source to load. Moreover, as it will be shown, the control using MPPT algorithm is simple, meets our needs, and is efficient (at least for static charging).

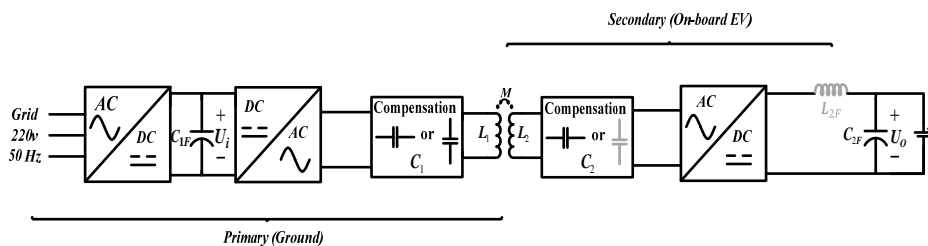


Fig. III.1: Overall system of contactless battery charger

### **III.2. Comparison between Different Compensation Topologies**

The compensation of the inductive elements of the ICT is needed to transfer the maximum power possible to the load. The goal is to find the frequency where the system works at maximum power. It means that the module of the input impedance seen by the source is purely resistive at this frequency. At this point the reactive power will be equal to zero (ideal case) and so the VA rating of the source is minimum as mentioned in Chapter I.

This section details the behaviors of different compensation topologies that are mostly used by the designers of IPT system. The first harmonic approximation is used to model the system and the load (battery) is modeled by a resistive load. The comparisons between the topologies are based on the global resonant frequency and electrical quantities.

In order to get explicit expressions for the global resonance frequency and for the electrical quantities at this frequency from the first harmonic model, the battery load is represented by a resistive load. The desired power  $P_0$  transferred to the battery corresponds (for a given state of charge) to a battery voltage  $U_0$ . For this operating point, the battery can be represented by a resistive load  $R_L = U_0^2/P_0$  [23] ,[33]. So for all next analytical derivations, the values of  $R_e$  (derived in the Appendix A) are fixed.

#### **III.2.a. General Electrical Model Presentation**

In Chapter I, three different topologies of double resonance circuit are taken into account. They are redrawn in Fig. III.2. In our application the inverter is fed by a voltage source. The parallel primary resonant (PS, PP) is discarded for 2 reasons:

- It would be necessary to introduce an inductor at the input to filter the input current as the inverter is for this case a CSI (Current Source Inverter).
- The value of the parallel capacitors will depend on the load which is not a practical solution [10].

In consequence, the two topologies that will be considered here are SS and SP.

In fact, it is difficult to compare the compensation topologies using three configurations of the electrical model of compensated ICT in Fig. III.2. Each designer uses one of them that is suited for his application. But if a comparison is made, it should be stated on one configuration for the three compensation topologies.

For that purpose, a general configuration for the ICT electrical model is derived where the three topologies can be then compared. The basic elements of the T-model (Fig. III.3) are derived from the equivalent physical model that was shown before in Fig. I.6. The circuits' analyses are made and the results are compared to find the corresponding elements that represent the physical model.

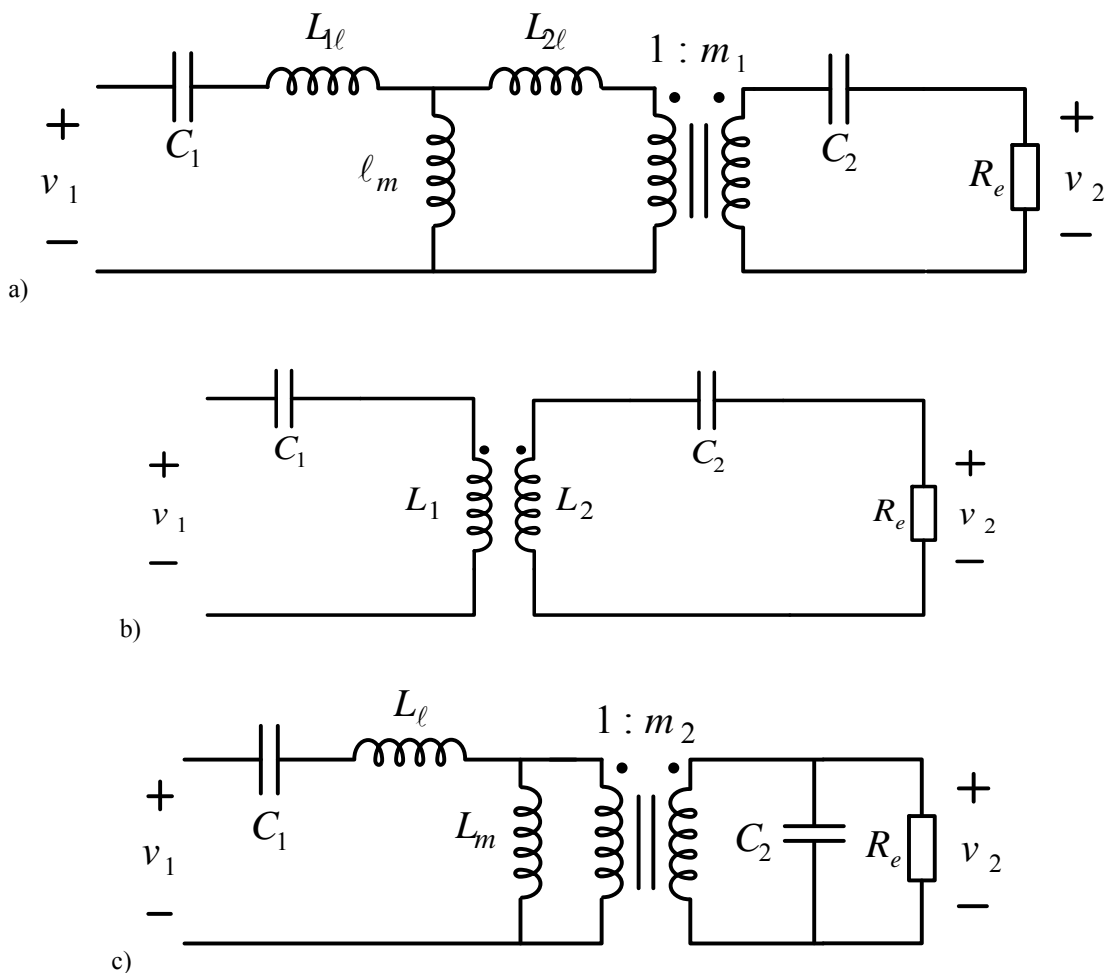


Fig. III.2: Three different compensation topologies shown in Chapter I: a) SS leakage b) SS self and c) SP

Also it should be noted for the T-model that there are 4 unknown elements ( $\ell_1, \ell_2, \ell_3, m$ ), whereas for the physical model there are only three: ( $L_1, L_2, M$ ). Hence, there is an infinite set of solutions for the parameters of the T-model. In order to avoid this problem one element of the three should be fixed. Here the transformation ratio is chosen equal to the ratio of the number of turns:  $m = \frac{n_2}{n_1}$ . The coils' resistances are neglected in all calculations for all models.

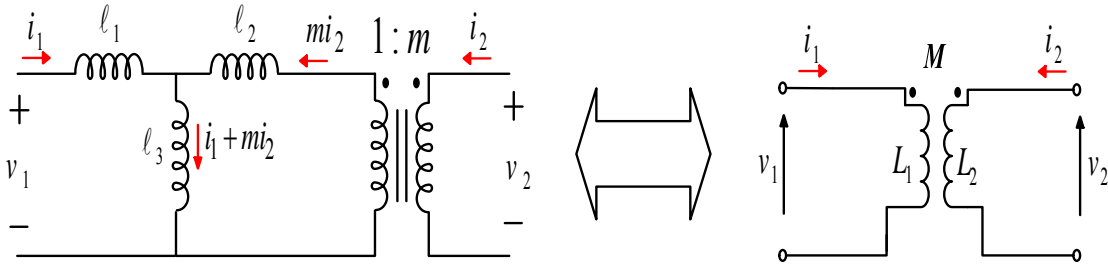


Fig. III.3: Global T-model (left) compared with the physical model (right) for ICT

For the two models

$$v_1 = \ell_1 \frac{di_1}{dt} + \ell_3 \frac{di_1}{dt} + m\ell_3 \frac{di_2}{dt} = L_1 \frac{di_1}{dt} + M \frac{di_2}{dt} \quad (31)$$

$$v_2 = m^2\ell_2 \frac{di_2}{dt} + m\ell_3 \frac{di_1}{dt} + m^2\ell_3 \frac{di_2}{dt} = L_2 \frac{di_2}{dt} + M \frac{di_1}{dt} \quad (32)$$

so after comparing these equations it yields:

$$L_1 = \ell_1 + \ell_3, L_2 = m^2(\ell_2 + \ell_3) \text{ and } M = m\ell_3 \quad (33)$$

or

$$\ell_1 = L_1 - \frac{M}{m}, \ell_2 = \frac{L_2}{m^2} - \frac{M}{m} \text{ and } \ell_3 = \frac{M}{m} \quad (34)$$

These values will help to express the compensations capacitors  $C_1, C_2$  for the three topologies and facilitate the comparison between the different topologies. Three values of coupling are considered in the study of the input impedance behavior. These values are taken from the simulation results mentioned in Chapter II section 3.b (Fig. II.8 , Fig. II.9) (RNO-RNO prototype), and they are summarized in TABLE VI.



The reference case for all studies is considered for the configuration where the air gap distance  $d = 0.15 \text{ m}$ , and without axes shift between the power pads ( $sh = 0$ ). The coupling factor for this case is denoted by  $k_2 = 0.33$ .

TABLE VI: DIFFERENT COUPLING CASES PARAMETERS (RNO-RNO PROTOTYPE)

$d(m)$	$sh(m)$	$L_1(\mu H)$	$L_2(\mu H)$	$M(\mu H)$	$k$
0.10	0	283.82	278.17	145.73	0.52 ( $k_3$ )
0.15	0	266.16	256.79	85.46	0.33 ( $k_2$ ) (reference case)
0.25	0.1	262.63	247.87	28	0.11 ( $k_1$ )
$d(m)$	$sh(m)$	$\ell_1(\mu H)$	$\ell_2(\mu H)$	$\ell_3(\mu H)$	$k$
0.10	0	138.09	132.44	145.73	0.52 ( $k_3$ )
0.15	0	180.7	171.33	85.46	0.33 ( $k_2$ ) (reference case)
0.25	0.1	234.63	219.87	28	0.11 ( $k_1$ )

### III.2.b. Compensation Topologies

The three types shown in Fig. III.2 now can be represented by the general model derived in the previous section. The connections of each structure of compensation are shown in Fig. III.4. The connections for SS self and SS leakage compensations are the same. The differences are the values of the capacitances  $C_1$  and  $C_2$ .

The comparison between the compensation topologies implies the study of several parameters concerning the global system impedance and each element's voltage or current. Then the design of the resonant converter must take into account all these parameters in order to find the most suited solution. The parameters that concerned in the study are:

$Z_{in}$ : Impedance modulus seen by the source.

This parameter will show the behavior of the system in frequency domain and it determines the operating point of the system. It gives information about the switching mode of the primary inverter topology and the amplitude of the primary current [31]. Moreover, from the phase of  $Z_{in}$ ,

the position of the global resonant frequency can be found. Also the power factor is derived from  $Z_{in}$ .

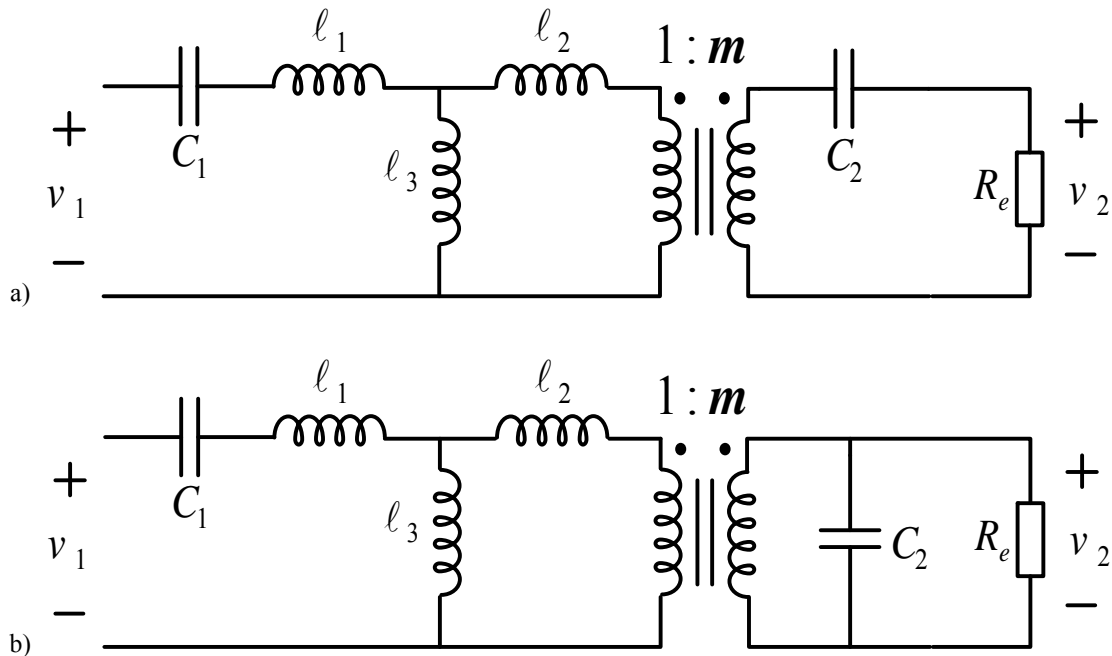


Fig. III.4: Different compensation topologies with the general connections

**$Pf$** : Power factor.

The power factor is useful to determine the size (VA ratings), so as the  $Pf$  is close to unity then the inverter cost will be low while the same power consumption remains the same. But if the  $Pf$  is much less than 1 this means that a higher current is needed though the inverter to absorb the same power and so the size of the inverter needed is costly. Moreover the wiring is also more expensive.

**$G_v$** : Voltage gain.

This parameter determines the ratio of the output voltage (battery) to the input voltage (DC source). Also it is the ratio of the output voltage of the equivalent resistor  $R_e$  (Diode Bridge + DC filter + battery) to the output voltage of the inverter. So from this parameter the voltage ratings of the inverter can be found. As the secondary voltage is imposed by the battery voltage ( $U_0$ ), and it is

constant for a determined battery and state of charge; it will be favorable to study the inverse of voltage gain ( $1/G_v$ ).

$v_{res\_elem}$ : Voltage across the resonant elements of the compensated ICT.

It is the measure of the voltage of the inductors and capacitors of the IPT (4 elements:  $C_1, L_1, L_2$  and  $C_2$ ). This will determine the electrical ratings of the chosen compensation capacitances, and so to avoid their damage. As the secondary voltage is constant, this parameter is normalized to the secondary voltage;  $V_{res\_elem}N = v_{res\_elem}/v_2$ . So we have:  $V_{C1}N, V_{L1}N, V_{C2}N$  and  $V_{L2}N$ .

$i_{res\_elem}$ : Current through the resonant elements of the compensated ICT.

This parameter gives a measure of the current circulating in the resonant circuit. It also determines the electrical elements ratings. As the current absorbed by the battery is supposed constant for an operating point ( $P_0, U_0$ ), thus the secondary current  $i_2$  is unchanged. So this parameter is normalized to this secondary current;  $I_{res\_elem}N = i_{res\_elem}/i_2$ . Thus the results will be:  $I_{C1}N, I_{L1}N, I_{C2}N$  and  $I_{L2}N$ .

$R_e$ : The reflected equivalent resistor seen by secondary.

Three values of this parameter are tested: for normal load (i.e.400V),  $R_e \rightarrow \infty$  (~open circuit fault) and  $R_e \rightarrow \mathbf{0}$  (~short circuit fault). However, the last one can't be exactly equal zero because if the load is short circuited, then there is no DC filter at the output, then the first harmonic assumption is no more valid.

A general objective of the frequency response is to study the characteristic of each resonant topology. Their behaviors as a function of frequency for different parameters of the system are shown. The plots will give a general idea about the functionality of the system. A large band frequency response of  $Z_{in}$ , its phase and  $Pf$  is needed to locate the overall frequency of the system for each value of  $k$ . However, because the battery is represented by a resistive load, the frequency dependence given by the analytical model do not corresponds to the frequency response of the real system. In consequence, the values of the other electrical parameters are given only for the global

resonance of the system. As the same system could also be connected to a resistive load, the frequency response are shown in Appendix B for completeness.

The next section presents the pertinent electrical quantities and their dependence on the positioning in order to facilitate the comparison and the choice of the most suitable solution for our application. Before passing to followings, the different characteristic frequencies are defined in TABLE VII.

TABLE VII: FREQUENCY SYMBOLS AND THEIR DEFINITIONS

<b>Symbol</b>	<b>Definition</b>
$f_{0,1}$	Primary Resonant frequency.
$f_{0,2}$	Primary Resonant frequency.
$f_0$	Global Resonant frequency (total system).
$f_{0\text{ref}} = f_{0,1\text{ref}} = f_{0,2\text{ref}}$	Reference frequency = 30kHz. The values of $C_1$ and $C_2$ are calculated from this frequency in the reference configuration.
$f_s$	Operation (Switching) frequency of the inverter.
$\omega_N = \frac{f_s}{f_{0\text{ref}}}$	Normalized switching frequency to the reference frequency.
$\omega_{0N} = \frac{f_0}{f_{0\text{ref}}}$	Normalized global resonant frequency to the reference one.
$\omega_{0,1N} = \frac{f_{0,1}}{f_{0\text{ref}}}$	Normalized primary resonant frequency to the reference one.
$\omega_{0,2N} = \frac{f_{0,2}}{f_{0\text{ref}}}$	Normalized secondary resonant frequency to the reference one.

#### A) *SS Self Inductances ( $SS_L$ ) Compensation*

The  $SS_L$  compensation topology circuit using the FHA is shown in Fig. III.5. The resonant capacitors  $C_1$  and  $C_2$  are connected in series with the ICT and their values are chosen in order to tune

out the self- inductors  $L_1$  and  $L_2$  respectively for the reference configuration ( $k_2 = 0.33$ ). We then define the primary and secondary resonant frequencies as:

$$f_{0,1} = 1/2\pi\sqrt{L_1C_1} = 1/2\pi\sqrt{(\ell_1 + \ell_3)C_1} \quad (35)$$

$$f_{0,2} = 1/2\pi\sqrt{L_2C_2} = 1/2\pi\sqrt{m^2(\ell_2 + \ell_3)C_2} \quad (36)$$

where  $m = \frac{n_2}{n_1}$  is the transformation ratio. In our study  $m = 1$ .

As mentioned before, the input impedance seen by the source is a good key to get information about the operation behavior of the circuit, the switching mode of the inverter, and the amplitude of the input primary current. Also the power factor ( $PF$ ) also can be drawn from the phase of this impedance. The input impedance seen by the source for the  $SS_L$  compensation is:

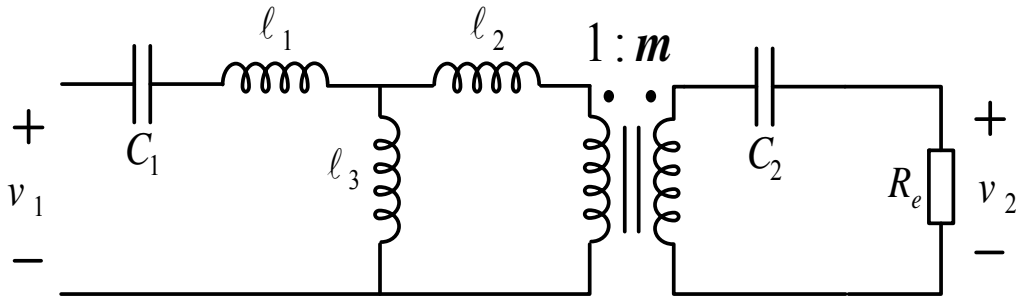


Fig. III.5: FHA of the SS compensation topology circuit

$$(Z_{in})_{SS} = j\left(\omega_s(\ell_1 + \ell_3) - \frac{1}{\omega_s C_1}\right) + \frac{\omega_s^2 m^2 \ell_3^2}{R_e + j\left(\omega_s m^2(\ell_2 + \ell_3) - \frac{1}{\omega_s C_2}\right)} \quad (37)$$

where  $\omega_s$  is the operating frequency of the system. If the values of  $\ell_1, \ell_2, \ell_3$  are expressed by their equivalents derived before from (34), then the  $(Z_{in})_{SS}$  in (37) becomes:

$$(Z_{in})_{SS} = j\left(\omega_s L_1 - \frac{1}{\omega_s C_1}\right) + \frac{\omega_s^2 M^2}{R_e + j\left(\omega_s L_2 - \frac{1}{\omega_s C_2}\right)} \quad (38)$$

The value of  $R_e$  can be calculated from Appendix A for the SS compensation ( $U_0 = 400V$ ,  $P_0 = 3kW$ ,  $I_0 = 7.5A$ ,  $R_e = 43.23\Omega$ ). Three values of coupling shown in TABLE VI are taken

into account in the study of the circuit behavior. The values of the resonant capacitors ( $C_1, C_2$ ) are calculated in the reference case,  $k_2 = 0.33$  and fixed for all configurations. All further calculations and studies in this chapter follow the same approach. So the values of the resonant capacitors are found for a design frequency  $f_{0ref} = 30kHz = f_{0,1ref} = f_{0,2ref}$ :

$$C_1 = 1/\left((2\pi f_{0,1ref})^2 L_{1ref}\right) = 105.74 \text{ nF} \quad (39)$$

$$C_2 = 1/\left((2\pi f_{0,2ref})^2 L_{2ref}\right) = 109.60 \text{ nF} \quad (40)$$

Then impedance seen by source at  $f_{0ref}$ , in the reference configuration will be:

$$(Z_{in})_{SSL}(f_{0ref}) = \frac{\omega_{0ref}^2 M_{ref}^2}{R_e} \quad (41)$$

The power factor  $Pf$  is the measure of the cosine angle of the phase shift between the supplying AC voltage and current. It can be derived from the phase of the input impedance by dividing the real part by the magnitude as in (42):

$$PF = \cos(\theta_{in}) = \frac{\Re(Z_{in})}{|Z_{in}|} \quad (42)$$

The voltage gain  $G_v$  that is the voltage at the output across  $R_e$  ( $v_2$ ) to the input voltage ( $v_1$ ) is:

$$\begin{aligned} |G_v|_{SS} &= \frac{|v_2|}{|v_1|} = \frac{|i_2 R_e|}{|i_1 (Z_{in})_{SS}|} = \left| \frac{j\omega_s M i_1 R_e}{\left(R_e + j\left(\omega_s L_2 - \frac{1}{\omega_s C_2}\right)\right) i_1 (Z_{in})_{SS}} \right| \\ &= \frac{|j\omega_s M R_e|}{\left| \left(R_e + j\left(\omega_s L_2 - \frac{1}{\omega_s C_2}\right)\right) (Z_{in})_{SS} \right|} \\ &= \frac{|j\omega_s m \ell_3 R_e|}{\left| \left(R_e + j\left(\omega_s m^2 (\ell_2 + \ell_3) - \frac{1}{\omega_s C_2}\right)\right) (Z_{in})_{SS} \right|} \end{aligned} \quad (43)$$

Finally, as stated before, the resonant elements (L's & C's) voltages and current stress are studied. For this purpose, each element's voltage is normalized to the fixed output voltage imposed by the battery  $U_0$  and fixed absorbed current  $I_0$  (i.e.,  $U_0 = 400V$ ,  $I_0 = 7.5A$ ).

Here, the normalized voltages  $V_{L1}N$ ,  $V_{C1}N$ ,  $V_{L2}N$ ,  $V_{C2}N$  on the L's and C's are derived in (46)-(49). These are the ratio of the voltage on an element (primary and secondary sides) to the output voltage  $v_2$  in the physical equivalent circuit shown in Fig. III.3.

$$|V_{L1}N| = \frac{|v_{L1}|}{|v_2|} = \left| \frac{j\omega_s L_1}{Z_{in\_SS} G_{v\_SS}} \frac{1}{G_{v\_SS}} \right| \quad (46)$$

$$|V_{C1}N| = \frac{|v_{C1}|}{|v_2|} = \left| \frac{1}{G_{v\_SS}} - V_{L1}N + \frac{j\omega_s M}{R_e} \right| \quad (47)$$

$$|V_{L2}N| = \frac{|v_{L2}|}{|v_2|} = \left| \frac{j\omega_s L_2}{R_e} \right| \quad (48)$$

$$|V_{C2}N| = \frac{|v_{C2}|}{|v_2|} = \left| \frac{j\omega_s M}{Z_{in\_SS} G_{v\_SS}} \frac{1}{G_{v\_SS}} - V_{L2}N - 1 \right| \quad (49)$$

In fact, It can be easily shown if (49) is simplified, the result (50) depends only on  $\omega_s$  and the other elements are fixed. So it is independent of the changes of  $k$ .

$$|V_{C2}N| = \frac{|v_{C2}|}{|v_2|} = \left| \frac{1}{j\omega_s C_2 R_e} \right| \quad (50)$$

The same hypothesis for the normalized currents  $I_{L1}N$ ,  $I_{C1}N$ ,  $I_{L2}N$ ,  $I_{C2}N$  through the L's and C's are derived in (51)-(54). These are the ratio of the current in an element (primary and secondary sides) to the output current  $i_2$  in the physical equivalent circuit shown in Fig. III.3, so:

$$|I_{L1}N| = \frac{|I_{L1}|}{|I_2|} = \left| \frac{R_e}{Z_{in\_SS} G_{v\_SS}} \frac{1}{G_{v\_SS}} \right| \quad (51)$$

$$|I_{C1}N| = \frac{|I_{C1}|}{|I_2|} = \left| \frac{R_e}{Z_{in\_SS} G_{v\_SS}} \frac{1}{G_{v\_SS}} \right| \quad (52)$$

$$|I_{L2}N| = \frac{|I_{L2}|}{|I_2|} = 1 \quad (53)$$

$$|I_{C2}N| = \frac{|I_{C2}|}{|I_2|} = 1 \quad (54)$$

**B)  $SS_{\ell}$  Leakage Inductances ( $SS_{\ell}$ ) Compensation**

The  $SS_{\ell}$  compensation topology circuit using the FHA is shown in Fig. III.5. The resonant capacitors  $C_1$  and  $C_2$  are connected in series to tune out the leakage inductors  $\ell_1$  and  $\ell_2$  respectively. So the primary and secondary resonant frequencies are:

$$f_{0,1} = 1/2\pi\sqrt{\ell_1 C_1} = 1/2\pi\sqrt{\left(L_1 - \frac{M}{m}\right) C_1} \quad (44)$$

$$f_{0,2} = 1/2\pi\sqrt{m^2 \ell_2 C_2} = 1/2\pi\sqrt{(L_2 - mM) C_2} \quad (45)$$

where  $m = \frac{n_2}{n_1}$  is the transformation ratio.

In fact, the  $SS_{\ell}$  and  $SS_L$  have the same analytical calculations except the values of the compensation capacitors  $C_1$  and  $C_2$ . So all the equations derived before for the  $SS_L$  are also valid for  $SS_{\ell}$ . For the reference case, the values of the resonant capacitors ( $C_1, C_2$ ) are calculated and fixed for all other cases (as stated before). Hence the values of the resonant capacitors are found for a design frequency  $f_{0ref} = 30kHz = f_{0,1ref} = f_{0,2ref}$ :

$$C_1 = 1/\left((2\pi f_{0,1ref})^2 \ell_{1ref}\right) = 155.75 \text{ nF} \quad (46)$$

$$C_2 = 1/\left((2\pi f_{0,2ref})^2 m^2 \ell_{2ref}\right) = 164.27 \text{ nF} \quad (47)$$

Then impedance seen by source at  $f_{0ref}$  in the reference configuration will be:

$$\begin{aligned} (Z_{in})_{SS_{\ell}}(f_{0ref}) &= j\omega_0 \ell_{3ref} + \frac{\omega_{0ref}^2 \ell_{3ref}^2}{\frac{R_e}{m^2} + j\omega_{0ref} \ell_{3ref}} \\ &= \frac{\omega_{0ref}^2 M_{ref}^2 R_e}{R_e^2 + \omega_{0ref}^2 M_{ref}^2} + j \frac{\omega_{0ref} M_{ref} R_e}{R_e^2 + \omega_{0ref}^2 M_{ref}^2} \end{aligned} \quad (48)$$

**C) SP Inductances Compensation**

This topology, as mentioned in Chapter I, uses the series connection of  $C_1$  in the primary side to compensate the total leakage inductance seen by the primary, and it uses the parallel connection



of  $C_2$  at the secondary side to compensate the self-secondary inductance (see Fig. III.2 c)). The general model that established for comparison is drawn for  $SP$  connection as in Fig. III.6.

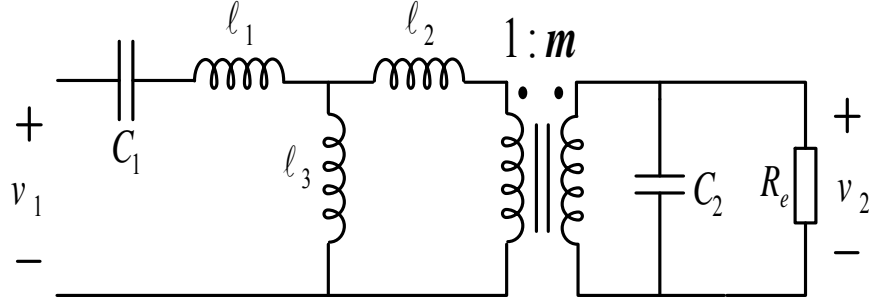


Fig. III.6:  $SP$  topology connection for the developed T-model.

So the values of the primary and secondary resonant frequencies for the  $SP$  compensation are:

$$f_{0,1} = \frac{1}{2\pi\sqrt{\left(\ell_1 + \frac{\ell_2\ell_3}{\ell_2 + \ell_3}\right)C_1}} = \frac{1}{2\pi\sqrt{\left(L_1 - \frac{M^2}{L_2}\right)C_1}} = \frac{1}{2\pi\sqrt{(1-k^2)L_1C_1}} \quad (49)$$

$$f_{0,2} = 1/2\pi\sqrt{m^2(\ell_2 + \ell_3)C_2} = 1/2\pi\sqrt{L_2C_2} \quad (50)$$

Here the series compensated primary inductance (i.e primary full leakage) is found by short circuiting the secondary and calculating the inductance seen by the primary. Then the input impedance seen by the source  $(Z_{in})_{SP}$  and the voltage gain  $(G_v)_{SP}$  are calculated as:

$$(Z_{in})_{SP} = j\left(\omega_s(\ell_1 + \ell_3) - \frac{1}{\omega_s C_1}\right) + \frac{\omega_s^2 m^2 \ell_3^2}{j\left(\omega_s m^2(\ell_2 + \ell_3) + \frac{R_e}{1 + j\omega_s R_e C_2}\right)} \quad (51)$$

or

$$(Z_{in})_{SP} = j\left(\omega_s L_1 - \frac{1}{\omega_s C_1}\right) + \frac{\omega_s^2 M^2}{j\left(\omega_s L_2 + \frac{R_e}{1 + j\omega_s R_e C_2}\right)} \quad (52)$$

$$\begin{aligned}
 |G_v|_{SP} &= \frac{|v_2|}{|v_1|} = \frac{|i_{R_e} R_e|}{|i_1 (Z_{in})_{SP}|} = \left| \frac{j\omega_s M i_1 R_e^2}{(R_e + j(\omega_s L_2 + j\omega_s^2 R_e C_2 L_2))} \right| \\
 &= \frac{|j\omega_s M R_e^2|}{\left| (R_e + j\omega_s L_2 (1 + j\omega_s R_e C_2)) (Z_{in})_{SP} \right|} \\
 &= \frac{|j\omega_s m \ell_3 R_e^2|}{\left| (R_e + j\omega_s m^2 (\ell_2 + \ell_3) (1 + j\omega_s R_e C_2)) (Z_{in})_{SP} \right|} \quad (53)
 \end{aligned}$$

In the SP case, the value of  $R_e$  ( $U_0 = 400V$ ,  $P_0 = 3kW$ ,  $I_0 = 7.5A$ ,  $R_e = 63.23\Omega$ ) is different from the SS case because of the parallel connection of the secondary resonant capacitor (see Appendix A for the derivation).

For the reference case, the values of the resonant capacitors ( $C_1$ ,  $C_2$ ) are calculated and fixed for all other cases (as stated before). Hence the values of the resonant capacitors are found for a design reference frequency  $f_{0ref} = 30kHz = f_{0,1ref} = f_{0,2ref}$ :

$$C_1 = 1 / \left( (2\pi f_{0,1ref})^2 \left( \ell_{1ref} + \frac{\ell_{2ref} \ell_{3ref}}{\ell_{2ref} + \ell_{3ref}} \right) \right) = 118.39 \text{ nF} \quad (54)$$

$$C_2 = 1 / \left( (2\pi f_{0,2ref})^2 L_{2ref} \right) = 109.60 \text{ nF} \quad (55)$$

The  $(Z_{in})_{SP}$  at resonance in the reference case will be:

$$(Z_{in})_{SP} (f_{0ref}) = \frac{M_{ref}^2 R_e}{L_{2ref}^2} \quad (56)$$

Finally the normalized voltages and currents of L's and C's for the SP compensation are found as:

$$|V_{L1}N| = \frac{|v_{L1}|}{|v_2|} = \left| \frac{j\omega_s L_1}{Z_{in\_SP}} \frac{1}{G_{v\_SP}} \right| \quad (55)$$

$$|V_{C1}N| = \frac{|v_{C1}|}{|v_2|} = \left| \frac{1}{G_{v\_SP}} - V_{L1}N + \frac{j\omega_s M}{R_e} \right| \quad (56)$$

$$|V_{L2}N| = \frac{|v_{L2}|}{|v_2|} = 1 \quad (57)$$

$$|V_{C2}N| = \frac{|v_{C2}|}{|v_2|} = 1 \quad (58)$$

$$|I_{L1}N| = \frac{|I_{L1}|}{|I_2|} = \left| \frac{R_e}{Z_{in\_SP}} \frac{1}{G_{v\_SP}} \right| \quad (59)$$

$$|I_{C1}N| = \frac{|I_{C1}|}{|I_2|} = \left| \frac{R_e}{Z_{in\_SS}} \frac{1}{G_{v\_SS}} \right| \quad (60)$$

$$|I_{L2}N| = \frac{|I_{L2}|}{|I_2|} = |1 + j\omega_s R_e C_2| \quad (61)$$

$$|I_{C2}N| = \frac{|I_{C2}|}{|I_2|} = j\omega_s R_e C_2 \quad (62)$$

Before of all steps of comparison in the section that follows, the values of each compensation capacitors for the three topologies are scheduled in TABLE VIII as a function of the equivalent derived model parameters  $\ell_1$ ,  $\ell_2$  and  $\ell_3$ .

 TABLE VIII: COMPUTATIONS OF  $C_1$  AND  $C_2$  FOR THE THREE COMPENSATION TOPOLOGIES

Topology	SS (self)	SS (leakage)	SP
<b>Resonant Freq.</b>			
$\omega_{01}$	$1/\sqrt{(\ell_1 + \ell_3)C_1}$	$1/\sqrt{\ell_1 C_1}$	$\frac{1}{\sqrt{(\ell_1 + \frac{\ell_2 \ell_3}{\ell_2 + \ell_3}) C_1}}$
$\omega_{02}$	$1/\sqrt{m^2(\ell_2 + \ell_3)C_2}$	$1/\sqrt{m^2 \ell_2 C_2}$	$1/\sqrt{m^2(\ell_2 + \ell_3)C_2}$

### III.2.c. Comparison of The Compensations

The equation giving the phase of  $Z_{in}$ , or  $Pf$  are used to calculate the global resonant frequency at each coupling factor  $k$ . As mentioned before, these quantities are shown as functions of the frequency in order to locate the global resonance for different values of  $k$ . After that, these values of resonant frequencies are applied to the equations of all parameters and then their values are plotted in order to establish the comparison. This will lead to a clear idea about the chosen topology for the determined constraints demanded by the designer application. In a first step, the plots of the input impedance, their phases and  $Pf$  for the three topologies are considered as in Fig. III.7 and Fig. III.8 to locate  $(\omega_{0N1}, \omega_{0N2}, \omega_{0N3})$ . The location of the global resonant frequency is marked by a dot. Then, the different parameters are evaluated at global resonance (Fig. III.10 - Fig. III.13).

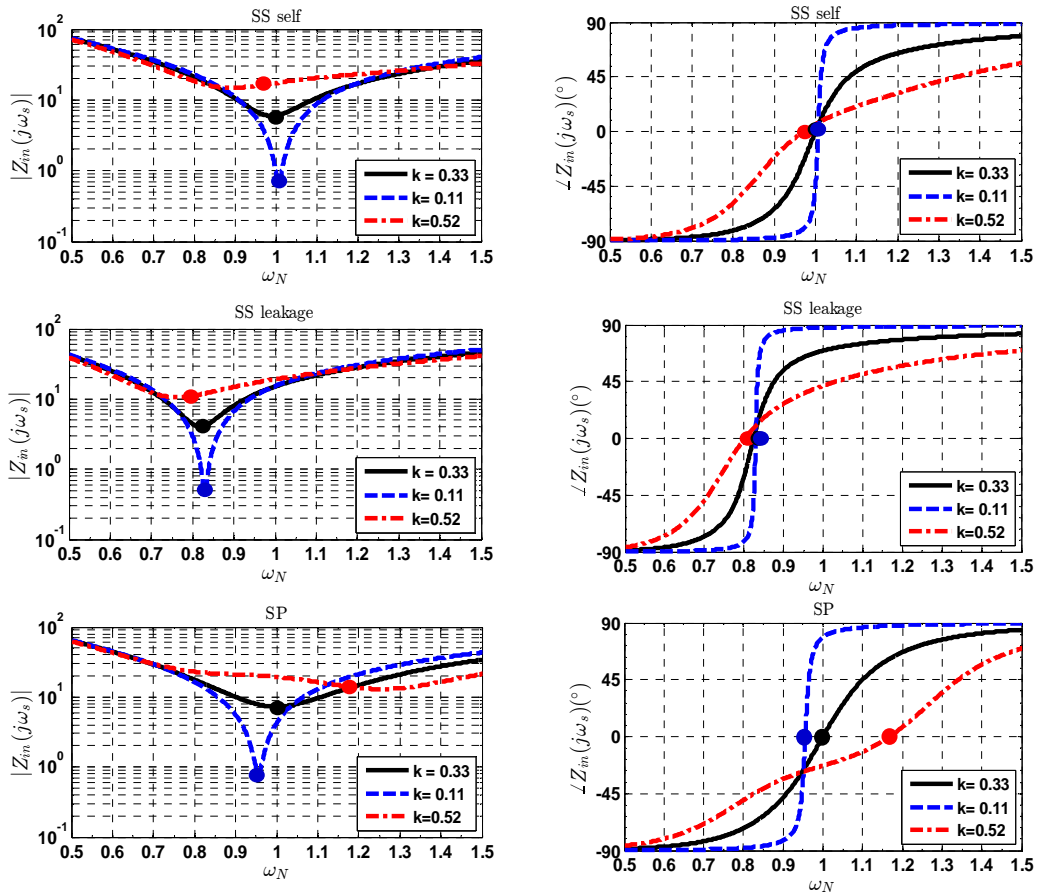


Fig. III.7: Plot of  $|Z_{in}|$  and their phases as a function of  $\omega_N$  for different values of  $k$ . Markers added to show the resonance frequency corresponding to each case of  $k$  for the three topologies

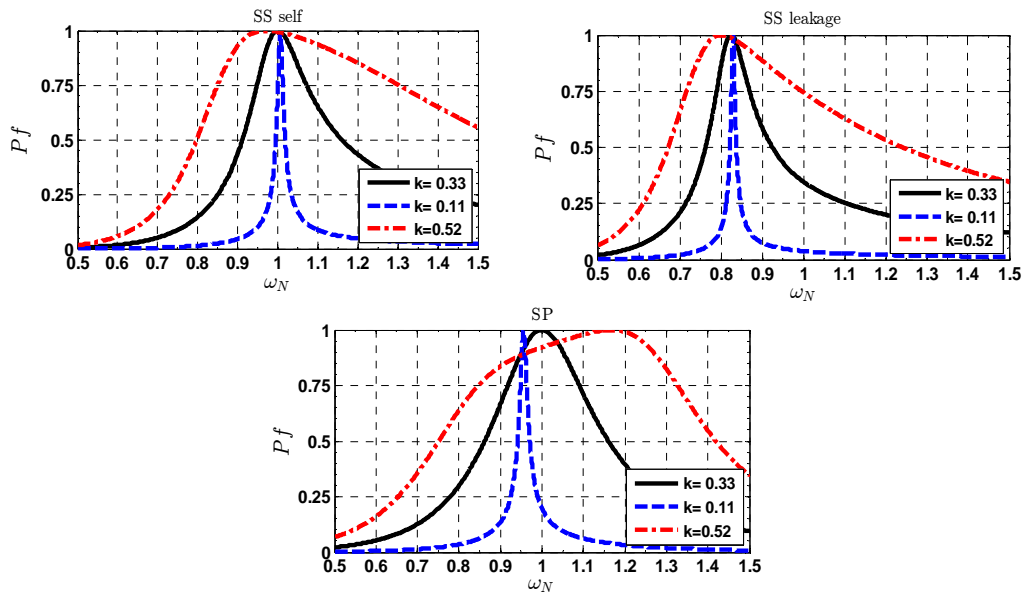


Fig. III.8: Different topologies  $Pf$ .plot as a function of  $\omega_N$  for different values of  $k$

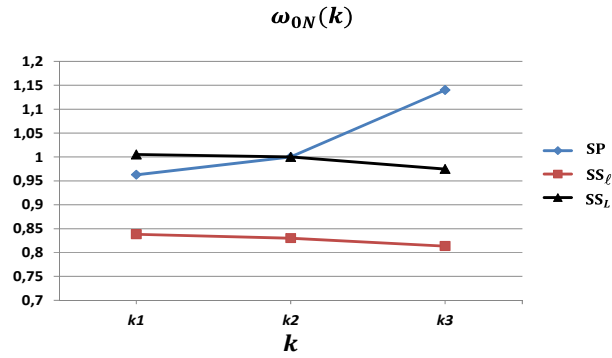


Fig. III.9: Values of the normalized resonance frequency for each topology at different  $k$  ( $k_1 < k_2(ref) < k_3$ )

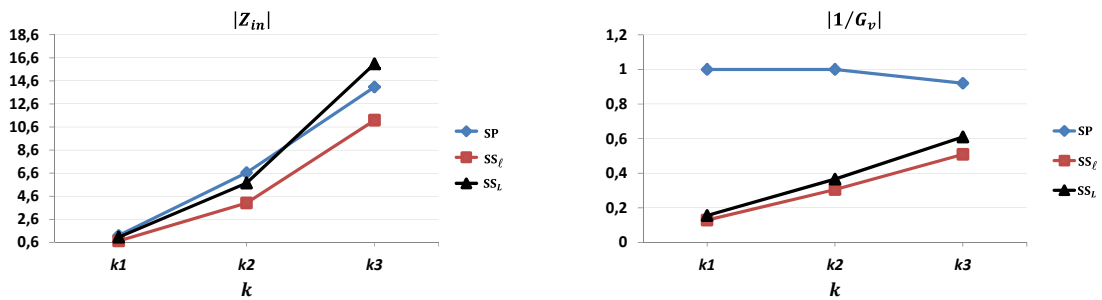


Fig. III.10: Impedance and inverse of gain for each topology at the resonance frequency for different  $k$  (following Fig. III.9)

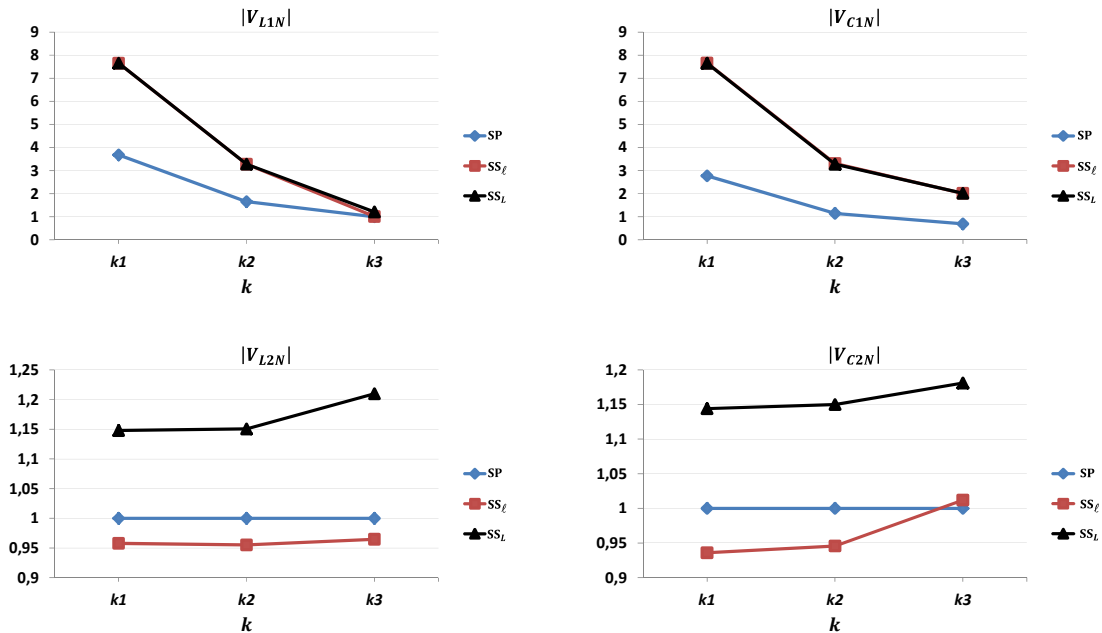


Fig. III.11: Normalized voltages for each topology at the resonance frequency for different  $k$  (following Fig. III.9)

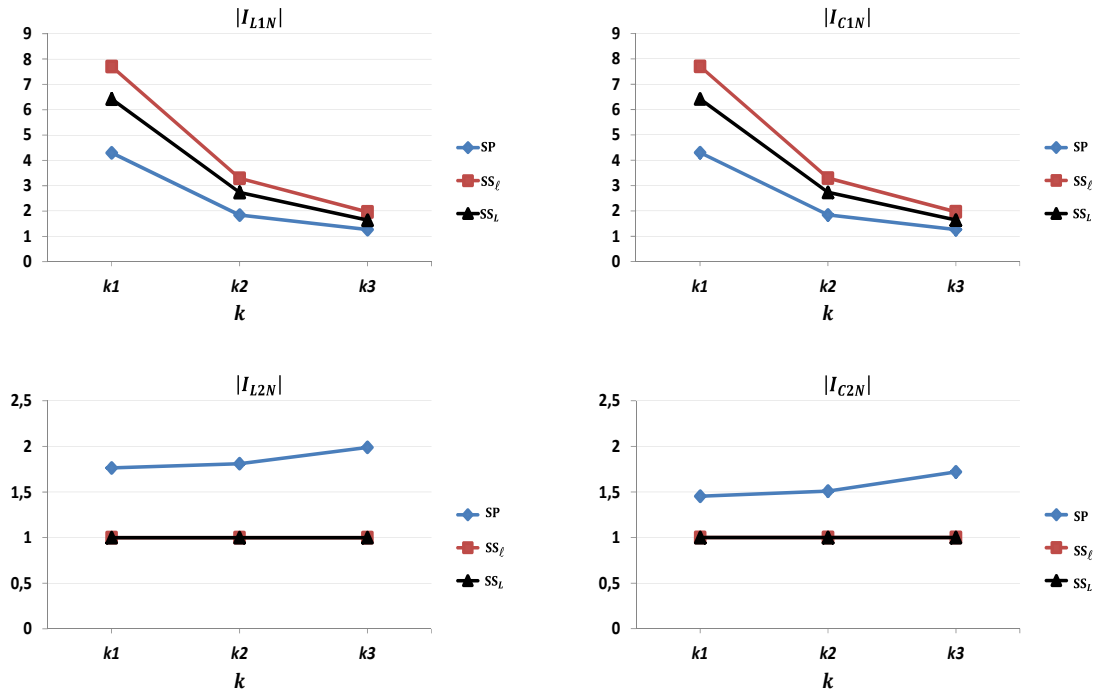


Fig. III.12: Normalized currents for each topology at the resonance frequency for different  $k$  (following Fig. III.9)

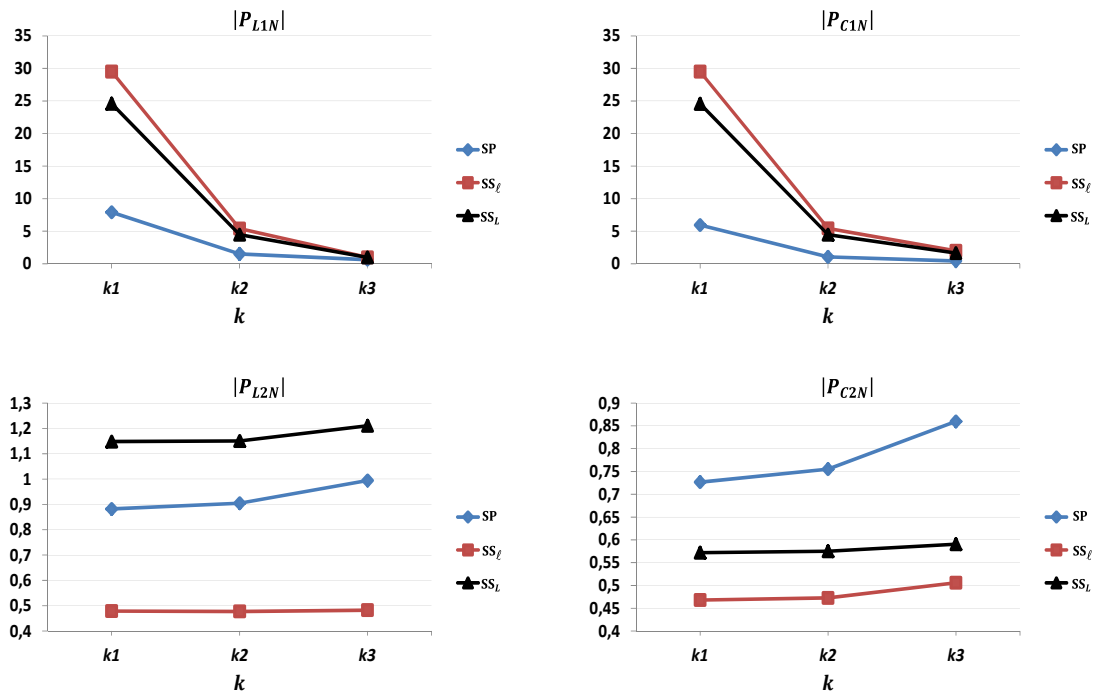


Fig. III.13: Normalized elements power for each topology at the resonance frequency for different  $k$  (following Fig. III.9)

The frequency response of  $|G_v|$  in a large frequency band can be done to test the case of faults at the load as mentioned before:  $R_e \rightarrow \infty$  ( $\sim$ open circuit fault) and  $R_e \rightarrow 0$  ( $\sim$ short circuit fault). The plots of the equations for these values of  $R_e$  can be accepted since they are independent of the frequency (the battery is even open or short circuited). For this reason a plot of  $|G_v|$  for the three topologies for the reference case ( $k_2$ ) are traced in Fig. III.14.

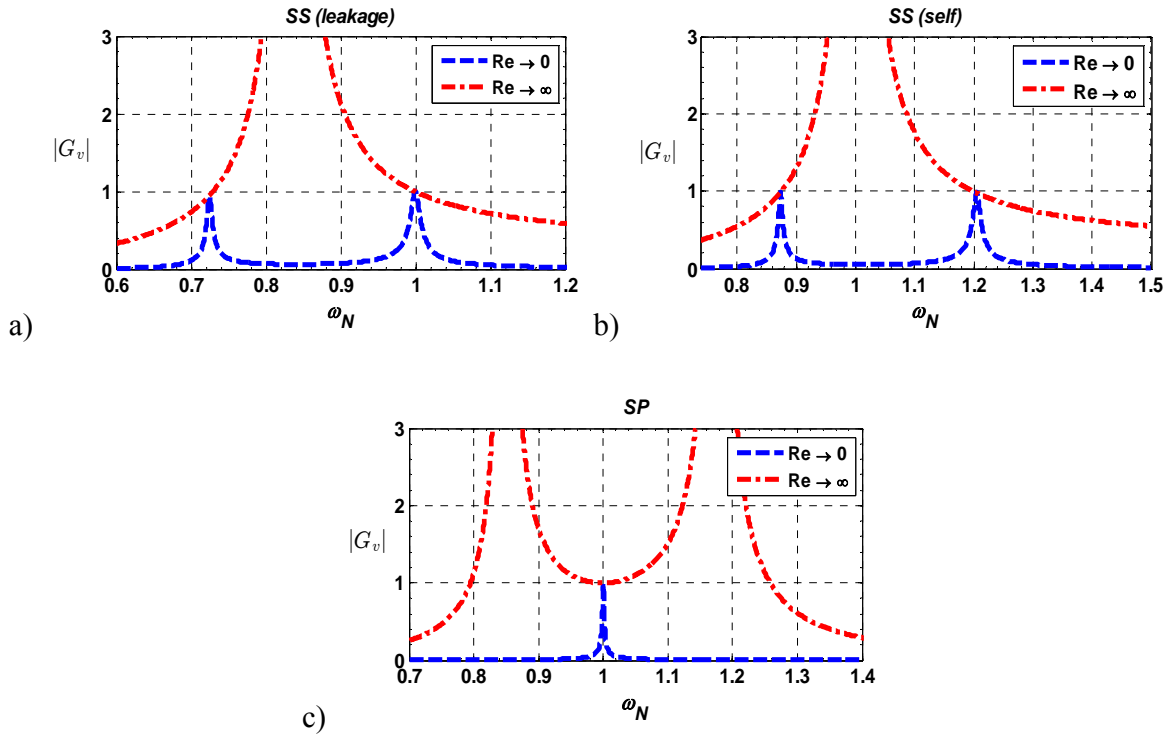


Fig. III.14:  $|G_v|$  plot as a function of  $\omega_N$  for different values of  $R_e$  for  $k_2$ (ref. case) for the three topologies

From all the graphs, conclusions are obtained in order to choose the most preferable topology (in our case of study) can be summarized:

A) Fig. III.9: The global resonance frequency is less sensitive to dispositioning using SS compensations. And they are closed to  $\omega_N = 1$  for the  $SS_L$ . It means that these frequencies are not far from the 30 kHz while changing  $k$ .

B) Fig. III.10: the  $1/G_v$  is minimum for SS compensations. It means that the input primary voltage needed to give a certain fixed value of output is smaller for these two topologies. The minimum value is for  $SS_\ell$ . So the SS resonant circuit can be used to step up the input voltage if the

operation normalized frequency is near 1. At these frequencies,  $G_v$  depends on the circuit elements that are described by  $k$  and  $\omega_0$ . On the other hand, for the SP resonant circuit,  $G_v$  is always equal to 1 at resonance. Furthermore the  $|G_v|$  dependency of  $k$  and  $R_e$  could be avoided if the circuit always works at resonance

Also for the open and short circuit limits from Fig. III.14 , it can be seen for the SS compensations there are two frequencies where  $|G_v| = 1$ . It means that they are independent of  $k$  and  $R_e$ , and protection for the faults can be done at these frequencies. However, at these points the impedance is either highly capacitive or inductive (see Fig. III.7). In the contrary, the SP compensation has a  $|G_v| = 1$  for both faults at  $\omega_N = 1$ .

C) Fig. III.11, Fig. III.12 and Fig. III.13: from the electrical constraints on each element at resonance ( $V_{C1N}, V_{L1N}, V_{L2N}$  and  $V_{C2N}$ ), ( $I_{C1N}, I_{L1N}, I_{L2N}$  and  $I_{C2N}$ ), and their products ( $P_{C1N}, P_{L1N}, P_{L2N}$  and  $P_{C2N}$ ): The best topology is the SP one for  $(L_1, C_1)$ , and for  $SS_\ell (L_2, C_2)$  because the required element electrical ratings are the smallest.

However, in all cases the ratings of the resonant elements should carefully be chosen to avoid their damage considering the operating frequency. It can be expected that sometimes the voltage at some frequencies cross these elements may be several times  $v_2$  (especially for the primary side at weak coupling). So frequency control should be designed very well to avoid the extremely high voltages drops values. In the contrary, for the secondary part, the values of voltages drops are high with higher values of  $k$ , but with less factor ratio with respect to  $v_2$  compared to what happens at the primary side for SS compensations, whereas they are equal to secondary voltages for the SP compensation.

The comparison here tries to make a clear image about different topologies. A compromise can be done to take a decision to choose the proper topology that meets the designer needs. In this project, as the dimensions of the system were given in the predesign by the industrial partners, a decision was made to use the SS self ( $SS_L$ ) for the reasons mentioned in A) and B). However, that doesn't prevent the selection for the other topologies for another design requests.

Now, as this decision is selected, another point of view is taken for the  $SS_L$  primary and secondary resonance frequencies that compared by the system resonance frequency. From Fig. III.7;



the normalized resonant frequency for the total system  $\omega_{0N}$  for the different values of coupling factor  $k$  are plotted in Fig. III.15. It also contains the plots of the normalized primary and secondary resonance frequencies  $\omega_{01N}$  and  $\omega_{02N}$  that are computed from the corresponding values of  $L_1$  and  $L_2$ , and the chosen values of  $C_1$  and  $C_2$ .

The resonance of the system for each value of  $k$  is very close or equal to primary resonance frequency. This is due to that the primary capacitor  $C_1$  is in series with all elements seen by the primary including the secondary reflected impedance, so it is dominant as mentioned in [64],[40]. The system being non-symmetrical because of the chassis, the resonant frequencies at primary and secondary are different when the system is not in the reference configuration. In the considered configurations the difference between the primary and the secondary resonances is less than 1%.

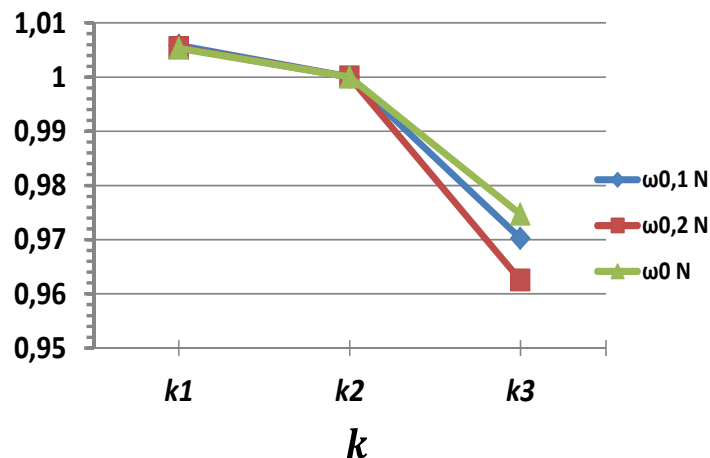


Fig. III.15:  $SS_L$  compensation topology normalized frequencies for the primary, the secondary and the whole system for different values of  $k$  ( $k_1 < k_2(\text{ref}) < k_3$ ).

### III.2.d. $SS_L$ Compensated Interoperable Systems Study

As the decision has been made to consider the self series-series  $SS_L$  compensation, the behavior of this topology for different interoperability systems study is performed. The interoperability between any two systems combines an independent structure for both of them. It also considers that each system has its compensation capacitor that is calculated in the predesign to tune out the self inductance at the reference frequency (30 kHz), for a reference positioning ( $d = 0.15$  m,  $sh = 0$ ) and for a reference configuration (RNO-RNO, NTC-NTC, SE-RNO). After that, the two interoperable sides are connected together to form the prototype concerned. To make it

clear, the different compensated combinations that were discussed before in Chapter II are illustrated in the diagram of Fig. III.16.

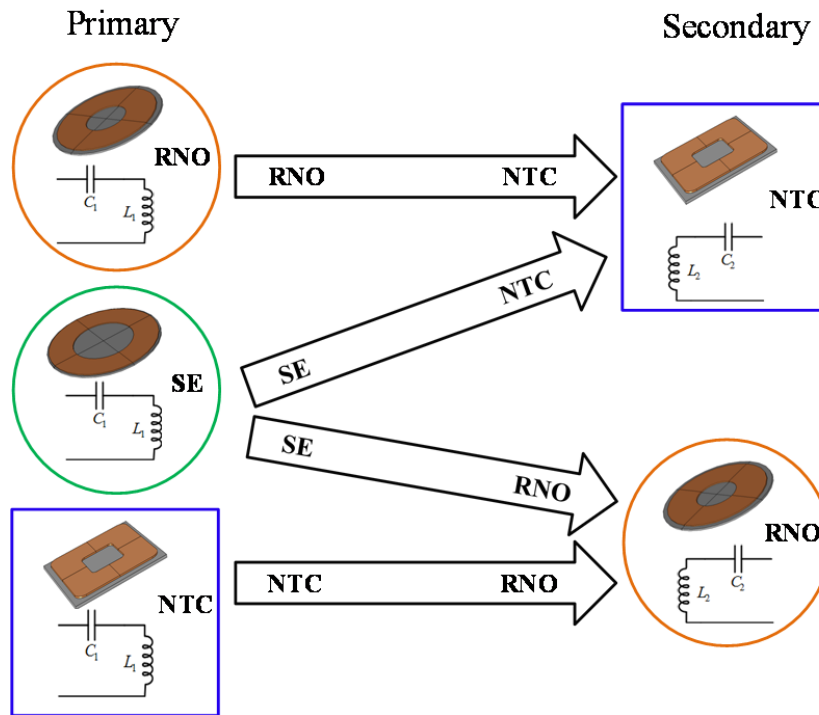


Fig. III.16: Compensated SS interoperability prototypes discussed in Chapter II

The results of different interoperable prototypes for different parameters are shown in Fig. III.17 and Fig. III.18. They correspond to the systems' responses for two cases of coupling:  $k_3$  (good coupling) and  $k_1$  (worst case) respectively.

The reference case  $k_2$  is the one where the resonant capacitors are calculated and added for compensation, and they are fixed. So it is not necessary to show the plots since all resonant frequencies for all prototypes will be at  $\omega_N = 1$ . (The notation of coupling factors  $k_1$ ,  $k_2$  and  $k_3$  are only used to present the different three configurations for  $d$  and  $sh$ , their values are not same as in the previous studies).

Also the plot of  $1/|G_v|$  for all prototypes for the three cases of coupling are plotted in Fig. III.19, as stated before, the secondary voltage is fixed at  $U_0$  that is imposed by the battery.

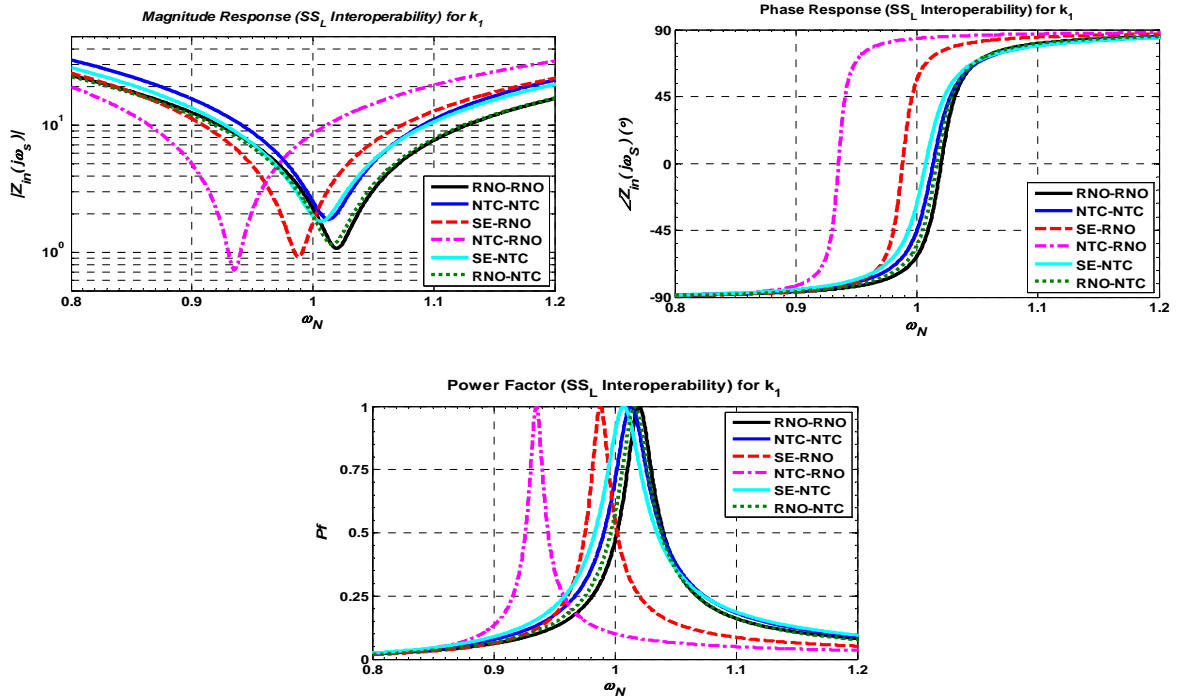


Fig. III.17: Interoperability study for SS self parameters plot as a function of  $\omega_N$  for  $k_1$ :  $|Z_{in})_{SS_L}|$ , its phase and  $Pf$

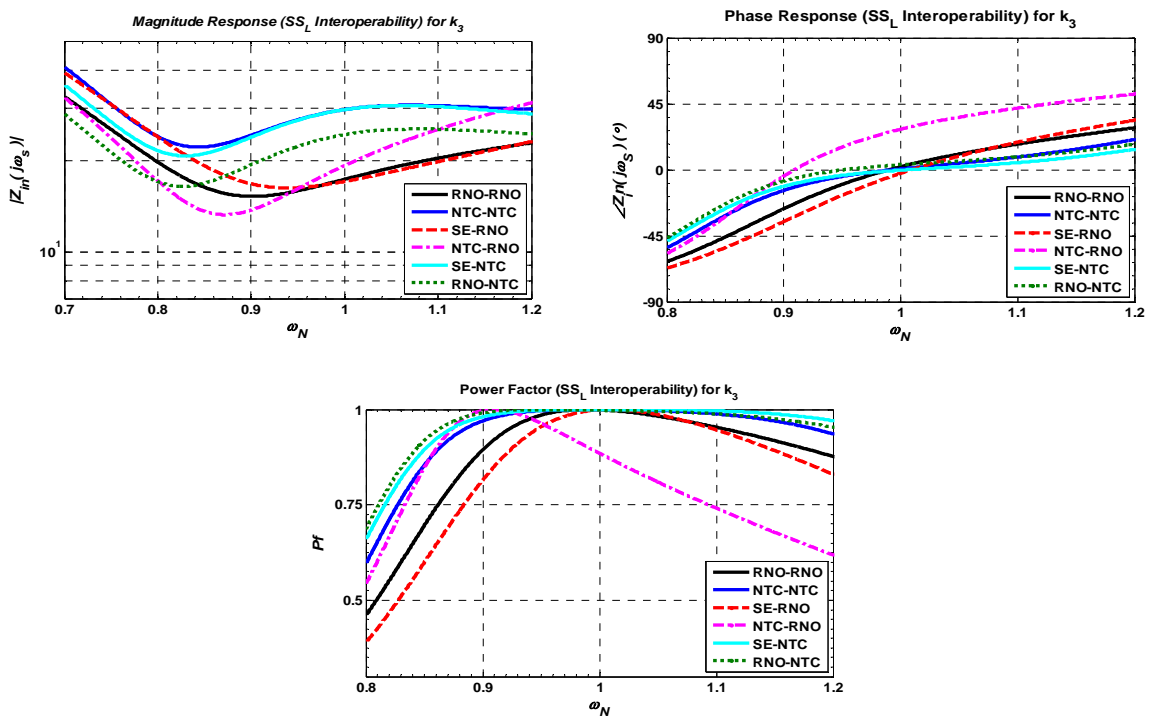


Fig. III.18: Interoperability study for SS self parameters plot as a function of  $\omega_N$  for  $k_3$ :  $|Z_{in})_{SS_L}|$ , its phase and  $Pf$

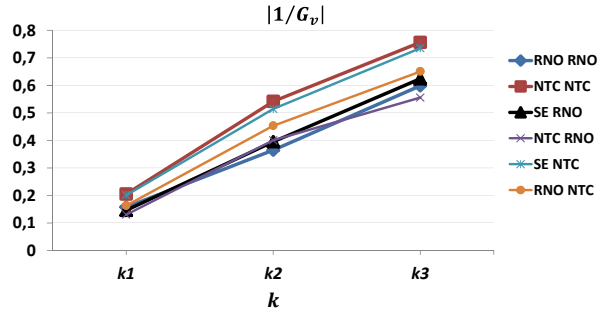


Fig. III.19: Interoperability study of  $1/|G_v|$  for SS self compensation as a function of  $k$

From the graphs we can state the followings:

A) Fig. III.17 and Fig. III.18: all resonant prototypes have a global resonant frequency close to  $\omega_N = 1$  except for NTC-RNO prototype. It is because that the primary resonant frequency is lowest. If the values of primary resonant frequency are calculated from the figures presented in Chapter II that consider the evolution of  $L_1$  (see Fig. II.19), one can find that the plot in Fig. III.20. As shown before, for the  $SS_L$  compensation, the value of the global resonant frequency is equal or close to the primary one (dominant frequency). However for all cases, a frequency control is needed to work at global resonance.

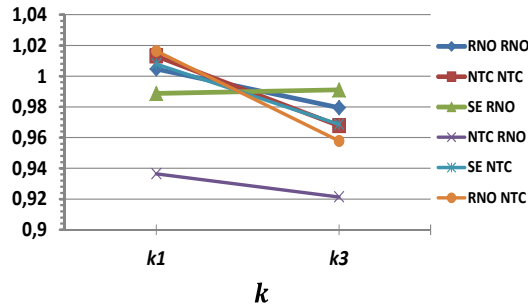


Fig. III.20: Normalized primary resonant frequency ( $\omega_{01N}$ ) for all topologies for  $k_1$  and  $k_3$

B) Fig. III.19: if a fast calculation for  $|G_v|$  (45) is done at  $\omega_{0ref}$  (30 kHz) we can get the following:

$$|G_v|_{SS_L}(f_{0ref}) = \frac{\omega_{0ref} M_{ref}}{|Z_{in}|_{SS_L}(\omega_{0ref})} \quad (57)$$

from (43), the equation (59) will be:

$$|G_v|_{SS_L}(f_{0ref}) = \frac{\omega_{0ref}M_{ref}}{\frac{\omega_{0ref}^2M_{ref}^2}{R_e}} = \frac{R_e}{\omega_{0ref}M_{ref}} \quad (58)$$

$$\frac{1}{|G_v|_{SS_L}(f_{0ref})} = \frac{\omega_{0ref}M_{ref}}{R_e} \quad (59)$$

It means that at 30 kHz and fixed  $R_e$  (for the reference case), the inverse of the voltage gain depends proportionally on  $M_{ref}$ . So the prototypes that have larger mutual inductance will have lower voltage gain and so more primary input voltage needed, leads to cost in the size of the inverter. From Chapter II (Fig. II. 21), it is found that NTC-NTC prototype have the largest values of  $M_{ref}$ , so this gives a reason why it is the highest in Fig. III.19 (at least for  $k_2$  as explains (59)). Hence all others prototypes follows this hypothesis.

For the other cases ( $k_1, k_3$ ), the voltage gain will depend inversely on the multiplication of both the mutual and the resonant frequency ( $\omega_0M$ ). However the largest impact will be for the mutual as the difference between the resonant frequencies for all prototypes are nearly close for a certain case of coupling (especially for good coupling  $k_3$  where the mutual is larger).

Finally, the normalized resonant elements electrical voltage ratings are shown in Fig. III.21 for all prototypes. From the plots we can state the following:

A) The highest values are for the primary parts for weak coupling as drawn before. Moreover, for the secondary parts, the highest values are for good coupling but the sensitivity is much lower.

B) For a reference prototype (RNO-RNO) or (NTC-NTC), the values change significantly when considering different interoperable configurations. The voltages may become up to 3 times greater at the primary side and 1.5 greater at the secondary side.

Hence, the stresses on these elements at resonant frequencies can be known for any interoperability configuration, which is necessary for design.

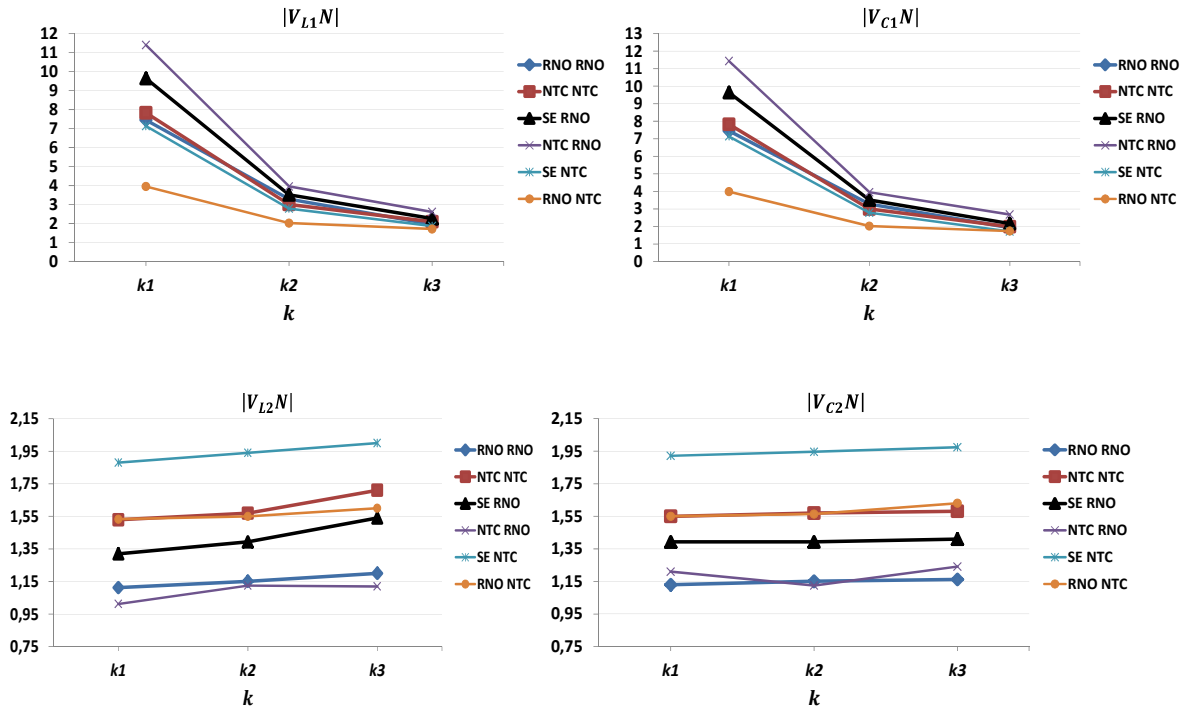


Fig. III.21: Normalized voltages for each  $SS_L$  resonant interoperable prototype at the resonant frequency for different  $k$

### III.3. $SS_L$ Compensated ICT Model in COMSOL with Electrical Coupling

One of the interesting point in the FEM modelling is the structure coupling with the electrical circuit. This leads to check the electrical behavior of the modeled ICT developed in COMSOL that connected to the compensated resonant capacitors. Hence the system can be valid as a step before adding the other electronic to the ICT to build the whole IPT system. The considered circuitis the  $SS_L$  compensated ICT of RNO-RNO prototype (as an example), and the system is shown in Fig. III.22 (2D axisymetric including the chassis).

The simulation configuration is taken for the reference case that belongs to  $k_2$  ( $d = 15cm$ ,  $sh = 0$ ). So the system resonance is  $f_0 = 30kHz$ , and the resonant capacitors ( $C_1, C_2$ ) for this case are the ones that calculated in (41) and (42) respectively. The other parameters are:  $U_0 = 400V$ ,  $P_0 = 3kW$ ,  $I_0 = 7.5A$  and  $R_e = 43.23\Omega$ . From this information and with the help of circuit analysis at resonance, the primary current can be found as following:

$$|i_1| = \left| \frac{R_e}{j\omega_0 M} i_2 \right| = \left| \frac{43.23\Omega}{j(2\pi \times 30\text{kHz}) \times 83.89\mu\text{H}} \left( 7.5 \left( \frac{\pi}{2} \right) \right) \right| \cong 32\text{A} \quad (60)$$

So a current source of 32A and 30kHz is applied at the primary. The results of calculation using COMSOL are illustrated in Fig. III.23. The power  $P_0$  that can be delivered to the load is:

$$P_0 = Su \cdot Q_s = (V_{oc} * I_{sc}) \cdot Q_s = \frac{\omega_0^2 M^2 I_1^2}{R_e} \quad (61)$$

where  $\omega_0 = 2\pi f_0$ ,  $Su$  is the uncompensated power drawn from the supply,  $V_{oc}$  is the open-circuit secondary voltage,  $I_{sc}$  is the short-circuit secondary current, and  $Q_s$  is the series compensation quality factor [15], [40].

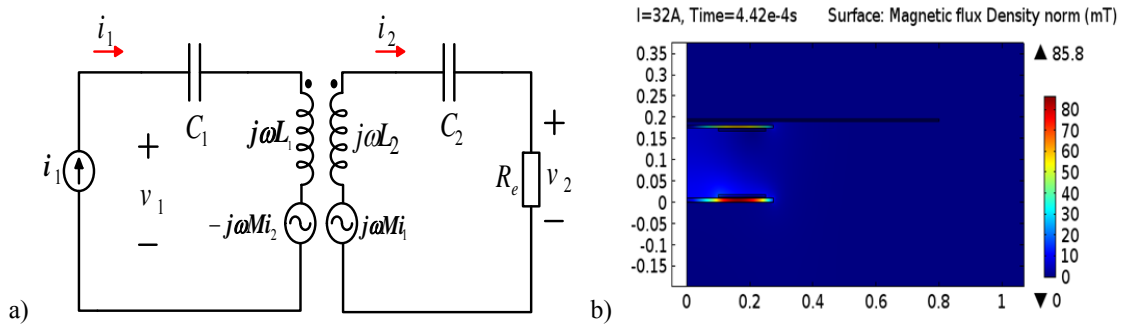


Fig. III.22: Electrical interface of  $SS_L$  compensated ICT in COMSOL: a) FHA equivalent circuit b) FE calculation results

The results in Fig. III.23 show that the system is almost at resonance (not exactly because the calculated the capacitances were based on the values of the corresponding inductances found by FEM 3D). The currents are  $90^\circ$  out of phase which proofs the angle between them in (60). Moreover, at each side of the transformer, the current is almost in phase with the voltage (input for primary and output for the secondary).

The simulation results also enforce the conclusions that the SS compensation topology can be used to step up the voltage as can be seen from Fig. III.23. In addition it shows the drawback of using this topology that the voltages stress over the coils inductances are very high (also the same for the capacitors) as illustrated in Fig. III.23. The results meet the previous calculation of the

voltage gain and the values of the voltages across the resonant elements that were discussed and shown before in the previous sections.

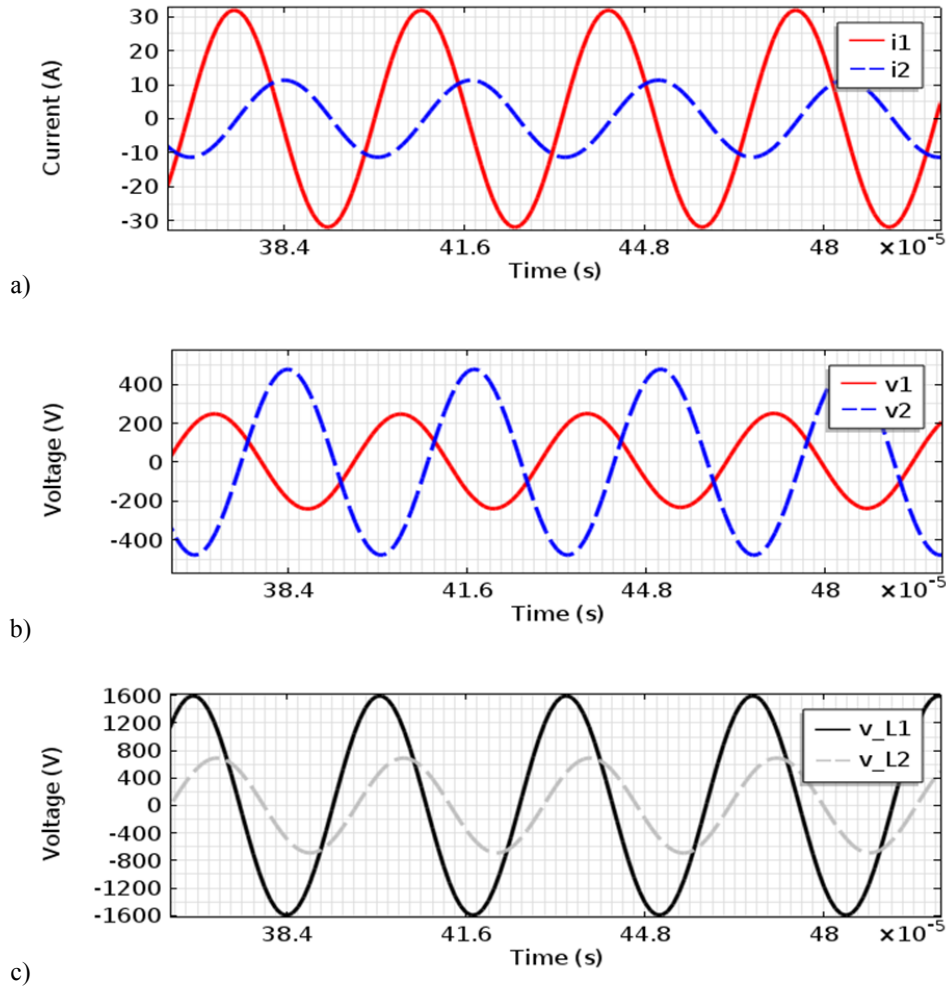


Fig. III.23: Electrical behavior results of the calculation in Fig. III.22: a) primary and secondary currents, b) primary and secondary voltages and c) voltage stress over the primary and secondary coils

In fact, this coupled FEM-circuit simulation and the circuit analysis are almost the same. The only difference is that the FEM takes into account induced currents in the ferrites that imply Joule losses which are not present in the circuit analysis. These losses are very low and have no significant effect on the system behavior. So we can consider the electrical model in the circuit simulation presents the FEM model of the ICT.



### III.4. $SS_L$ Resonant IPT Full System and Control

As the decision is made to use the  $SS_L$  compensation topology, the compensated ICT is now connected to all other electronic parts to form the resonant IPT full system as shown in Fig. III.24. The whole system is modeled using Matlab-Simulink and time domain simulation are done.

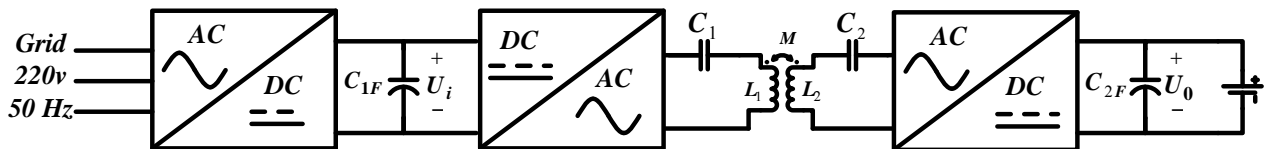


Fig. III.24: IPT full system main blocks with  $SS_L$  compensation

#### III.4.a. Open Loop System

The study begins with the open loop system of Fig. III.24 without any parameter control. All the values are fixed during the simulation. Moreover, the DC-DC resonant converter is taken into account. That means that the studied system begins with the DC source  $U_i$  across the DC bulk capacitance of the filter  $C_{1F}$ . The other stages that are included are:

- **DC/AC:** This stage is presented by the full bridge inverter of 4 power switches (IGBT or MOSFET) that is commanded with a driver. It may be also made of other inverter structures like the half bridge or NPC (neutral point clamped 3 level inverter). However in [50] the author made a comparison between these three inverters in function of different parameters like THD (total harmonic distortion), losses or size and showed that the best one for resonant IPT system is the full bridge inverter.
- **AC/DC:** A full bridge rectifier, that is made of four power DIODEs, is connected to a large enough capacitor  $C_{2F}$  to maintain a pure (or mostly pure) DC output voltage  $U_0$  at the load. This stage also possibly can be made of other inverter that works in the mode of a rectifier with well controlling between the primary and the secondary. This gives an opportunity for the power flow from the output to the input (if needed) by applying a command strategy for each inverter as seen in [65] that depends on the power sign.

Two types of load are considered in the simulation: a resistive load that presents the battery ( $R_L$ ) and a battery model that presented by a voltage source  $V_{bat}$  with a small series internal resistor  $R_{int}$  (as shown before in Chapter I Fig. I. 17). Now the  $SS_L$  resonant DC-DC converter can be mounted as shown in Fig. III.25.

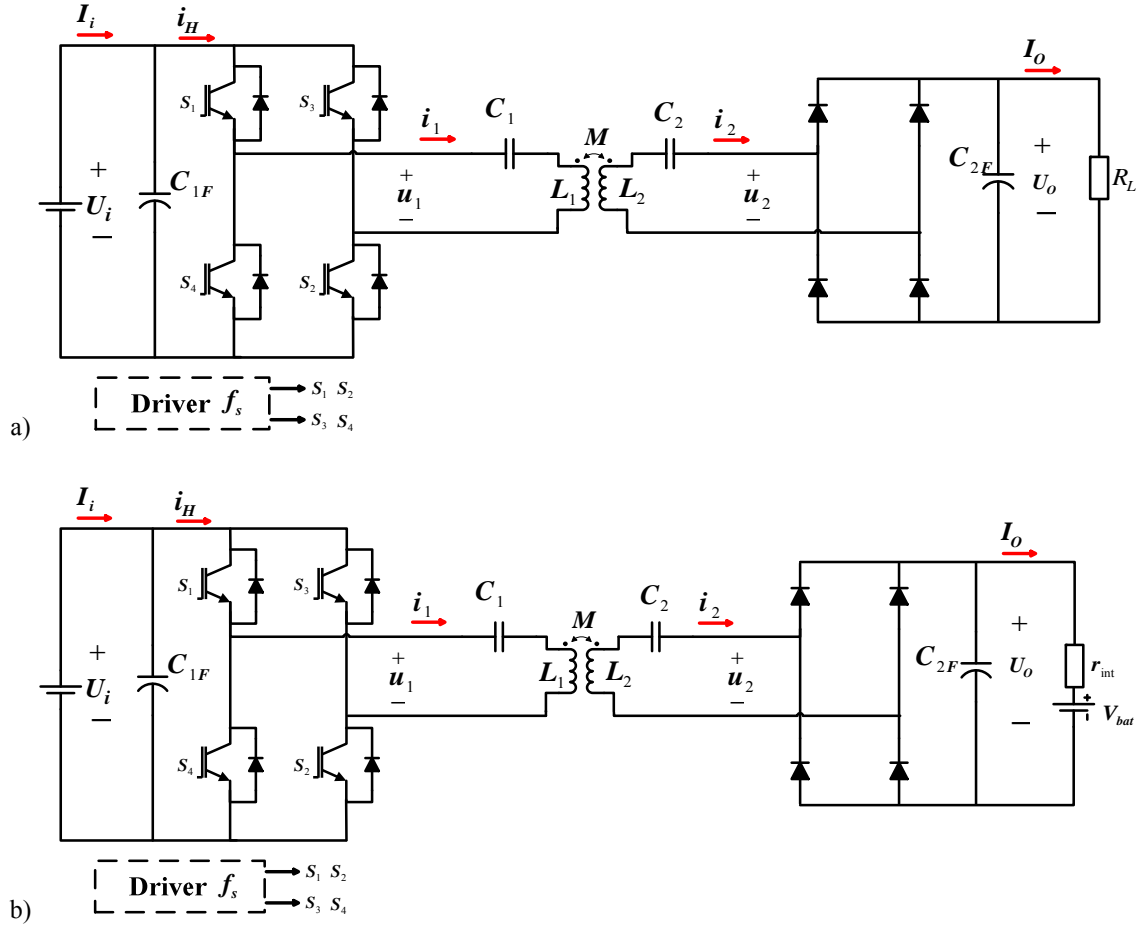


Fig. III.25: Electrical circuit of  $SS_L$  compensated IPT system with: a) resistive load and b) model of battery

The simulation for this open loop system at the reference case is done (so a resistive load can be valid as a battery model as mentioned before, at least when the steady state is reached). The values are taken as:  $d = 0.15 m$ ,  $sh = 0$ , so from TABLE VI:  $L_1 = 266.16 \mu H$  and  $L_2 = 256.79 \mu H$  and  $M = 85.46 \mu H$ . Also,  $f_s = f_0 = 30 kHz$ ,  $U_0 \cong 400 V$ ,  $P_0 = 3 kW$ , so  $R_L = \frac{400^2}{3000} = 53.32 \Omega$ , and the input voltage from the value of  $G_v$  (or  $1/G_v$ ) is:  $U_i = \frac{U_0}{G_v} = \frac{400}{2.366} \cong 169 V$ .  $C_1 = 105.74 nF$ ,  $C_2 = 109.60 nF$ ,  $C_{1F} = C_{2F} = 300 \mu F$  and the duty cycle of the inverter  $D = 0.5$ .

Furthermore for the battery model:  $r_{int} = 0.1 \Omega$  and  $V_{bat} = 400V$ . The results for simulations are shown in Fig. III.26 and Fig. III.27.

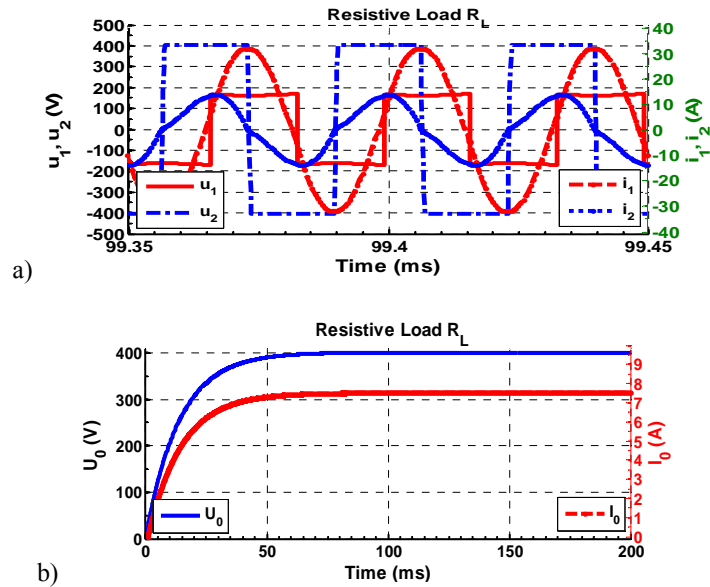


Fig. III.26: Simulation results of the circuit shown in Fig. III.25 a) for voltages (left axe) and currents (right axe): a) primary and secondary and b) output

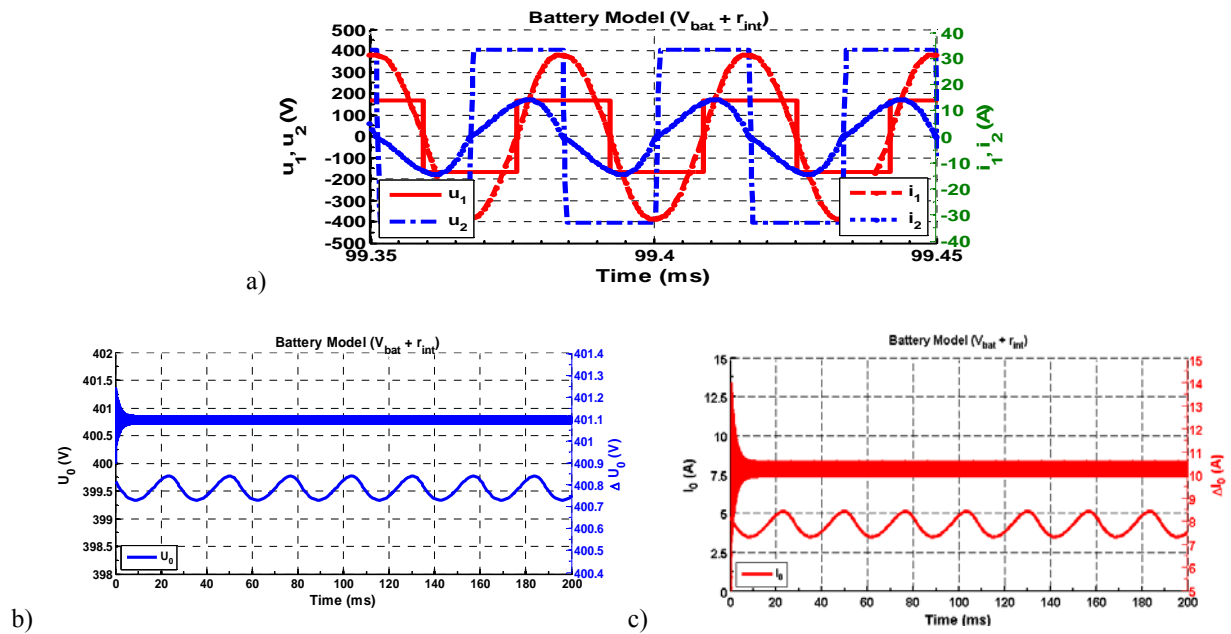


Fig. III.27: Simulation results of the circuit shown in Fig. III.25 a) primary and secondary for voltages (left axe) and currents (right axe), b) output voltage (left axes) and voltage ripple (right axes) and c) output current (left axes) and current ripple (right axes)

The Figures Fig. III.26 and Fig. III.27 show the waveforms of the primary and secondary currents and voltages and the output load voltages and currents respectively. Again, as shown in the previous sections, the currents are in phase with the voltages at each side, and they are out of phase from each other.

It can be shown from the output voltage and current in Fig. III.27 for the battery load model that there are ripples associated with the waveforms, whereas they don't appear in the case of resistive load (Fig. III.26 b)). This is because of the internal series resistance of the battery model  $r_{int}$  that is much smaller than the value of resistor  $R_L$  ( $R_L \gg r_{int}$ ), and so the time constants are such that ( $\tau_L = R_L C_{2F} \gg \tau_{int} = r_{int} C_{2F}$ ).

For the battery model,  $V_{bat}$  is imposed and the following relation holds:

$$I_0 = \frac{U_0 - V_{bat}}{r_{int}} \quad (62)$$

From Fig. III.25, the value of the primary fundamental component of the squared inverter output voltage  $u_1(t)$  can be given as:

$$v_1(t) = \frac{4}{\pi} U_i \sin(\pi D) \sin(\omega_s t) \quad (63)$$

where  $D$  is the inverter duty cycle. The primary input current is expressed as:

$$i_1(t) = I_1 \sin(\omega_s t - \varphi_s) \quad (64)$$

$$I_1 = \left| \frac{v_1}{Z_{in}} \right| \quad (65)$$

where  $\varphi_s$  is the phase shift angle between  $v_1(t)$  and  $i_1(t)$ . The average value of the input current of the inverter  $i_H(t)$  can be found as [23]:

$$\langle i_H(t) \rangle_{T_s} = I_H = \frac{2}{T_s} \int_0^{T_s/2} i_H(t) \cdot dt = \frac{2}{\pi} I_1 \cos(\varphi_s) \quad (66)$$

The signals illustrations for the equations (63)-(66) are shown in Fig. III.28 [23]. At resonance, the output voltage of the inverter  $v_1(t)$  and the input primary current  $i_1(t)$  are in phase. So the value of  $\varphi_s$  is zero and  $\cos(\varphi_s) = 1$ .

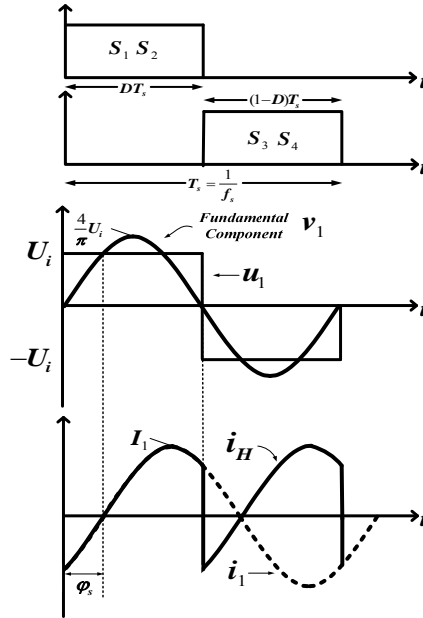


Fig. III.28: Waveforms of the command signals, inverter output voltages and inverter input and output currents [23].

It means that the maximum possible power is transferred and so the inverter frequency should be regulated to meet the resonant frequency of the system. A closed loop design is needed.

### III.4.b. Closed Loop System

The final design of the system includes an automatic regulation for the needed parameters during the charging. Here; two parameters should be well controlled and regulated, the first one is the frequency of the inverter driver  $f_s$  in order to work at resonance ( $f_s = f_0$ ) and so maximum power transfer is done. In fact, the changes in the ICT parameters for different coupling cases will change the system global resonance frequency.

Besides the frequency regulation which is done considering a constant input voltage, the output power should also be regulated. In the complete system, the power is regulated by acting on the input voltage. This outer loop is slower than the inner frequency regulation loop.

Many authors proposed solutions for the power loop control in the IPT charger. They suggest to add a chopper circuit between the rectifier and the load at the secondary side (on board of EV). This circuit could be a boost or a buck-boost in order to regulate the output power by controlling the chopper circuit duty cycle ( $\alpha$ ) (switch mode controller) [61].

However, the solution consisting in adding a buck-boost on the primary side before the DC filter capacitor  $C_{1F}$  and the inverter is preferred here as the area and the size for the electronics parts are limited in the secondary part (on board of EV). By this way, the current (or power) absorbed by the battery is measured (as mentioned before in (64)), and the input voltage of the inverter is controlled through the duty cycle  $\alpha$  in order to get the desire current (or power).

Only the frequency regulation loop will be studied in what follows, considering a constant input voltage. We propose to use a Maximum Power Point Tracking (MPPT) method that was usually used in PV (photovoltaic) systems. In fact, the authors in [66] proposed a circuit to apply the MPPT scheme for IPT frequency regulation while the car is moving. However, here a MPPT algorithm embedded in MATLAB function is implemented without the needs of a designed circuit. Moreover, the authors in [67] mentioned the MPPT method for frequency control, however their controller is not detailed.

The general closed loop system is shown in Fig. III.29. The frequency regulation loop is detailed in Fig. III.30. The MPPT procedure can use the feedback of the primary current and voltage. Then the real power should be calculated as these waveforms are AC ones before implement the MPPT algorithm. It means that a calculation of the phase shift angle  $\varphi_s$  can't be avoided to find the real power from this feedback. So this method that depends on the MPPT algorithm can be used as a  $Pf$  correction (as the reactive power will be eliminated).

However, another solution is driven to simplify this MPPT procedure for our frequency regulation. The idea is to take the feedback from input DC part of the system as always used in PV system when MPPT procedure is implemented as shown in Fig. III.30. The input DC voltage  $U_i$  and the DC input current  $I_i$  are used to calculate the DC input power that applied to the MPPT algorithm.

The MPPT algorithm will then calculate; for each iteration; the power and gives a value of the frequency as its output. This frequency is then applied to a variable frequency PWM generator (or VCO) to produce the command signals of the inverter power switches. The procedure continues until a maximum point of the power is found.

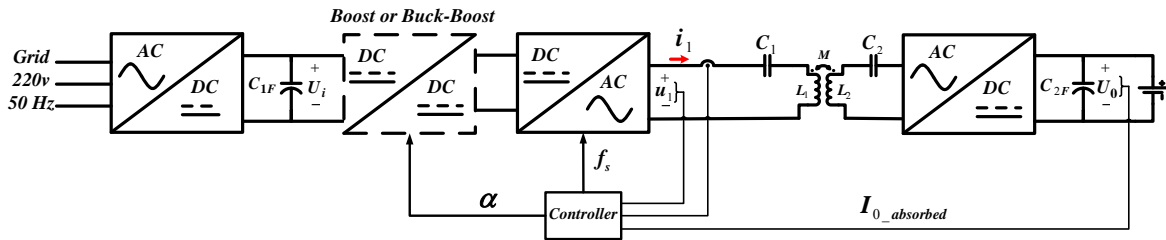


Fig. III.29: Closed loop full IPT system with frequency and power loops controllers

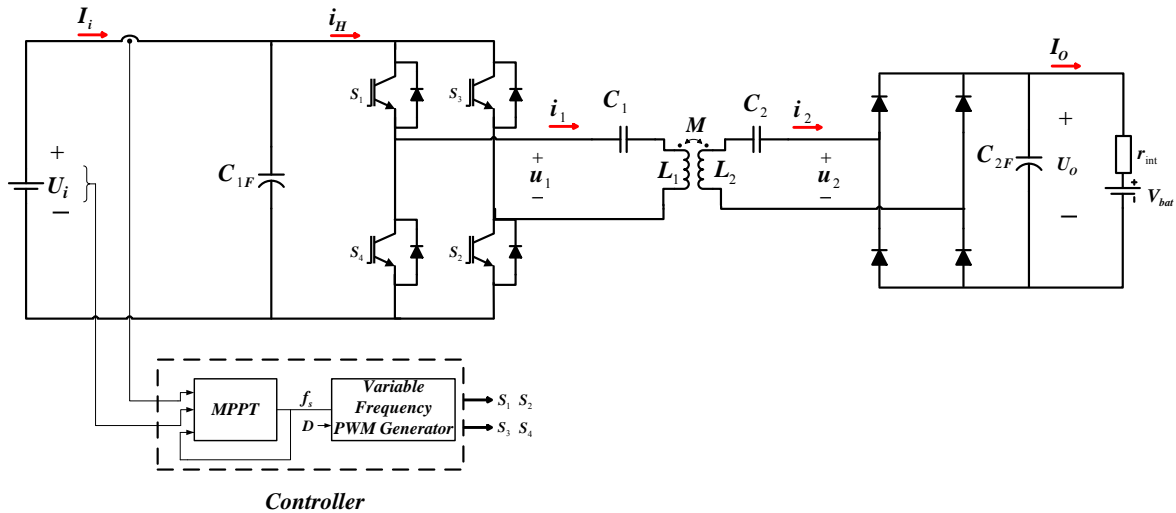


Fig. III.30: Closed loop IPT system with frequency controller using MPPT algorithms

Many algorithms of MPPT are used by the designers in the PV applications [68], [69]. The MPPT algorithm flow chart that used here is shown in Fig. III.31. It depends on the fact that at MPP, the derivative of the power with respect to the frequency is zero ( $\frac{dP}{df} = 0$ ). Also the slope is positive in the left and negative in the right of the MPP ( $\frac{dP}{df} > 0$ ,  $\frac{dP}{df} < 0$  respectively). This method behavior looks like a known method that is called Incremental Conductance (IC). The method searches the MPP as the same way as Perturbation and Observation (PO) method. So a perturbation is imposed to the frequency (incrimination or discrimination) and then observing the power by comparing the power in the previous iteration with its value at the current iteration.

Also another modification has been taken to develop the ordinary IC method used in PV duty cycle ( $D$ ) control. It is drawn from [70] that uses the algorithm of Fig. III.31 applied to a PV system controller to find the duty cycle ( $D$ ) of a buck-boost circuit that searches the MPP. The idea is that to compare the difference between two iterations power values ( $P_k - P_{k-1}$ ) to a small error  $\varepsilon$  rather than zero and then a proper decision is made to perturb the frequency. This is a good solution to avoid loss of power if the difference of power compared to a zero value for huge number of iterations as each one perturbs the frequency. In fact, the two algorithms have same ideas with different types of applications. So the duty cycle  $D$  in [70] is replaced by  $f$  in our algorithm of Fig. III.31. In addition, a limitation is included by upper and lower frequencies to ensure the stability of the system.

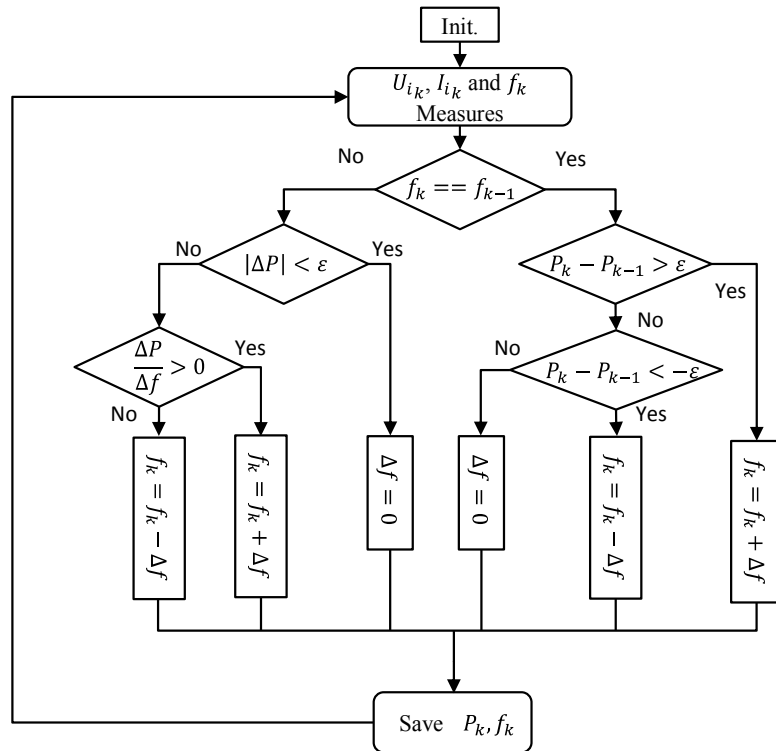


Fig. III.31: MMPT algorithm flow charts used in our IPT system to control the frequency; where:  $k$  is the iteration number,  $P_k = U_{i_k} I_{i_k}$ ,  $\Delta P = P_k - P_{k-1}$ ,  $\varepsilon = 1$ ,  $\Delta f = 100\text{Hz}$  (if not set to zero). Same algorithm used in [70] to control the duty cycle  $D$  with fixed frequency

• **Simulation Results:**

Two cases have been simulated for the full IPT system using the closed loop control that was shown before in Fig. III.30. Both cases were taken for the reference position of the EV ( $d = 0.15m$ ,



$sh = 0$ ), and the desired power at the load is  $3\text{ kW}$ . So the resonant frequency that maximizes the transferred power is  $f_0 = 30\text{ kHz}$ . This should be the frequency that the controller finds. The inverter duty cycle is  $D = 0.5$  and the load is the battery model as in Fig. III.30. The upper and lower frequencies limitations are chosen to  $[25\text{ kHz}, 35\text{ kHz}]$ , so in this frequency band all possible situations of  $k$  are included in the frequency regulation.

The first case takes an initial frequency value of  $26\text{ kHz}$  and the second one takes  $34\text{ kHz}$ , the simulation results are illustrated in Fig. III.32 - Fig. III.35. They show that the system tracks the MPP and reaches the desired output power of  $3\text{ kW}$  at a resonance frequency of almost  $30\text{ kHz}$  with an error of  $100\text{ Hz}$ . This error can be minimized but the cost of regulation will be large.

It can be seen that the algorithm follows the steps in the power with increments in frequencies. Fig. III.32 - Fig. III.35 show the behavior of the power for the full model as a function of the frequency with constant input voltage. The input current  $I_i$  and the output voltage  $U_0$  have also the same behaviour Fig. III.33 and Fig. III.35. However, the changes of the battery voltage is small

The results of simulations verify that the controller for frequency regulation is working very well. Other cases for different EV position can be also examined. For example, starting from the frequency  $30\text{ kHz}$  the position is changed (in fact  $k$  is changed) and the controller finds the new resonant frequency where the power is maximum (Fig. III.35). The main drawback of the proposed control loop is that it takes between  $1.5\text{ s}$  to  $2\text{ s}$  to find the needed frequency as shown in Fig. III.32 - Fig. III.35. However, this controller is very efficient for our IPT system that considers the static charging, since the EV will take a position and stay for charging. But for the dynamic charging, a very fast controller is highly needed which is not in the aim of this project.

And to compare the results with a resistive load, the MPPT controller is applied to a check the validity to use  $R_L$  for frequencies different from the resonant one. The results of simulation are shown in Fig. III.36 for the case shown before of starting frequency  $f_s = 26\text{ kHz}$  for an example. The results are same as the ones with a battery model load (Fig. III.32).

But the plot in Fig. III.37 shows that the output voltage across  $R_L$  varies with frequency. So it is not fixed as the other situation when using a battery model (Fig. III.33). So it is not correct to use  $R_L$  if the system is not working at resonance.

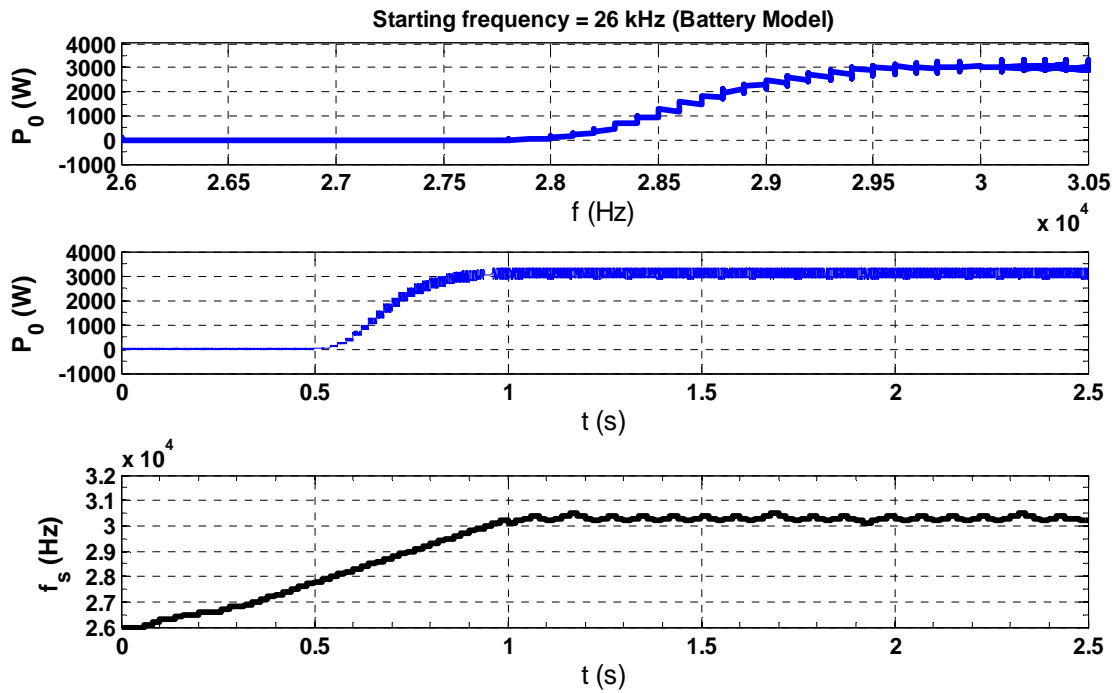


Fig. III.32: MPPT controller for battery model plots for initial frequency 26 kHz: plot of: the output power with frequency and time response, and the controller frequency in time response

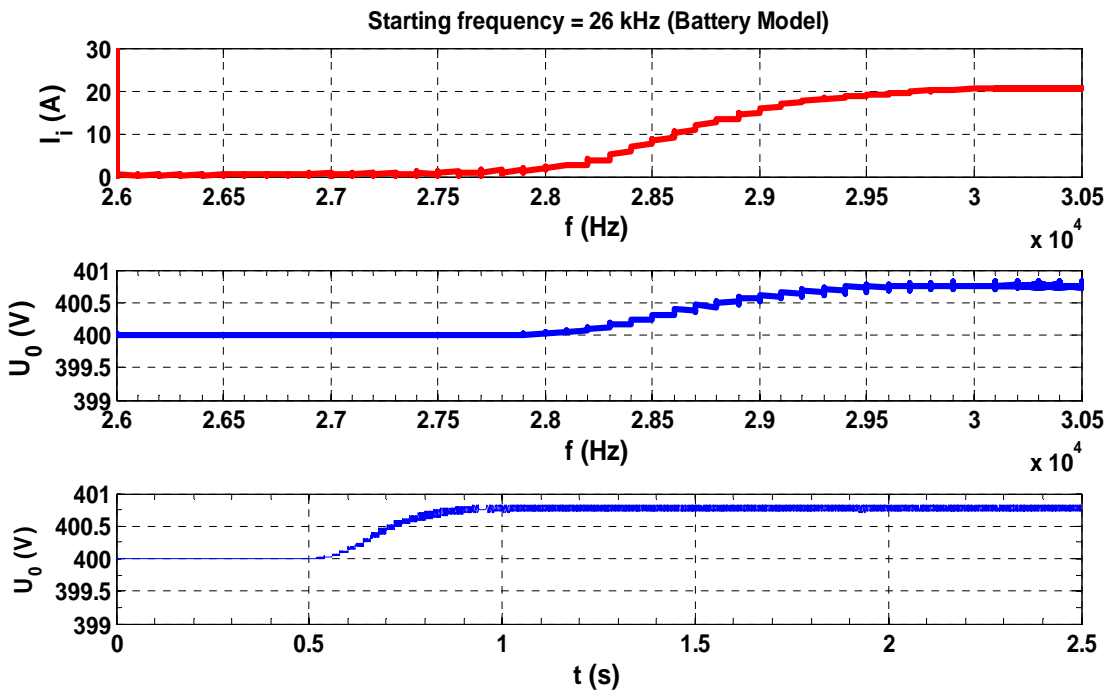


Fig. III.33: MPPT controller for battery model plots for initial frequency 26 kHz: input current with frequency, and the output voltage in frequency and time domain

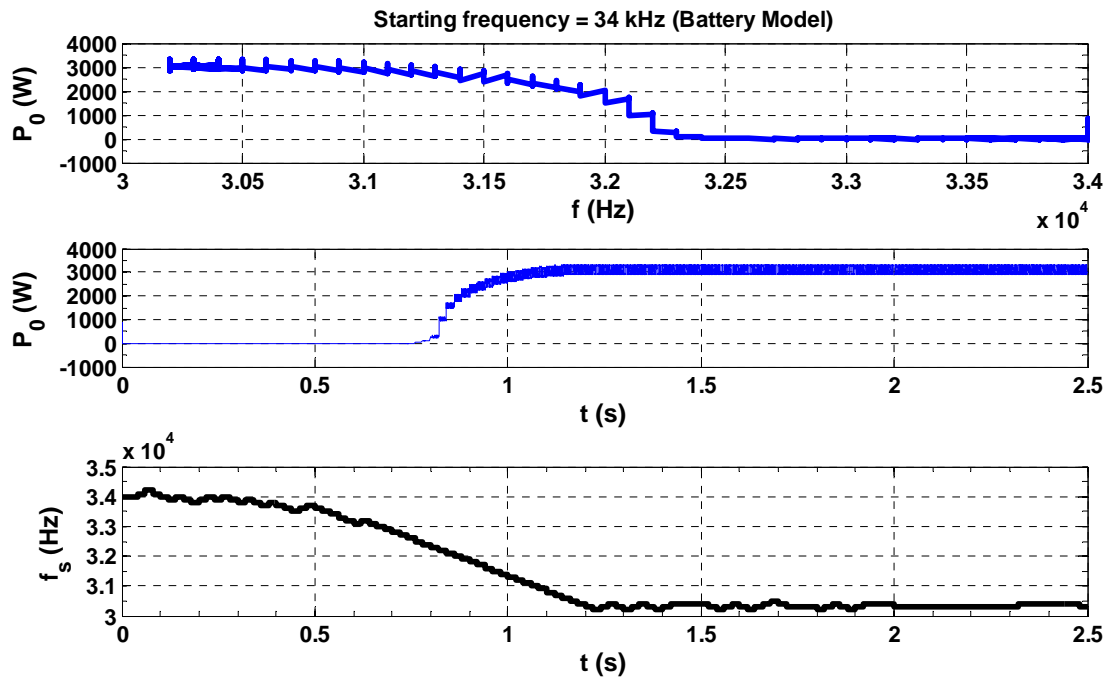


Fig. III.34: MPPT controller for battery model plots for initial frequency 34 kHz: plot of: the output power with frequency and time response, and the controller frequency in time response

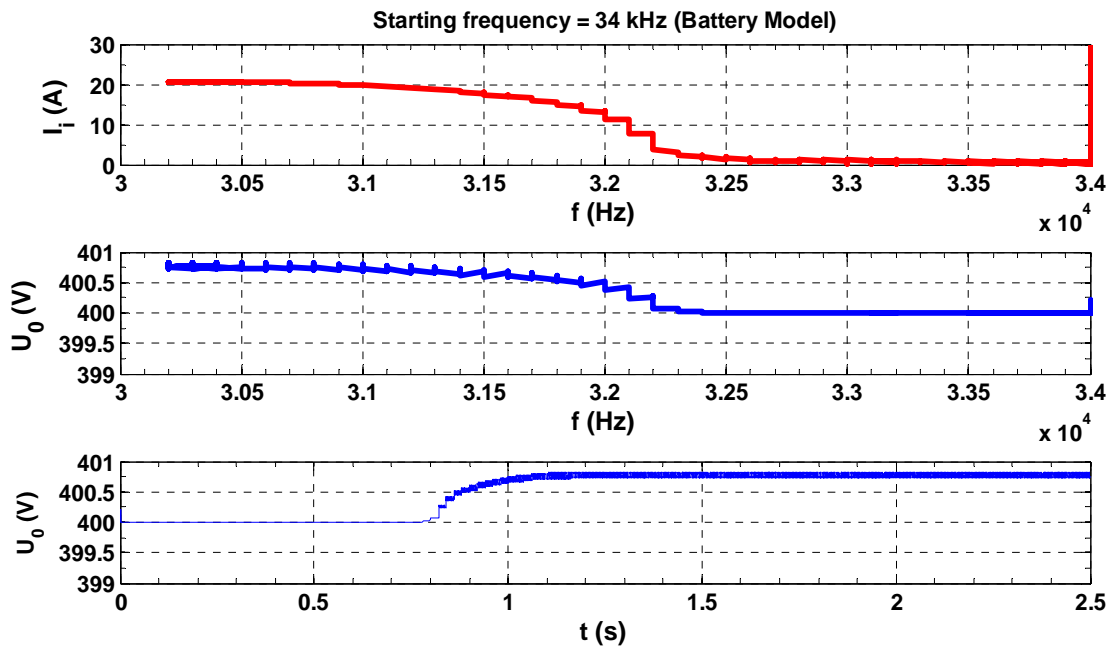


Fig. III.35: MPPT controller for battery model plots for initial frequency 34 kHz: input current with frequency, and the output voltage in frequency and time domain

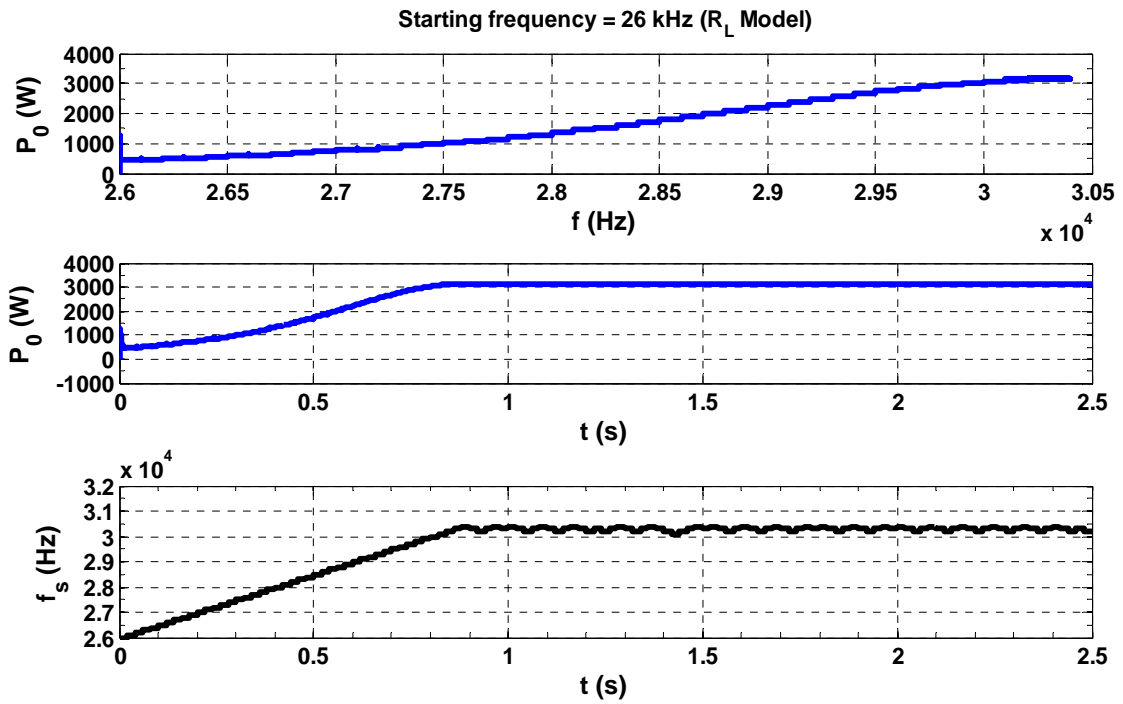


Fig. III.36: MPPT controller for  $R_L$  model plots for initial frequency 26 kHz: plot of: the output power with frequency and time response, and the controller frequency in time response

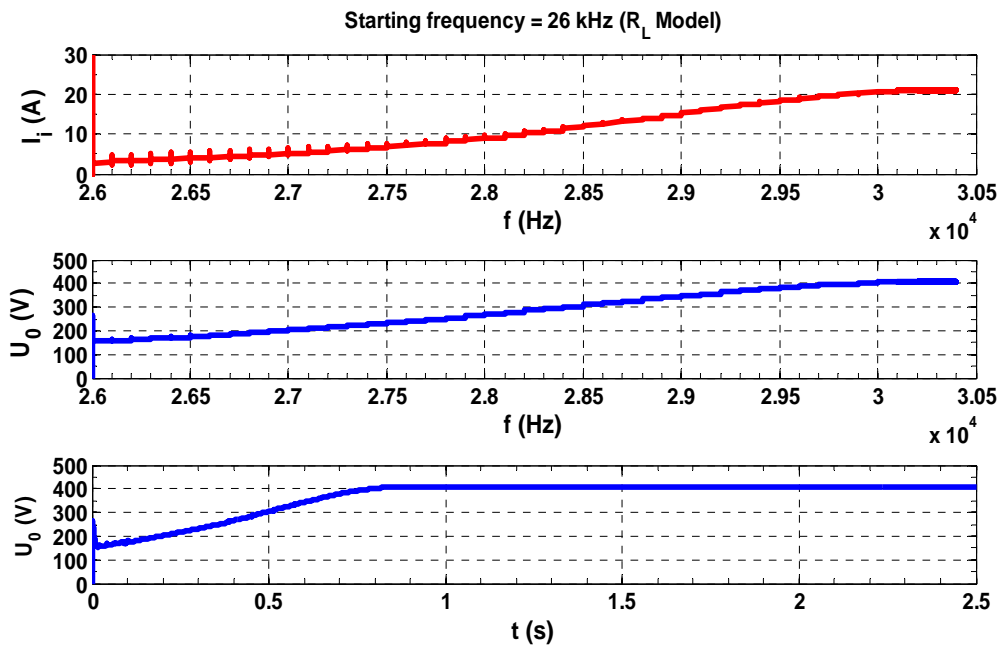


Fig. III.37: MPPT controller for  $R_L$  model plots for initial frequency 26 kHz: input current with frequency, and the output voltage in frequency and time domain

### **III.5. Conclusion**

This chapter deals with the design of the electronic part of the IPT system. It considers at the first part a comparison between three different types of inductive compensation by well define criteria. A compromise is taken to choose the Series-Series Self compensation that meets the industrial goals. The equivalent circuit represented by FHA with the FE interface is tested in COMSOL to show the electrical behavior of the ICT connected to the compensation capacitors using the FE modelling.

As a second part of this chapter, the full IPT system starting with the input DC stage and ending with an equivalent load that presents the battery and a battery model are analyzed and simulated in MATLAB/Simulink using: firstly, the open loop system. And secondly, the closed loop system with a feed back to regulate the system frequency that meets the resonant one where the power transferred is maximum.

Finally, the controller that used in the frequency correction depends on the MPPT algorithm. Since the MPP changes with changing the parameters like the coupling factor  $k$ ,  $sh$ ,  $d$  ....etc, a frequency loop is needed in our case to find the resonant frequency where the power is maximum.

This controller is verified for our IPT system by showing the system behavior in time and frequency domains with a battery model load. The results of simulation for the reference case ( $k_2$ ) showed a proper response that finds the resonant frequency and so a maximum power is transferred. Although the response time is nearly slow, but it is sufficient for the case of static battery charging that takes 3-4 hours for full charging.

In fact, the frequency that the controller finds (can be said) is the exact resonant frequency; this can be seen in Fig. III.38 that shows the primary voltage and current at this frequency, the phase between the two waveforms is almost zero.

Finally, a resistive load with the MPPT controller explained that the assumption to use a  $R_L$  to model the battery at fixed output voltage and power is only valid for the case where the operating frequency is close to the global system resonance.

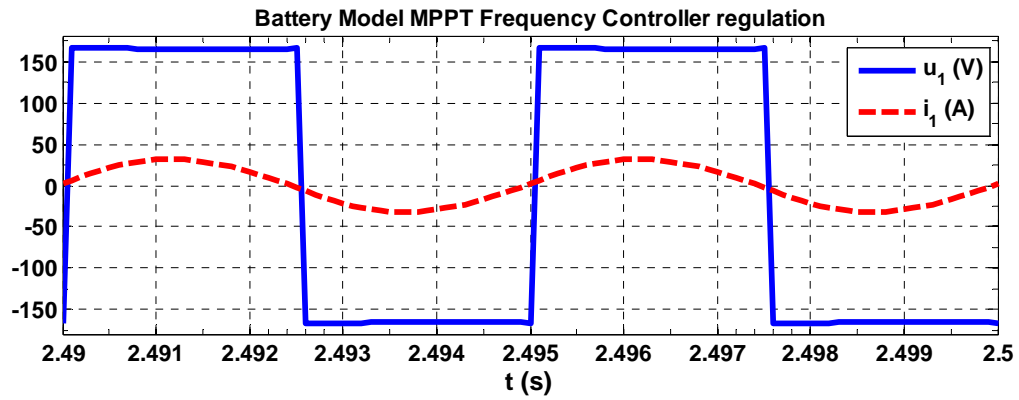


Fig. III.38: Primary voltage and current at the resonant frequency value fund by the MPPT controller for a battery model load and starting frequency 26 kHz. Following the simulations in Fig. III.32 and Fig. III.33



***Chapter IV : Interoperability Experimental Tests and Models Validations***



### **IV.1. Introduction**

As the IPT system is completely designed, the final step is to validate the proposed theoretical analysis and the results of simulations by experimental tests. This chapter includes experimental setups of different prototypes studied before. As mentioned in Chapter II, the coils and ferrites of different prototypes have different shapes and/or sizes. The installations of the desired IPT systems are done in RENAULT laboratory with the help of industrial partners who fabricated their own pads, power converters and controllers. The interoperability between different industrial partner's prototypes is also tested.

Two test benches are installed for measurements:

- Test bench V1: the power pads are installed in a part of the EV chassis as explained in Chapter II. Here the secondary power pad is centralized in the middle of the chassis.
- Test bench V2: the installation of the power pads and measurements had been taken a place in the EV (KANGOO-RENAULT). The secondary power pad is shifted toward the backend of the EV chassis with a distance of 50 cm from the end of the chassis and the center of secondary power pad.
- For all cases, the distance between the secondary ferrite and the chassis is 20 cm and it is fixed.

### **IV.2. RNO-RNO Prototype (Test Bench V1)**

A part of this prototype test results was shown in Chapter II in order to validate the FEM calculation. Detailed information about the total test is shown here. As a validation for the developed full model that is shown in Fig. IV.1, a 2kW IPT existing system for charging a 300  $V_{DC}$  battery is used.

Measurements have been carried out to check the  $|B|$  levels at various points close to the EV (KANGOO-RENAULT) chassis and in the nearby environment using a Magnetic Field HiTester

3470 (HIOKI) [71] as shown in Fig. IV.2. The ICT is installed in the center of the EV chassis. The test equipment installation is shown in Fig. IV.3. The positioning parameters were taken as:  $d=10$  cm,  $sh=0$  (corresponding to  $k_3$  configuration) and the inverter driver frequency  $f_s=33$  kHz (global resonant that was found in practical test with RNO frequency regulation loop).

The primary inverter is made of 4 IGBTs, and the secondary bridge rectifier constructed by 4 DIODES, the two bridges (inverter, rectifier) are modules of INFINEON technology. For a resonance frequency  $f_0 = 30$  kHz,  $C_1, C_2$  values are found from (41), (42) where the values of  $L_1$  and  $L_2$  at reference case ( $d = 15$  cm,  $sh = 0$ ) are (TABLE VI):  $L_1 = 266.16 \mu H$ ,  $L_2 = 256.79 \mu H$  (theoretically), so  $C_1 \cong 105.74$  nF and  $C_2 \cong 109.60$  nF.

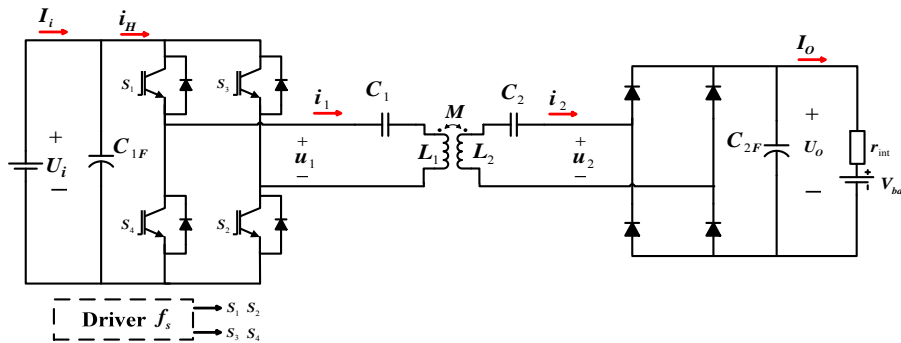


Fig. IV.1: Electrical circuit of  $SS_L$  compensated IPT system

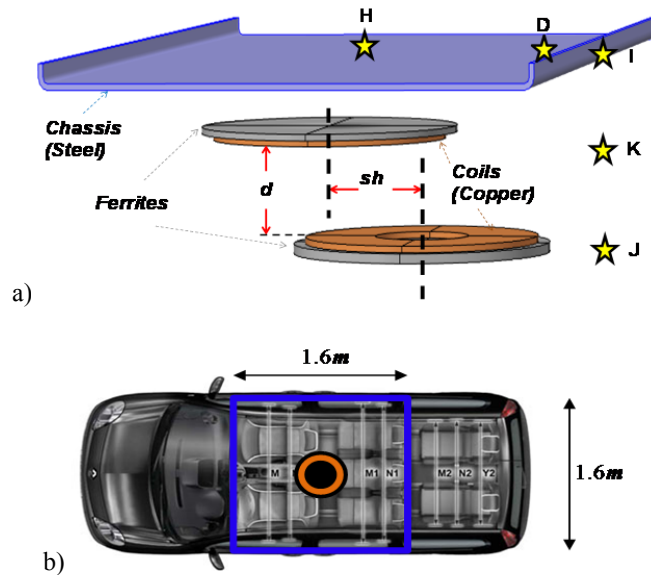


Fig. IV.2: a) 3D structure of an ICT with shielding, simple EV chassis and measurement positions (stars) for the magnetic field density, b) top view of the EV to show the considered chassis and the position of secondary pad

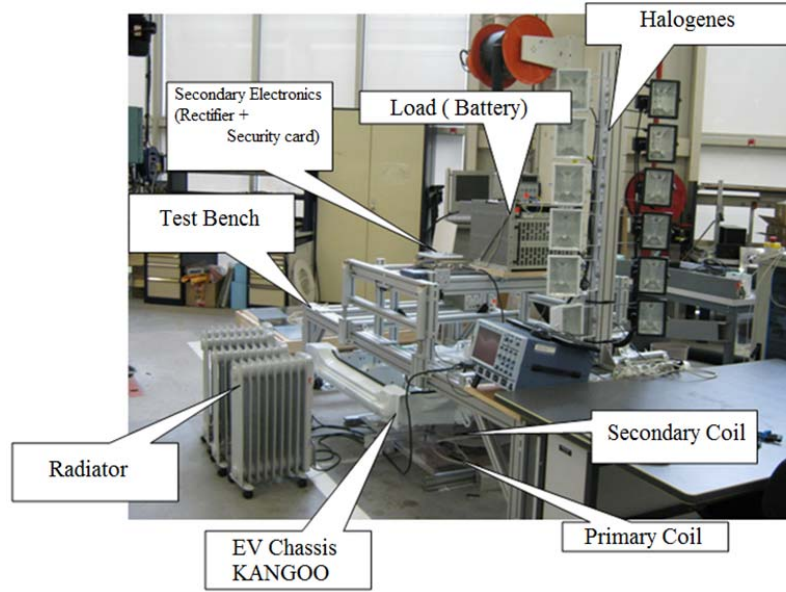


Fig. IV.3: Picture of the experimental test equipment installation for RNO-RNO IPT prototype

In the predesign, the maximum current of the primary coil  $i_1$  is 40 A for a 3 kW power transfer at 400 V battery so:  $I_{1,rms} \approx 30A$ . From Fig. III .11, the maximum normalized voltage for the worst case ( $k_1 = 0.11$ ) across  $C_1$  at resonance  $V_{C1N} \approx 7.5$ . So  $V_{c1,max}rms = V_{C1N} * \frac{4}{\pi\sqrt{2}}U_0 = 7.5 \frac{4}{\pi\sqrt{2}}400 = 2700 V$ . These values are also taken for  $C_2$ . The value of  $C_{2F}$  is taken as 300  $\mu F$  with maximum rated voltage 450 V, and a protection is designed to switch the output to a resistive load (radiator for an example) above this value.

The design dimensions of the ICT elements with the EV chassis were listed before in Chapter II TABLE III. The values of self and the mutual inductances shown before in Fig. II. 15, are presented here with their corresponding measurements in Fig. IV.4.

The inductances are measured using a RLC meter. The self inductances are found by opening the circuit on the secondary side and measure the primary coil impedance to find  $L_1$ , and the process is inversed to find  $L_2$ . Then the coupling factor is determined by measuring the primary or secondary leakage inductance. This inductance can be found by short circuiting the secondary and measure the primary impedance (or vice versa for secondary leakage inductance). As these values are known, then the mutual inductance can be calculated from the coupling factor, primary and

secondary self inductances. The results of simulations show good agreement with respect to the measured ones.

The simulations and test results are shown in TABLE IX. This table includes two columns: the first one is simulated in which the values are drawn from the calculation and takes the same operating frequency and input voltage as the measurements. The second one lists the values of practical test results.

TABLE X includes the measurements of  $|B|$  levels at the points shown in Fig. IV.2 (points H, D, I, J and K) for an input resonance current  $I_1 = \frac{15}{\sqrt{2}} A$  and secondary one  $I_2 = \frac{10}{\sqrt{2}} A$  with a  $\pi/2$  phase shift. These values are compared to the 3D FEM computation cartography of  $|B|$  shown in Fig. IV.5. The tables show a good coherence between the simulated and tested results. It is found that the maximum level is at point K and  $K_{test} = 3.4 \mu T$ ,  $K_{sim} = 3.54 \mu T$ . The two values are under the maximum allowed magnetic flux density level for human exposure ( $6.25 \mu T$ ), and thus all other points are below the limit.

The efficiency presented in TABLE IX can be calculated as:

$$\eta = \frac{P_{out}}{P_{in}} = \left( \frac{P_0}{P_{in}} \right)_{DC} = \frac{P_{bat}}{P_{in}(DC)} = \frac{P_0}{(V_{in}, DC) (I_{in}, DC)} = \frac{1812}{271V * 7.5A} \approx 90\% \quad (67)$$

For the full model, the same formula is used for the efficiency. The only losses that are considered come from power electronic components (due to commutations and conduction) modeled with Simulink library. Resistive losses in the coils and losses in the materials (chassis and ferrites) due to the radiated field are neglected. The design shows a high efficiency ( $\sim 90\%$ ), and it shows safety to human exposure.

In other part, the calculation of the induction  $|B|$  is also performed on a segment of  $1 m$  from the edge of the chassis outside of the vehicle and the midpoint from the two coils with  $d = 0.15 m$  in order to compare results from excitation of the primary coil with  $\frac{15}{\sqrt{2}} A$  and  $\frac{40}{\sqrt{2}} A$ . Here as the study took the maximum current possible could be injected in the primary ( $40 A$ ), the secondary is an open circuit so as to protect the elements of power stages and the ICT primary side from any over currents risks may be drawn if the load is connected.

Two cases are considered: a case without a shift ( $sh = 0$ ), and the case with shift ( $sh = 0.1$  m). The system studied is shown in Fig. IV.6. The simulation results are shown in Fig. IV.7 and compared with the limits for human exposure (ICNIRP 1998). These results show that the shift between coils axes has an important effect on the radiation field. The field value may exceed the norm even for current values that correspond to normal operation of the system.

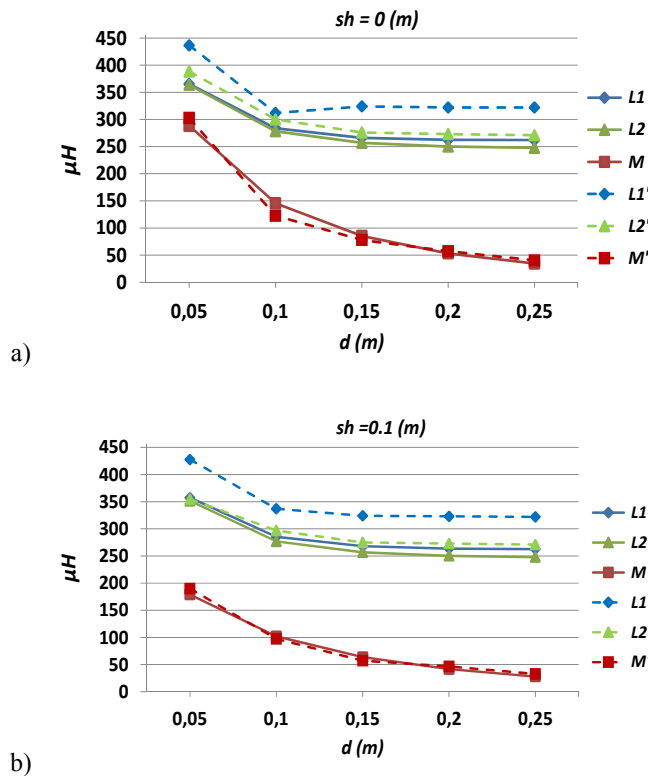


Fig. IV.4: Values of ( $L_1, L_2, M$ ) for different air gap  $d$  (m): Simulated (solid lines) and Measured (dashed lines), a)  $sh = 0$  and b)  $sh = 0.1$  m

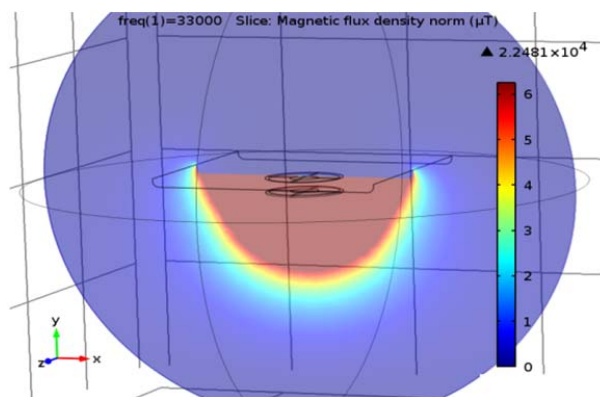


Fig. IV.5: 3D Cartography for  $|B|$  in  $\mu T$ , maximum data range is  $2.2481 \times 10^4 \mu T$  and maximum color range is  $6.25 \mu T$

TABLE IX: COMPARISON BETWEEN THEORETICAL AND EXPERIMENTAL ELECTRICAL PARAMETERS AND QUANTITIES FOR RNO-RNO IPT PROTOTYPE BENCH V1

<b>Parameter</b>	<b>Simulated</b>	<b>Measured</b>
$U_i(DC)$	271 V	271 V
$I_i(DC)$	8.263 A	7.5 A
$f_s$	33 kHz	33 kHz
$L_1$	284 $\mu$ H	312 $\mu$ H
$L_2$	278 $\mu$ H	300 $\mu$ H
$M$	145.7 $\mu$ H	125 $\mu$ H
$k$	0.5	0.4
$C_1$	105.74 nF	80 nF
$C_2$	109.60 nF	94 nF
$i_1$	14.7 A	15 A
$i_2$	11 A	10 A
$V_{C1}$	675 V	904 V
$V_{C2}$	482 V	513 V
$U_0(DC)$	300 V	300 V
$I_0(DC)$	6.77 A	6.04 A
$P_0$	2031 W	1812 W

TABLE X:  $|B|$  LEVELS VALUES FOR RNO-RNO TEST BENCH V1

<b>Point</b>	<b>Simulated</b>	<b>Measured</b>
$H$	0	0.42 $\mu$ T
$D$	1.33 $\mu$ T	1.36 $\mu$ T
$I$	3.40 $\mu$ T	3 $\mu$ T
$K$	3.54 $\mu$ T	3.4 $\mu$ T
$J$	3.30 $\mu$ T	3.32 $\mu$ T

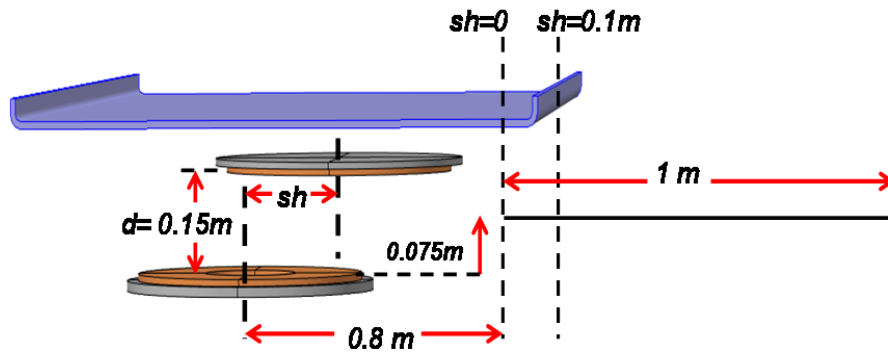


Fig. IV.6: Schematic configuration of the line where the calculation of  $|B|$  is performed (outside the EV)

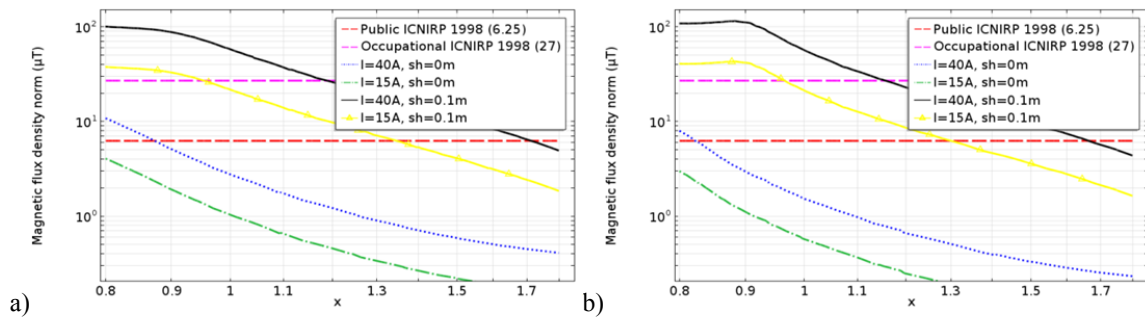


Fig. IV.7: Plot of  $|B|$  ( $\mu\text{T}$ ) calculated in a 1 m line outside the EV that shown in Fig. IV.6 for two excitation currents. The values compared with ICNIRP 1998 public and occupational and standard norms: a)  $d = 0.1\text{ m}$  and b)  $d = 0.15\text{ m}$

### IV.3. SE-RNO, NTC-RNO, NTC-NTC and SE- NTC Prototypes (Test Bench V1)

In order to check human safety compliance all the studied systems and in particular considering interoperability configurations, experimental tests are carried out for (3 kW, 300 V) and ( $d = 0.1\text{ m}$ ,  $sh = 0$ ). The values of  $|B|$  are given for the point shown in Fig. IV.2. TABLE XI includes the measurements of  $|B|$  levels at the points (H, D, I, J and K) for different prototypes for the input primary and output secondary currents ( $I_1[0^\circ$ ,  $I_2[90^\circ$  respectively in rms values) at the resonant frequencies that appear in Appendix C.

TABLE XI:  $|B|$  LEVELS VALUES FOR DIFFERENT PROTOTYPES TEST BENCH VI

		SE-RNO		NTC-RNO		NTC-NTC		SE-NTC	
		Sim.	Measu.	Sim.	Measu.	Sim.	Measu.	Sim.	Measu.
	$i_1$	$\frac{15}{\sqrt{2}} A$		$\frac{15}{\sqrt{2}} A$		$\frac{11.5}{\sqrt{2}} A$		$\frac{11.5}{\sqrt{2}} A$	
	$i_2$	$\frac{16}{\sqrt{2}} A$		$\frac{15.3}{\sqrt{2}} A$		$\frac{15.8}{\sqrt{2}} A$		$\frac{15.6}{\sqrt{2}} A$	
P O I N T	H	0.2 $\mu T$	0.6 $\mu T$	0.2 $\mu T$	0.46 $\mu T$	0.2 $\mu T$	0.3 $\mu T$	0.2 $\mu T$	0.3 $\mu T$
	D	2 $\mu T$	2.2 $\mu T$	1.4 $\mu T$	0.82 $\mu T$	4.5 $\mu T$	3.65 $\mu T$	4.35 $\mu T$	3.4 $\mu T$
	I	4 $\mu T$	3.7 $\mu T$	3.8 $\mu T$	2.5 $\mu T$	3.5 $\mu T$	2.49 $\mu T$	3.3 $\mu T$	2.3 $\mu T$
	K	5.35 $\mu T$	5 $\mu T$	5 $\mu T$	3.7 $\mu T$	8.5 $\mu T$	7.08 $\mu T$	8.5 $\mu T$	7 $\mu T$
	J	4.3 $\mu T$	4.5 $\mu T$	4 $\mu T$	3.05 $\mu T$	4 $\mu T$	3.04 $\mu T$	4 $\mu T$	3 $\mu T$

#### IV.4. Comparison between Different Prototypes for Test Bench VI

##### IV.4.a. RNO-RNO Prototype

As the only complete data we have is for RNO-RNO prototype (2kW, 300V battery), a comparison between the simulation and measured results is made. The parameters that considered in the comparison study are the normalized values relatives to tests, and the points of  $|B|$  levels values normalized to 6.25  $\mu T$ . The results are shown in Fig. IV.8.

The Fig. IV.8 a) shows that some simulations parameters are slightly far from the test ones. Actually this comes from the fact that for the simulations, the resonant frequency and the gain are chosen as same as in practical test as in TABLE IX. And because of different values of L's and C's, so the impedances will differ and also the currents and voltages in the circuits. However the two cases lead to the desired charging power.

For the levels values of  $|B|$  in Fig. IV.8 b), the calculation is close to the test values for same injected currents and same frequency. The differences may come from the simplified chassis in modeling. However all data are lower than the public ICNIRP 1998 standard norm (6.25  $\mu T$ ).



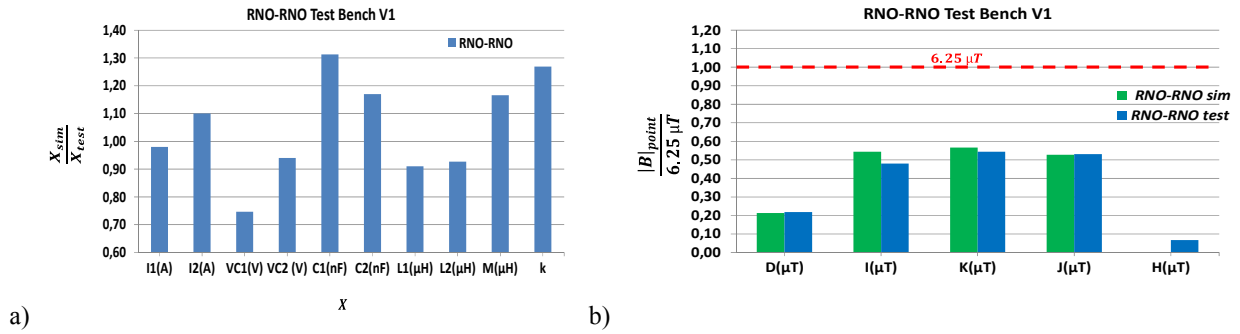


Fig. IV.8: Comparison between simulation and test values for RNO-RNO bench test V1: a) electrical parameters and b)  $|B|$  levels values for the points in Fig. IV.2

#### IV.4.b. SE-RNO, NTC-RNO, NTC-NTC and SE- NTC Prototypes

Since the information available for the tests are the measurement points for the values of  $|B|$  for these prototypes; the comparison based only in these results and compared to the theoretical calculation. The values are firstly normalized to  $6.25 \mu T$ , and secondly the simulation values are normalized to the test ones. The results of comparison are illustrated in Fig. IV.9.

It can be seen that simulation results may significantly differ from the test ones as shown in Fig. IV.9 a). A great part of this error is due to the lack of precision in the positioning of the magnetic field sensor. Actually the measurements were done manually using the sensor, the only point that marked in manipulation was *D*. So a difficulty was encountered to position the same point at each test. Moreover from Fig. IV.9 b) it can be noticed that all values are under the norm except for the point *K* for the prototypes NTC-NTC, SE-NTC for both simulation and test results (for same charging characteristics (3kW, 300V battery)).

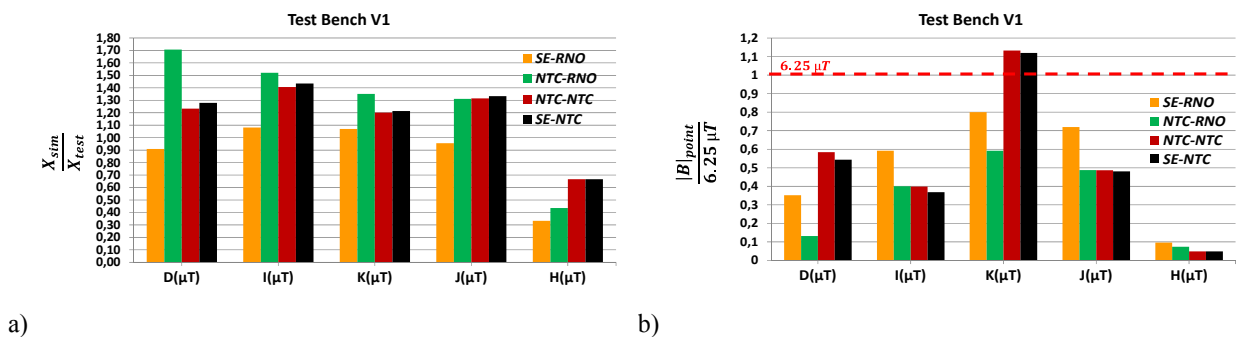


Fig. IV.9: Comparison of values of  $|B|$  levels of interoperability prototypes for bench test V1: a) simulation results normalized to test ones and b) tests results normalized to  $6.25 \mu T$

Considering the interoperability, if one looks to the flux density at critical point K, it can be said that:

- Coupling systems having the same size in the considered direction (D-K) but different shapes do not significantly change the induction (SE-NTC versus NTC-NTC).
- Coupling systems of different sizes lead to an intermediate value of induction compared to the original systems (NTC-RNO versus NTC-NTC).

It also can be drawn that as the flux density is concentrated in the ferrites, the relevant size to be considered in this analysis is given by the size of the ferrite, which in the studied systems is close to the size of the coils.

#### **IV.5. Test Bench V2**

Before passing to the next prototype tests, some modifications were made:

- The ICTs were installed on the full EV (KANGOO-RENAULT) not only a part of its chassis.
- The position of the power pads are fixed closer to the back of the EV (not centered in the middle of the chassis). The distance from the center of the pads and the backend of the chassis is 50 cm, and the air gap  $d$  is fixed at 13 cm with  $sh=0$ .
- The ICT configurations are same as before except for:  
NTC ferrites primary height = 5 mm.  
SE coil: 33 turns with an extern diameter of 480 cm.
- A new point ( $O$ ) is added to the  $B$  measurements at the backend of the EV.
- The values of  $B$  were calculated in simulation by injecting the currents found in measurements.
- The frequency regulations were manually for SE and automatically for NTC.
- The desired output power is 3 kW for charging a 300 V battery.

To clearly show the test bench V2, an example of EV with ICT installation is shown in Fig. IV.10. The next subsections for this test bench include the tables for simulation and measured

parameters, and the waveforms of electrical quantities when available. Then comparisons are established.

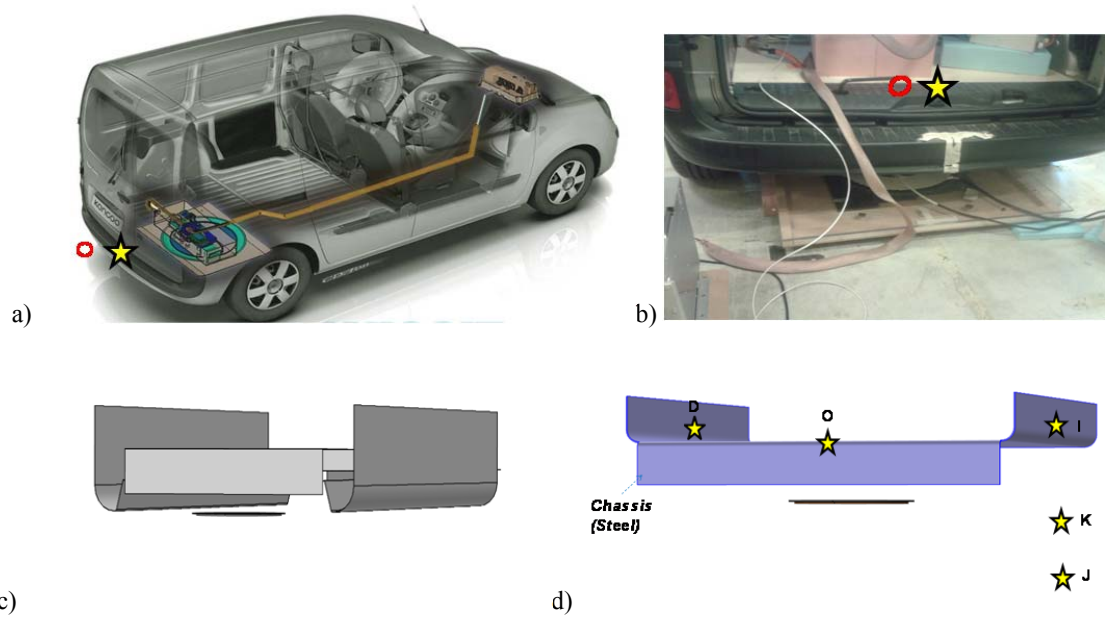


Fig. IV.10: ICT installation in the full EV: a) and b) real system, c) full EV chassis developed in CAD 3D and c) 3D ICT structure with simplified chassis and the desired points to test the  $|B|$  levels

**IV.5.a. NTC-NTC Prototype (Test Bench V2 (EV))**

TABLE XII: VALIDATION TEST PARAMETERS FOR NTC-NTC IPT PROTOTYPE BENCH V2

Parameter	Simulated	Measured	Parameter	Simulated	Measured
$U_i(DC)$	262 V	262 V	$i_1$	17.98 A	17.5 A
$I_i(DC)$	11.5 A	11.24 A	$i_2$	15 A	12.5 A
$f_s$	30.1 kHz	30.1 kHz	$V_{C1}$	1250 V	1157 V
$L_1$	380 $\mu$ H	375 $\mu$ H	$V_{C2}$	1073 V	826 V
$L_2$	373 $\mu$ H	370 $\mu$ H	$U_o(DC)$	300 V	300 V
$M$	115 $\mu$ H	122.5 $\mu$ H	$I_o(DC)$	9.55 A	8.9 A
$k$	0,31	0,33	$P_o$	2865 W	2670 W
$C_1$	76 nF	80 nF	$\eta$	0.95	0.906
$C_2$	78 nF	80 nF			

TABLE XIII:  $|B|$  LEVELS VALUES FOR NTC-NTC TEST BENCH V2

Point	Simulated	Measured
<i>O</i>	10.7 $\mu\text{T}$	8.4 $\mu\text{T}$
<i>D</i>	0.26 $\mu\text{T}$	0.33 $\mu\text{T}$
<i>I</i>	6.4 $\mu\text{T}$	3.6 $\mu\text{T}$
<i>K</i>	7.7 $\mu\text{T}$	7.5 $\mu\text{T}$
<i>J</i>	4.8 $\mu\text{T}$	3.16 $\mu\text{T}$

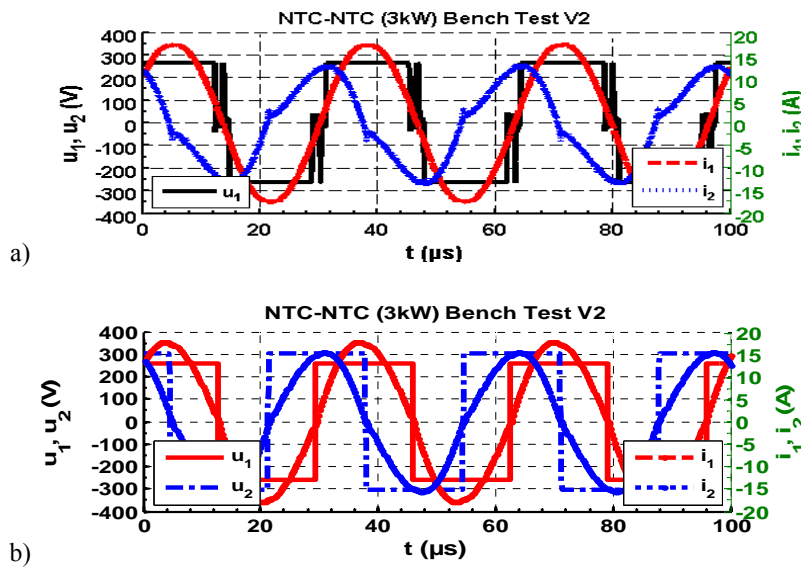


Fig. IV.11: Plots of  $u_1$ ,  $i_1$  and  $i_2$  for NTC-NTC Bench V2: a) experimental test measurements and b) simulation results

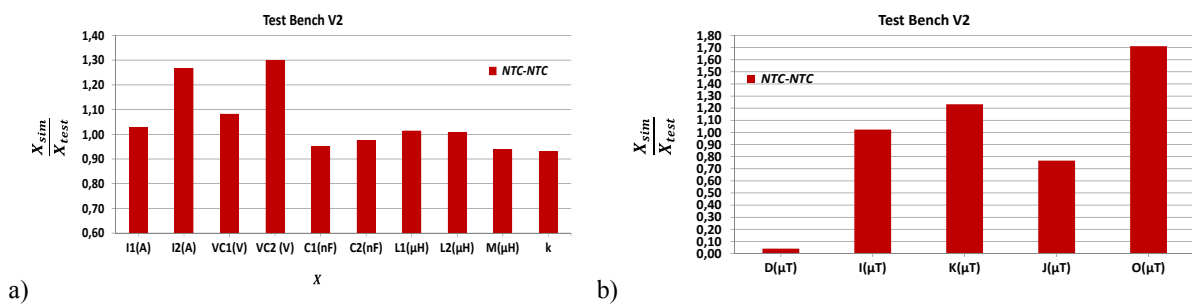


Fig. IV.12: Comparison between simulation and test values for NTC-NTC prototype of bench test V2: a) electrical parameters and b)  $|B|$  levels values

The current in Fig. IV.11 is nearly sinusoidal with very little higher harmonics content which validates the first harmonics approach and frequency domain simulations at the resonant global frequency. The same figure also includes the simulation results.

The behavior of the 4 antiparallel diodes that are connected to each inverter power switch appears in Fig. IV.11. Because of their conduction periods during the transitions of the inverter legs switches, they give a path for the current to flow toward the load.

**IV.5.b. NTC-RNO Prototype (Test Bench V2 (EV))**

TABLE XIV: VALIDATION TEST PARAMETERS FOR NTC-RNO IPT PROTOTYPE BENCH V2

Parameter	Simulated	Measured	Parameter	Simulated	Measured
$U_i(DC)$	300 V	300 V	$i_1$	19 A	16.42 A
$I_i(DC)$	10.6 A	10 A	$i_2$	17.8 A	13.65 A
$f_s$	29.05 kHz	29.05 kHz	$V_{C1}$	991 V	857 V
$L_1$	380 $\mu$ H	375 $\mu$ H	$V_{C2}$	929 V	712 V
$L_2$	280 $\mu$ H	310 $\mu$ H	$U_0(DC)$	300 V	300 V
$M$	125 $\mu$ H	130 $\mu$ H	$I_0(DC)$	9.36 A	8.68 A
$k$	0,38	0,38	$P_0$	2808W	2604 W
$C_1$	78 nF	80 nF	$\eta$	0.883	0.868
$C_2$	110 nF	92 nF			

TABLE XV:  $|B|$  LEVELS VALUES FOR NTC-RNO TEST BENCH V2

Point	Simulated	Measured
$O$	8.8 $\mu$ T	8 $\mu$ T
$D$	0.2 $\mu$ T	0.4 $\mu$ T
$I$	5 $\mu$ T	4.5 $\mu$ T
$K$	6.11 $\mu$ T	5.25
$J$	4.1 $\mu$ T	4.8 $\mu$ T

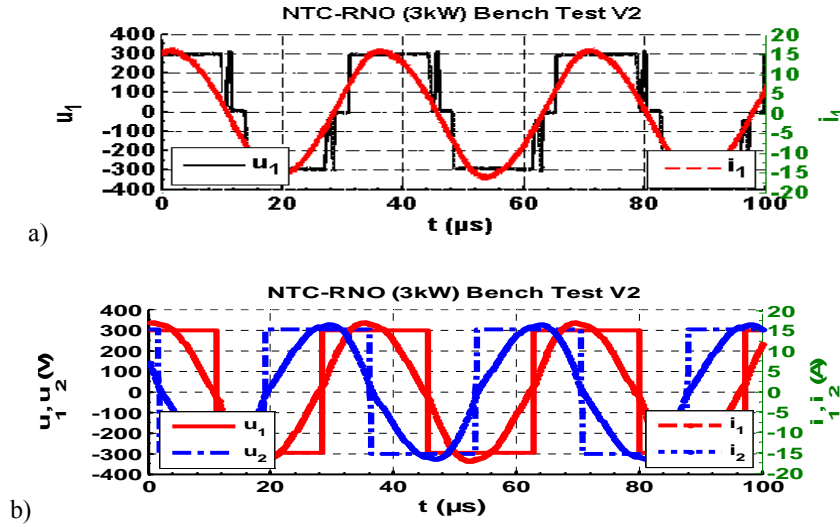


Fig. IV.13: Plots of  $u_1$  and  $i_1$  for NTC-RNO Bench V2: a) experimental test measurements and b) simulation results

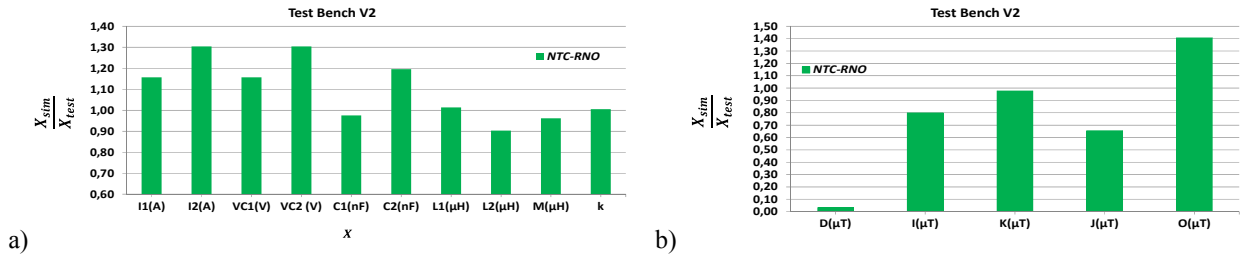


Fig. IV.14: Comparison between simulation and test values for NTC-RNO prototype of bench test V2: a) electrical parameters and b)  $|B|$  levels values

#### IV.5.c. SE-NTC Prototype (Test Bench V2 (EV))

TABLE XVI: VALIDATION TEST PARAMETERS FOR SE-NTC IPT PROTOTYPE BENCH V2

Parameter	Simulated	Measured	Parameter	Simulated	Measured
$U_i(DC)$	333 V	333 V	$i_1$	14.6 A	15 A
$I_i(DC)$	9.35 A	9.66 A	$i_2$	16 A	15.7 A
$f_s$	29.2 kHz	29.2 kHz	$V_{C1}$	758 V	779 V
$L_1$	550 $\mu$ H	593 $\mu$ H	$V_{C2}$	830 V	815 V
$L_2$	385 $\mu$ H	395 $\mu$ H	$U_0(DC)$	300 V	300 V
$M$	145 $\mu$ H	154 $\mu$ H	$I_0(DC)$	9.54 A	9.33 A
$k$	0,317	0,318	$P_0$	2862 W	2800 W
$C_1$	55 nF	48.4 nF	$\eta_1$	0.92	0.867
$C_2$	80 nF	80 nF			

TABLE XVII:  $|B|$  LEVELS VALUES FOR SE-NTC TEST BENCH V2

Point	Simulated	Measured
<i>O</i>	9.15 $\mu\text{T}$	9.5 $\mu\text{T}$
<i>D</i>	0.25 $\mu\text{T}$	0.6 $\mu\text{T}$
<i>I</i>	6.3 $\mu\text{T}$	6.7 $\mu\text{T}$
<i>K</i>	7.4 $\mu\text{T}$	9.8 $\mu\text{T}$
<i>J</i>	5 $\mu\text{T}$	4.6 $\mu\text{T}$

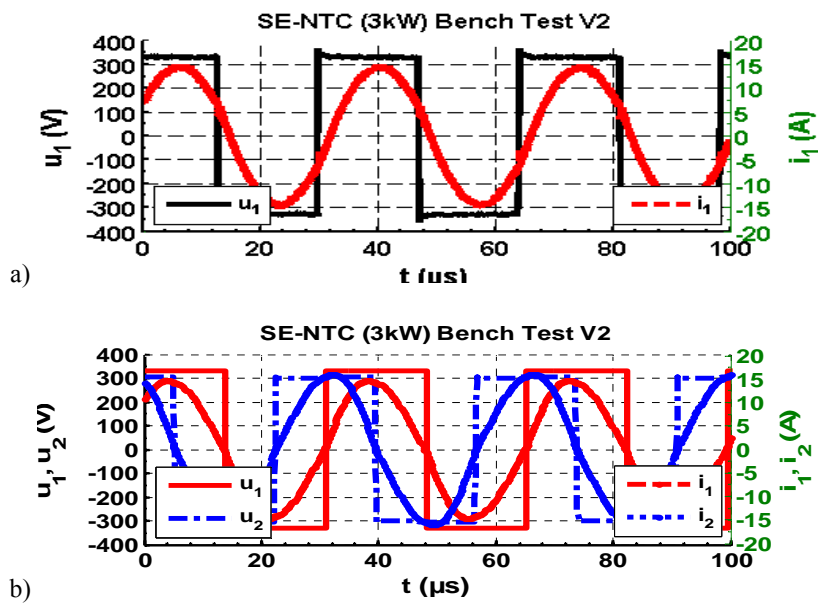


Fig. IV.15: Plots of  $u_1$  and  $i_1$  for SE-NTC Bench V2: a) experimental test measurements and b) simulation results.

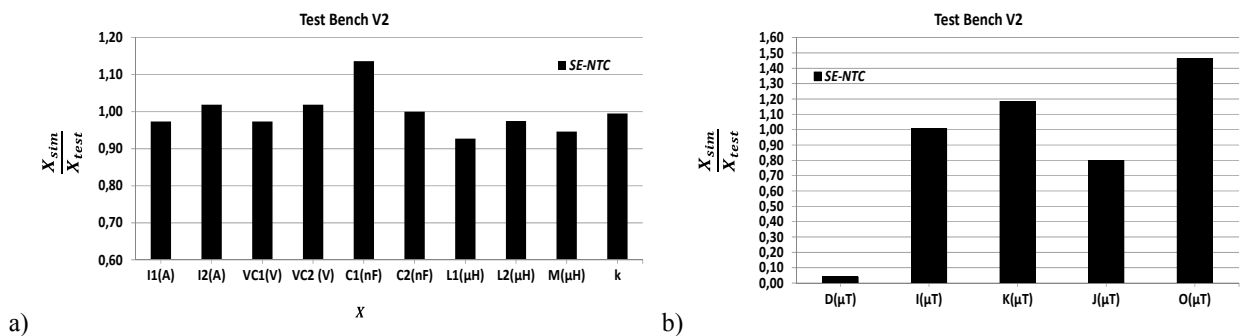


Fig. IV.16: Comparison between simulation and test values for SE-NTC prototype of bench test V2: a) electrical parameters and b)  $|B|$  levels values

### ***IV.6. Comparison between Different Prototypes for Test Bench V2***

#### A) Comparison between simulation and manipulation results:

The previous figures (Fig. IV.11-Fig. IV.16) that considered the comparison results show a good correlation between the simulation and the tests results. In fact, as stated before, errors in simulations results with respect to the tests may come from working at same practical tests resonant frequencies and input voltage. Also the values of the self and mutual inductances are different because using of simplified chassis. So the impedances will differ and also the currents and voltages in the circuits. The same conclusion is drawn for the values of  $|B|$  levels.

#### B) Comparison between Manipulations Results:

Comparisons between practical test results are established. It should be noted that the output power and voltage gains are not equal for all tests. The normalized values of  $|B|$  levels are shown in Fig. IV.17. The following can be stated:

- Point *O*: all prototypes are above the norm for general public ICNIRP 1998 ( $6.25 \mu\text{T}$ ). It is due to the positions of the ICT pads that are close to the backend of the EV unlike the test bench V1. However they respect the occupational one ( $24 \mu\text{T}$ ), ( $\frac{Occupat.Norm}{Public.Norm} = \frac{27 \mu\text{T}}{6.25 \mu\text{T}} = 4.32$ ).
- Point *K*: the same remarks are correct except for NTC-RNO prototype. This is because the RNO pad has the smallest ferrite size.
- All other points respect the general public ICNIRP 1998 ( $6.25 \mu\text{T}$ ).

Furthermore, for the results of practical tests, the electrical parameters values are normalized to NTC-NTC prototype values and traced in Fig. IV.18. It can be said that, for a reference prototype NTC-NTC, the largest differences will appear if the primary pad is changed as for the configuration SE-NTC. However, in the contrary of Chapter II for discussing the coupling factor behaviors of the interoperable prototypes, the relative coupling factor for NTC-RNO is increased here. This may be caused by the relative positions of the pads with respect to the chassis (middle or backend).



Finally, the normalized tests resonant frequency to 30 kHz, and the total test efficiency are shown in Fig. IV.19. It illustrates that the position of the normalized resonant frequencies are close to 1 (or 30 kHz) as the benefits of using the SS self compensation (as stated in Chapter III). The different tests show good efficiencies (86% - 90%), which implies the feasibility for using the inductive charging as a solution to supply the EV battery.

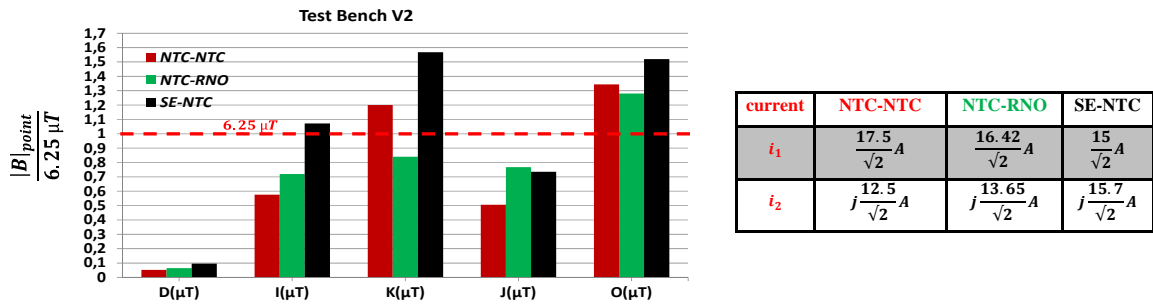


Fig. IV.17: Comparison between tests of normalized  $|B|$  values for different prototypes of bench test V2

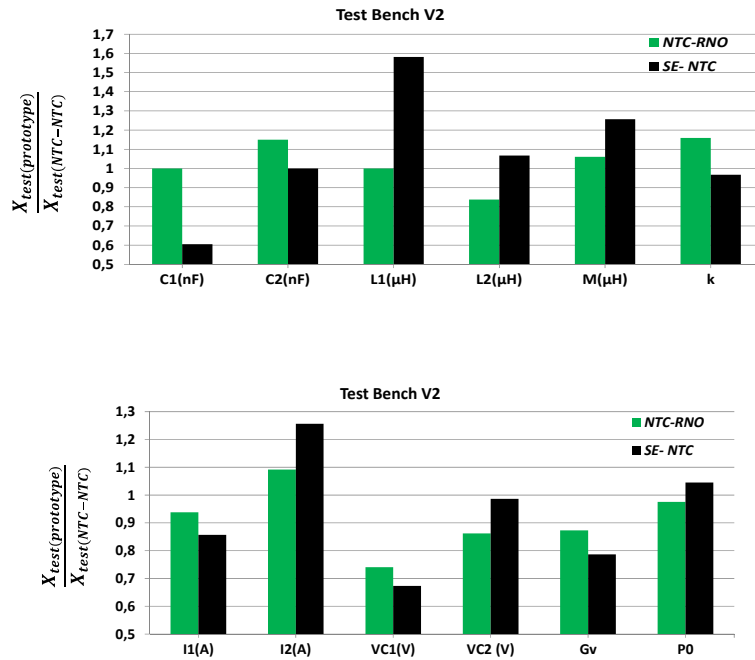


Fig. IV.18: Normalized electrical parameters of the different prototypes tests bench V2 results to NTC-NTC prototype (practical results)

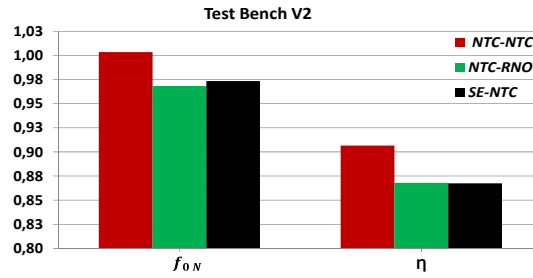


Fig. IV.19: Overall resonant frequency and efficiency for the practical results of test bench V2

In fact, the validation for the electrical field  $E$  is missing in all previous researches for EV inductive charging. The general standards for ICNIRP 1998 [59] stated that there is a limitation for human exposition to the general public  $E$  field of a value  $|E| = 87 V/m$ . For that reason, the last prototype test (SE-NTC) included two measurements points for  $|E|$ : 1 m and 0.5 m from the backend of EV. The results of measurements are plotted in Fig. IV.20 using a NARDA EHP 200 tester [72].

The two points are under the norm but with more risks for the second point (0.5 m). And if the point is get nearer to EV backend, the value will pass the norm due to the high voltage drop across the coils of the ICT power pads. Moreover, because of the permittivity of human tissues, the electric field may concentrates near the body. Future investigations should consider the norm of  $E$ .

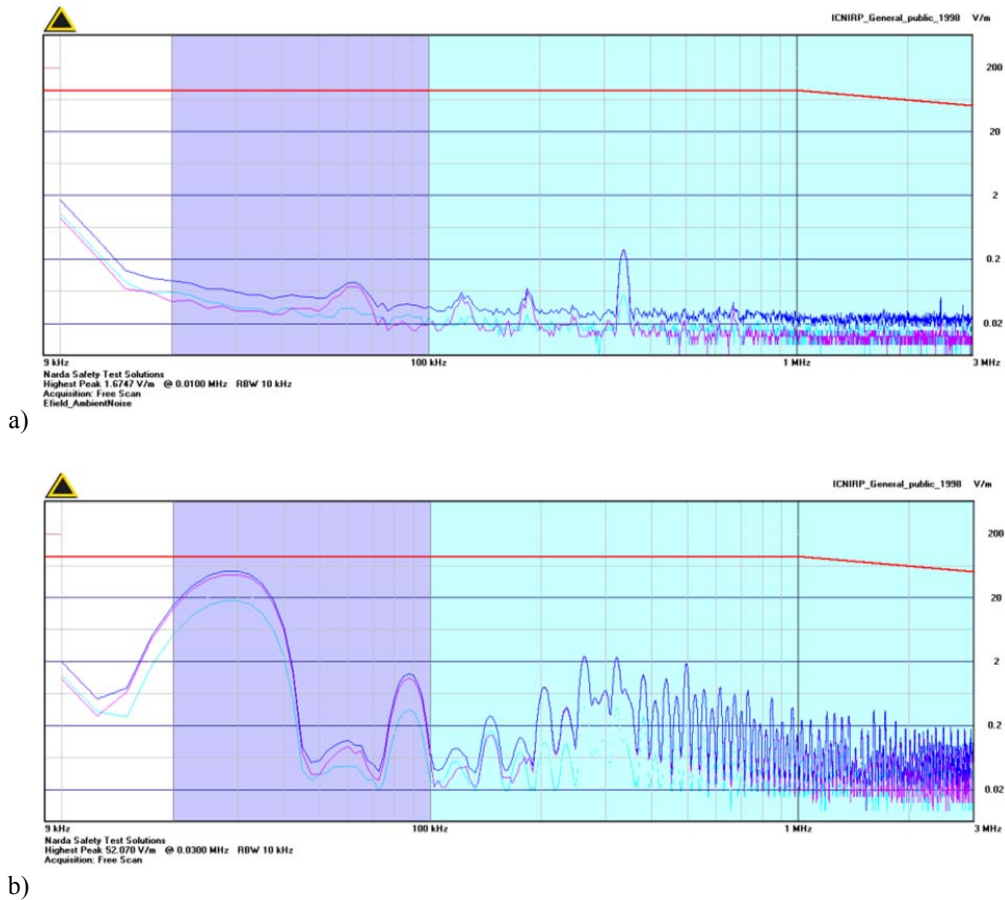


Fig. IV.20: Spectrum of electrical field intensity using NARDA EHP 200 for two points : a) 1 m and b) 0.5 m far from ICT power pads of SE-NTC test bench V2. The ICNIRP 1998  $E$  norm is 87 V/m

### IV.7. Conclusion

This chapter deals with the validations tests equipment's for the interoperability resonant IPT prototypes. Comparisons are made to the tests results to check the validity simulations results. The comparisons based on: electrical parameters values and the values of  $|B|$  levels.

Two test benches were installed, a part of an EV chassis taken from its middle where the ICT is fixed in the center of the chassis. The other one is in the EV of KANGOO RENAULT, where the ICT is installed in the backend.

The investigations about the validity of the simulations results from circuit analysis and EM modelling to the realistic manipulations results show good matching between them. However some

errors are found in the simulations results. The practical test showed a high efficiency for such type of charging.

Moreover, it is drawn that the position of the ICT pads with respect to the EV chassis (middle or backend) has an impact on the coupling factor for interoperability configurations. For the prototypes installed in the middle of EV, it is shown that for wider secondary systems the coupling factor is higher whereas the inverse trend is observed when the prototype is installed at the backend of the EV (smaller size of secondary system correspond to an increased coupling factor) as shown in Fig. IV.21.

The respect of the tests magnetic radiation measurements at points in the EV and the near environment are checked to meet the ICNIRP 1998 standard public norm to human exposition. Some points are above the norms but under the occupational standard norm.

Finally, future investigations should consider the norm of the electrical field  $E$  compliance. It was shown that the points near the ICT power pads won't respect the standard norm. This result is drawn from a practical test. It will be necessary to study the electrical field theoretically and then be compared to the manipulation tests.

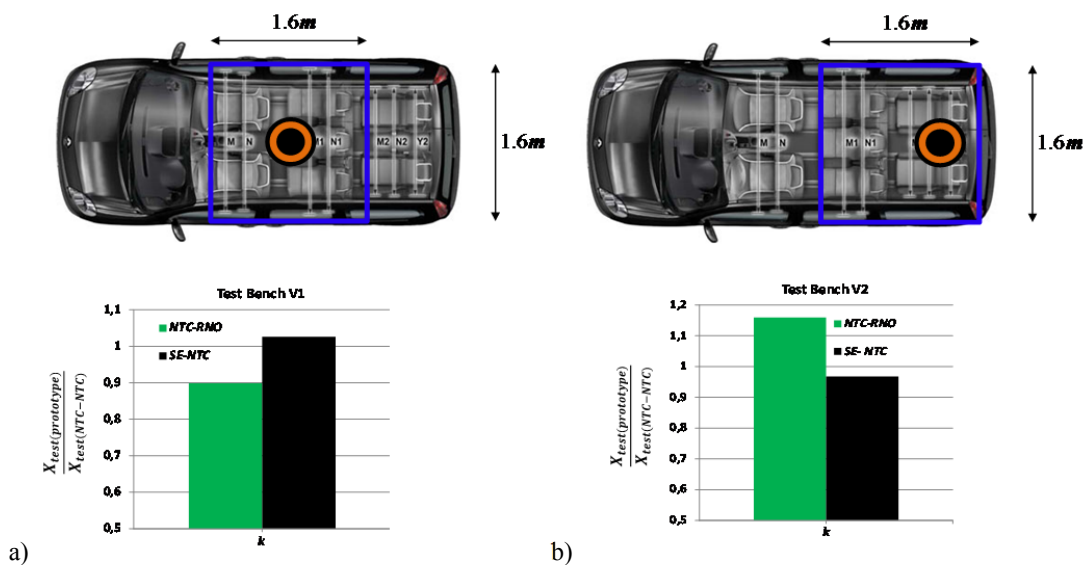


Fig. IV.21: Effect of ICT interoperable prototypes position installation to EV on the coupling factor with respect to a reference prototype



## *General Conclusion & Perspectives*

The work presented in this thesis memory was linked to the CINELI project that includes collaboration with three industrial partners: Renault, Schneider Electric and NewTech Concept. The main objective of this project is to develop a standard for interoperability between different systems of contactless EV battery static charging by inductive coupling.

To understand the IPT systems, this manuscript studied different ICT systems that were built by different structures/infrastructures (and belong to different industrial companies) using advanced modeling. The work highlighted the influence of the EV chassis and the system positioning parameters. The chassis greatly affects the EMF radiation, and together with the axis shift (flexibility for the driver for parking) and the air gap (relevant to the EV load), they have a significant influence on the self and mutual inductances. The asymmetries of the ICT combined with changes in the positioning imply different resonances at the primary and secondary sides.

As a goal to deliver the maximum power from the source to the battery load, resonant capacitors in both sides of the IPT system are used. Three different resonant topologies that are widely used in the literature were investigated and analyzed through an analytical model based on the first harmonic approximation. A comparison was established regarding many parameters: the positions of the global resonant frequencies with respect to 30 kHz (CINELI design frequency), the voltage gain and the stresses on the resonant elements at these global frequencies. The choice to use the series-series self inductances compensation topology was made to meet the needs of the industrial partners.

Circuit simulations were performed using a resistive load that modeled the battery and a battery model (internal resistance in series with an electromotive force). The results showed that the last one is closer to a realistic situation for IPT systems. A frequency regulation is an essential issue in this kind of charging to control the inverter frequency to operate at the resonance. So the maximum possible power is delivered to the load and the VA ratings of the input supply is minimized. This regulation was developed thanks to MPPT algorithm implemented in MATLAB/Simulink to achieve a power factor near to zero and also that the active power is transferred to the battery.

The proposed designs were tested on an EV (KANGOO RENAULT) using two different experimental setups in order to validate the modeling and simulations. The first one included a

part of EV chassis (taken from the middle of EV) for 2 kW power transmission supplying a 300V battery. The second one shown was for the ICT's installed in the backend of whole EV for a 3 kW and 300V battery.

Investigations were done for the electrical parameters and values of magnetic induction defined in the EV and nearby environment. Two groups of comparisons between the simulation and practical tests results were defined: validity of simulations results with respect to the practical ones, and practical tests with respect to a reference one.

The results of the two last comparisons showed a good coherence between the results of simulations and manipulations. However simulations errors relatives to practical tests appeared due to many reasons: considering a simplified EV chassis in EM modelling (difficulty to consider all EV body in the available computer due to model complexity), testing tools and the precisions of measurements.

Finally, from the results of the practical tests, the conclusions are drawn for the possibility use of the interoperability for wireless charging by different inductive loops: it will be reliable to supply the EV battery as the tests mentioned efficiencies of 86-90%, and for the important issue in this work, is the safety of humane exposure to EMF radiation standard norm ICNIRP 1998.

Some perspectives and future works may be interesting in the goal of such interoperable IPT systems, they are listed in following:

- Investigations about the coils, the ferrites and chassis losses (considering its magnetic characteristics if it is possible) to be added in the EM modelling. Moreover the thermal analysis could be also studied in the modelling. Also a plan for the energy efficiency including switching losses could be performed to evaluate more accurately the overall efficiency.
- Adding the conducted EMC for the whole circuit. The internal and different coupling parasitic capacitors can be calculated by an electrostatic study based on electromagnetic tools, and then integrated with stray capacitances that are coupled with ground from power switches. Such whole system simulation could be performed in MATLAB/Simulink.



- Including the passengers and/or any object in the EV and/or around it in the nearby environment for the computation of the radiated fields and the study of safety compliance.
- Using other types of magnetic coupling loops. Propositions to use solenoids and DD architectures power pads were developed by [73] and [74] respectively and such ideas could be integrated in the interoperability study as shown recently in [75], [76], [77].
- Furthermore, the different resonant topologies could be compared in the framework of interoperability. This will give more solutions to show their behaviors with the interoperable IPTs and other conclusions may appear.
- Design for a power loop control in the whole system.
- Last but not least, using new architectures for the input power stages. A study to use series/parallel multilevel converter will give the opportunity to increase the power transmission with multiple coils. The parallel architecture proposed by [78] showed an optimization of the power electronics stages and input currents equally divided by the number of parallel modules. So as a result less element stresses and less radiation. However, this solution will add complexity in the design and a larger volume.

## *References*

## References

---

- [1] Olivier CAYOL, Report avancement de projet Cineli, Paris, 2013.
- [2] Movéo, Poster Cineli (2012).
- [3] Y. Matsuda, H. Sakamoto, H. Shibuya, and S. Murata Sojo, “A non-contact energy transferring system for an electric vehicle-charging system based on recycled products,” *Journal of Applied Physics* 99, 08R902 2006.
- [4] M. Budhia, G.A. Covic, J.T. Boys, and C.Y. Huang, “Development and evaluation of single sided flux couplers for contactless electric vehicle charging”, in *Proc. IEEE Energy Conv. Cong*, pp. 614- 621, 2011.
- [5] K. W. Klontzl A. Esse, P. J. Wolfs, and D. M. Divan, “Converter Selection for Electric Vehicle Charger Systems with a High-Frequency High-Power Link,” in *Rec. IEEE Power Electron. Spec Conf. (PESC)*, pp. 855-861, 1993.
- [6] A. J. Moradewicz and M. P. Kazmierkowski, “Contactless energy transfer system with FPGA-controlled resonant converter,” *IEEE Trans. Ind. Electron.*, vol. 57, no. 9, pp. 3181–3190, Sep. 2010.
- [7] N. Chawla and S. Tosunoglo, “State of the Art in Inductive Charging for Electronic,” in *2012 Florida Conference on Recent Advances in Robotics*, 2012.
- [8] Joshua Le-Wei Li, “Wireless Power Transmission: State-of-the-Arts in Technologies,” in *Proceedings of the Asia-Pacific Microwave Conference 2011*.
- [9] C. S. Wang, O. H. Stielau, and G. A. Covic, “Design consideration for a contactless electric vehicle battery charger,” *IEEE Trans. Ind. Electron.*, vol. 52, No. 5, pp. 1308–1313, Oct. 2005.
- [10] A. Neves, D. M. Sousa, A. Roque and J. M. Terras, “Analysis of an inductive charging system for a commercial electric vehicle,” *Power Electronics and Applications (EPE 2011)*, pp.1-10, Sep. 2011.

## References

---

- [11] P. Si, A. P. Hu, J. W. Hsu, M. Chiang, Y. Wang, S. Malpas and D. Budgett, "Wireless power supply for implantable biomedical device based on primary input voltage regulation," in Proc. 2nd IEEE Conf. Industrial Electron., pp. 235-239, May 2007.
- [12] S.Y.R. Hui and W.W.C Ho, "A new generation of universal contactless battery charging platform for portable Consumer Electronic equipment," IEEE Trans. Power Electronics, vol. 20, pp. 620-627, May. 2005.
- [13] S. Brehaut and F. Costa, "Gate driving of high power IGBT by wireless transmission," International Power Electronics Motion Control, 2006, 5th IEEE IPEMC 2006. conference record of the 2006 IEEE, pp. 1-5, vol.1, Shanghai, china, Aug. 2006.
- [14] O. Lucia, L. A. Barragan, J. M. Burdio, O. Jiménez, and D. Navarro, "A versatile power electronics test-bench architecture applied to domestic induction heating," IEEE Trans. on Industrial Electronics, vol. 58, no. 3, pp. 998-1007, 2011.
- [15] M. Budhia, G.A. Covic and J.T. Boys, "Design and optimization of circular magnetic structures for lumped inductive power transfer systems," IEEE Trans. Power Electronics, vol. 26, No. 11, pp 1115-1123, Nov. 2011.
- [16] S. Valtchev, B. Borges, K. Brandisky, and J. Ben Klaassens, "Resonant Contactless Energy Transfer With Improved Efficiency," IEEE Trans. on Power Electronics, vol. 24, No. 3, pp. 685-699, Mar. 2009.
- [17] Y. P. Su, L. Xun, and S. Y. R. Hui, "Mutual inductance calculation of movable planar coils on parallel surfaces", in Power Electronics Specialists Conference , vol. 24, pp. 3475-3481, June 2008.
- [18] J. Acero, C. Carretero, I. Lope, R. Alonso, O. Lucia, and J.M. Burdio, "Analysis of the Mutual Inductance of Planar-Lumped Inductive Power Transfer Systems," IEEE Trans. Industrial Electronics, vol. 60, pp. 1-11, Jul. 2011.

## References

---

- [19] O. C. Onar, J. M. Miller, S. L. Campbell, C. Coomer, C. P. White and L. E. Seiber, "A Novel Wireless Power Transfer for In-Motion EV/PHEV Charging," IEEE 28th Power Electronics Conf. and Expos. APEC'2013, pp. 3073 - 3080, Long Beach, CA, Mar. 2013.
- [20] C. Yu, R. Lu, Y. Mao, L. Ren, and C. Zhu, "Research on the Model of Magnetic-Resonance Based Wireless Energy Transfer System," in Proc. IEEE2009 Vehicle Power and Propulsion Conference, Dearborn, MI, 7-10 Sep. 2009.
- [21] Bernard Multon, "Modèles électriques du transformateur électromagnétique," Antenne de Bretagne de l'École Normale Supérieure de Cachan, 1997.
- [22] Dragan Maksimovic, Robert W. Erickson, and Carl Griesbach, "Modeling of Cross-Regulation in Converters Containing Coupled Inductors," IEEE Trans. Power Electronics, vol. 15, No. 4, pp. 605-617, Jul. 2000.
- [23] R.W. Erickson and D. Maksimovic, Fundamentals of Power Electronics, 2<sup>nd</sup> ED., Kluwer Academic Publisher, 2004.
- [24] R. Laouamer, M. Brunello, J. P. Ferrieux, O. Normand, and N. Buchheit, "A multi-resonant converter for non-contact charging with electromagnetic coupling," in Proc. 23rd Int. Conf. Ind. Electron. Control Instrum., 1997, vol. 2, pp. 792-797.
- [25] A.P. Sample, D.A. Meyer and J.R. Smith, "Analysis, experimental results, and range adaptation of magnetically coupled resonators for wireless power transfer," IEEE Trans. Industrial Electronics, vol. 58, No. 2, pp. 544-554, Feb. 2011.
- [26] S. Cheon, Y.-H. Kim, S.-Y. Kang, M.L. Lee, J.-M. Lee, and T. Zyung, "Circuit-model-based analysis of a wireless energy-transfer system via coupled magnetic resonances," IEEE Trans. Industrial Electronics, vol. 58, No. 7, pp. 2906-2914, July 2011.
- [27] R. Bosshard, J. Muehlethaler, J. W. Kolar, and I. Stevanovic, "Optimized magnetic design for inductive power transfer coils," in Applied Power Electronics Conference, 2013.

## References

---

- [28] J.T. Boys, A.P. Hu and G.A. Covic, “Critical Q analysis of a current-fed resonant converter for ICPT applications,” *Electronics Letters*, vol. 36, No. 17, pp. 1140-1142, Aug. 2000.
- [29] R. Laouamer, Thèse de l’Institut National Polytechnique de Grenoble – INPG 1998, “Chargeur de Batteries à Couplage Inductif pour Véhicule Electrique,” G2ELAB, Grenoble, France.
- [30] T.C.Y. Ho, B. Gomersall and R. Li, “Contactless Charging for Electric Vehicles with a Large Air Gap,” *IEEE Power Electronics and Applications Conference EPE’11*, Birmingham, UK Aug. 2011.
- [31] A. Ecklebe, and A. Lindemann, “Analysis and Design of a Contactless Energy Transmission System with Flexible Inductor Positioning for Automated Guided Vehicles,” *IEEE 32nd Conf. Industrial Electron. IECON’2006*, pp. 1721–1726, Paris, France, Nov. 2006.
- [32] H. H. Wu, A. Gilchrist, K. D. Sealy, and D. Bronson, “A high efficiency 5 kW inductive charger for EVs using dual side control,” *IEEE Trans. Ind. Inf.*, vol. 8, no. 3, pp. 585–595, Aug. 2012.
- [33] R. Bosshard, U. Badstübner, J. W. Kolar, and I. Stevanovic, “Comparative evaluation of control methods for inductive power transfer,” in *Proc. of the 1st International Conference on Renewable Energy Research and Applications (ICRERA)*, 2012.
- [34] R. Bosshard, J. Mühlethaler, J. W. Kolar, and I. Stevanovic, “The  $\eta - \alpha$  Pareto front of inductive power transfer coils,” in *Proc. of the 38th IEEE Industrial Electronics Conference (IECON)*, 2012.
- [35patent] Brevet: Inventeurs: Patric Camaruti et Henri Bondar. Numéro de demande internationale: PCT/FR2006/000614 Numéro de publication internationale: WO 2007/107642 A1. Date de dépôt international: 21 mars 2006 (21.03.2006). Titre: Dispositif de transport de l’énergie par influence partielle à travers un milieu diélectrique.

## References

---

- [36] M. Hanazawa and T. Ohira “Power Transfer for Running Automobiles” 2011 IEEE MTT-S International Microwave Workshop Series on Innovative Wireless Power Transmission: Technologies System and Application, pp. 77-80, 2011.
- [37] R. El Chami and S. Loudot, “Charge sans contact de véhicule électrique avec couplage par champs électrique”, RENAULT, Oct. 2012.
- [38] Murata Manufacturing, “Wireless Power Transmission Modules”, site web [www.murata.com](http://www.murata.com).
- [39] K. Piiipponen, R. Sepponen, and P. Eskelinen, “A biosignal instrumentation system using capacitive coupling for power and signal isolation,” IEEE Trans. on Biomedical Engineering, vol. 54, no. 10, pp. 1822–1828, Oct. 2007.
- [40] J. Sallán, J. L. Villa, A. Llombart, and J. Fco. Sanz, “Optimal design of ICPT systems applied to electric vehicle battery charge,” IEEE Trans. Ind. Electron., vol. 56, No. 6, pp. 2140 – 2149, Jun 2009.
- [41] C.-S. Wang, G. A. Covic, and O. H. Stielau, “Power transfer capability and bifurcation phenomena of loosely coupled inductive power transfer systems,” IEEE Trans. Ind. Electron., vol. 51, no. 1, pp. 148–157, Feb. 2004.
- [42] X. Fang, H. Hu, Z. John Shen, and I. Batarseh, “Operation mode analysis and peak gain approximation of the LLC resonant converter,” IEEE Trans. on Power Electronics, vol. 27, No. 4, pp. 1985-1995, Apr. 2012.
- [43] J.P. Ferrieux, F. Forest, “Alimentations à découpage, convertisseur à résonance”, Dunod, 2006.
- [44] S. Lacroix, Thèse de l’Université Paris Sud 2013, “Modélisation et commande d’une chaîne de conversion pour véhicule électrique intégrant la fonction de charge des batteries”, LGEP, Paris, France.

## References

---

- [45] K. Young, C. Wang, Le Yi Wang, and K. Strunz, “Chapter 2: Electric Vehicle Battery Technologies”, from the book “Electric Vehicle Integration into Modern Power Networks”, Springer, 2012. [<http://pdf.investingx.net/c/chapter-2-electric-vehicle-battery-technologies-w2638/>].
- [46] MIT Electric Vehicle Team, “A Guide to Understanding Battery Specifications”, December 2008.
- [47] TEXAS Instrumentation, “SNVA533: Characteristics of Rechargeable Batteries”, [<http://www.ti.com>].
- [48] Hongwen He , Rui Xiong and Jinxin Fan, “Evaluation of Lithium-Ion Battery Equivalent Circuit Models for State of Charge Estimation by an Experimental Approach”, Energies Journal, ISSN: 1996-1073, Mar. 2011.
- [49] Nathan IDA, Joao P.A. BASTOS, “Electromagnetics and Calculation of Fields”, 2<sup>nd</sup> edition, Springer, 1997.
- [50] E. Goenaga, Thèses Institut National Polytechnique de Grenoble – INPG 2013 “Conception d'alimentations de puissance d'actionneurs piézo-électriques, avec et sans contact électrique, pour la génération des vibrations mécaniques”, G2ELAB, Grenoble, France.
- [51] D. Kürschner and C. Rathge, “Contactless energy transmission systems with improved coil positioning flexibility for high power applications,” IEEE Power Electronics Specialists Conference, pp. 4326–4332, Greece, Jun. 2008.
- [52] Provision of Evaluation, Impact Assessment and Related Services to the Commission in the Areas of Public Health, Consumer Protection and Food Chain Specific Evaluation of the Health Reported by “Public Health Evaluation and Impact Assessment Consortium” (PHEIAC), 09th August 2011.
- [53] [http://www.arpansa.gov.au/radiationprotection/basics/ion\\_nonion.cfm](http://www.arpansa.gov.au/radiationprotection/basics/ion_nonion.cfm).



## References

---

- [54] D. Hui, Z. Yisheng and Z. Baishan, “Research on the Electromagnetic Radiation of A PCB Planar Inductor”, IEEE Trans., vol. 1, Microwave Conference Proceedings, APMC 2005.
- [55] X. Liu and S. Y. R. Hui, “Optimal design of a hybrid winding structure for planar contactless battery charging platform,” IEEE Trans. Power Electron., vol. 23, no. 1, pp. 455–463, Jan. 2008.
- [56] P. Si, A. P. Hu, S. Malpas, and D. Budgett, “A frequency control method for regulating wireless power to implantable devices,” IEEE Trans. Biomed. Circuits Syst., vol. 2, no. 1, pp. 22–29, Mar. 2008.
- [57] T. D. Dissanayake, A. P. Hu, S. Malpas, L. Bennet, A. Tab, L. Booth, and D. Budgett, “Experimental Study of a TET System for Implantable Biomedical Devices,” IEEE Transactions on Biomedical Circuits and Systems, vol. 3, no. 6, pp. 370–378, Dec. 2009.
- [58] International Commission on Non-Ionizing Radiation Protection, [ICNIRP] "Guidelines for limiting exposure to time-varying electric, magnetic, and electromagnetic fields", Health Physics, vol. 74, No. 4, Apr 1998.
- [59] International Commission on Non-Ionizing Radiation Protection, [ICNIRP] "Guidelines for limiting exposure to time-varying electric, magnetic, and electromagnetic fields", Health Physics, vol. 99, No.6, pp. 818–836, Jun 2010.
- [60] [www.comsol.com](http://www.comsol.com)
- [61] J.T. Boys, G.A. Covic and A.W. Green, “Stability and control of inductively coupled power transfer systems”, IEE Proc. Electr. Power Appl., 2000, 147, (1), pp. 37–43.
- [62] S. Bouissou, Thèse de doctorat, Université Paris VI, 1994. “Comparaison des formulations en potentiel, pour la résolution numérique en 3D des équations magnétiques couplées aux équations de circuit électrique”, LGEP, Paris, France.
- [63] S. Seely and A. D. Poularikas, “Electromagnetics: Classical and modern theory and applications/8” (Electrical engineering and electronics), Marcel Dekker Publisher, NY, 1979.

## References

---

- [64] J.R. Sibué, J.P. Ferrieux, G. Meunier and R. Periot, “Convertisseurs à Double Résonance pour l’Alimentation de Transformateurs Faiblement Couplés”, EPF2010, Saint-Nazaire, France, 2010.
- [65] U. K. Madawala and D. J. Thrimawithana, “A bidirectional inductive power interface for electric vehicles in V2G systems,” IEEE Trans. Ind. Electron., vol. 58, no. 10, pp. 4789–4896, Oct. 2011.
- [66] M. Jufer and P. Germano, “Contactless power transmission: Frequency tuning by a maximum power tracking method,” in 7th Eur. Conf. Power Electronics and Applications, vol. IV, Trondheim, Norway, Sept. 8–10, 1997, pp. 693–697.
- [67] V. J. Brusamarello, Y. B. Blauth, R. Azambuja, I. Muller, and F. R. de Sousa, “Power Transfer with an Inductive Link and Wireless Tuning,” IEEE Trans. Instrum. Meas., vol. 62, no. 5, pp. 924–931, May 2013.
- [68] M.A.G. de Brito, L.P. Sampaio, G. Luigi, G.A. e Melo and C.A. Canesin, “Comparative analysis of MPPT techniques for PV applications,” International Conference on Clean Electrical Power, ICCEP 2011, pp.99-104.
- [69] A.F Murtaza, H. A. Sher, M. Chiaberge, D. Boero, M. De Giuseppe and K. E Addoweesh, “Comparative analysis of maximum power point tracking techniques for PV applications,” International Conference on Multi Topic, INMIC 2013, pp.83-88.
- [70] Copyright (c) 2012, Truong Nguyen Xuan, All rights reserved, “Solar and MPPT,” [Online] available: <http://www.mathworks.com/matlabcentral/fileexchange/35736-solar-and-mppt>.
- [71] Magnetic Field HiTester 3470 HIOKI, [Online] available: <http://www.hioki.com/discon/pdf/enviro/3470E4-18B.pdf>.
- [72] NARDA EHP 200 Electrical and Magnetic fields tester [Online] available: [http://www.narda-sts.us/pdf\\_files/DataSheets/EHP200\\_DataSheet.pdf](http://www.narda-sts.us/pdf_files/DataSheets/EHP200_DataSheet.pdf).

## References

---

- [73] Y. Nagatsuka, S. Noguchi, Y. Kaneko, S. Abe, T. Yasuda, K. Ida, A. Suzuki and R. Yamanouchi, "Contactless Power Transfer System for Electric Vehicle Battery Charger," The 25th World Battery, Hybrid and Fuel Cell Electric Vehicle Symposium & Exhibition, China, Nov. 5-9, 2010.
- [74] M. Budhia, J. T. Boys, G. A. Covic and C.Y. Huang, "Development of a single-sided flux magnetic coupler for electric vehicle IPT charging systems," *IEEE Trans. Ind. Electron. Soc.*, vol. 60, no. 1, pp. 318–328, Jan. 2013.
- [75] G. Ombach, "Design and Safety Considerations of Interoperable Wireless Charging System for Automotive," Ninth International Conference on Ecological Vehicles and Renewable Energies, EVER 2014, 25-27 March 2014, pp.1-4.
- [76] R. Shimizu, Y. Kaneko and S. Abe, "A New Hc Core Transmitter of a Contactless Power Transfer System that is Compatible with Circular Core Receivers and H-shaped Core Receivers," in *Proc. 3rd Int. Electric Drives Production Conf. (EDPC)*, 2013, pp. 1–7.
- [77] A. Zaheer, H. Hao, G. A. Covic and D. Kacprzak, "Investigation of Multiple Decoupled Coil Primary Pad Topologies in Lumped IPT Systems for Interoperable Electric Vehicle Charging," *IEEE Trans. on Power Electronics*, vol. 30, no. 4, pp. 1937–1955, Apr. 2015.
- [78] H. Hao, G. A. Covic and J. T. Boys, "Parallel Topology for Inductive Power Transfer Power Supplies," *IEEE Trans. on Power Electronics*, vol. 29, no. 3, pp. 1140–1151, Mar. 2014.

## *Appendices*

## ***Appendix A: Equivalent Resistive Load $R_e$***

The method of Fundamental Harmonic Approximation (FHA) is widely used in resonant converter analysis. It consists in treating the current and voltage waveforms as pure sinusoids at the fundamental frequency and neglects other high-order harmonics [23], [33], [43]. The effective resistance  $R_e$  seen by the secondary is equal to the FHA of  $\frac{u_2(t)}{i_2(t)}$ . The value of  $R_e$  depends on the secondary compensation topology: series (S) or parallel (P). Then the value of  $R_e$  for the two cases can be derived as (6) [23].

$$R_e = \begin{cases} \frac{8}{\pi^2} R_L & \text{for Series secondary compensation} \\ \frac{\pi^2}{8} R_L & \text{for Parallel secondary compensation} \end{cases} \quad (68)$$

### ***A.I: SS Resonant DC-DC Converter***

The SS resonant converter shown in Fig. A.1 has a squared voltage  $u_2(t)$  and a sinusoidal current  $i_2(t)$  as inputs for the diode bridge. Considering the FHA mentioned in I.4; the following relations can be stated:

$$u_{2_{FH}} = \frac{4}{\pi} U_0 \text{ (First Harmonic of the input voltage of the rectifier with respect to output voltage)}$$

$$|i_2| = \frac{2}{\pi} i_{2_{FH}} \quad \text{(The output current is the rectification of the first harmonic of input current to the bridge rectifier)}$$

$$\text{But } R_e = \left( \frac{u_2}{i_2} \right)_{FH} = \frac{\frac{4}{\pi} U_0}{\frac{2}{\pi} |i_2|} = \frac{8}{\pi^2} \frac{U_0}{|i_2|} = \frac{8}{\pi^2} R_L.$$

The simplified circuit of secondary series resonant converter is shown in Fig. A1.

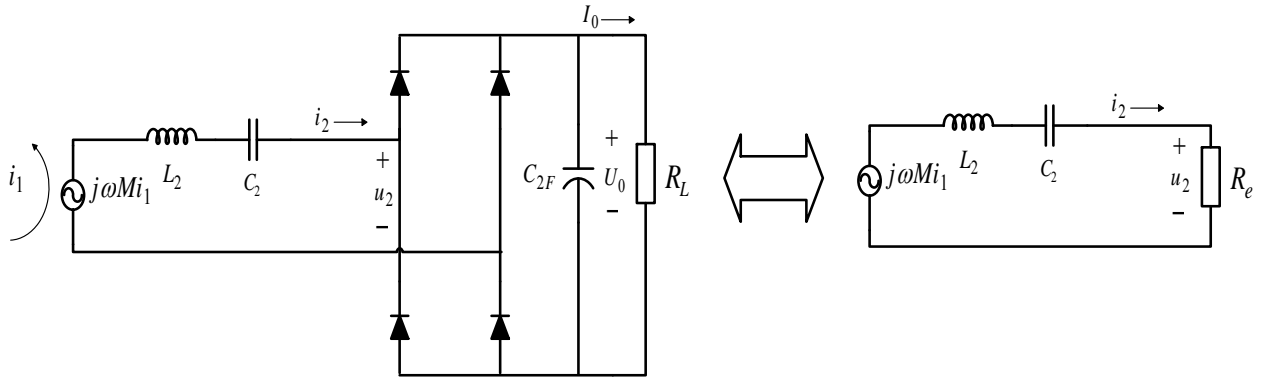


Fig. A.1: Schematics of secondary side Series compensation: full circuit (left) and equivalent circuit of FHA (right)

### A.II: SP Resonant DC-DC Converter

The SP resonant converter shown in Fig. A.2 has a sinusoidal voltage  $u_2(t)$  and a squared current  $i_2(t)$  as inputs for the diode bridge. Thus for validating the FHA, a series inductor  $l_{2f}$  is inserting at the output of the diode bridge as a filter (large enough) for the output current  $|i_2|$ . And so:

$$U_0 = \frac{2}{\pi} u_{2FH} \quad (\text{The output voltage is the rectification of the first harmonic of input voltage of the bridge rectifier})$$

$$i_{2FH} = \frac{4}{\pi} |i_2| \quad (\text{First Harmonic of the input current of the rectifier with respect to output current})$$

$$\text{But } R_e = \left( \frac{u_2}{i_2} \right)_{FH} = \frac{\frac{\pi}{2} U_0}{\frac{4}{\pi} |i_2|} = \frac{\pi^2}{8} \frac{U_0}{|i_2|} = \frac{\pi^2}{8} R_L$$

The simplified circuit of secondary parallel resonant converter is shown in Fig. A.2.

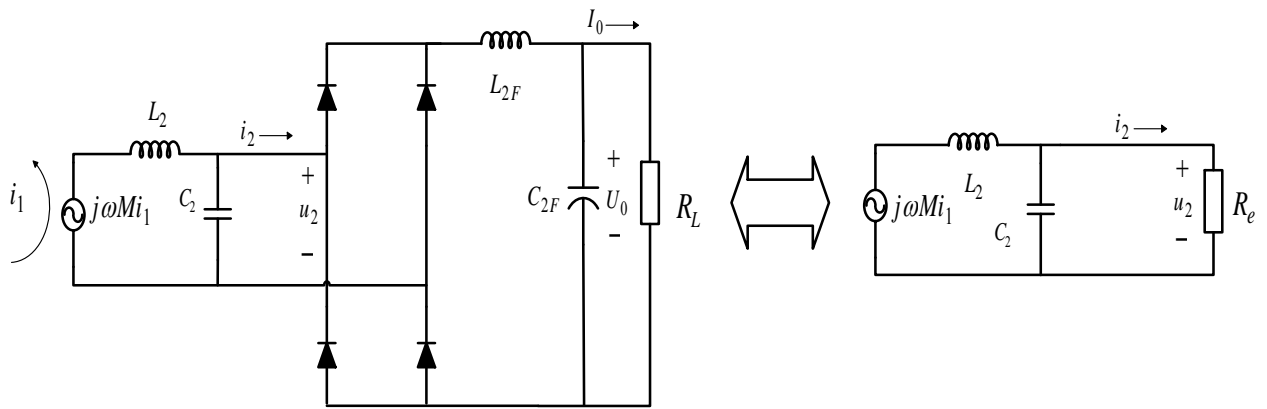


Fig. A. 2: Schematics of secondary side Parallel compensation: full circuit (left) and equivalent circuit of FHA (right)

## Appendix B: Frequency Behavior for a Resistive Load

Here, different parameters frequency responses plots for the three compensations topologies detailed in Chapter III are shown. The plots are drawn from the analytical equations presented in Chapter III. The load considered here is the resistive load  $R_e$  from the FHA analysis.

### B.I: SS Self Inductances Compensations $SS_L$

For the  $SS_L$  circuit shown before in Chapter III; all plots of  $(Z_{in})$  and its phase, and  $PF$  for the three values of  $k$  can be given as a function of the normalized frequency  $\omega_N$ .

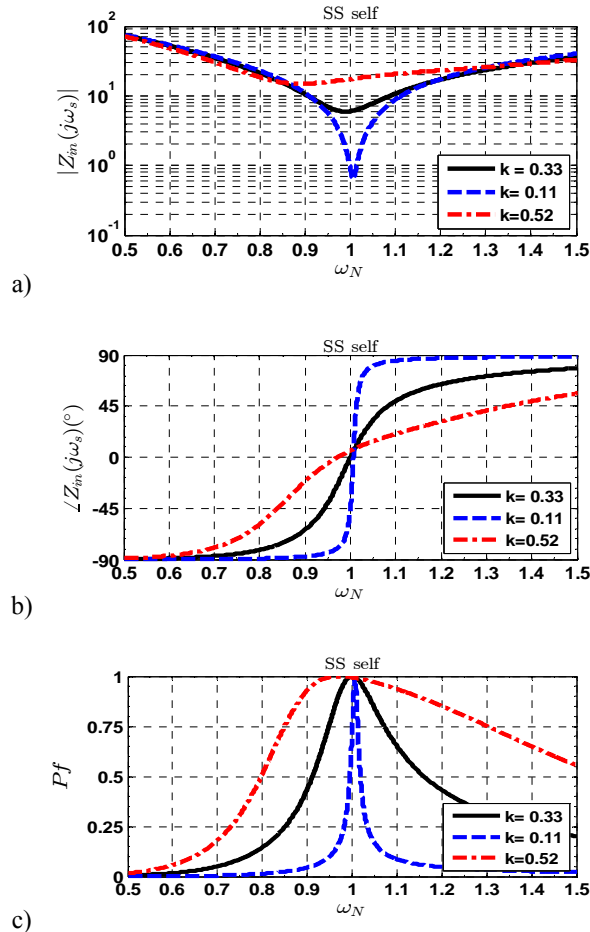


Fig. B.1: SS self parameters plot as a function of  $\omega_N$  for different values of  $k$ : a)  $|(Z_{in})_{SS}|$  b) phase of  $(Z_{in})_{SS}$  and c)  $Pf$



$|G_v|$  is plotted as a function of  $\omega_N$ . Moreover, it is interesting to plot the inverse of  $G_v$  as the secondary voltage is unchanged since the charger output is always  $U_0$ . This gives information about the input primary voltage at the inverter output  $v_1$ .

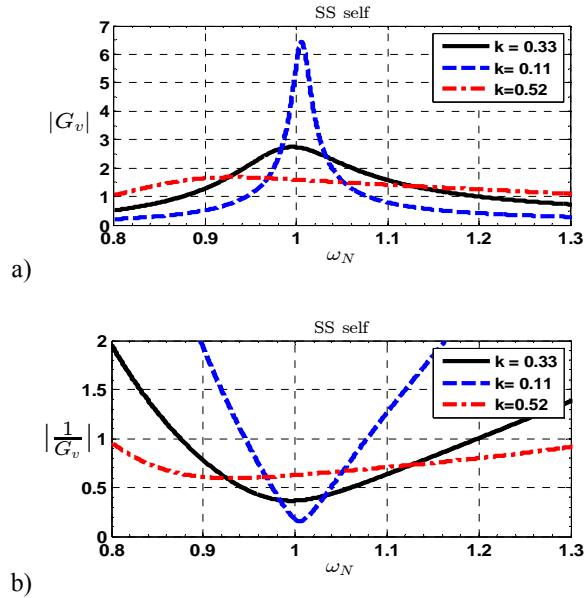


Fig. B.2: Plot of: a)  $|G_v|$  and b)  $1/|G_v|$  as a function of  $\omega_N$

Also three values of  $R_e$  are considered: a reference value of  $R_e$  ( $U_0 = 400V$ ,  $P_0 = 3kW$ ,  $I_0 = 7.5A$ ,  $R_e = 43.23\Omega$ ),  $R_e$  very high ( $R_e \rightarrow \infty$ , open circuit default) and very low ( $R_e \rightarrow 0$ , short circuit default). The two last cases are considered as limits.

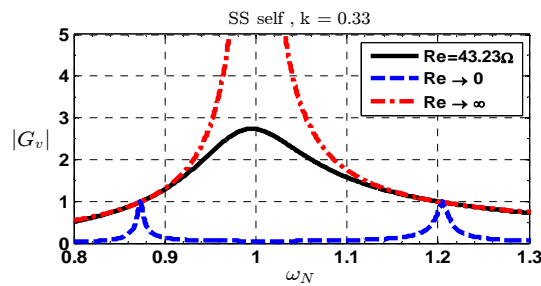


Fig. B.3: SS self  $|G_v|$  plot as a function of  $\omega_N$  for different values of  $R_e$  for  $k_2$ (ref. case)

Finally, as stated before, the resonant elements (L's & C's) voltages and current stress are studied. The normalized of elements voltages to a fixed output voltage imposed by the battery  $U_0$  and fixed absorbed current  $I_0$  (i.e.,  $U_0 = 400V$ ,  $I_0 = 7.5A$ ) are derived as usual, in all

derivations,  $R_e$  is fixed. The normalized voltages  $V_{L1N}$ ,  $V_{C1N}$ ,  $V_{L2N}$ ,  $V_{C2N}$  and the normalized currents  $I_{L1N}$ ,  $I_{C1N}$ ,  $I_{L2N}$ ,  $I_{C2N}$  (51)-(54). Their variations as function of  $\omega_N$  are also traced.

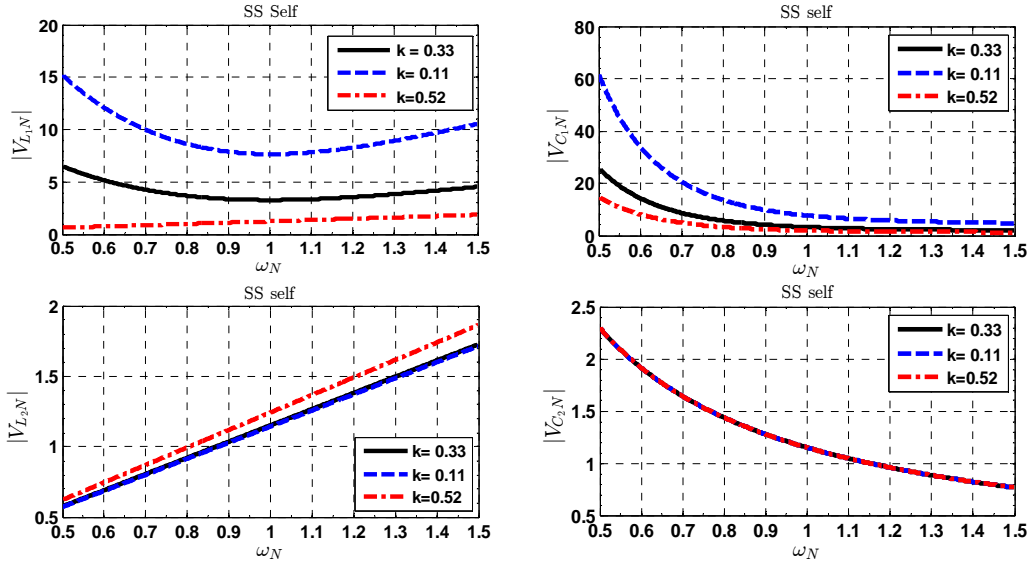


Fig. B.4: SS leakage compensation topology normalized L's and C's Currents of the resonant circuit as a function of the normalized frequency  $\omega_N$  for different  $k$

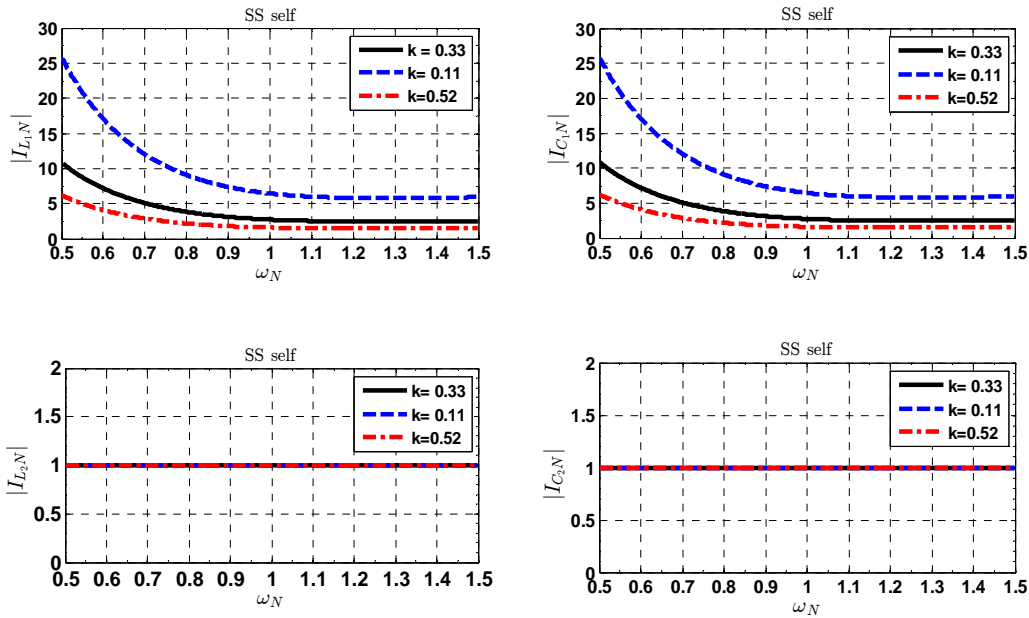


Fig. B.5: SS leakage compensation topology normalized L's and C's Currents of the resonant circuit as a function of the normalized frequency  $\omega_N$  for different  $k$

### B.II: SS Leakage Inductances Compensations $SS_{\ell}$

Same procedure as in previous, all graphs presents the parameters' plots as a function of  $\omega_N$  for the  $SS_{\ell}$ .

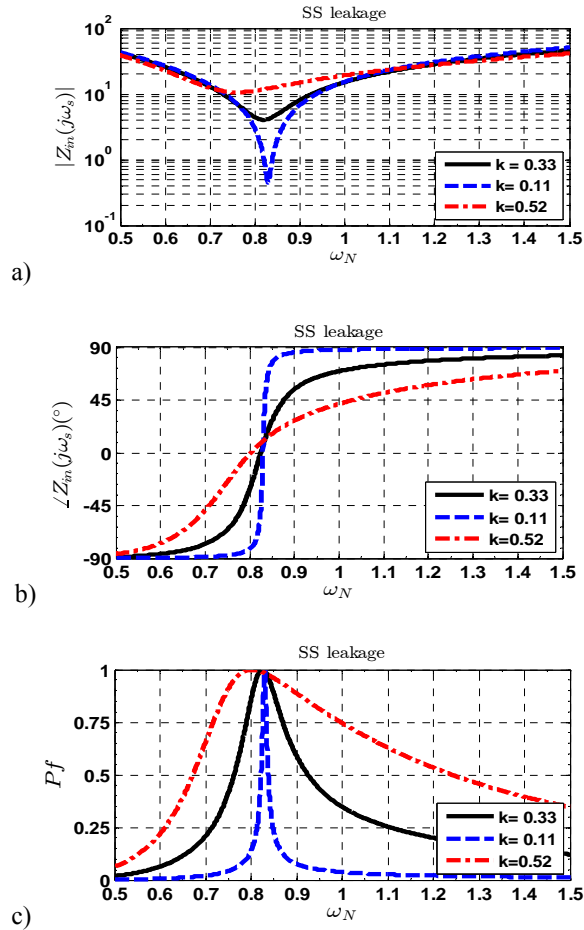


Fig. B.6: SS leakage parameters plot as a function of  $\omega_N$  for different values of  $k$ : a)  $|Z_{in}|_{SS_{\ell}}$  b) phase and c)  $Pf$

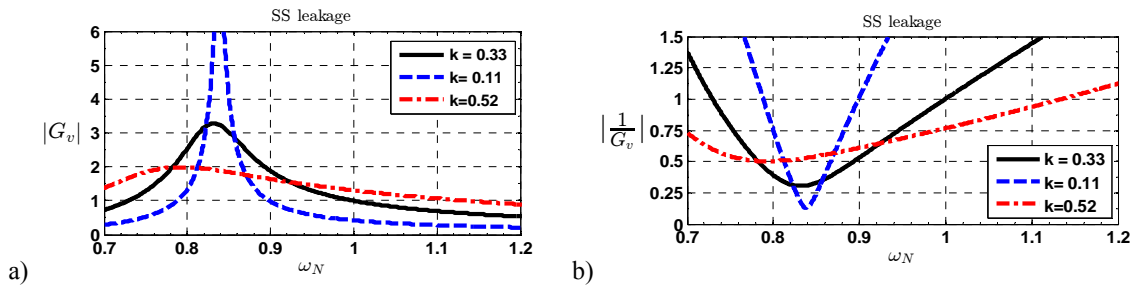


Fig. B.7: Plot of: a)  $|G_v|$  and b)  $|1/G_v|$  as a function of  $\omega_N$  for  $SS_{\ell}$

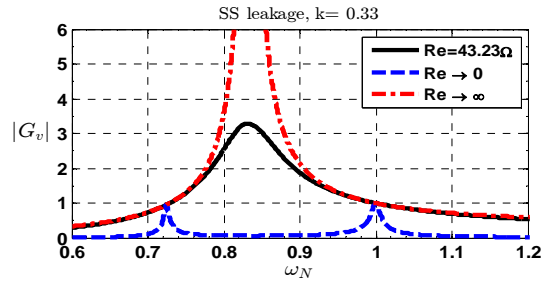


Fig. B.8: SS leakage  $|G_v|$  plot as a function of  $\omega_N$  for different values of  $R_e$  for  $k_2$ (ref. case).

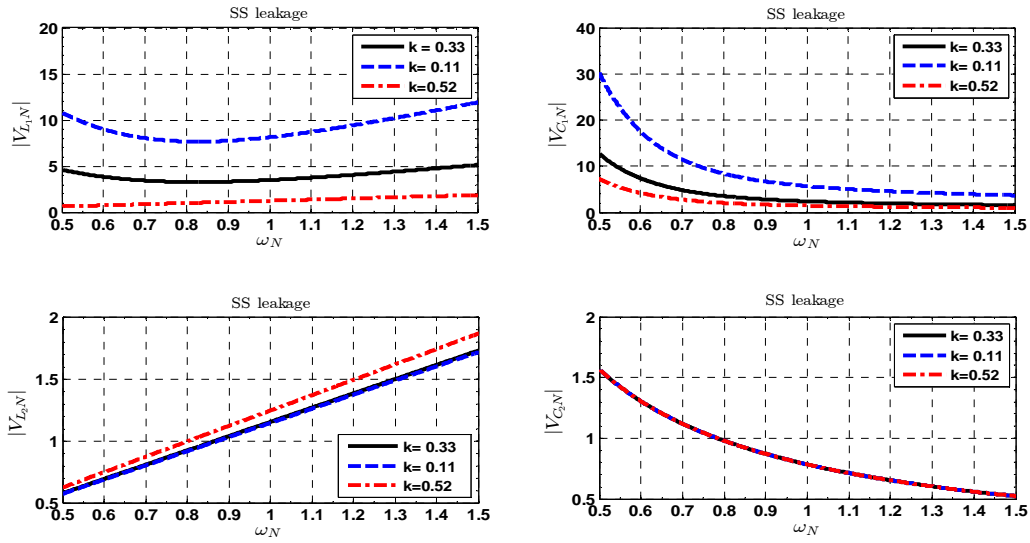


Fig. B.9:  $SS_\ell$  topology normalized L's and C's Voltages as a function of  $\omega_N$  for different  $k$

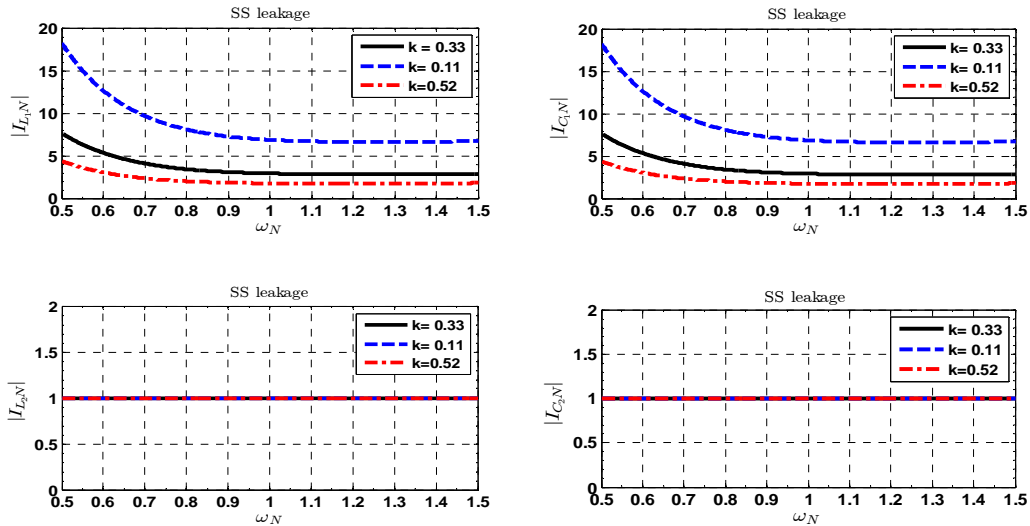


Fig. B.10:  $SS_\ell$  topology normalized L's and C's Currents as a function of  $\omega_N$  for different  $k$

### B.III: SP Inductances Compensations

Finally the parameters plots as a function of  $\omega_N$  for SP topology are shown here.

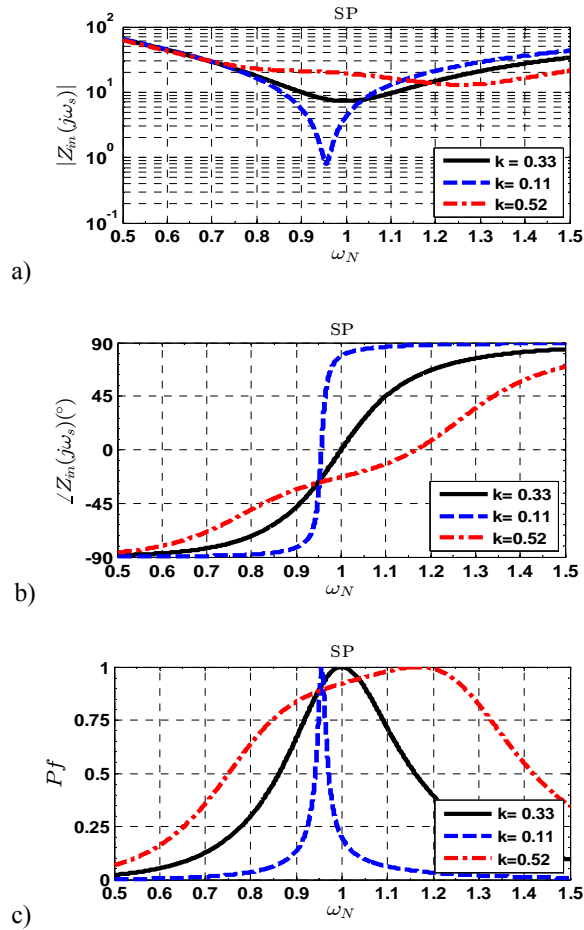


Fig. B.11: SP parameters plot as a function of  $\omega_N$  for different values of  $k$  :a)  $|Z_{in})_{SP}$  | b) its phase and c)  $Pf$

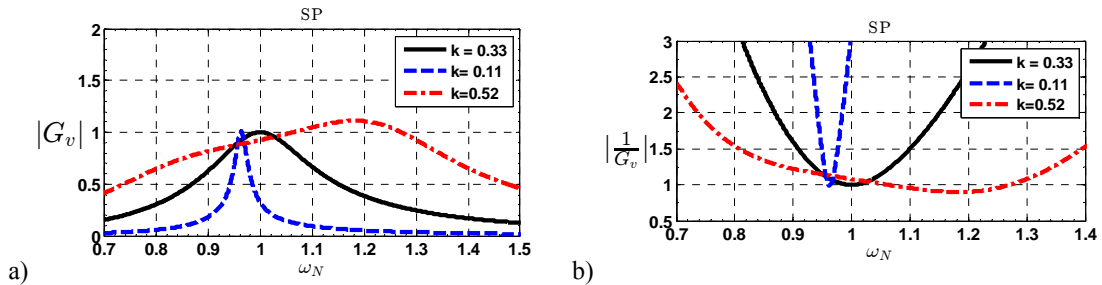


Fig. B.12: SP topology, Plot of: a)  $|G_v|$  and b)  $|1/G_v|$  as a function of  $\omega_N$

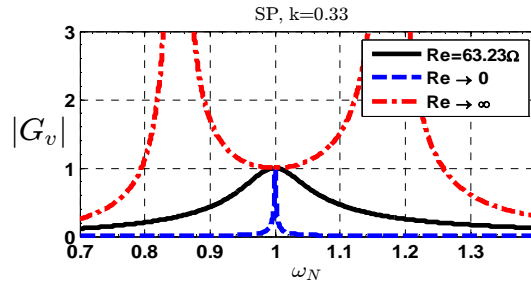


Fig. B.13: SP  $|G_v|$  plot as a function of  $\omega_N$  for different values of  $R_e$  for  $k_2$ (ref. case)

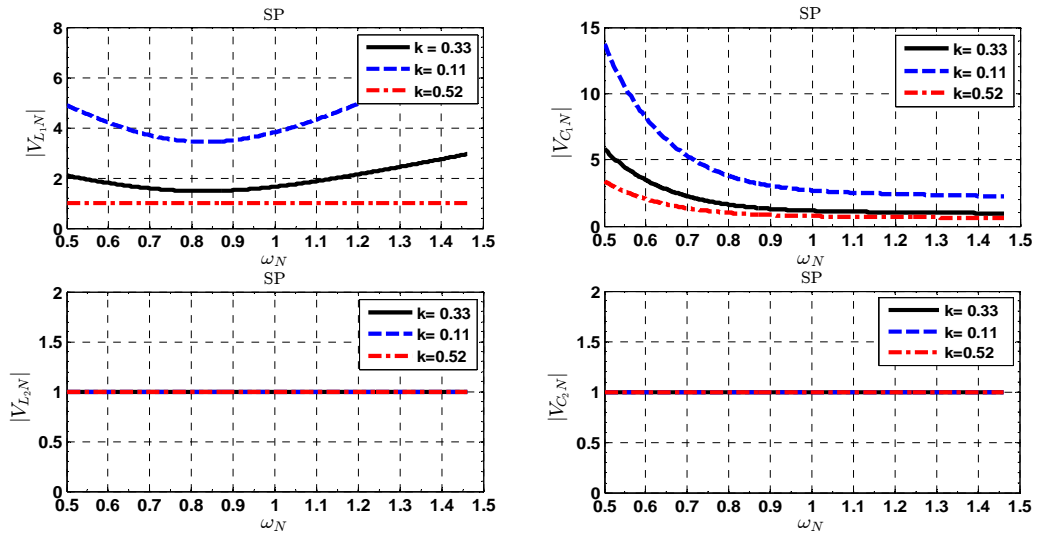


Fig. B.14: SP topology normalized L's and C's Voltages as a function of  $\omega_N$  for different  $k$

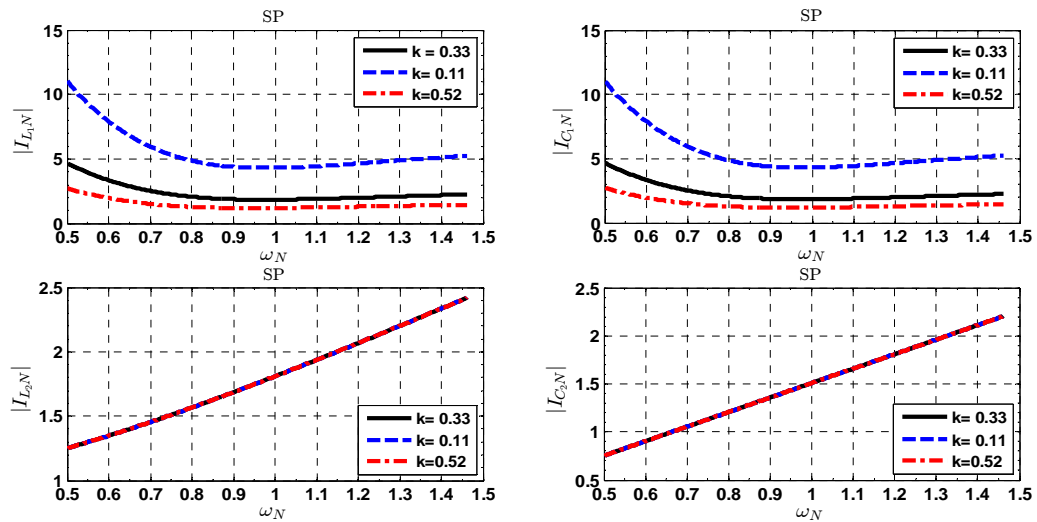


Fig. B.15: SP topology normalized L's and C's Currents as a function of  $\omega_N$  for different  $k$

## ***Appendix C: Simulation Results for Test Bench V1 for Different Prototypes.***

The only results from this test (3 kW, 300 V) that are available are for the measurements of the  $|B|$  levels in the points that shown before in Fig. IV.2. Simulation results are shown for a 3 kW, 300 V battery charging for the same situation appeared in RNO-RNO prototype test ( $d = 0.1 m$ ,  $sh = 0$ ). The values of the resonant capacitors are calculated from the reference inductances case ( $d = 0.15 m$ ,  $sh = 0$ ) at 30 kHz.

The values of the  $L_1$ ,  $L_2$  for all prototypes are found from Fig. II.20 and Fig. II.21. Moreover the global frequency can be obtained from Fig. III.18. The ICT pads dimensions were shown before in Chapter II TABLE III and TABLE V.

Next tables include: the electrical quantities for each test simulation, the measurements of  $|B|$  levels at the points (H, D, I, J and K) for an input resonance current  $\frac{I_1}{\sqrt{2}} [0^\circ A$  and secondary one  $\frac{I_2}{\sqrt{2}} [90^\circ A$  that found in simulation.

### ***C.1 SE-RNO Prototype (Test Bench V1)***

TABLE XVIII: SIMULATION PARAMETERS FOR SE-RNO IPT PROTOTYPE BENCH V1

<b>Parameter</b>	<b>Simulated</b>	<b>Parameter</b>	<b>Simulated</b>
$U_i(DC)$	330 V	$i_1$	15 A
$I_i(DC)$	9.3 A	$i_2$	16 A
$f_s$	30.3 kHz	$V_{C1}$	985 V
$L_1$	324 $\mu$ H	$V_{C2}$	764 V
$L_2$	283 $\mu$ H	$U_0(DC)$	300 V
$M$	145 $\mu$ H	$I_0(DC)$	9.83 A
$C_1$	88 nF	$P_0$	2949 W
$C_2$	110 nF	$\eta$	95%

TABLE XIX:  $|B|$  LEVELS VALUES SE-RNO TEST BENCH V1

Point	Simulated	Measured
$H$	0.2	0.6 $\mu\text{T}$
$D$	2 $\mu\text{T}$	2.2 $\mu\text{T}$
$I$	4 $\mu\text{T}$	3.7 $\mu\text{T}$
$K$	5.35 $\mu\text{T}$	5 $\mu\text{T}$
$J$	4.3 $\mu\text{T}$	4.5 $\mu\text{T}$

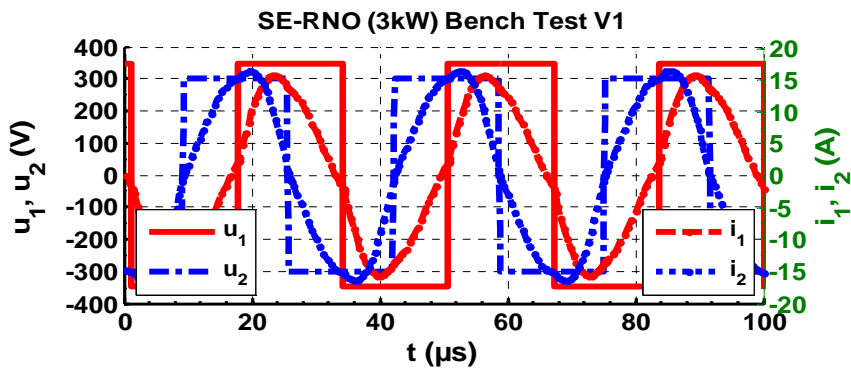


Fig. C.1: Plots of  $u_1$  and  $i_1$  SE-RNO Bench V1 simulation results

### C.2 NTC-RNO Prototype (Test Bench V1)

TABLE XX: SIMULATION PARAMETERS FOR NTC-RNO IPT PROTOTYPE BENCH V1

Parameter	Simulated	Parameter	Simulated
$U_i(DC)$	310 V	$i_1$	15 A
$I_i(DC)$	9.55 A	$i_2$	15.3A
$f_s$	27.3 kHz	$V_{C1}$	1121 V
$L_1$	375.53 $\mu\text{H}$	$V_{C2}$	810 V
$L_2$	276.63 $\mu\text{H}$	$U_0(DC)$	300 V
$M$	151.2 $\mu\text{H}$	$I_0(DC)$	9.65 A
$C_1$	78 nF	$P_0$	2895 W
$C_2$	110 nF	$\eta$	97%



TABLE XXI:  $|B|$  LEVELS VALUES NTC-RNO TEST BENCH V1

Point	Simulated	Measured
<i>H</i>	0.2	0.46 $\mu\text{T}$
<i>D</i>	1.4 $\mu\text{T}$	0.82 $\mu\text{T}$
<i>I</i>	3.8 $\mu\text{T}$	2.5 $\mu\text{T}$
<i>K</i>	5 $\mu\text{T}$	3.7 $\mu\text{T}$
<i>J</i>	4 $\mu\text{T}$	3.05 $\mu\text{T}$

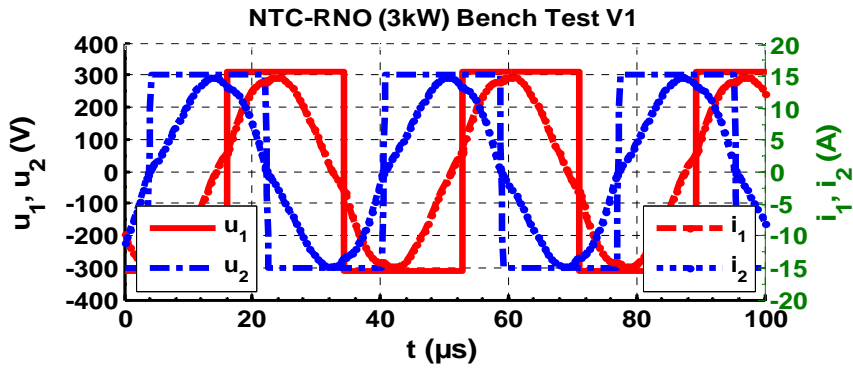


Fig. C.2: Plots of  $u_1$  and  $i_1$  NTC-RNO Bench V1 simulation results

### C.3 NTC-NTC Prototype (Test Bench V1)

TABLE XXII: SIMULATION PARAMETERS FOR NTC-NTC IPT PROTOTYPE BENCH V1

Parameter	Simulated		
$U_i(DC)$	405 V	$i_1$	11.5 A
$I_i(DC)$	7.3 A	$i_2$	15.8 A
$f_s$	30 kHz	$V_{C1}$	802 V
$L_1$	398 $\mu\text{H}$	$V_{C2}$	1074 V
$L_2$	394 $\mu\text{H}$	$U_o(DC)$	300 V
$M$	194 $\mu\text{H}$	$I_o(DC)$	9.8 A
$C_1$	76 nF	$P_0$	2940 W
$C_2$	78 nF	$\eta$	99%

TABLE XXIII:  $|B|$  LEVELS VALUES NTC-NTC TEST BENCH V1

Point	Simulated	Measured
<i>H</i>	0.2	0.3 $\mu\text{T}$
<i>D</i>	4.5 $\mu\text{T}$	3.65 $\mu\text{T}$
<i>I</i>	3.5 $\mu\text{T}$	2.49 $\mu\text{T}$
<i>K</i>	8.5 $\mu\text{T}$	7.08 $\mu\text{T}$
<i>J</i>	4 $\mu\text{T}$	3.04 $\mu\text{T}$

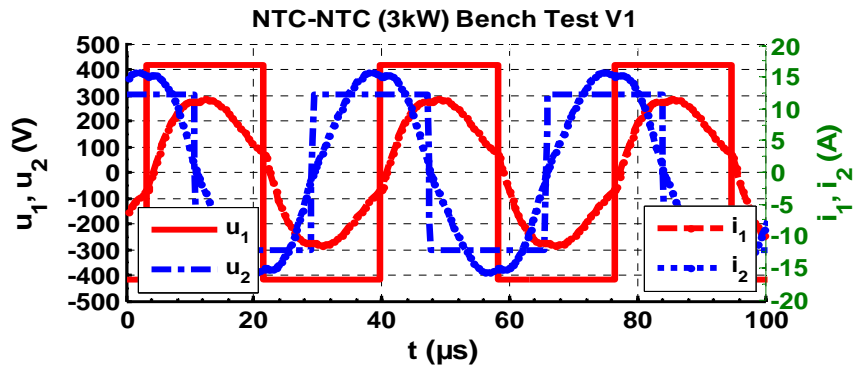


Fig. C.3: Plots of  $u_1$  and  $i_1$  NTC-NTC Bench V1 simulation results

### C.5 SE-NTC Prototype (Test Bench V1)

TABLE XXIV: SIMULATION PARAMETERS FOR SE-NTC IPT PROTOTYPE BENCH V1

Parameter	Simulated	Parameter	Simulated
$U_i(DC)$	400 V	$i_1$	11.5 A
$I_i(DC)$	7.32 A	$i_2$	15.6 A
$f_s$	30 kHz	$V_{C1}$	717 V
$L_1$	353 $\mu\text{H}$	$V_{C2}$	1061 V
$L_2$	394 $\mu\text{H}$	$U_0(DC)$	300 V
$M$	192 $\mu\text{H}$	$I_0(DC)$	9.4 A
$C_1$	85 nF	$P_0$	2820 W
$C_2$	78 nF	$\eta$	96%

TABLE XXV:  $|B|$  LEVELS VALUES SE-NTC TEST BENCH V1

Point	Simulated	Measured
<i>H</i>	0.2	0.3 $\mu\text{T}$
<i>D</i>	4.35 $\mu\text{T}$	3.4 $\mu\text{T}$
<i>I</i>	3.3 $\mu\text{T}$	2.3 $\mu\text{T}$
<i>K</i>	8.5 $\mu\text{T}$	7 $\mu\text{T}$
<i>J</i>	4 $\mu\text{T}$	3 $\mu\text{T}$

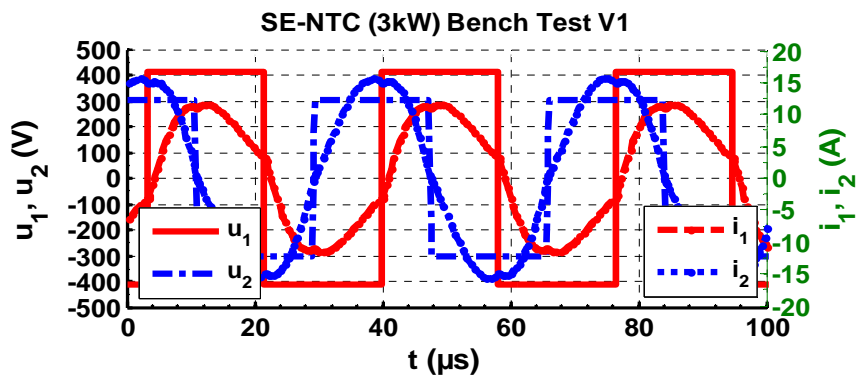


Fig. C.4: Plots of  $u_1$  and  $i_1$  SE-NTC Bench V1 simulation results





## *Curriculum Vitae*

Mohammad IBRAHIM

☎ : (+33) 6 44 26 74 91, ✉ [mf.ibrahim@hotmail.com](mailto:mf.ibrahim@hotmail.com)

### *Academic*

**Nov/2011-Nov/2014: Ph.D. student, Electrical Engineering, Thesis « Wireless Inductive Charging of Electrical Vehicles: Electromagnetic Modelling and Interoperability Analysis »**, University of PARIS-SUD, FRANCE.

**Date of PH.D Defense: 9.12.2014.**

**2010-2011: M.Sc.**, M2R PIE (Physics and Engineering Energy), SPEE (Science Prospective of Electrical Energy), (ENS-CACHAN University and PARIS-SUD University).

**2003-2008: B.Sc.** in Electrical Engineering, Faculty of Engineering, BirZeit University, Palestine. Double Major: Power & Control, Communications.

### *Professional Experience*

**2011-2014: (3 Years) Ph.D. preparation**, Laboratory of “Laboratoire de Génie Electrique de Paris- LGEP”, Gif sur Yvette, FRANCE. The PhD thesis is under project CINELI (Chargeur INductif ELectrique et Interoperabilité) with industrial partners: RENAULT, Schneider-Electric and NewTech Concept. Key Words: Contactless EV Charger, EMC Radiation, Electromagnetic Modelling, Advanced Power Electronics, Resonant Converter, Human Exposure, Interoperability, MATLAB, COMSOL.

**2010-2011: (6 months) Internship for Master study**, « **EMC of Power Electronics: HF Modeling of a Commutation Cell** », Laboratory of “Laboratoire-SATIE”, ENS-CACHAN, FRANCE. Key Words: Conducted EMC, Advanced Power Electronics, Signal Processing, State Equations, Transfer Function, MATLAB, SPICE.

**2009-2010: (12 months) Electrical Engineer**, Department of Electrical Engineering and Sales, (Electrical Generators, UPSs, Construction and Installation of cables and network, PV and Wind Turbines Systems), The Engineering for Trading & Contracting Company (ETCO), Ramallah, Palestine.

**2008-2009: (3 months) Engineer** of products, Department of Radio Communication, *Baransi for Communications and Intelligent* Company (BCI), Ramallah, Palestine.

**2008: Final year project of undergraduate study, « The Design of a Treadmill for Sports »:** Application of advanced power electronics and DC machine drive, BirZeit University, Palestine. Teacher assistant for third and fourth year's students.

**2007: (2 months) Internship** at Palestine Communications PALTEL Company and JAWWAL Wireless Mobile Communications Company, Ramallah, Palestine.

### Conferences

-IBRAHIM, M.; PICHON, L.; BERNARD, L. and RAZEK, A., "A 3D Electromagnetic Analysis and Circuit Modeling for Wireless Charging of Electrical Vehicles", international conference on *Computation of Electromagnetic Fields (COMPUMAG)*, Budapest 2013.

-IBRAHIM, M.; PICHON, L.; BERNARD, L. and RAZEK, A., " Electromagnetic Model of EV Wireless Charging Systems in view of Energy Transfer and Radiated Field Control", *International Symposium on Electromagnetic Fields (ISEF)*, Ohrid, Macedonia, 2013.

-IBRAHIM, M.; PICHON, L.; BERNARD, L. and RAZEK, A., " Wireless Charging of Electrical Vehicle Battery by Magnetic Inductive Loops and its Radiation Field Study", *Palestinian Conference on Graduate Student Research in Natural and Applied Sciences, BirZeit University, Palestine, 22 Mar. 2014. (Best Presentation Oral in the Conference )*.

-IBRAHIM, M.; PICHON, L.; BERNARD, L. and RAZEK, A., " Etude des caractéristiques et du champ rayonné par le coupleur inductif d'un système de recharge sans contact pour véhicule électrique ", Symposium de Génie Electrique, 8-9 Juillet 2014, Cachan, Paris/France.

### Journals

-M. Ibrahim, L. Pichon, L. Bernard, A. Razek, J. Houivet, O. Cayol, "Advanced Modeling of a 2kW Series-Series Resonating Inductive Charger for Real Electric Vehicle", to appear in *IEEE Vehicular Technology Transaction*, 2014.

-M. Ibrahim, L. Bernard, L. Pichon, A. Razek, "Electromagnetic Model of EV Wireless Charging Systems in View of Energy Transfer and Radiated Field Control, *International Journal of Applied Electromagnetics and Mechanics*, 46, pp 355–360, 2014.